SEARCH FOR THE RARE CHARGED DECAY KAON –> PION NEUTRINO ANTINEUTRINO

By

Jean Roy

B. Sc., Université de Montréal, 1986

M. Sc., The University of British Columbia, 1988

A THESIS SUBMITTED IN PARTIAL FULFILLMENT OF

THE REQUIREMENTS FOR THE DEGREE OF

DOCTOR OF PHILOSOPHY

in

THE FACULTY OF GRADUATE STUDIES

PHYSICS

We accept this thesis as conforming

to the required standard

THE UNIVERSITY OF BRITISH COLUMBIA

December 1994

In presenting this thesis in partial fulfilment of the requirements for an advanced degree at the University of British Columbia, I agree that the Library shall make it freely available for reference and study. I further agree that permission for extensive copying of this thesis for scholarly purposes may be granted by the head of my department or by his or her representatives. It is understood that copying or publication of this thesis for financial gain shall not be allowed without my written permission.

(Signature)

Department of PHYSICS

The University of British Columbia
Vancouver, Canada

Date 9-MARCH-1995

DE-6 (2/88)

Abstract

An experimental search for the flavour-changing weak neutral current decay $K^+ \rightarrow \pi^+\nu\overline{\nu}$ was performed in the π^+ kinematic energy range $60 < T_{\pi^+} < 100$ MeV. The Standard Model theoretical prediction for the branching ratio is within the bounds $(0.5\text{–}4.5)\times10^{-10}$. An observation at a rate significantly in excess of the prediction would be an indicator of new physics. The experiment was also sensitive to decays of the type $K^+ \rightarrow \pi^+X^0$, where X^0 is a weakly interacting massive neutral particle with mass in the range $150 < M_{X^0} < 260$ MeV/c^2.

The search was carried out at Brookhaven National Laboratory, using an intense beam of positively charged kaons. A specialized detector selected candidate $K^+ \rightarrow \pi^+\nu\overline{\nu}$ decays among a large background of other processes by identifying K^+ decays at rest, measuring the momentum, kinetic energy and range of the π^+ , recording its decay sequence for positive identification and vetoing photons from background processes. Data were collected in two different periods in 1989 and 1991.

After analysis of the 1989 data set, no events were observed, allowing a 90% confidence level upper limit of 1.7×10^{-8} to be set for the branching ratio. This is a factor of 55 improvement over the previous experiment using the same region of phase space. Studies performed after the analysis was completed led to an estimated expected background of less than one event.

In the 1991 data set, a total of 4 events were observed, with an estimated background of less than two events. The studies leading to this estimate were performed before the final analysis was carried out, resulting in reduced bias. However, uncertainties in the background estimate precluded the identification of the source of the events. Therefore, an upper limit of 5.0×10^{-8} was set for the branching ratio, based on the observation of 4 events.

Table of Contents

List of Tables

List of Figures

Acknowledgement

As I finally bring this work to a conclusion after so many years of research, I look back and realize how fortunate I was to interact with the people in the BNL E787 group. Pretty much all I have learned as an experimentalist I owe to them. I can honestly say that I benefited from the knowledge of each and every one of them. There were of course some key figures: My advisor, Jean-Michel Poutissou, who was always there to help me and communicate some of his great passion for research, even though his duties made him one of the busiest people at TRIUMF: Doug Bryman, on whom I could always count to put me back on the right track when I got confused, and who always made sure that our research environment was the best it could be: Finally, Akira Konaka, whose endless enthusiasm and insightful ideas were a constant source of inspiration. Thanks to all.

I was just as fortunate to have the support of some wonderful people outside of the academic world. Even though they were so far away, my family managed to provide constant encouragement. They have taught me that even though it is nice to gain knowledge about the intricacies of the Universe, there is no substitute for good values of honesty and determination. Merci du fond du coeur à mes parents Louise et Gilles, et ma soeur Line.

My in-laws, Jean and Ian Beveridge, were always there to help and make me feel like their son. Many thanks to them. Also thanks to the Norbies (who ever came up with that name anyway ?) for the soccer games and the long discussions about the space-time continuum (there, I said it) over a few (!!!) beers.

And finally, I must thank my wife Jennifer, whose undying support pulled me through the good and bad times. I cannot find the right words to express my gratitude to her, and how much it means to me to have her as my companion. I just hope that over the years I will be able to repay her for all she did for me.

To the memory of

J. Armand Samoisette

Chapter 1

The Experiment

1.1 Introduction

The current theoretical framework describing the interactions of elementary particles, known as the Standard Model, is one of the most resounding successes of modern physics. Over the past 60 years, knowledge of the basic constituents of matter and their interactions has evolved through many experimental and theoretical breakthroughs; this knowledge is now embodied in the Standard Model. In the past several years, essentially all results predicted by the Standard Model have agreed with amazing accuracy with experimental observations.

Despite this great success, the Standard Model is lacking in some ways. To calculate physical observables, it requires a large number of quantities, such as elementary particles masses, to be taken as parameters and be determined experimentally. The model does not make any predictions for these parameters as to their relationship or origin. Furthermore, elementary particles appear to be grouped in "families", or "generations"; the Standard Model accommodates this very well by using mathematical group theory representations. However, there is no indication as to the origin of these families and, in fact, no compelling reason to have more than a single family, other than perhaps to provide a mechanism for the violation of CP, the combined operation of charge conjugation (particle–anti-particle interchange) and parity inversion.

For these reasons, recent experimental and theoretical efforts have centered on the search for phenomena that are not described by the Standard Model, or for deviations between calculated observables and the experimental measurements. The experimental effort has been directed at

two fronts : the energy frontier and the precision frontier. By pushing the available energy in elementary particles collisions to higher and higher levels, smaller and smaller distances can be probed, potentially revealing structure hitherto undiscovered. The large available energy also allows for the production of new particles which might herald the discovery of new phenomena. Undiscovered interactions or particles can also be observed indirectly through their effects on lower energy processes; this requires the investigation of such processes using high precision techniques. This could be a search for processes not allowed by the Standard Model, or a search for deviations from predictions for allowed but rare processes.

This thesis describes one such endeavour, the experimental search for the decay of a positively charged K-meson (or kaon) into a positively charged π-meson (or pion) and a neutrino–anti-neutrino pair, represented by

$$K^+ \to \pi^+ \nu\overline{\nu} \,. \tag{1.1}$$

This decay is allowed in the Standard Model, and is predicted to occur approximately once in every 10 billion kaon decays; it has never been observed experimentally. One of the most attractive features of this process is the reliability of the theoretical calculation for its rate within the Standard Model. The decay rate is more commonly expressed as a branching ratio, the ratio of the decay rate for a particular process to the total rate for all possible decay processes. Some level of uncertainty remains in the calculation of the $K^+ \to \pi^+ \nu\overline{\nu}$ branching ratio due to the imprecise knowledge of some of the parameters required for the calculation. A measurement of the branching ratio would then allow the determination of these parameters with very little theoretical uncertainty. Also, an observation of this decay at a rate deviating significantly from the theoretical prediction would clearly be an indication of phenomena not accounted for by the Standard Model.

The remainder of this chapter will discuss the decay $K^+ \to \pi^+ \nu\overline{\nu}$ within the context of the Standard Model and present an overview of the experimental search. Chapter 2 describes the apparatus and Chapter 3 the experimental procedure. Studies of background processes are described in Chapter 4. Results are described in Chapter 5 and discussed in Chapter 6. Finally, a conclusion is given in Chapter 7.

1.2 Theoretical considerations

1.2.1 The Standard Model

A full description of the Standard Model would require far too much space for inclusion in this thesis. Extensive coverage of the subject can be found in the literature (see [1] for example); only a very brief overview will be presented here, introducing the key elements of the model. Because the decay $K^+ \to \pi^+\nu\overline{\nu}$ proceeds via the weak force, more details on weak interactions will be given below.

In our present description of the basic building blocks of Nature, elementary particles are classified in two groups, quarks and leptons. Both groups are spin 1/2 fermions; experiments place limits on their structure at the 10^{-17} cm level. There are currently six known leptons and five quarks, with strong theoretical bias and some experimental evidence for a sixth quark. In addition, each quark or lepton has an anti-particle counterpart, with the same mass and spin angular momentum but opposite values for other quantum numbers. The leptons consist of the electron (e), the muon (μ) and the tau (τ), and their associated neutrinos, ν_e, ν_μ and ν_τ. The e, μ and τ leptons each have unit electric charge; in fact, essentially all their properties are identical except for mass. The neutrinos are electrically neutral, and current experimental evidence is consistent with them being massless. The quarks have fractional charges (in units of the electron charge); three have charge -1/3, the down (d), strange (s) and bottom (b) quarks, and three have charge +2/3, the up (u), charm (c) and the as yet unconfirmed top (t).

Elementary particles interact via the four fundamental forces : electro-magnetism, weak, strong and gravity. These forces are mediated by the exchange of particles called intermediate vector bosons. Relativistic quantum field theory is the theoretical framework used to describe the interactions of elementary particles. The best example of such a theory is quantum electro-dynamics (QED), developed in the early 1930's, describing the interactions of charged particles and photons. This theory has enjoyed tremendous success, and has been tested with great accuracy; it served as a blueprint for theories describing other interactions.

In 1933, Fermi proposed his theory of weak interactions to describe nuclear beta decay.

The theory remains to this day, with a few modifications. A major breakthrough came in the 1960's by Glashow, Weinberg and Salam, who proposed a model unifying the electro-magnetic and weak interactions into a single framework based on the mathematical group $SU(2) \times U(1)$; it described the weak force as the exchange of massive bosons, and predicted their mass. Confirmation of the existence of these particles only came recently in investigations of high energy proton–anti-proton collisions [2]. This model became known as the Standard Model of electro-weak interactions. The Standard Model now also encompasses the description of strong interactions by quantum chromodynamics (QCD), a theory based on the mathematical group $SU(3)$. Strong interactions involve only the quarks and the massless mediators of the force, the gluons.

1.2.2 Weak Interactions

The weak interaction theory proposed by Fermi was analogous to QED in that it described processes in terms of the interaction between two currents. Figure 1.1a shows a graphical representation of the electro-magnetic interaction between an electron and a proton (assumed point-like) as the exchange of a photon, carrier of the force. Such representations, or Feynman diagrams, are associated with terms in a perturbative series describing the interaction. Figure 1.1a shows a first order term and figure 1.1b shows an example of a second order diagram describing the same process. These terms are used to calculate the invariant amplitude for the process; the square of the amplitude is proportional to the probability for the process.

The amplitude for the QED process in figure 1.1a is given by

$$\mathcal{M} = (e\overline{\psi}_p \gamma^\mu \psi_p) \left(\frac{-1}{q^2}\right) (-e\overline{\psi}_e \gamma_\mu \psi_e) \tag{1.2}$$

where the ψ and $\overline{\psi}$ are four-component spinors, solutions of the Dirac equation describing the proton and electron, γ_μ are the Dirac matrices ($\mu = 0, 1, 2, 3$), q is the momentum of the exchanged photon and e is the electric charge of the electron and proton. Here we have used the Heaviside–Lorentz convention for electro-magnetic units in which ϵ_0, the permittivity of free space, is set to unity, and "natural" units in which $\hbar$ and c are also set to unity. With these conventions, we have $e^2 = 4\pi\alpha$, where $\alpha \simeq 1/137.036$ is the fine structure constant. The

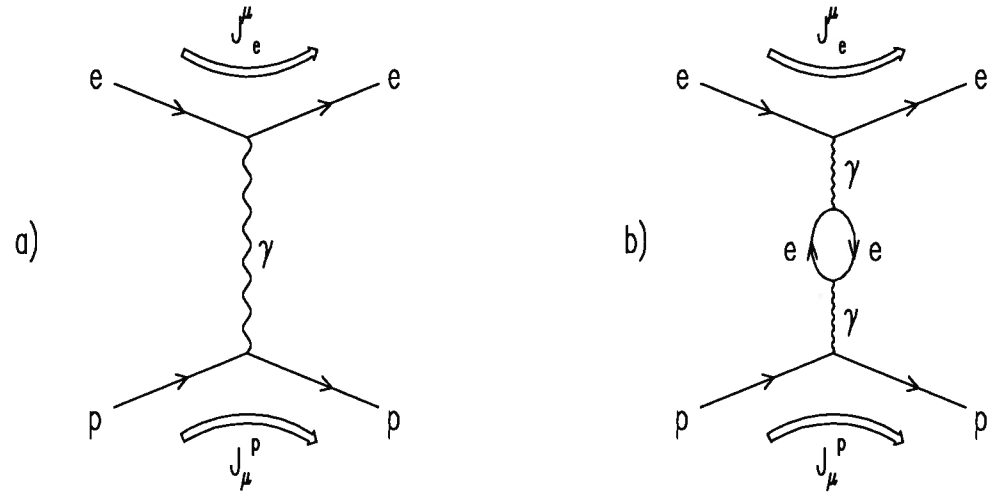

Figure 1.1: Feynman diagrams for electron–proton electro-magnetic scattering; a) first order and b) example of second order interaction.

amplitude $\mathcal{M}$ can be re-written as

$$\mathcal{M} = -\frac{e^2}{q^2} J_p^\mu J_\mu^e \tag{1.3}$$

where J_p^μ and J_μ^e are the proton and electron electro-magnetic currents respectively; the square of the electric charge e^2 is the constant coupling the two currents.

The Fermi theory was used to describe processes such as neutron decay :

$$n \rightarrow p\, e^-\, \overline{\nu}_e\,. \tag{1.4}$$

The process, or its equivalent crossed reaction $n\nu_e \rightarrow pe^-$, was viewed as a four particle point interaction, as shown by figure 1.2. The amplitude was given by

$$\begin{aligned} \mathcal{M} &= G(\overline{\psi}_p \gamma^\mu \psi_n)(\overline{\psi}_e \gamma_\mu \psi_\nu) \\ &= G_F J_N^\mu J_\mu^{e\nu} \end{aligned} \tag{1.5}$$

where J_N^μ and $J_\mu^{e\nu}$ are the neutron–proton and electron–neutrino weak currents respectively and G_F is the coupling constant for the interaction, determined by experiment.

This theory was successful at describing some properties of neutron decay and beta decays, but not all. One of the keys to solving this problem was the fact that Fermi had used only a vector form for the weak interaction. The γ^μ term in equation 1.5 behaves like a vector under

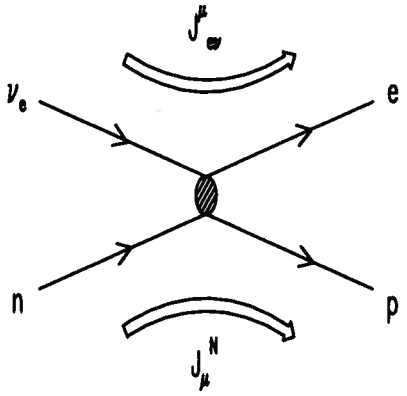

Figure 1.2: Feynman diagram for neutron decay in Fermi theory. The hashed circle indicates the point interaction.

Lorentz transformations. Other possibilities, namely scalar, tensor, axial vector and pseudo-scalar, had to be investigated. The next twenty years saw attempts at finding the correct structure of the weak interactions. One of the major stumbling blocks involved the decay of the newly discovered strange particles (particles containing a strange quark); these particles were produced in strong interactions, but they displayed the relatively long lifetime characteristic of weak interactions. The problem, the so-called θ–τ puzzle, was that the positively charged kaon, K^+, was observed to apparently have two different decay modes, $K^+ \rightarrow \pi^+\pi^0$ and $K^+ \rightarrow \pi^+\pi^+\pi^-$, in which the final states have opposite parity. Originally it was thought that two different types of charged kaons existed, the θ and τ, since it was believed that parity (or space inversion) was conserved in all interactions.

In 1956, Lee and Yang [3] carefully reviewed all available information on the weak interactions and argued that the problems could be solved if these interactions violated parity, and that this had never been tested experimentally. Experiments soon confirmed that this was indeed the case. It was eventually shown that the γ^μ term in the weak current should be replaced by $\gamma^\mu(1-\gamma^5)$ [4]. The $\gamma^\mu\gamma^5$ term transforms like an axial-vector under Lorentz transformation, hence the usual designation of weak interactions as having $V-A$ structure.

For many years, it was believed that although they violated parity (P), weak interactions were invariant under the combined operation CP, where C is the charge conjugation operator, or particle–anti-particle interchange. In 1964, a small CP violating effect was observed in neutral

kaon decay [13]. To this date, it is still the only known system in which CP violation has been observed. It will be shown below how a measurement of the branching ratio for the process $K^+ \to \pi^+ \nu \overline{\nu}$ may help to unravel the origin of this phenomenon.

In the modern version of the theory [5], the weak interactions are viewed as the exchange of massive vector bosons between quarks and leptons and among themselves. This construction reduces to the Fermi point interaction for low energy processes where the momentum of the exchanged boson is much lower than its mass. Quarks and leptons are grouped into doublets of the mathematical group $SU(2)$:

$$\begin{pmatrix} \nu_e \\ e^- \end{pmatrix} \quad \begin{pmatrix} \nu_\mu \\ \mu^- \end{pmatrix} \quad \begin{pmatrix} \nu_\tau \\ \tau^- \end{pmatrix}$$

$$\begin{pmatrix} u \\ d \end{pmatrix} \quad \begin{pmatrix} c \\ s \end{pmatrix} \quad \begin{pmatrix} t \\ b \end{pmatrix}$$

suggesting a "family" or generation structure to elementary particles. Doublets from each generation are treated identically by the theory.

In this framework, the example of neutron decay can be represented by the Feynman diagram of figure 1.3. The neutron and proton are identified as groups of three quarks, *udd* and *uud* respectively. One of the d quarks of the neutron decays into a u quark with emission of a W^- boson; the other quarks do not participate in the interaction and are referred to in this case as spectators. The emitted W^- then decays to an electron and an anti-neutrino.

1.2.3 Quark mixing

Another problem of the theory of the weak interactions in the early days was the calculation of the decay rate for strange particles, which did not agree with experimental observations. It appeared that the coupling constant G_F, determined from beta decay, was not universal for all weak decays. In 1963, Cabibbo [6] proposed that the weak current for strongly interacting particles (hadrons) was a sum of a strangeness conserving (j_μ^0) and a strangeness non-conserving

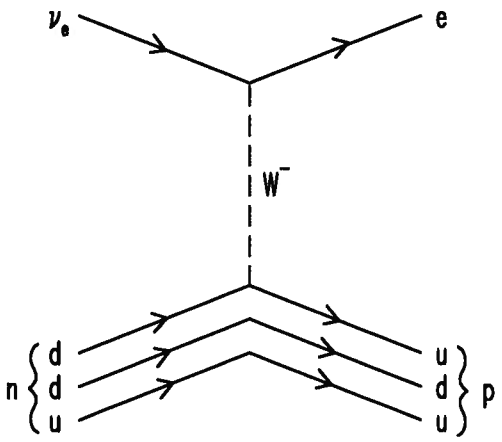

Figure 1.3: Feynman diagram for neutron decay in the Standard Model.

(j_μ^1) parts, related by

$$J_\mu^H = \cos\theta_c j_\mu^0 + \sin\theta_c j_\mu^1 \tag{1.6}$$

where the angle θ_c is now known as the Cabibbo angle. Therefore, for the decay of strange particles, the effective coupling was $G_F \sin\theta_c$ instead of simply G_F. Cabibbo obtained a consistent value for θ_c from the available data on various weak decays. The currently accepted value is $\theta_c = 0.22$.

In the framework of quark interactions, and for a situation where only three quarks are known (u, d and s), this formulation is equivalent to saying that the weak eigenstate for the charge -1/3 quarks (d') is an admixture of the d and s (quarks strong interaction eigenstates). The weak current can then be written as

$$\begin{aligned} J_\mu^H &= \overline{u}\gamma^\mu(1-\gamma^5)d' \\ &= \overline{u}\gamma^\mu(1-\gamma^5)(d\cos\theta_c + s\sin\theta_c) \end{aligned} \tag{1.7}$$

where u and d represent the quark spinors. Because it transforms a quark of electric charge -1/3 into a charge +2/3 quark (and vice-versa), this current is referred to as the charged weak current. In contrast, the electro-magnetic current of QED is neutral. This leads to a discussion of the possibility of weak neutral currents.

1.2.4 Neutral currents

In the early days of weak interactions, there were no reason to consider weak neutral currents simply because there were no experimental observation of such currents. This absence of observed weak neutral currents was a serious hurdle in the acceptance of a unified theory of the weak and electro-magnetic interactions [5]. Furthermore, we see that if we form the neutral current between the weak interaction quark eigenstates using the formalism of Cabibbo, we get, recognizing only u and d' as ingredients in the theory

$$\begin{aligned} J_\mu^{NC} &= \overline{u}u + \overline{d'}d' \\ &= \overline{u}u + (\overline{d}\cos\theta_c + \overline{s}\sin\theta_c)(d\cos\theta_c + s\sin\theta_c) \\ &= \overline{u}u + \overline{d}d\cos^2\theta_c + \overline{s}s\sin^2\theta_c + (\overline{d}s + \overline{s}d)\sin\theta_c\cos\theta_c \end{aligned} \tag{1.8}$$

where the $\gamma^\mu(1-\gamma^5)$ factors have been omitted for clarity. In addition to neutral interactions between the three types of quarks, or flavours, we have interactions where an s quark is transformed into a d quark, and vice-versa. Interactions of this type are known as flavour-changing neutral currents. Early searches for these interactions included $K^+ \to \pi^+e^+e^-$, $K_L^0 \to \mu^+\mu^-$ and $K^+ \to \pi^+\nu\overline{\nu}$, but no evidence was found. The first search for $K^+ \to \pi^+\nu\overline{\nu}$ was in 1969, finding that the branching ratio was less than 1×10^{-4} [32].

In 1970, Glashow, Iliopoulos and Maiani [7] proposed that there existed another charge $+2/3$ quark analogous to the u quark, which they named charm (c). The possibility of neutral currents remained, but the inclusion of the charm quark removed the flavour-changing neutral currents. This can be seen by arranging the quarks of same charge in column vectors $\mathcal{U}$ and $\mathcal{D}$:

$$\mathcal{U} \equiv \begin{pmatrix} u \\ c \end{pmatrix} \quad \mathcal{D} \equiv \begin{pmatrix} d \\ s \end{pmatrix}$$

The Cabibbo mixing is then given by a unitary rotation matrix M_c :

$$\begin{aligned} \mathcal{D}' &= M_c\,\mathcal{D} \\ \begin{pmatrix} d' \\ s' \end{pmatrix} &= \begin{pmatrix} \cos\theta_c & \sin\theta_c \\ -\sin\theta_c & \cos\theta_c \end{pmatrix} \begin{pmatrix} d \\ s \end{pmatrix} . \end{aligned} \tag{1.9}$$

We can then write the neutral current as a generalization of the previous guess :

$$\begin{aligned} J_\mu^{NC} &= \overline{\mathcal{U}}\mathcal{U} + \overline{\mathcal{D}'}\mathcal{D}' \\ &= \overline{\mathcal{U}}\mathcal{U} + \overline{\mathcal{D}}M_c^\dagger M_c\mathcal{D} \\ &= \overline{\mathcal{U}}\mathcal{U} + \overline{\mathcal{D}}\mathcal{D} \\ &= \overline{u}u + \overline{c}c + \overline{d}d + \overline{s}s \end{aligned} \tag{1.10}$$

where the $\gamma^\mu(1-\gamma^5)$ terms have again been omitted for clarity. We see that all we have left are neutral currents between quarks of the same flavour. This cancellation of flavour-changing neutral currents, shown here for first-order interactions, is exact to all orders; it is commonly referred to as "GIM mechanism". This mechanism would prohibit decays such as $K^+ \to \pi^+\nu\overline{\nu}$; however, as will be discussed below, the mass of the different quark flavours being unequal, this exact cancellation is spoiled and a small non-zero amplitude remains at second order and beyond.

Neutral currents were also predicted for leptons. The first direct evidence for neutral currents came in 1973 in neutrino and anti-neutrino interactions in a bubble chamber [8]. Also, in 1974 the charm quark was discovered simultaneously by two research groups [9, 10], establishing the theory of weak neutral currents on firmer ground. In modern electro-weak theory, neutral weak current processes are viewed as the exchange of neutral weak bosons (Z^0). As with the charged weak bosons (W^+ and W^-), the Z^0 was discovered only relatively recently [11].

1.2.5 Three generations quark mixing

The unitary matrix M_c introduced above, was described by a single real parameter θ_c, and combined the charge -1/3 mass eigenstates to obtain the weak interaction eigenstates for two generations of quarks. In 1973, Kobayashi and Maskawa [12] realized that for a model with three generations of quarks, the unitary matrix would be described by three real angles and one complex phase, and that this complex phase can describe for CP violation. This provides a natural link between the existence of three generations of elementary particles and the phenomenon of CP violation.

For three generations of quarks, we can write the 3×3 rotation matrix (usually referred to as the CKM, or Cabibbo–Kobayashi–Maskawa matrix) in the general form

$$V = \begin{pmatrix} V_{ud} & V_{us} & V_{ub} \\ V_{cd} & V_{cs} & V_{cb} \\ V_{td} & V_{ts} & V_{tb} \end{pmatrix} . \tag{1.11}$$

Note that the cancellation of flavour-changing neutral currents by the GIM mechanism is still valid for the three generations case, guaranteed by the unitarity of the matrix V.

In their original paper Kobayashi and Maskawa parameterized the matrix V as

$$V = \begin{pmatrix} c_1 & -s_1 c_3 & -s_1 s_3 \\ s_1 c_2 & c_1 c_2 c_3 - s_2 s_3 e^{i\delta} & c_1 c_2 s_3 + s_2 c_3 e^{i\delta} \\ s_1 s_2 & c_1 s_2 c_3 + c_2 s_3 e^{i\delta} & c_1 s_2 s_3 - c_2 s_3 e^{i\delta} \end{pmatrix} \tag{1.12}$$

where $c_i \equiv \cos\theta_i$ and $s_i \equiv \sin\theta_i$ and the parameters θ_1, θ_2, θ_3 and δ are real. These parameters have to be determined by experiment. In principle, all the elements V_{ij} can be determined independently, over-constraining the four parameters describing the matrix. In practice, some elements, such as V_{td}, are not accessible directly by current experiments. As will be seen below, processes like $K^+ \to \pi^+ \nu\overline{\nu}$ can be used for an indirect determination of those elements.

Current measurements of the elements of the CKM matrix show that it is nearly a unit matrix, with the diagonal elements close to one and with small off-diagonal elements. Wolfenstein [14] introduced a useful and much simpler parameterization of the CKM matrix, in which he set $V_{us} = \sin\theta_c = \lambda$ and expanded the other elements in powers of λ. To order λ^3, the matrix has the form

$$V \simeq \begin{pmatrix} 1 - \frac{1}{2}\lambda^2 & \lambda & A\lambda^3(\rho - i\eta) \\ -\lambda & 1 - \frac{1}{2}\lambda^2 & A\lambda^2 \\ A\lambda^3(1 - \rho - i\eta) & -A\lambda^2 & 1 \end{pmatrix} \tag{1.13}$$

where A, ρ and η are real parameters. In this parameterization, η determines the CP violation phase.

1.2.6 $K^+ \to \pi^+\nu\overline{\nu}$ branching ratio calculation

As noted above, the decay $K^+ \to \pi^+\nu\overline{\nu}$ is strictly forbidden at first order in the Standard Model. Inami and Lim [15] were the first to compute the branching ratio for a general case with an arbitrary number of generations of quarks and leptons. Figure 1.4 shows the second order Feynman diagrams contributing to the amplitude : a box diagram and two so-called penguin diagrams. Note that each diagram involves a loop containing a charge 2/3 quark. These loops have two quark vertices, one transforming an s quark into a charge 2/3 quark and one transforming the latter into a d quark. These vertices bring $V_{is}^* V_{id}$ terms to the amplitude, where V_{ij} are CKM matrix elements, each multiplied by a function dependent on the mass of the quark in the loop. The overall amplitude is a sum of the contributions from all quark flavours; if all had the same mass, the mass dependent functions could be factored out and the amplitude would contain a sum of the form $\sum_{i=1}^{N} V_{is}^* V_{id}$, where N is the number of generations. But this sum is simply the product of two columns of the CKM matrix, and is zero since the matrix is unitary. Therefore, the GIM mechanism makes the amplitude vanish if all quarks have same mass.

As this is not the case, we expect a small amplitude to remain at second order. For the case of three generations of quarks, and assuming three light neutrino types, the formula obtained by Inami and Lim for the branching ratio can be expressed as

$$B(K^+ \to \pi^+\nu\overline{\nu}) = \frac{3\alpha^2 B(K^+ \to \pi^0 e^+ \nu_e)}{8\pi^2 \sin^4\theta_W} \frac{|V_{cs}^* V_{cd} D(x_c) + V_{ts}^* V_{td} D(x_t)|^2}{|V_{us}|^2} \tag{1.14}$$

where α is the electro-magnetic fine structure constant, θ_W is the Weinberg angle defined by $\cos\theta_W = M_W/M_Z$, where M_W and M_Z are the masses of the W and Z bosons respectively, and $D(x_i)$ is given by

$$D(x_i) = \frac{1}{8}[1 + \frac{3}{(1-x_i^2)} - \frac{(4-x_i)^2}{(1-x_i)^2}]x_i \ln x_i + \frac{x_i}{4} - \frac{3}{4}\frac{x_i}{(1-x_i)} \tag{1.15}$$

where $x_i \equiv m_i^2/m_W^2$, with m_i the mass of the heavy quark in the loop (charm or top). In the expression for $D(x)$, it has been assumed that the mass of the charged leptons is small compared to the mass of the W boson [22].

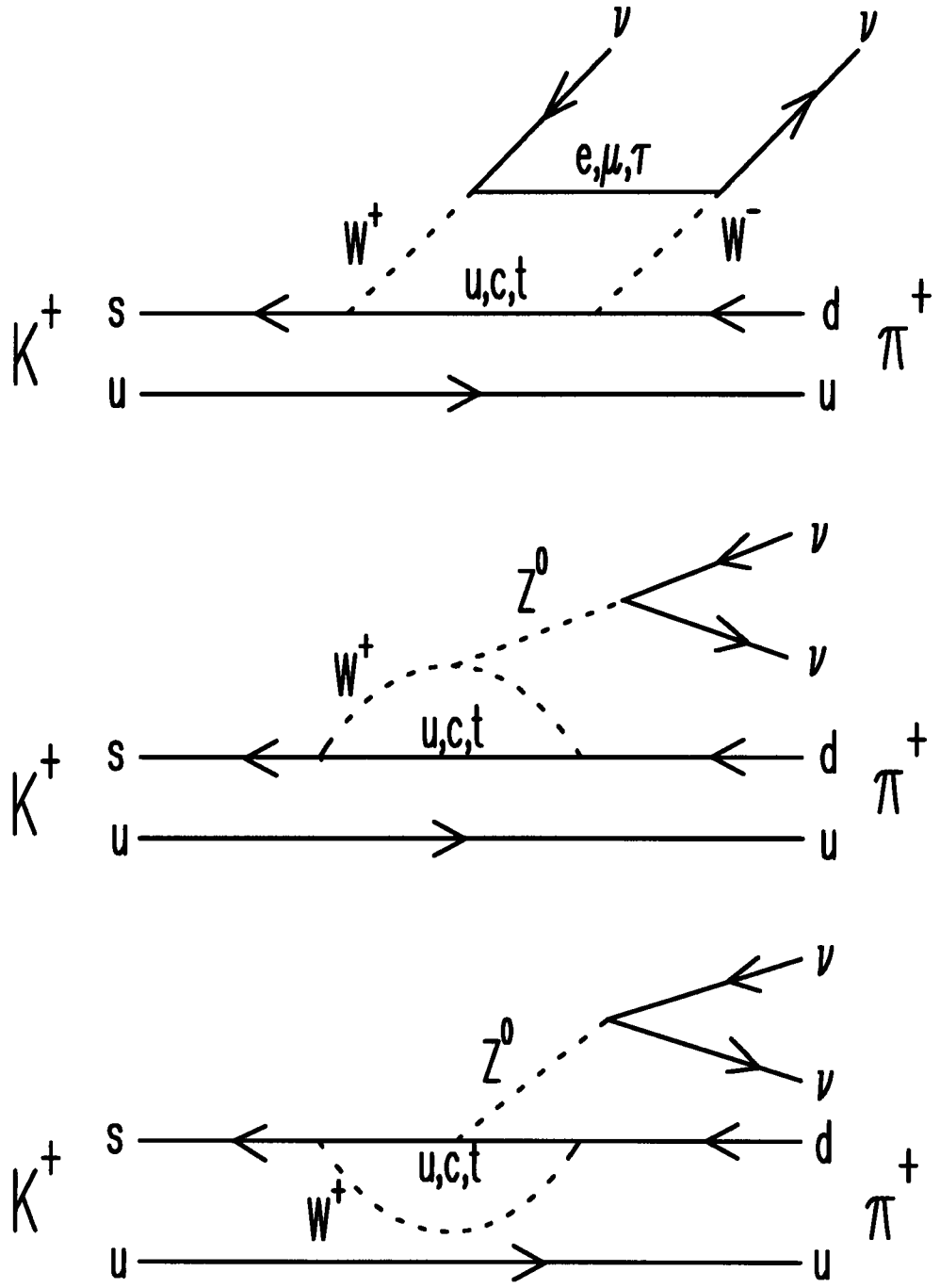

Figure 1.4: Second order Feynman diagrams for $K^+ \to \pi^+\nu\overline{\nu}$ for three generations of quarks and leptons.

Effects due to strong interactions between the kaon in the initial state and the pion in the final state of $K^+ \to \pi^+\nu\overline{\nu}$ decay are taken care of by relating $B(K^+ \to \pi^+\nu\overline{\nu})$ to the branching ratio for the first order decay $K^+ \to \pi^0 e^+ \nu_e$ [16]. This can be seen in figure 1.5: both decays contain a kaon in the initial state and a pion accompanied by two light leptons in the final state. The two decays can be related easily by strong isospin. The branching ratio for $K^+ \to \pi^0 e^+ \nu_e$ has been measured to be $(4.82 \pm 0.06)\%$ [17]. Interactions between the initial and final state and effects due to the structure of the hadrons involved in the process often lead to complications in the theoretical calculation of the decay rate. The simple relationship allowing the extraction of the relevant quantities from a known process is one of the main virtues of $K^+ \to \pi^+\nu\overline{\nu}$.

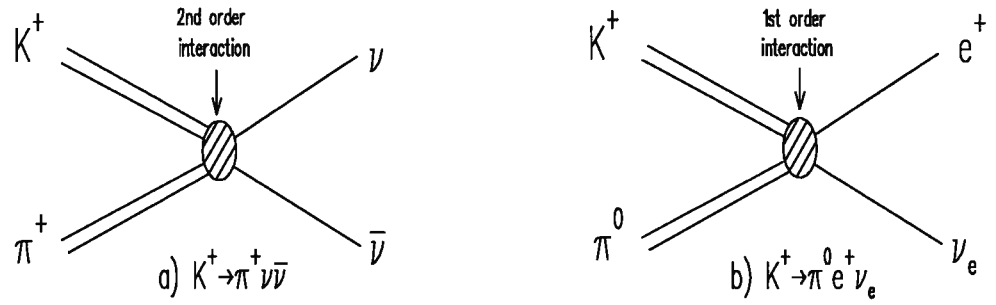

Figure 1.5: Relation between $K^+ \to \pi^+\nu\overline{\nu}$ and $K^+ \to \pi^0 e^+ \nu_e$ decays.

The functions $D(x_i)$ must be corrected for strong interaction effects in the quark loops. These corrections have been calculated to first order in QCD perturbation theory [18]; the result was to reduce the charm quark contribution to the amplitude by about 35%. However, uncertainties in the calculation resulted in an uncertainty of 20–30% in the branching ratio. A recent complete calculation to first order for the correction to the top quark loop and a next-to-leading order calculation for the charm quark correction has reduced this purely theoretical uncertainty to only about 7% [19].

With these corrections made, the only parameters in equation 1.14 that are not well known are the CKM matrix element V_{td} and the mass of the top quark, assuming that $|V_{ts}| \simeq |V_{cb}|$. Recently, evidence has been reported for top quark production in proton–anti-proton collisions, with a mass of $174 \pm 10^{+13}_{-12}$ GeV/c^2 [20]. This value is consistent with the value determined

indirectly through electro-weak radiative corrections [21]. This would leave V_{td} as the only undetermined parameter in equation 1.14. Therefore, a measurement of the $K^+ \to \pi^+\nu\bar{\nu}$ branching ratio would provide a determination of V_{td} with very little theoretical uncertainty. Other processes, such as B^0–$\overline{B^0}$ mixing and CP violation in the neutral kaon system can presently yield values for V_{td}, but with considerable theoretical uncertainty. As will be discussed below, these values can be used to estimate the $K^+ \to \pi^+\nu\bar{\nu}$ branching ratio.

1.2.7 Long distance effects

There are contributions to the amplitude for the decay $K^+ \to \pi^+\nu\bar{\nu}$ from processes other than the second order diagrams of figure 1.4; the latter are usually referred to as short distance processes. In long distance processes, the K^+ decays through an intermediate virtual meson state which results in a final state containing a π^+ and two neutrinos. Figure 1.6a shows an example of such a process where the decay is through a virtual muon. The rate for this and similar processes has been calculated [22, 23]; the sum of all contributions results in a branching ratio of order 10^{-13}, which is significantly smaller than what is expected from the short distance amplitude. A recent calculation of long distance effects based on chiral perturbation theory [24] essentially reached the same conclusion.

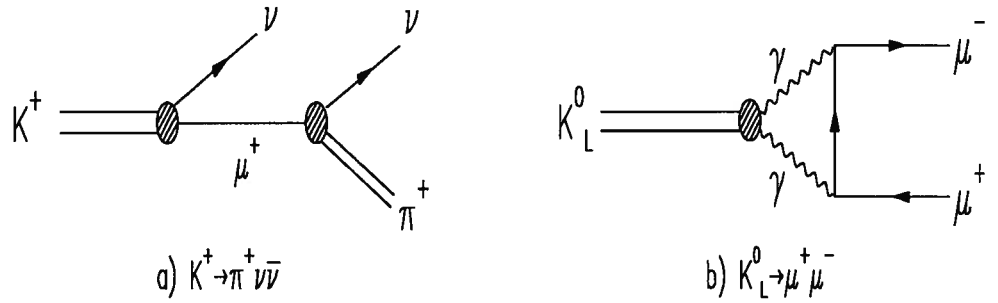

Figure 1.6: Examples of long distance effects for a) $K^+ \to \pi^+\nu\bar{\nu}$ and b) $K_L^0 \to \mu^+\mu^-$.

This is in contrast to other second order weak processes such as $K_L^0 \to \mu^+\mu^-$. Figure 1.6b shows an example of a long distance process for this decay, which has been observed with a branching ratio of $(7.4 \pm 0.4) \times 10^{-9}$ [17]. In this case, long distance effects contribute significantly to the overall amplitude, making the extraction of meaningful quantities related

to short distance physics difficult. The absence of significant long distance effects is another advantage of $K^+ \to \pi^+ \nu\overline{\nu}$.

1.2.8 Relationship to the CP violation problem

One of the main reasons for the importance of a measurement of V_{td} is its relation to the CP violation problem. As alluded to above, a non-zero complex phase in the CKM matrix would result in CP violation. If we take the product of the first and third column of the CKM matrix, we obtain the following relation

$$V_{ud}V_{ub}^* + V_{cd}V_{cb}^* + V_{td}V_{tb}^* = 0 \tag{1.16}$$

which defines a triangle in the complex plane. This is known as the unitarity triangle, and is shown in figure 1.7a. Using the Wolfenstein parameterization of the CKM matrix and rescaling the triangle by $|V_{cd}V_{cb}^*|$, we get a triangle in the (ρ, η) plane, shown in figure 1.7b. Since η is the complex phase, the position of the apex of the triangle defines the Standard Model contribution to CP violation. Currently, the position of the apex is not very well determined [25].

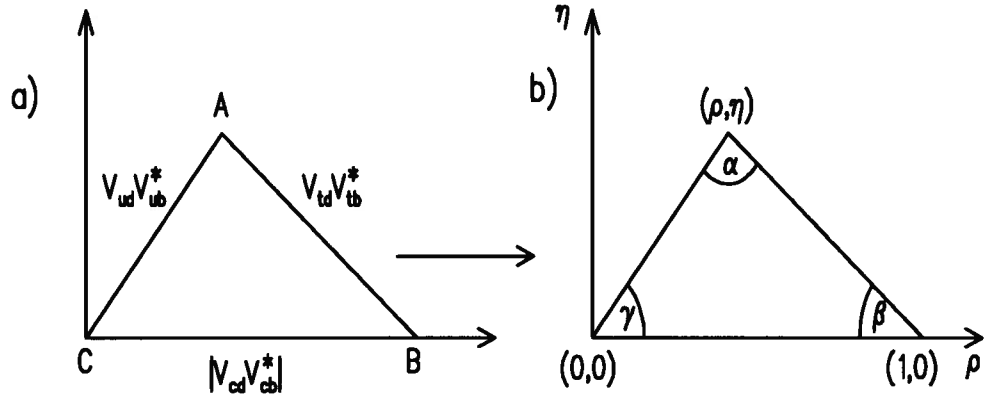

Figure 1.7: a) unitarity triangle and b) same triangle rescaled by $|V_{cd}V_{cb}^*|$ in the (ρ,η) plane.

Writing the CKM matrix in terms of λ, A, ρ and η, equation 1.14 can be recast to give

$$\frac{B(K^+ \to \pi^+\nu\overline{\nu})}{B(K^+ \to \pi^0 e^+ \nu_e)} \frac{8\pi^2 \sin^4\theta_W}{3\alpha^2} \frac{1}{A^4\lambda^8 D^2(x_t)} = \eta^2 + \left[1 + \frac{(1-\lambda^2/2)}{A^2\lambda^4}\frac{D(x_c)}{D(x_t)} - \rho\right]^2 \tag{1.17}$$

which defines a circle in the (ρ,η) plane, with radius proportional to the square root of the $K^+ \to \pi^+\nu\overline{\nu}$ branching ratio and center on the ρ axis slightly displaced from the point (1,0) [26]. Using

this information combined with the ratio $|V_{ub}/V_{cb}|$ measured in B meson decays, which defines a circle centered at the (ρ,η) origin, the apex of the unitarity triangle could be determined [27]. Another way to determine the unitarity triangle would be to combine a measurement of the $K^+ \to \pi^+\nu\overline{\nu}$ branching ratio with a measurement of the neutral kaon decay $K_L^0 \to \pi^0\nu\overline{\nu}$; this determination would have almost no theoretical uncertainty [28]. Thus we see that a measurement of the $K^+ \to \pi^+\nu\overline{\nu}$ branching ratio would greatly help in understanding the origin of CP violation.

1.2.9 Estimate for $K^+ \to \pi^+\nu\overline{\nu}$ branching ratio

As noted above, present constraints on V_{td} from other processes can be used to estimate the branching ratio for $K^+ \to \pi^+\nu\overline{\nu}$. Figure 1.8 shows the branching ratio for the sum of all known neutrino flavours as a function of the mass of the top quark, taken from reference [29]. The authors obtained two different solutions for V_{td} based on an analysis of the theoretical formula for the experimentally determined CP violation parameter ϵ from neutral kaon decays. This analysis was performed using experimental input for $|V_{cb}|$ and $|V_{ub}/V_{cb}|$, both determined in the decay of B mesons. Overlayed on the graphs is the one standard deviation range for the top quark mass based on the reported evidence [20]. This restricts the allowed range for the branching ratio to

$$B(K^+ \to \pi^+\nu\overline{\nu}) \approx (0.5 - 4.5) \times 10^{-10} \, . \tag{1.18}$$

1.2.10 Non-Standard Model Physics

The predicted value of the $K^+ \to \pi^+\nu\overline{\nu}$ branching ratio in the Standard Model is quite firm, with the major limitation currently being the accuracy of the knowledge of V_{td} and the mass of the top quark. Therefore, observation of this decay at a level significantly above the prediction would be a clear indication for new physics. However, most of the possible scenarios for new physics do not substantially increase the predicted rate. In reference [39], the authors review the possibilities and conclude by describing $K^+ \to \pi^+\nu\overline{\nu}$ as a "Standard Model standard". The least exotic scenario would be the presence of a fourth generation of fermions with high mass.

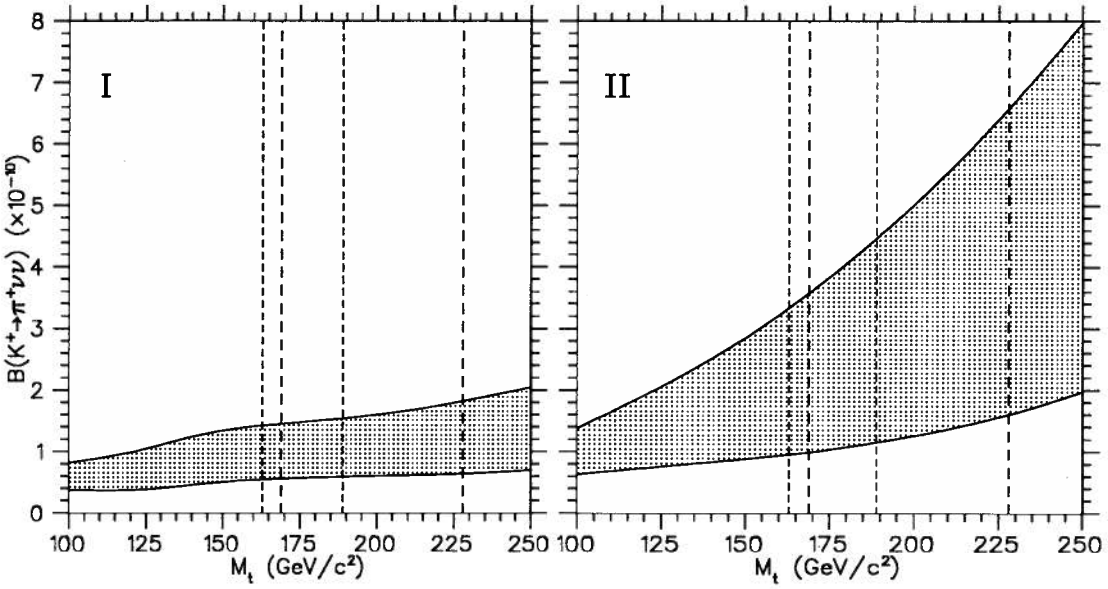

Figure 1.8: Expected $K^+ \to \pi^+\nu\overline{\nu}$ branching ratio as a function of the top quark mass (M_t), taken from reference [29]. The two graphs correspond to two different solutions for V_{td}. The dashed lines indicate the range for the top quark mass, assumed to be 174 ± 16 GeV/c^2.

This would enhance the decay rate if the couplings of the new charge 2/3 quark to the d and s quarks is not too small. Models such as multiple Higgs doublet, left-right symmetric and minimal supersymmetric produce no significant enhancement of the decay rate. In the case of non-minimal supersymmetry and other exotics, enhancements are possible but the models make no definite predictions for the rate.

If non-Standard Model physics were involved in the decay $K^+ \to \pi^+\nu\overline{\nu}$, it is likely that the π^+ spectrum shape would be different than normally expected. Figure 1.9 shows the theoretical π^+ momentum spectrum in the rest frame of the K^+ for $K^+ \to \pi^+\nu\overline{\nu}$, assuming a Standard Model V-A coupling and hypothetical scalar and tensor couplings. It is clear from this that a determination of the π^+ spectrum shape would be sensitive to non-Standard Model effects.

An obvious change in the spectrum shape would also occur if the neutrinos had a finite mass. In the minimal Standard Model, neutrinos are assumed massless, but a small mass could be accomodated. The present limits of $m_{\nu_e} < 5.1$ eV/c^2 (95% C.L.) and $m_{\nu_\mu} < 270$ keV/c^2 (90% C.L.) [17] indicate that it would be very difficult to observe their effect on the $K^+ \to$

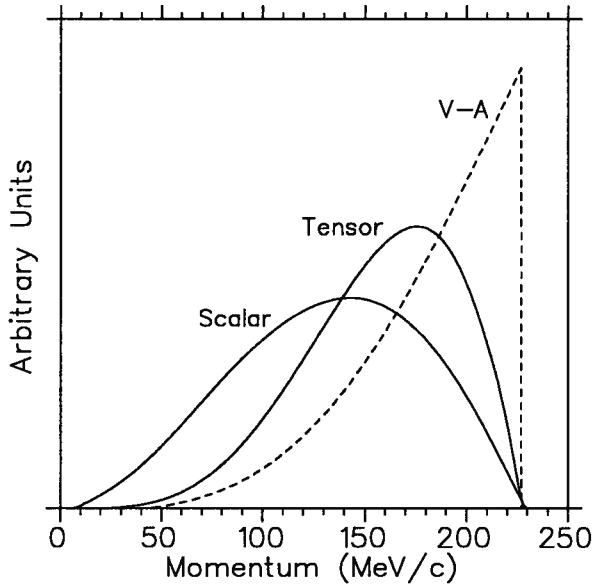

Figure 1.9: π^+ momentum spectrum for $K^+ \to \pi^+\nu\bar{\nu}$ with Standard Model V-A coupling and hypothetical scalar or tensor couplings.

$\pi^+\nu\bar{\nu}$ spectrum. For m_{ν_τ}, the 95% C.L. upper limit is presently at 31 MeV/c^2; a neutrino mass of that order would affect the spectrum shape significantly, as well as its end-point. However, from various cosmological arguments m_{ν_τ} must be less than a fraction of an MeV [17]. Therefore, until a very high statistics measurement of the spectrum shape of $K^+ \to \pi^+\nu\bar{\nu}$ can be made, effects due to a finite neutrino mass are not likely to be observed by this experiment.

1.2.10.1 $K^+ \to \pi^+ X^0$

As will be discussed in the next section, the experimental signature for $K^+ \to \pi^+\nu\bar{\nu}$ is $K^+ \to \pi^+$ *nothing*. Therefore, this experiment is also sensitive to non-Standard Model processes of the type

$$K^+ \to \pi^+ X^0 \tag{1.19}$$

where X^0 is any neutral weakly interacting particle or group of particles. The π^+ kinematic region investigated in this experiment limits the mass of X^0 to the region $150 < M_{X^0} < 260$ MeV/c^2. Possibilities for X^0 include new bosons, a pair of Majorons [41] or a pair of supersymmetric particles. Some authors determined that the latter is not likely to contribute

significantly [22]. Others have reported that the most favorable mass for new bosons produced in $K^+ \rightarrow \pi^+ X^0$ is near 200 MeV/c^2 [42]; also, the lower part of the π^+ spectrum may be enhanced for Majoron production [43].

The general theoretical conclusion about a non-Standard Model contribution to $K^+ \rightarrow \pi^+$nothing is that although it is not likely, unexpected results are possible and should be investigated.

1.3 Experimental search

Based on the expected $K^+ \rightarrow \pi^+ \nu\overline{\nu}$ branching ratio, we see that a large number of kaons, of the order of 10^{11}–10^{12}, depending on the detection efficiency of the experiment, will be required for an experimental measurement. The experimental signature of $K^+ \rightarrow \pi^+ \nu\overline{\nu}$ is very simple : a charged kaon decays to a charged pion and nothing else, since the two neutrinos in the final state cannot readily be detected. Figure 1.10 shows the π^+ momentum spectrum for $K^+ \rightarrow \pi^+ \nu\overline{\nu}$ in the rest frame of the kaon, typical of a three body final state. The end point of the distribution is at $p_{\pi^+} = 227$ MeV/c. Also shown are the charged particle momentum spectra for the seven most likely K^+ decays channels.

All other kaon decay channels are potential sources of background in a search for $K^+ \rightarrow \pi^+ \nu\overline{\nu}$. A survey of K^+ decays with a π^+ in the final state reveals that except for $K^+ \rightarrow \pi^+ \nu\overline{\nu}$, and the rare and as yet unobserved decay $K^+ \rightarrow \pi^+ \gamma\gamma$ [31], the final state also contains at least one neutral pion, which decays to two photons[1] with a mean life of 8.4×10^{-17} s, or a pair of charged particles. Decays with no π^+ in the final state involve either a μ^+ or e^+, in most cases accompanied by a π^0 , photons or other charged particles. Therefore, decays other than $K^+ \rightarrow \pi^+ \nu\overline{\nu}$ become backgrounds when either photons or other charged decay products are not detected, or a charged lepton is mis-identified as a π^+ , or both.

The two most prominent potential background processes are $K^+ \rightarrow \mu^+ \nu_\mu$ ($K_{\mu 2}$) and $K^+ \rightarrow \pi^+ \pi^0$ ($K_{\pi 2}$), with branching ratios of 63.51% and 21.17% respectively. Because they are two body decays, their charged particle spectrum is mono-chromatic in the rest frame of the K^+ .

[1]The Dalitz decay $\pi^0 \rightarrow \gamma e^+ e^-$ also contributes with a branching ratio of ~1.2%.

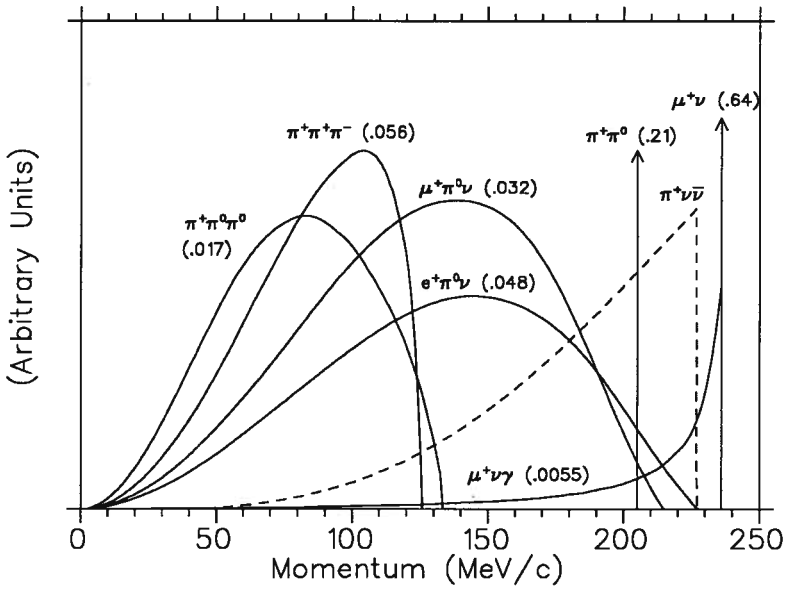

Figure 1.10: Final state charged particle momentum distribution in the rest frame of the K^+ for $K^+ \to \pi^+\nu\bar{\nu}$ (dashed line) and the seven most likely K^+ decay channels (the branching ratio is indicated in parentheses).

There are also potential sources of background which do not involve K^+ decay. Pions produced in proton–nucleus collisions contaminate the kaon beam and could fake a $K^+ \to \pi^+\nu\bar{\nu}$ decay. Also, a K^+ propagating through matter can interact and produce a neutral kaon through the charge exchange reaction $K^+n \to K^0p$; the neutral kaon can then result in a final state including a π^+ .

Based on these facts, the following strategy was used in the design of the experiment :

1. Positive identification of the K^+ . This defines the initial state and guards against non-K^+ decay backgrounds.

2. Observation of K^+ decays at rest in the laboratory. This ensures that the two most important background processes $K_{\mu 2}$ and $K_{\pi 2}$ can be clearly identified by their mono-chromatic kinematic peak, which would be smeared by the Lorentz boost if the K^+ decayed in flight.

3. Require a delayed decay of the K^+ . This guarantees that the K^+ decay is at rest and further suppresses non-K^+ decay backgrounds.

4. Positive identification of the π^+ in the final state.

5. High efficiency photon detection.

These points affected both the design of the apparatus used in the experiment and the analysis of the collected data. The identification of the K^+ can be accomplished by installing in the incoming particle beam detectors sensitive to the particle type. The K^+ are brought to rest by placing in their path a block of material of appropriate thickness. Decay products of the K^+ have to be analyzed by a spectrometer. In particular, the kinematic properties of charged decay products should be well measured to help in the identification of the π^+ . Figure 1.11 shows the distribution of momentum, kinetic energy and range in plastic scintillator for the π^+ in $K^+ \to \pi^+\nu\overline{\nu}$ and for charged particles from three other prominent K^+ decays. Typical experimental resolutions were included in these distributions. Also shown in the figure is the kinematic region investigated in this work; more will be said on this below.

The range of a particle is equivalent to its path length in a material. For a charged particle of mass $M \gg m_e$, where m_e is the mass of the electron, kinetic energy loss is primarily through ionization of atomic electrons. Due to the random nature of the collisions between the charged particle and the electrons in the material, the path length will vary for particles with identical kinetic energy. The mean range of a charged particle of kinetic energy E is given by

$$R = \int_E^0 \frac{1}{-dE/dx} dE \tag{1.20}$$

where dE/dx is the mean rate of energy loss of the particle in the material. The latter is a function of the velocity of the particle in a given material. There is therefore a direct relationship between the kinetic energy and mean range of a particle. In particular, particles of a given kinetic energy will have a different mean range depending on their rest mass. Hence, any two of the momentum, kinetic energy and range can be combined to determine the particle type. In practice, because of finite experimental resolution, the measurement of all three quantities is necessary. Because of the significant difference in mass and energy loss behaviour between electrons and pions, mis-identification of an e^+ as a π^+ is not a major concern. However, muons and pions have similar masses and therefore similar kinematic properties; muons are essentially

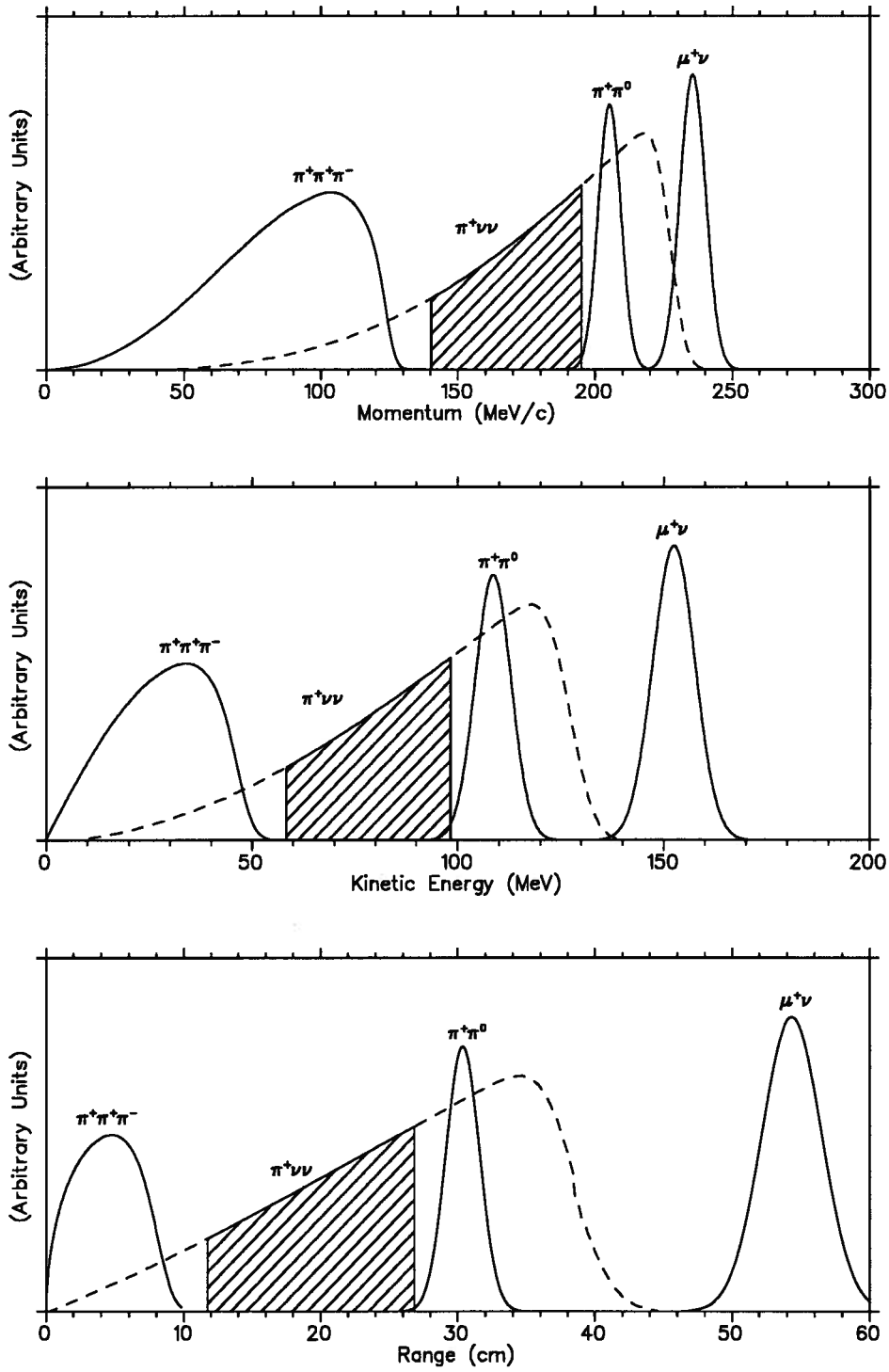

Figure 1.11: Momentum, kinetic energy and range spectrum in the rest frame of the K^+ for charged particles in $K^+ \to \pi^+\nu\overline{\nu}$ (dashed line), $K_{\mu 2}$, $K_{\pi 2}$ and $K^+ \to \pi^+\pi^+\pi^-$ decays. Typical experimental resolutions were included for each quantity. The hashed area indicates the $K^+ \to \pi^+\nu\overline{\nu}$ kinematic search region used in this work.

the sole source of particle mis-identification background.

Another way to positively identify the π^+ is to use its characteristic decay sequence. Approximately 99.99% of the time a pion will decay via $\pi^+ \rightarrow \mu^+\nu_\mu$, with a mean life of 26 ns. This is then followed by the decay of the muon via $\mu^+ \rightarrow e^+\nu_e\overline{\nu_\mu}$, with a mean life of 2.2 μs and also nearly 100% probability. Therefore, by detecting the two secondary charged particles resulting from the cascade decay of the primary π^+ , positive identification can be made. This is in contrast to a primary μ^+ which results in only one secondary charged particle. Hence, the detection of the decay sequence of the charged decay product of the K^+ can also be used to reject background.

Finally, the detection of photons should be as efficient as possible in order to reject the numerous background processes which involve photons. The most prominent is $K^+ \rightarrow \pi^+\pi^0$, in which the π^0 has a total energy of 245 MeV. The energy of the photons emitted the decay of the π^0 are distributed between 20 MeV and 225 MeV. The extremes correspond to the case where one photon is emitted in the direction of motion of the π^0 and the other in the opposite direction. The minimum separation angle between the two photons is 67°; in this case, the two photons have equal energy (112.5 MeV). For other K^+ decays involving π^0 , the range of photon energies is not as wide and the minimum separation angle is larger. For K^+ radiative decays, in which individual photons are emitted, the photon energy is smaller and can be as low as a few MeV. Typical inefficiencies for photon detection obtained in this experiment varied according to the energy and direction of the photon, and were between 10^{-1} and 10^{-3}. The detection also has to be accomplished in an environment with a high rate of accidental particles, which results from the intense incoming beam of particles and leads to accidental vetoing.

Due to the limited photon detection capability, we see from figure 1.11 that the kinematic region defined by the $K_{\pi 2}$ decay kinematic peak should be avoided in the search for $K^+ \rightarrow \pi^+\nu\overline{\nu}$. The position of this peak at $p_{\pi^+} = 205.12$ MeV/c defines two regions of the $K^+ \rightarrow \pi^+\nu\overline{\nu}$ spectrum that can be exploited : one above the $K_{\pi 2}$ peak up to the end point of the $K^+ \rightarrow \pi^+\nu\overline{\nu}$ spectrum and one below the $K_{\pi 2}$ peak. The former region was the subject of a recent thesis [30]. The latter region was used in this work, and is indicated by a hashed region

in figure 1.11. It is about a factor of two larger than the more "conventional" higher momentum region, and in the case of a measurement would allow for a determination of the π^+ spectrum shape. It also involves backgrounds of a slightly different nature. The lower boundary of the region used was defined to some extent by the apparatus used and avoided most of the $K^+ \to \pi^+\pi^+\pi^-$ and $K^+ \to \pi^+\pi^0\pi^0$ background processes. It is worth noting that the vertical scale on the graphs of figure 1.11 is entirely arbitrary, including the relative height of the distributions for the different decay modes. The peaks of the $K_{\mu 2}$ and $K_{\pi 2}$ distributions are in reality some ten orders of magnitude higher than the maximum of the $K^+ \to \pi^+\nu\overline{\nu}$ distribution. The shape of the distribution for $K_{\mu 2}$ and $K_{\pi 2}$ was assumed Gaussian for the figure; this is not necessarily the case in practice.

1.3.1 Background overview

This section will give a brief overview of the background processes of concern for the search for $K^+ \to \pi^+\nu\overline{\nu}$ in the kinematic region below the $K_{\pi 2}$ peak. Each will be discussed in detail in Chapter 4. Table 1.1 gives a list of these background processes. The most important is $K^+ \to \pi^+\pi^0$ ($K_{\pi 2}$). It can mimic $K^+ \to \pi^+\nu\overline{\nu}$ if the photons from π^0 decay are not detected and either the kinematic quantities for the π^+ are mis-measured or the π^+ lost an undetected amount of energy in a collision. The latter effect is significant because the π^+ can undergo strong interactions in matter. There is also a radiative mode, $K^+ \to \pi^+\pi^0\gamma$, in which the π^+ is naturally lower in momentum than the $K_{\pi 2}$ mode; however, the photons from π^0 decay and the radiated photon have to be missed for this decay to be a background. Note that the $K^+ \to \pi^+\pi^0\gamma$ ratio indicated in the table is only for the kinematic region $55 < T_{\pi^+} < 90$ MeV [17]; for low energy radiated photons, most of the branching ratio is included in the $K_{\pi 2}$ mode.

The momentum spectrum of the μ^+ from $K^+ \to \pi^0\mu^+\nu_\mu$ ($K_{\mu 3}$) decay covers the kinematic search region. The μ^+ must be mis-identified as a π^+ and the photons from π^0 decay missed. The decay $K^+ \to \mu^+\nu_\mu$, with the largest of all K^+ decay branching ratios, is not a concern for this study because of the high momentum of the μ^+ (236 MeV/c). However, for the radiative

Table 1.1: Background processes to the search for $K^+ \to \pi^+\nu\overline{\nu}$ in the kinematic region below the $K_{\pi 2}$ peak. Also shown are branching ratios or probabilities for the various processes and the maximum momentum of the π^+ or μ^+ in the final state.

Background	**Branching ratio**	$\mathbf{P_{max}}$ **(MeV/c)**
$K^+ \to \pi^+\pi^0\,(K_{\pi 2}\,)$	0.212	205
$K^+ \to \pi^+\pi^0\gamma\,(K_{\pi 2\gamma}\,)$	2.75×10^{-4}	205
$K^+ \to \pi^0\mu^+\nu_\mu\,(K_{\mu 3}\,)$	0.0318	215
$K^+ \to \mu^+\nu_\mu\gamma\,(K_{\mu\nu\gamma}\,)$	5.50×10^{-3}	236
$K^+ \to \pi^+\pi^-e^+\nu_e\,(K_{e4}\,)$	3.91×10^{-5}	203
Beam pions	—	—
$K^+n \to K^0p$	Prob. = 0.0015	—
$\quad K_L^0 \to \pi^+\mu^-\overline{\nu}_\mu$	0.135	216
$\quad K_L^0 \to \pi^+e^-\overline{\nu}_e$	0.194	229
$K^0 \to \overline{K^0}$, $\overline{K^0}N \to \pi\Sigma^+$	Prob = 0.024	—
$\quad \Sigma^+ \to \pi^+n$	0.483	185

mode $K^+ \to \mu^+\nu_\mu\gamma$, the μ^+ spectrum does cover the $K^+ \to \pi^+\nu\overline{\nu}$ kinematic search region. Again in this case, μ^+ mis-identification and non-detection of the photon in the final state are necessary for this mode to be a background.

For the decay $K^+ \to \pi^+\pi^-e^+\nu_e$ $(K_{e4}\,)$, both the π^- and the e^+ in the final state have to be missed. There is also a similar decay, $K^+ \to \pi^+\pi^-\mu^+\nu_\mu$, with a branching ratio about three times smaller than K_{e4} . However, the maximum momentum for the π^+ in this decay is only 151 MeV/c, and therefore its contribution to the overall background is not significant.

Beam pions are a source of isolated pions which can simulate the final state of $K^+ \to \pi^+\nu\overline{\nu}$. The large number of pions which accompany kaons in the particle beam used in this experiment makes this process a potential background. Beam kaons can also interact in matter as they are being brought to rest and produce a neutral kaon via the charge exchange process $K^+n \to K^0p$. The neutral kaon is a superposition of the weak interaction eigenstates K_L^0 and K_S^0 . The K_L^0 can decay semi-leptonically via $K_L^0 \to \pi^+\ell^-\overline{\nu}_\ell$, where ℓ is either a muon or an electron. If the lepton is not detected, this decay can be a background to $K^+ \to \pi^+\nu\overline{\nu}$.

Finally, there is a finite probability that a neutral kaon produced in K^+ charge exchange will oscillate to an anti-kaon, or $\overline{K^0}$. The $\overline{K^0}$ can interact in matter and produce a Σ^+ hyperon,

which then decays 48% of the time to a π^+ and a neutron. The latter is difficult to detect. Therefore, if the interactions leading to the production of the Σ^+ are not detected, this process can also be a background to $K^+ \to \pi^+\nu\overline{\nu}$.

1.3.2 Previous searches

Figure 1.12 shows the historical progress in the experimental search for $K^+ \to \pi^+\nu\overline{\nu}$. No evidence for observation has been reported; therefore, all results are 90% confidence level upper limits. Each step on the graph represents a published measurement. The most recent result

$$B(K^+ \to \pi^+\nu\overline{\nu}) < 5.2 \times 10^{-9} \text{ (90\%C.L.)} \tag{1.21}$$

includes part of the work reported here, combined with an investigation of the higher momentum region of the $K^+ \to \pi^+\nu\overline{\nu}$ decay π^+ spectrum [37]. The best result in the kinematic region below the $K_{\pi 2}$ kinematic peak previous to this experiment was [34]

$$B(K^+ \to \pi^+\nu\overline{\nu}) < 9.4 \times 10^{-7} \text{ (90\%C.L.)} . \tag{1.22}$$

For $K^+ \to \pi^+\nu\overline{\nu}$ via scalar and tensor interactions, the best previous limits were $< 1.1\times10^{-6}$ and $< 7.1 \times 10^{-7}$ (90% C.L.) respectively. For $K^+ \to \pi^+X^0$, the most recent published result previous to this experiment that included the mass region probed by this experiment here was approximately

$$B(K^+ \to \pi^+X^0) < 2 \times 10^{-5} \text{ (90\%C.L.)} \tag{1.23}$$

with some dependence on M_{X^0} [38].

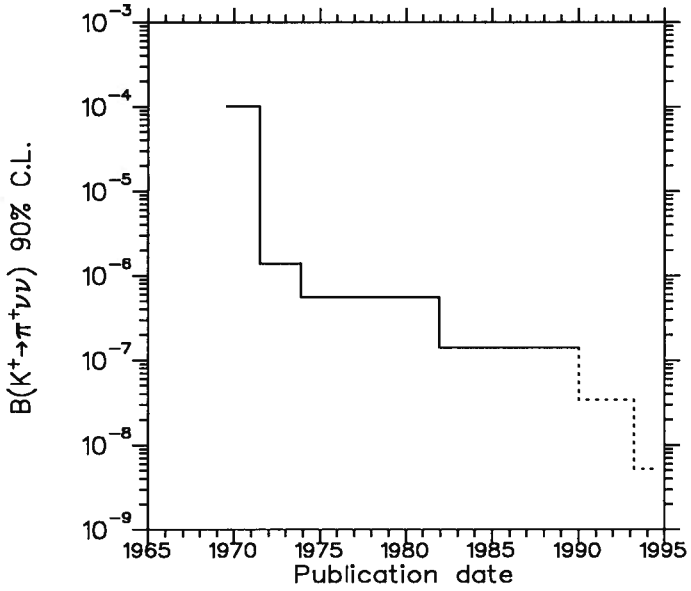

Figure 1.12: Historical progress in the experimental search for $K^+ \to \pi^+ \nu\overline{\nu}$. Each horizontal line represents a published result [32, 33, 34, 35, 36, 37]. The dashed lines indicate the results using the apparatus of this experiment.

Chapter 2

The Apparatus

This chapter gives a description of the apparatus used for the experiment. This apparatus, located at Brookhaven National Laboratory (BNL) in Upton, NY, USA, was used to study several different K^+ decays. It was designed, constructed and operated by a collaboration of physicists from three institutions : BNL, Princeton University and TRIUMF (see appendix A). The experiment as a whole was identified as BNL Experiment 787. The following description will focus on the use of the apparatus in the search for $K^+ \to \pi^+\nu\overline{\nu}$, which was the main goal of the collaboration. Experimental data used in the work described in this thesis was recorded in two different periods of a few months in 1989 and 1991. There were some differences in the apparatus used in the two periods; they will be pointed out in the appropriate sections.

2.1 Kaon beam

Kaons used for the experiment were produced in collisions between an accelerated beam of protons and a stationary target. The accelerator was the Alternating Gradient Synchrotron (AGS). Protons were first accelerated to 200 MeV with a linear accelerator and then injected in the 807 m circumference synchrotron where they were accelerated to a momentum of 24 GeV/c. Approximately 10^{13} protons were stored in the synchrotron before being extracted over a time period of 1.6 seconds; each extraction was referred to as a spill. The duration of one cycle of acceleration and extraction was approximately 3.2 seconds.

A portion of the extracted proton beam, typically 6×10^{12} protons, was directed on a 9 cm long platinum production target. Particles of several types and of various energies are produced

in the collisions between protons and platinum nuclei. Only a fraction of them were collected and guided towards the detector by the beam line, a series of dipole and quadrupole electro-magnets and collimators. Figure 2.13 schematically shows the proton beam from the accelerator, the production target and the beam line, LESB1 (Low Energy Separated Beam). The integrated path length of the particle beam from the production target to the final focus was 15.8 m. The dipole magnets' field polarity and strength was adjusted to select positively charged particles with a momentum of 800 MeV/c. The rms resolution of the beam line momentum selection was approximately 1%. The first dipole had a total angular acceptance of 2.5 msr and collected particles emitted at the production target at an angle of 10.5° with respect to the proton beam direction.

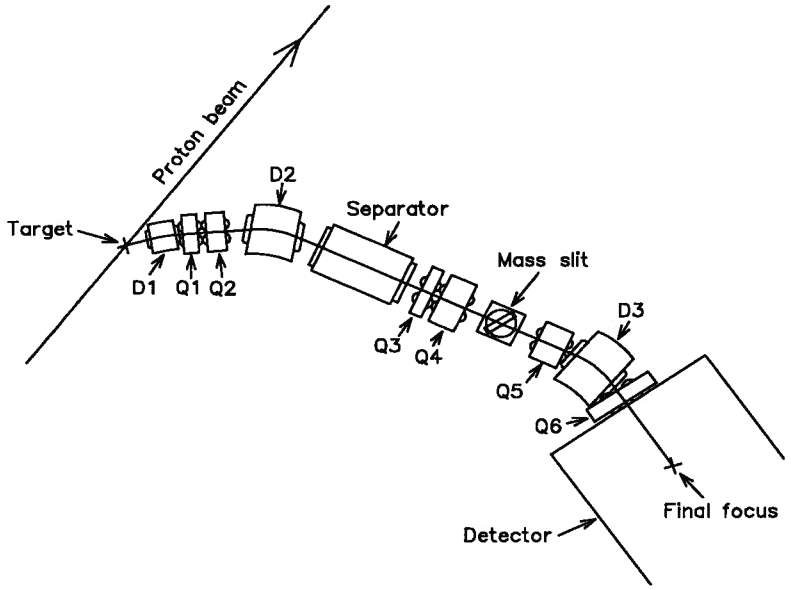

Figure 2.13: Schematic diagram of the LESB1 beam line[44]. Dipole magnets are designated Dn, while quadrupole magnets are designated Qn.

As was noted above, particles of several types emerge from the production target. The cross-section for pion production in proton-nucleus collisions is approximately 20 times the cross-section for kaon production. Also, a large number of protons are deflected via inelastic collisions with nuclei and can enter the beam line. Particle type separation was obtained using an electrostatic separator, or Wien filter, tuned for 800 MeV/c K^+ . Particles deflected by the crossed electric and magnetic fields of the separator were blocked by the mass slit, an adjustable

collimator installed following the separator.

This particle separation significantly reduced the non-K^+ components of the beam, but not entirely. At the exit of the last magnet the beam consisted of a mixture of π^+ , protons and K^+ in the proportion 2 : 1 : 1. Approximately 10^6 K^+ per AGS spill came through the last magnet, were slowed by a degrader and came to rest in the target located in the center of the detector. This was the most intense kaon beam available in the world at the time[1]. The distribution of the K^+ beam at the exit of the beam line was centered in the plane perpendicular to the beam axis, and occupied an area 12 cm wide (horizontally) and 4 cm high (vertically). The π^+ beam was off center and more diffuse, with a full width and height of 18 cm and 5.5 cm respectively.

2.2 Detector

The BNL E787 detector consists of a number of independent sub-detectors of various types working collectively to identify events consistent with a $K^+ \to \pi^+\nu\bar{\nu}$ decay. Each sub-detector is dedicated to a particular aspect of either the precise identification of a K^+ decaying at rest to a π^+ or the rejection of the numerous background processes. Figure 2.14 shows a detailed side view of the entire detector. Figure 2.15 shows an end view of the detector as well as the coordinate system used. The z axis is in the direction of the K^+ beam, perpendicular to and into the page in figure 2.15. Elements of the detector are often referred to in reference to the particle beam direction; upstream is closest to the beam origin (in the direction of the negative z axis), and downstream is the opposite.

The detector was designed based on the considerations discussed in Chapter 1. A set of sub-detectors placed in the incoming beam, referred to collectively as beam counters, identified the K^+ and other particles. Charged particles were slowed by the beryllium oxide degrader; its length was chosen such that kaons came to rest in a highly segmented target made of plastic scintillator, located downstream of the degrader. The high segmentation of the target allowed the identification of the K^+ decay vertex position and of the secondary charged particles.

[1]LESB1 was replaced in 1992 by LESB3, providing a factor of ~5 improvement in $K^+ : \pi^+$ ratio.

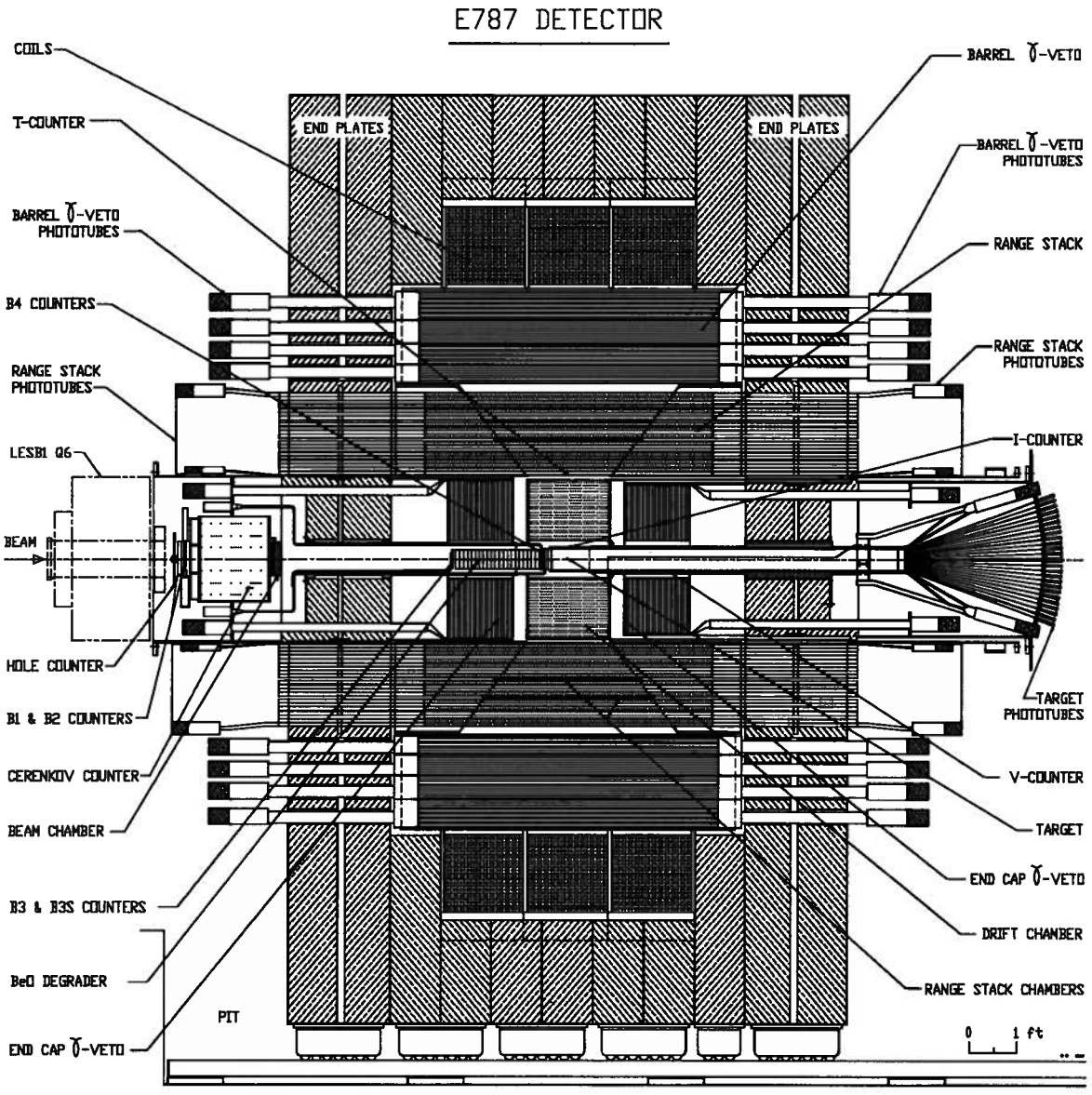

Figure 2.14: Schematic side view of the E787 detector [45].

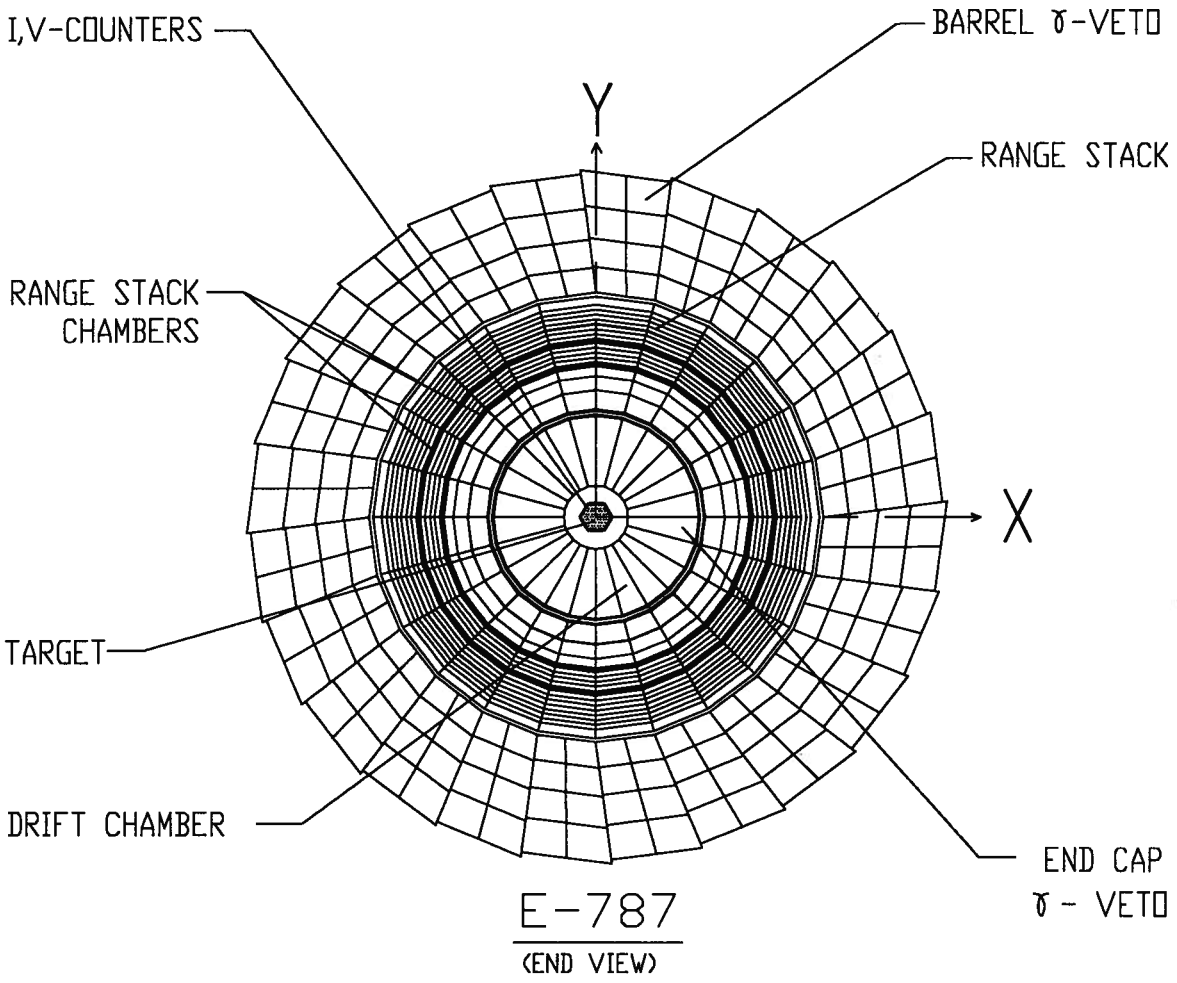

Figure 2.15: Schematic end view of the E787 detector [45].

Surrounding the target was a series of detectors with cylindrical symmetry with respect to the z axis, designed to identify the K^+ decay products. Precise position information about the charged particles emerging from the target was obtained by a drift chamber. A static magnetic field directed along the z axis of the detector allowed the determination of the momentum of charged particles using the position information from the drift chamber. The field of 1 Tesla was provided by a 3 m diameter conventional solenoid magnet surrounding the entire detector. Note also that since all sub-detectors were permeated by the magnetic field, nearly all photo-multiplier tubes (or phototubes) used to measure the light output of scintillator counters were installed outside of the magnet return iron.

Surrounding the drift chamber was the range stack, a segmented stack of plastic scintillator counters designed to measure the kinetic energy and range of the charged particles emerging from the drift chamber. Two layers of proportional chambers were embedded in the range stack to provide additional position measurements for charged particles. Photons were vetoed by electro-magnetic shower detectors arranged in three sub-systems, a barrel section surrounding the range stack and two endcaps located on either side of the drift chamber. This system covered nearly 4π sr, leaving only the beam–target axis and the region between the barrel and endcaps with limited coverage. The photon detection capability of the detector was augmented by the use of all active elements not struck by the K^+ or the π^+ .

The electrical signals output by all sub-detectors were carried via 30–50 m long coaxial cables to the counting house, where all electronic modules were located. The signals were processed with discriminators, coincidence units, analog-to-digital converters (ADC) and time-to-digital converters (TDC). A description of the electronics systems will be given with the description of the online event selection (section 3.1).

Figure 2.16 shows an end view display of a $K^+ \to \pi^+\pi^0$ event based on information recorded by the detector. Only the counters with recorded energy are indicated, as well as the xy plane position measurements from the drift chamber and the fitted trajectory. The π^+ is clearly seen from its path through the target, I-counters, drift chamber and range stack. The two photons from π^0 decay were detected in the barrel veto. The numbers indicated in each counter

represent the measured visible energy in units of MeV.

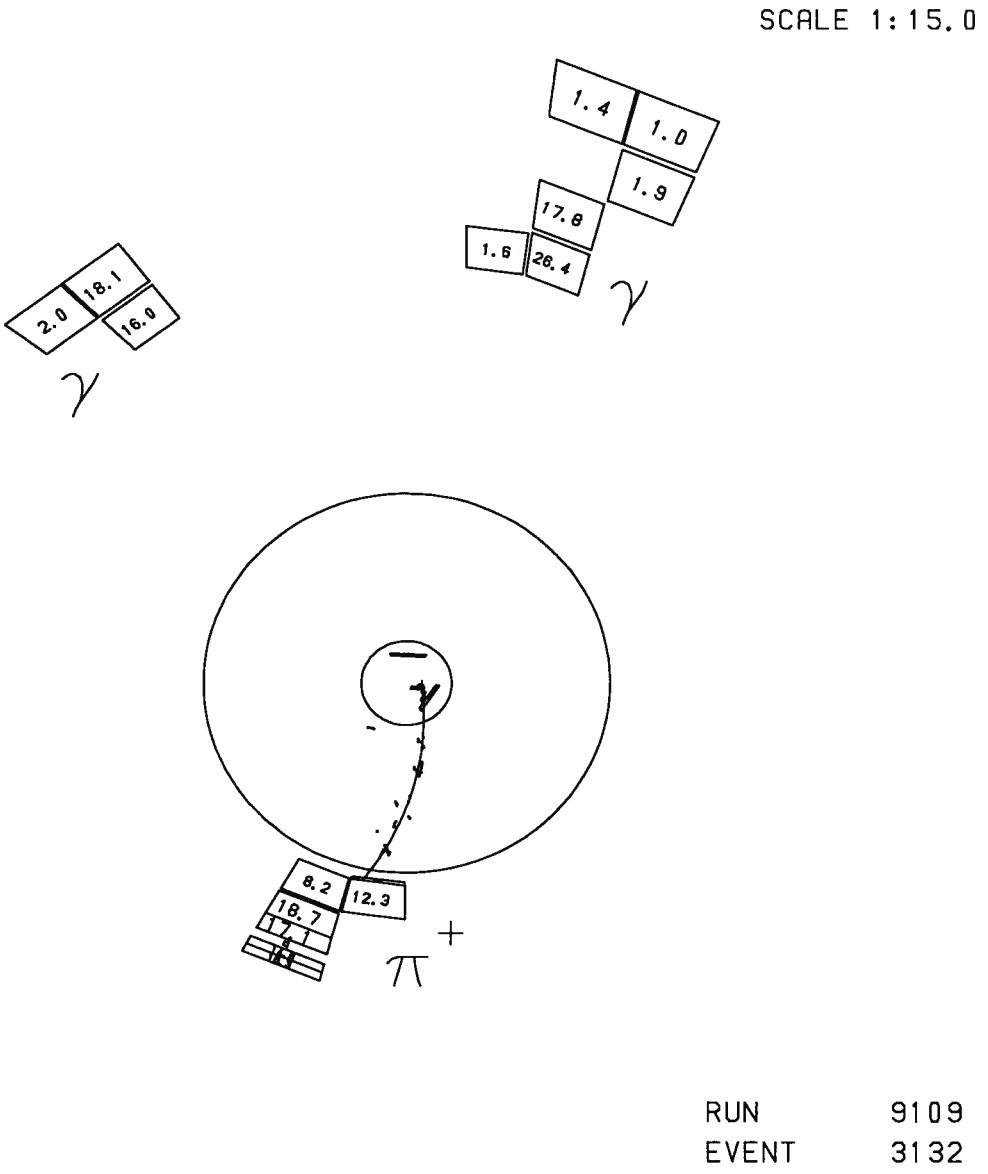

Figure 2.16: Detector display of a $K^+ \to \pi^+\pi^0$ event. See the text for explanations.

A description of each sub-detector will be given in the following sections. Elements with the most impact on the search for $K^+ \to \pi^+\nu\overline{\nu}$ will be emphasized. More technical details about all parts of the detector can be found in reference [46].

2.2.1 Beam counters

This system of detectors was used to monitor and identify beam particles from their exit from the beam line to the target at the center of the detector. Figure 2.17 gives a schematic side view of the system used for the 1991 data run. The various elements of the beam counter system will be described in the order in which they are encountered by beam particles.

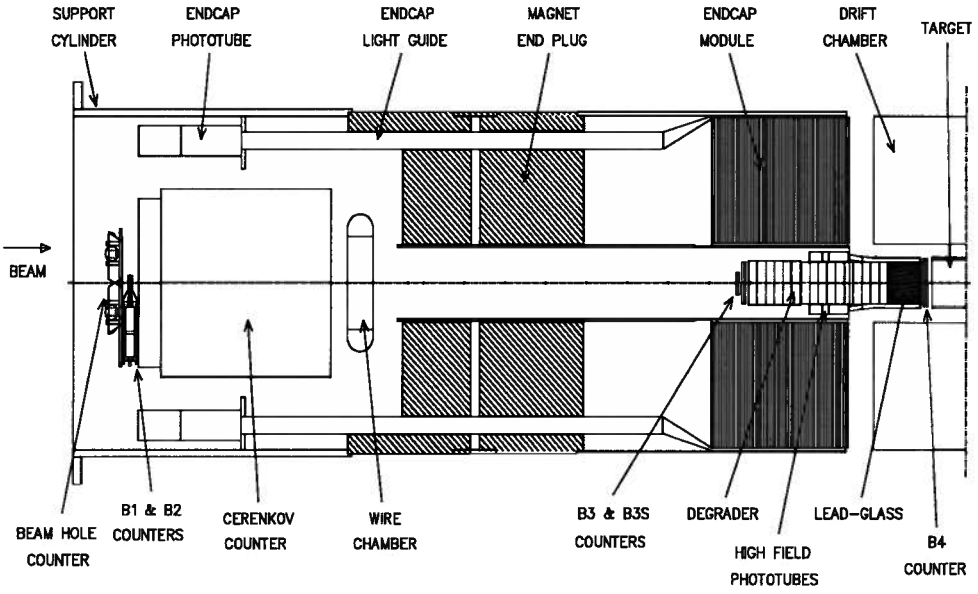

Figure 2.17: Schematic side view of the beam counters system for the 1991 run. Also shown here are the upstream endcap, and part of the drift chamber and target.

2.2.1.1 Beam hole, B1 & B2 hodoscopes

The first element is the beam hole counter. This counter consisted of two L-shaped plastic scintillator counters forming a square 23 cm to a side with an 18 cm wide (along the x axis) and 3 cm high (along the y axis) rectangular hole in its center, to accommodate the spatial distribution of the incoming K^+ beam. This counter was designed to identify beam particles that might be far off axis. All kaons should pass through the hole and traverse the B1 and B2 hodoscopes, which were located immediately following the beam hole counter. B1 and B2 were groups of plastic scintillator counters used to monitor the beam profile; they were not used in the search for $K^+ \to \pi^+ \nu\bar{\nu}$.

2.2.1.2 Čerenkov counter

Following the B1 and B2 hodoscopes is the Čerenkov counter. This counter used Čerenkov light emission resulting from the passage of beam particles through a dielectric medium, or radiator, for particle type identification; such counters have been used before in low energy kaon beams [48]. The Čerenkov light is emitted along the path of the moving charged particle with a characteristic angle θ_C with respect to the direction of motion of the particle. This angle is defined as

$$\cos\theta_C = \frac{1}{\beta n} \tag{2.24}$$

where $\beta = v/c$ is the ratio of the velocity of the charged particle in the medium to the velocity of light in vacuum (c), and n is the index of refraction of the medium. This defines a threshold velocity for emission of Čerenkov light, $\beta_t = 1/n$. The radiator was a 2.54 cm thick and 15 cm diameter acrylic disk. The index of refraction of acrylic is $n = 1.49$ in the frequency range of interest; therefore, the threshold velocity for Čerenkov light emission was $\beta_t = 0.67$. For a momentum of 800 MeV/c, both π^+ and K^+ have a velocity above this threshold; protons do not.

This counter also made use of the phenomenon of total internal reflection. The velocity at which Čerenkov light will be internally reflected in the radiator is defined as

$$\beta = \sqrt{\frac{1}{n^2 - 1}}\,. \tag{2.25}$$

For $n = 1.49$, we obtain $\beta = 0.90$; at 800 MeV/c, π^+ are above this threshold, but K^+ are not. This leads to the arrangement shown in figure 2.18, where Čerenkov light emitted in response to the passage of K^+ exits the radiator from the circular face and is focused by a parabolic mirror onto a ring of ten phototubes (PMTs). Internally reflected light emitted in response to the passage of π^+ exits the radiator from the conical edge and is reflected onto another ring of ten phototubes.

The output signals of the ten phototubes from each ring were sent to individual discriminator channels housed in two separate units. An output signal was available from these units providing a current proportional to the number of discriminator channels with an input voltage above

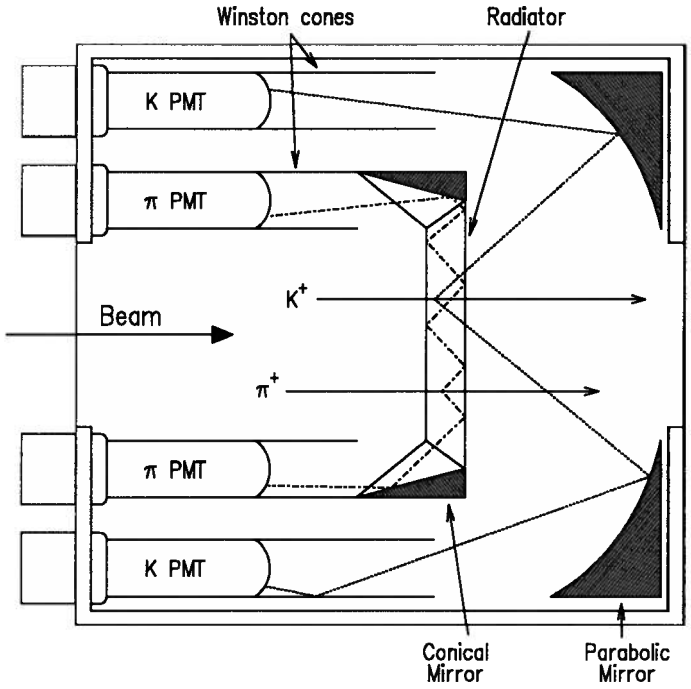

Figure 2.18: Čerenkov counter schematic side view. The dotted line shows the possible path for Čerenkov photons emitted after the passage of a beam kaon; the dashed-dotted line shows the same for a passing beam pion. Only two of the 10 PMTs in each ring are shown.

threshold. The threshold was set at the level of a single photo-electron for each phototube. The output signals of the two units were sent to another discriminator where a minimum of six phototube votes was required to define the passage of a K^+ or π^+ . In both cases the inefficiency of detection was of the order of 10^{-4}–10^{-5}. Copies of the final pion and kaon Čerenkov counter signals were sent to multi-hit TDCs for time measurement.

2.2.1.3 Beam wire chamber (BWPC)

Immediately after the Čerenkov counter was the beam multi-wire proportional chamber (BWPC), allowing precise monitoring of the beam profile and the identification of multiple incoming beam particles. Figure 2.19 schematically shows the arrangement of one of the three wire planes used in the BWPC. The gas used was an 80:20 mixture of CF_4–isobutane; the very fast response of this gas mixture allowed the operation of the BWPC in a high rate environment. The average time resolution was approximately 2.0 ns. In the first wire plane, 72 pairs of wires were positioned vertically. The other two planes consisted of 60 pairs of wires positioned at $\pm 45°$ to the vertical. The active area of the planes was approximately 19 cm wide along the x axis and 6 cm high along the y axis. The position resolution obtained was $\sigma \simeq 0.5$ mm along the x axis and $\sigma \simeq 0.7$ mm along the y axis. The efficiency of a single plane of the chamber was greater than 99%.

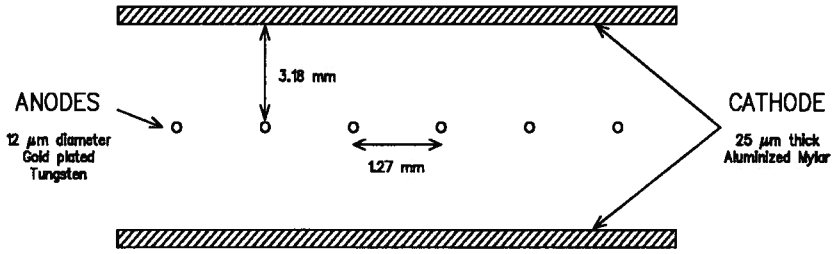

Figure 2.19: Schematic diagram of a section of one of the BWPC wire planes.

2.2.1.4 Degrader, B3 & B3S counters

Beam particles were slowed by a 535 mm long cylindrical beryllium oxide degrader. This material was chosen for its relatively high density (3.0 g/cm^3) and low average atomic number,

resulting in a good stopping power while minimizing multiple Coulomb scattering effects. The low atomic number also reduced the probability of absorption of photons emitted in the decay of kaons in the target. Located immediately upstream of the degrader were two scintillator counters, B3 and B3S, used for beam flux and position monitoring purposes only.

2.2.1.5 Lead-glass detector

In 1991, a part of the downstream end of the degrader was replaced by a 10 cm long and 11.2 cm diameter cylindrical piece of lead-glass, used primarily as a photon detector[2]. High-energy gamma rays traveling inside a medium can initiate an electro-magnetic shower. A useful quantity in characterizing the ability of a material to interact with electrons and photons is the radiation length. This length can be seen as the distance required for one layer of multiplication in the development of an electro-magnetic shower. The lead-glass used for this detector contained approximately 53% of lead oxide by weight (total density 3.85 g/cm^3), substantially increasing the probability for photons to convert in it because of lead's high atomic number; its radiation length was 2.84 cm.

Very little scintillation light is produced by charged particles in lead-glass. However, because it is transparent in the visible and UV region, Čerenkov light emitted in lead-glass can be detected. The refractive index of the lead-glass used in this detector was $n = 1.68$, resulting in a threshold velocity of $\beta_t = v_t/c \simeq 0.6$ which corresponds to an electron kinetic energy of 128 keV. The typical energy of photons incident on this detector is several MeV, which should result in the production of Čerenkov light if the photon initiates an electro-magnetic shower in the lead-glass.

A schematic side view of the lead-glass detector is shown in figure 2.20. The lead-glass cylinder was surrounded by a 1 cm thick cylinder of acrylic used to collect the Čerenkov light and guide it by total internal reflection to a ring of 16 phototubes. The delicate focusing of the electron's trajectories in the dynode array of conventional phototubes is upset by the presence of a magnetic field. Since this sub-detector was very close to the center of the detector assembly

[2]More technical details will be given about this sub-detector since it was not described in reference [46].

where strong magnetic fields are present, high-field mesh dynode phototubes[3] were used. This type of phototube can provide gains of 10^4–10^5 when the axis of the tube coincides with the magnetic field lines, compared to gains of order 10^7 for conventional phototubes in standard operation without a magnetic field. The relatively small output signals from the high field tubes were pre-amplified before being sent outside of the detector via coaxial cables. An alternative to the use of high field phototubes would have been to install conventional phototubes outside of the region of high magnetic field. However, the light attenuation in the very long light guides required would have made this design impractical.

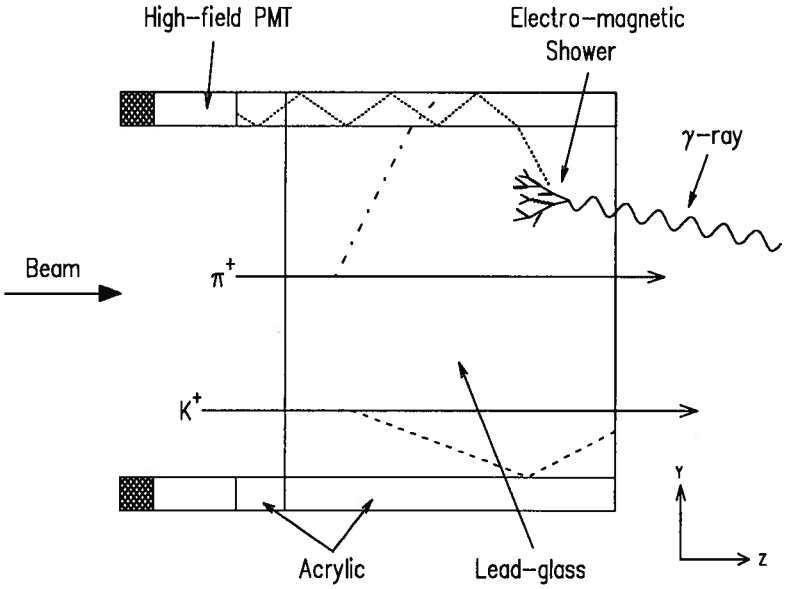

Figure 2.20: Lead-glass detector schematic side view. The dashed line indicates the path of a Čerenkov photon emitted by a beam K^+ ; the dashed-dotted line indicates the same for a beam π^+ . The dotted line indicates the path of a Čerenkov photon emitted by an electron from an electro-magnetic shower, from production in the lead-glass to the phototube via the acrylic cylinder.

As can be inferred from figure 2.20, Čerenkov light can be produced by beam π^+ and K^+ in the lead-glass. For most π^+ , the light produced exits the side of the lead-glass cylinder and a portion is trapped in the acrylic cylinder. For K^+ , their lower velocity results in a Čerenkov light emission angle (see equation 2.24) too shallow to exit the lead-glass cylinder side; the

[3] 2.5 cm diameter Hammamatsu R3432; the photo-cathode diameter was $\approx$ 1 cm.

light is totally reflected at that interface and exits from the end of the cylinder. To heighten this effect, the side of the lead-glass cylinder was wrapped in a thin film of transparent Teflon ($n \approx 1.35$), thereby decreasing the minimum angle for total internal reflection. Despite these precautions, light associated with beam K^+ was observed, typically enough to be detected by one or two phototubes. For comparison, the mean number for beam pions was 8–9 phototubes, and for photon showers the light output was about 1 phototube/10 MeV. The light seen for K^+ possibly came from cases where the K^+ trajectory had a significant component in the xy plane, resulting in Čerenkov light with a smaller incident angle with respect to the normal to the lead-glass–acrylic cylinder interface than for kaons travelling parallel to the z axis. Another contribution was from fluorescence in the lead-glass induced by the emitted Čerenkov light. This effect was confirmed in beam tests performed at TRIUMF [49].

Radiation damage also hindered the performance of this detector. The damage causes the normally clear glass to acquire a yellowish tint, reducing the transparency and resulting in a lower light output per energy deposited. After a few weeks of operation, the performance started to degrade; near the end of the data collection period, the light output was only 30–40% of its initial value.

Similarly to the Čerenkov counter, the output of the 16 PMTs was sent to a multi-channel discriminator unit which supplied an output current proportional to the number of channels above threshold. This signal was discriminated and sent to a multi-hit TDC, as well as a transient digitizer channel (see section 2.2.6.1). The measurement of the response of the lead-glass detector as a function of time allowed the separation of signals from kaons and from photons or late beam pions (see 3.3.3.5).

2.2.1.6 B4 hodoscope

Between the degrader and the target was the B4 scintillation counter hodoscope. It was used to identify the passage of charged particles from the degrader to the target. Its segmentation allowed the monitoring of the beam profile in the xy plane at the entrance to the target. There were significant differences between the devices used in 1989 and 1991, although not

in the purpose and general principle. In 1989, the B4 hodoscope consisted of three planes of scintillator counters. One was hexagonal in shape and covered the cross sectional area of the target; this counter was referred to as B4T. The other two planes each consisted of four individual rectangular counters arranged side by side to form a nearly square section covering the target front face. For one plane the individual counters were installed vertically while they were horizontal for the other. In 1991, the B4T counter was removed. The other two planes were replaced by two identical arrays of six individual counters forming a roughly hexagonal area covering the front face of the target. The width of the counters decreased with proximity to the center of the array to compensate for the variation in beam intensity. The two planes were installed at $\pm 45°$ to the vertical.

All counters in the B4 hodoscope were made of 6.25 mm thick plastic scintillator. The light emitted after the passage of a charged beam particle was collected with adiabatic light guides and carried parallel to the beam direction outside of the region of high magnetic field. Conventional phototubes detected the light at the end of the light guides.

2.2.2 Target (TG)

The target defines the central detector region where K^+ come to a stop and decay. On average, approximately 2×10^5 K^+ per accelerator spill came to rest in the target. It was designed with high segmentation to clearly identify the stopping K^+ region and charged particles emitted in its decay, and with minimal non-active regions to avoid undetected energy losses from charged particles or electro-magnetic showers. Figure 2.21 shows a schematic view of the upstream end of the target in the xy plane. It was a hexagonal array of 378 triangular elements. Each element consisted of six 2 mm diameter scintillating fibres, held together with epoxy. Each individual fibre had a sputtered aluminum coating to protect the surface and eliminate cross-talk between fibres. Overall, 75% of the target consisted of active scintillator material.

The fibres were approximately 3 m long, with the last metre in each element left without epoxy to allow more flexibility. The triangular elements were interlocked to form a hexagon 10 cm flat-to-flat; a single cylindrical fibre occupied the center of the target, for a total of 379

elements. The upstream end of the target was located approximately 12 cm along the z axis upstream of the detector's center of coordinates. An aluminum mirror was evaporated on the polished surface of the upstream end to reflect scintillation light towards the downstream end of the elements, where each was viewed by a 10 mm diameter phototube. The output from each phototube was brought to the counting house and fed to a $\times 10$ amplifier, the output of which was connected to a passive circuit designed to divide the charge of the signals in three parts. One part went to an ADC, one part to a discriminator which in turn fed a multi-hit TDC and a third part was summed with the output of all other elements. The resulting summed signal was then discriminated at a voltage equivalent to an energy deposition of 5 MeV in the target. This discriminator output signal defined the presence of a particle in the target. The division of the signal from each phototube to an ADC, a TDC and an analog sum is typical of all sub-detectors using scintillator counters.

Because of the large variation in the amount of scintillator crossed by charged particles in a given target element, the performance of the target was determined in terms of the number of photo-electrons obtained per mm of path length for a minimum ionizing[4] particle. The overall average was approximately one photo-electron per mm. The spatial resolution in the xy plane was 1.8 mm (rms) for a charged particle travelling transversely to the target elements. Figure 2.22 shows an xy plane event display of the time and energy information recorded by the target for the $K_{\pi 2}$ event shown in figure 2.16. The K^+ is clearly identified by its large early energy deposition in the target elements, because it travels mostly along the length of the scintillating fibres and it is near the end of its range where the rate of energy loss is largest. In contrast, the π^+ deposits a small amount of energy because of its high momentum and mostly transverse trajectory; we also see the clear time delay between the K^+ and π^+ , indicating that the K^+ decayed at rest. The time resolution for individual elements was typically $\sigma \simeq 1.3$ ns.

[4]The mean energy loss rate of a minimum ionizing particle in plastic scintillator is approximately 1.7 MeV/cm.

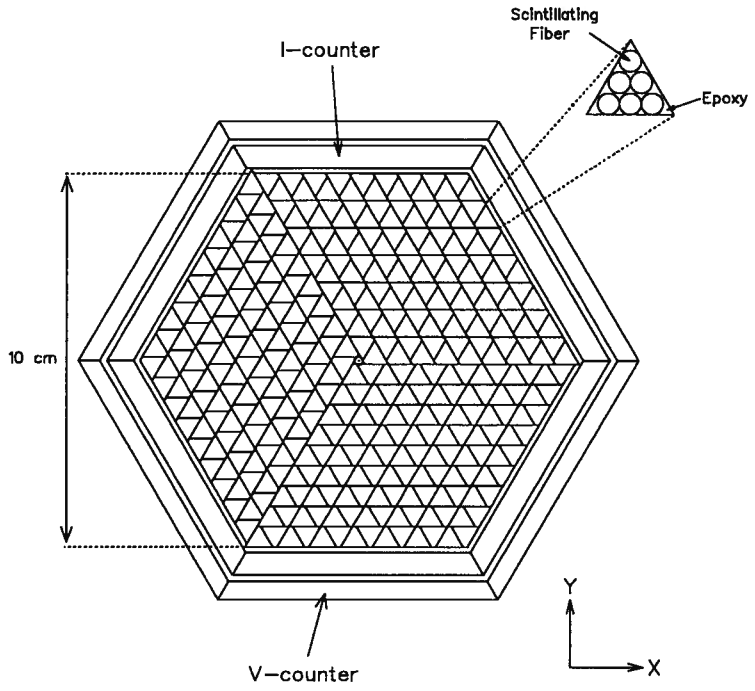

Figure 2.21: Schematic view of the upstream end of the target, I-counters and V-counters. Shown in the upper right hand corner are details of a target element.

2.2.3 I- and V-counters (IC and VC)

To define the target fiducial region along the z axis, six 6.4 mm thick and 24 cm long plastic scintillator counters surrounded the target, as shown on figure 2.21 and 2.23. Each counter was connected to a light guide and a phototube. Downstream of the I-counters were another six scintillator counters called V-counters. These were 1.96 m long and 5 mm thick, and overlapped by 6 mm with the downstream end of the I-counters. Each of the six V-counters was viewed by a phototube. The V-counters were used to veto charged particles which might originate from kaons decaying downstream of the target fiducial region. They were also used to detect electro-magnetic showers in the area between the target and the downstream endcap detector.

2.2.4 Drift chamber (DC)

Like multi-wire proportional chambers, drift chambers make use of the ionization caused by the passage of a charged particle in a gas volume. However, in this case, the time required by

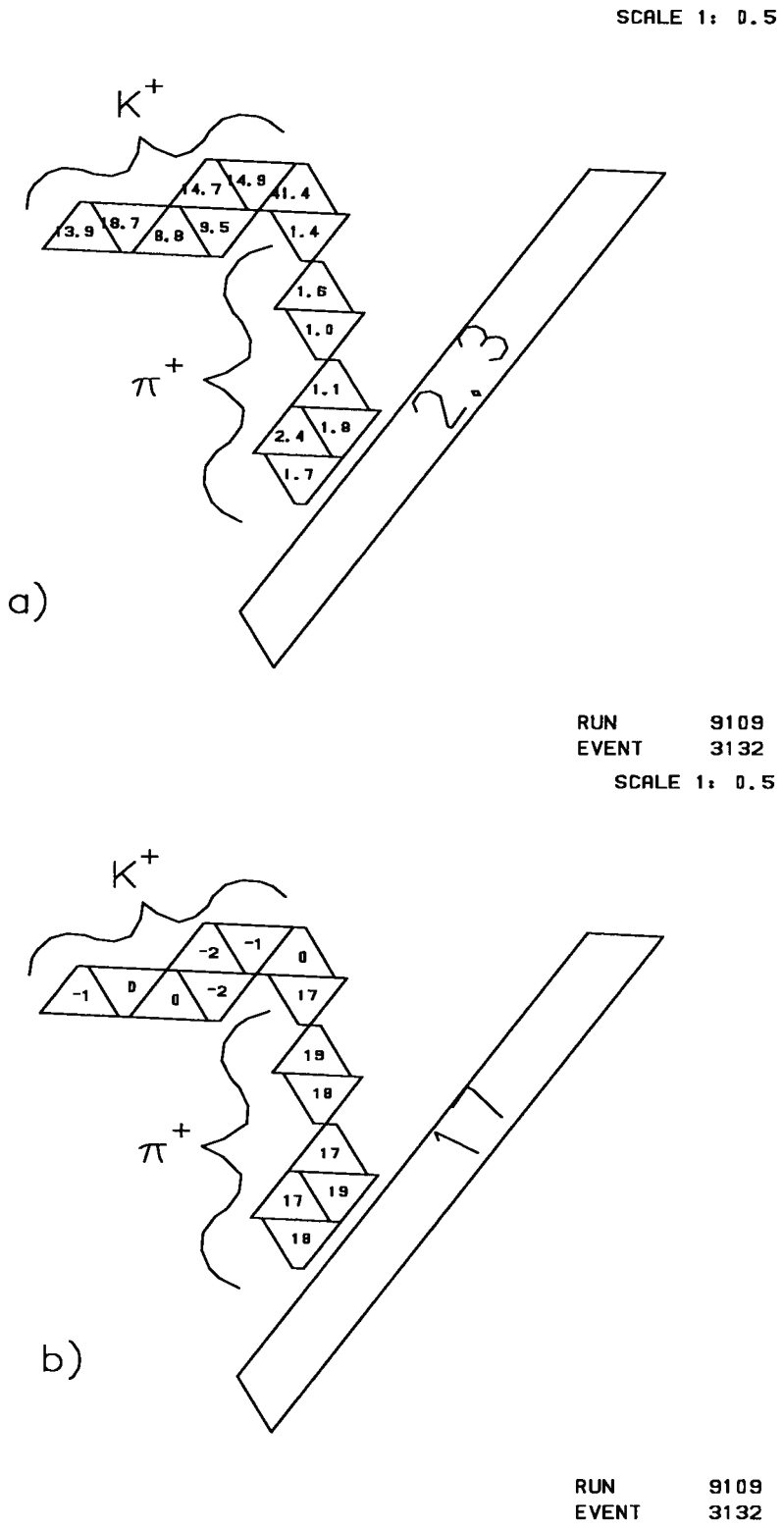

Figure 2.22: Target and I-counters event display for $K^+ \rightarrow \pi^+\pi^0$ event. a) shows the energy information in MeV and b) the time information in nanoseconds.

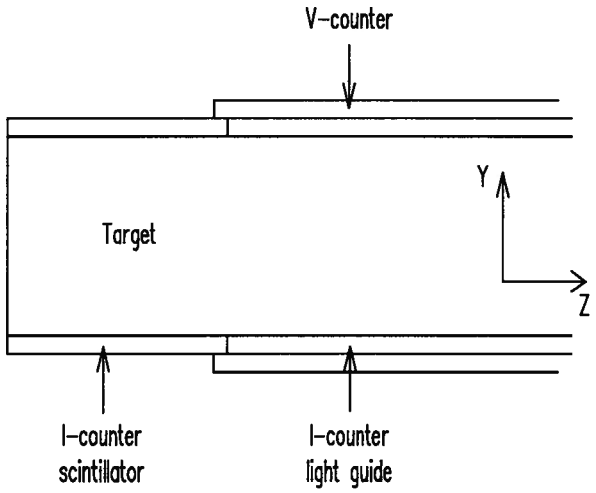

Figure 2.23: Schematic side view of the target, I-counters and V-counters.

the ionization electrons to reach the anode wires (drift time) is used to determine the point of closest approach of the particle to the wire. The reference time is provided by a scintillation counter external to the chamber and traversed by the charged particle.

The drift chamber used in this experiment was a cylinder surrounding the target, with an inner and outer radius of 9.5 cm and 43.2 cm respectively. Its function was to accurately determine the trajectory of charged particles emerging from the target and to measure their momentum. This was made possible by the presence of a 1 Tesla magnetic field in the direction of the z axis. The 50.8 cm long active volume of the drift chamber contained a gas mixture of 50:50 argon–ethane; the argon was bubbled through ethanol at 0°C; this mixture provided a gain of $\sim 10^5$. The inner and outer radius walls were made of graphite-fibre epoxy 0.4 mm and 0.47 mm thick respectively, and the end plates of 9.5 mm thick aluminum. The cylindrical volume was divided in five radial layers, which in turn were divided in 36, 40, 50, 60 and 70 azimuthal cells respectively, in order of increasing radius. Figure 2.24 schematically shows the design of individual cells. The planes of cathode wires, shared by neighboring cells, were held under negative high voltage. Ionization electrons drifted towards the grounded anode wires in the direction of the electric field thus created. However, the presence of the magnetic field tilted the trajectory of the electrons by an angle known as the Lorentz angle. This angle was empirically determined for each cell and was typically 25°.

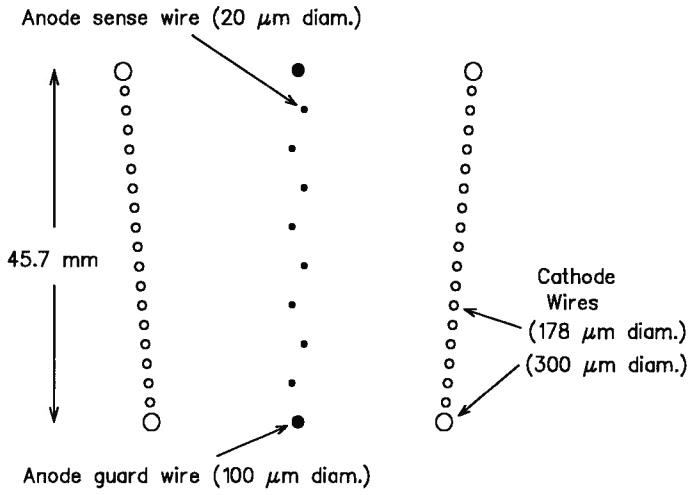

Figure 2.24: Drift chamber "jet" cell design. All cathode wires are made of beryllium–copper alloy, as are the anode guard wires. The anode wires are made of gold plated tungsten.

The wires in the innermost, middle and outermost cell layers (axial layers) were positioned parallel to the z axis of the detector. The wires in the other two layers (stereo layers) were offset by one cell in azimuth from one end plate to the other. This allowed the determination of the position along the z axis. As shown in figure 2.24, the anode sense wires were staggered alternately from the mid-plane, to resolve the left-right ambiguity in the position measurement. The innermost six anode wires were instrumented with pre-amplifiers, mounted on the chamber end-plates. Their output signals were carried to post-amplifiers located in the counting house, the output of which was fed to discriminators. These in turn fed multi-hit TDCs for drift time measurement.

Figure 2.25 shows a schematic end view of the cell boundaries. Superimposed are the position measurements for a positively charged particle and the fitted trajectory in the xy plane. A close-up of one of the cells crossed by the charged particle shows the effectiveness of the wire staggering in resolving the left-right ambiguity. The acceptance of the drift chamber was approximately 2π sr for charged particles of momenta greater than 150 MeV/c. The position resolution achieved in the xy plane varied between 130 μm and 250 μm. Along the z axis, the resolution obtained was between 2.2 and 4.2 mm. Figure 2.26a shows the π^+ total momentum distribution for $K^+ \to \pi^+\pi^0$ decays. Note that to obtain the total momentum, a correction

had to be applied for the energy lost by the π^+ in the target. The distribution was fit to a single Gaussian function using a chi-square minimization method; the results are indicated on the graph. The nominal value of the $K_{\pi 2}$ momentum peak is 205.12 MeV/c. The non-Gaussian tails of the distribution are caused by a combination of tracking errors, multiple scattering in the drift chamber and reconstruction errors, and π^+ scattering in the target. Based on the single Gaussian fit, the relative momentum resolution achieved was approximately $\sigma(p)/p = 2.2\%$ at the $K_{\pi 2}$ peak.

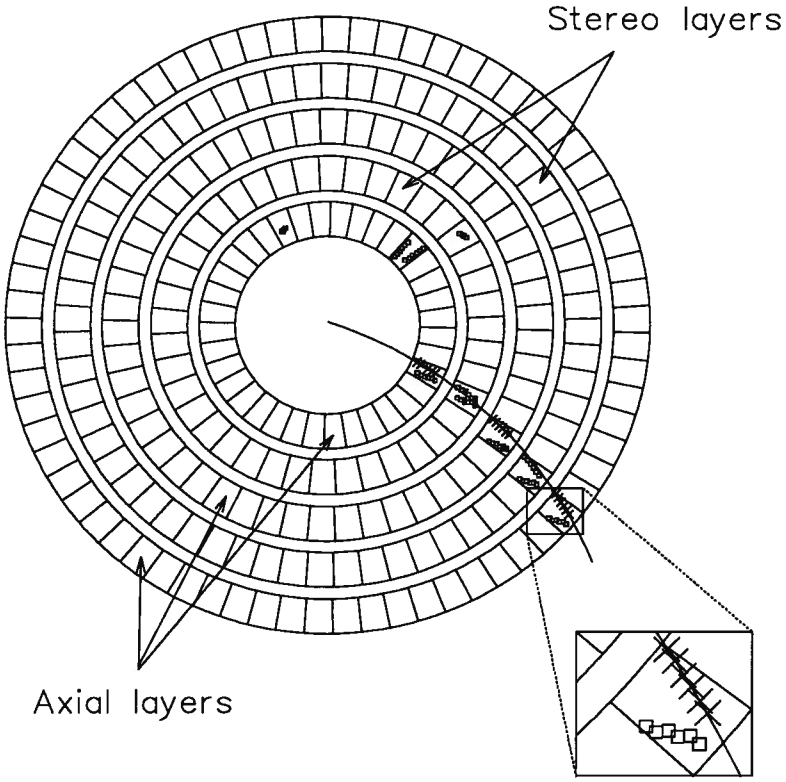

Figure 2.25: End view of drift chamber cell boundaries and fitted particle trajectory. The squares represent the position measurements, including mirror points due to the left-right ambiguity; the X's indicate the points in the axial layers chosen by the fitting algorithm.

2.2.5 Inner wire chamber (IWC)

In 1991, a thin cylindrical drift chamber, called inner wire chamber (IWC) [50], was installed between the target and the drift chamber. Its main purpose was to provide additional tracking

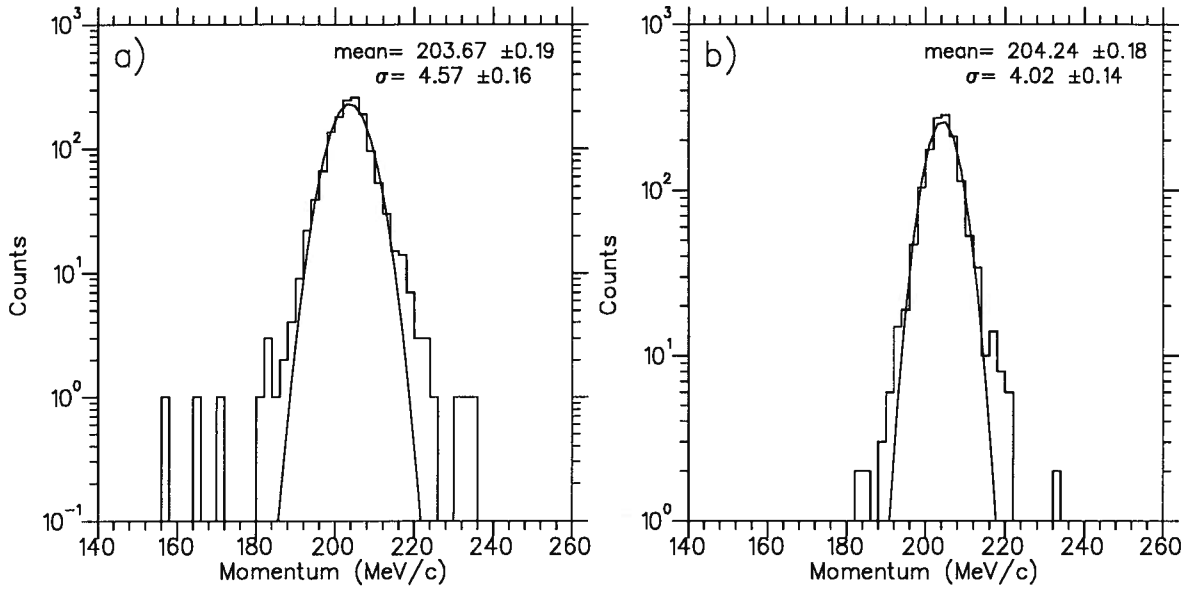

Figure 2.26: π^+ total momentum distribution for $K_{\pi 2}$ events a) from the drift chamber and b) combining the IWC and drift chamber information. In both cases a correction was applied for the energy lost by the π^+ in the target.

information to improve the resolution for position measurements of charged particles, primarily along the z axis. Figure 2.27 shows a schematic end view of a section of the IWC. It consisted of a single ring of axial wires located at a radius of 8.5 cm, between two concentric 50 μm thick Kapton foils. The wire plane was formed of 48 gold-plated tungsten anodes alternated with 48 gold-plated aluminum cathodes. The anode wires were held at a positive high voltage while the cathodes were grounded. Copper coating on the Kapton foils maintained at ground voltage completed the nearly square drift cells around each anode. A copper coated 225 μm thick G10 cylinder[5] at a radius of 7.6 cm and a copper coated Kapton foil at a radius of 9.4 cm formed the external walls of the chamber and defined the dimensions of the gas volume. These additional cylinders also provided mechanical support and additional electrical shielding. The gas mixture was the same as that used for the main drift chamber.

The copper coating on the innermost foil was formed of 5.1 mm wide parallel strips angled at 45° with respect to the z axis and separated by 0.78 mm gaps. The center of gravity of

[5]G10 is a trade name for a material made of 60% SiO_2 and 40% epoxy.

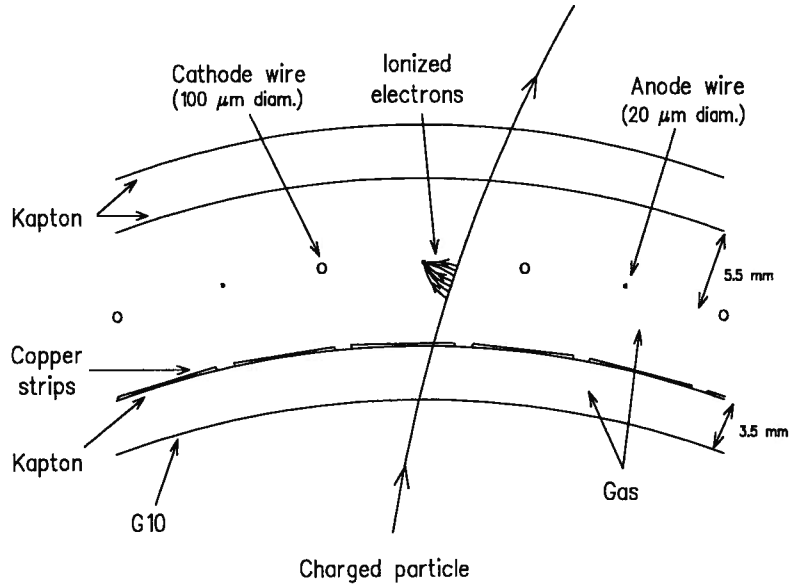

Figure 2.27: Schematic end view of a section of the inner wire chamber (IWC).

the measured charge induced on the strips by the ionization in the gas, combined with the azimuthal information provided by the anode wires, allowed the determination of the position of the ionization along the z axis. Measurements in the xy plane were obtained by measuring the drift time of the electrons to the anode wires. Each anode wire and cathode strip was instrumented with pre- and post-amplifiers, analogous to the ones used for the drift chamber. A copy of the output signals from all post-amplifiers was sent to ADCs and another was sent to discriminators which fed multi-hit TDCs. Figure 2.26b shows the total momentum distribution for the same events as in figure 2.26a obtained by including the IWC information to the track fit. As can be seen, the improvement in the momentum resolution was approximately 10%; this matched the design expectation.

2.2.6 Range stack (RS)

The range stack was a cylindrical array of plastic scintillator counters surrounding the drift chamber. Its function was the measurement of the kinetic energy and the range of charged particles emerging from the drift chamber. The range stack was divided in 24 azimuthal sectors and 21 radial layers, as shown in figure 2.15, and occupied the radial region between 45.1 cm

and 89.6 cm. The innermost layer consisted of 52 cm long and 6.35 mm thick plastic scintillator counters, designated as T-counters. These defined the 2π sr fiducial acceptance region of the range stack for charged particles emerging from the target, and corresponded more or less with the length of the drift chamber along the z axis. The other 20 layers consisted of 1.8 m long and 1.9 cm thick plastic scintillator counters. The counters were supported at both ends by a web-like stainless steel frame, away from the fiducial region. This guaranteed that charged particles accepted in the fiducial region would encounter minimal amounts of non-active material, mostly from wrapping of the counters. The range stack was constructed such that π^+ from $K^+ \to \pi^+\nu\overline{\nu}$ decays would come to rest within it; this was also true of π^+ from $K_{\pi 2}$ decays and a large fraction of the μ^+ from $K_{\mu 2}$ decays.

The kinetic energy of the charged particles stopping in the range stack was measured by detecting with phototubes the scintillation light from each counter struck by the particle. However, in a scintillator counter, the light emitted by the passage of a charged particle is attenuated according to

$$I = I_0 \exp\left(-d/L_{\text{att}}\right) \tag{2.26}$$

where I is the intensity of the light measured a distance d from the point of emission, I_0 is the intensity at the point of emission and L_{att} is the attenuation length. This length varies substantially depending on the composition of the plastic scintillator, the physical dimensions and the quality of the surfaces. For the scintillator counters used in the range stack, the attenuation length was of the same order as the length of the counters, meaning that this effect was important. To avoid this position dependence of the energy measurement, phototubes were installed at both ends of the counters. Since the measured energy is proportional to the amount of light detected, the measured energy at each end, denoted 1 and 2, for a charged particle crossing a counter of length L a distance x from end 1 can be expressed as

$$\begin{aligned} E_1 &= E\exp\left(-x/L_{\text{att}}\right) \\ E_2 &= E\exp\left(-(L-x)/L_{\text{att}}\right). \end{aligned} \tag{2.27}$$

From this, we can obtain

$$E = \left[\frac{E_1 E_2}{\exp\left(-L/L_{\text{att}}\right)}\right]^{\frac{1}{2}} , \tag{2.28}$$

giving the energy deposited by the particle as a function of the measured quantities E_1 and E_2, and independent of the position x. The constant $\exp\left(-L/L_{\text{att}}\right)$ can be determined by calibration.

The light from each end of the counters was collected with 0.9 m long acrylic light guides and brought to PMTs outside of the magnet through holes in the iron end plates. Figure 2.28 shows schematic details of one range stack and barrel veto sector; the latter is described in section 2.2.7.1. Layers 2 through 10 of each sector of the range stack were read out in groups of 4, 3 and 2 counters, designated as layers A, B and C respectively. This minimized complications in the installation of the PMTs, but adversely affected measurements for particles stopping in that region. The arrival time of signals from each PMT were not measured with TDCs but rather by transient digitizers; these will be described below. The average number of photo-electrons per MeV per end for range stack layers 11 and above was approximately 11.0, and 7.0 for layers A, B and C.

Figure 2.29a shows the total π^+ kinetic energy distribution for $K_{\pi 2}$ events. The total energy is obtained by adding the energy (measured via scintillation light) deposited by the charged particle in the target, I-counters and range stack. The nominal value of the $K_{\pi 2}$ energy peak position is 108.5 MeV. The relative resolution at the measured energy, based on a Gaussian fit, is 4.35%. The low energy tail is mostly due to inelastic scattering of the π^+ in the range stack. This could be substantially reduced by requiring consistency between the momentum measured in the drift chamber and the energy measured in the range stack. The high energy tail is caused by ~20 MeV photons from π^0 decay converting in the range stack on top of the charged track.

The radial segmentation allowed the measurement of the range of charged particles coming to rest in the range stack. For additional position information, multi-wire proportional chambers (RSPC) were installed in each sector, following layers C and 14 (see figure 2.28). The active length of each chamber was approximately 1 m long. Axially positioned wires provided position

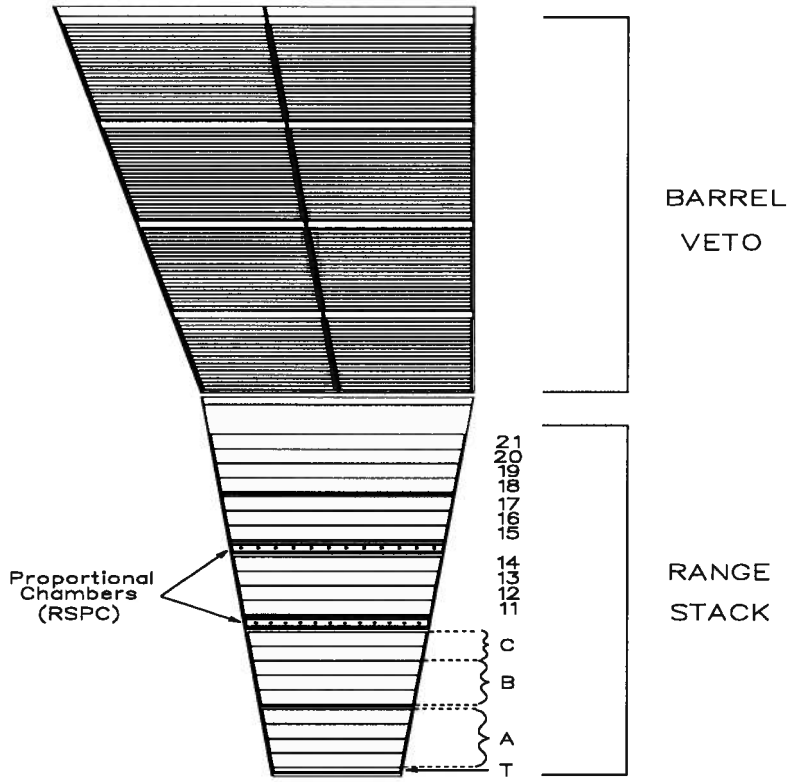

Figure 2.28: Schematic end view of one range stack and barrel veto sector.

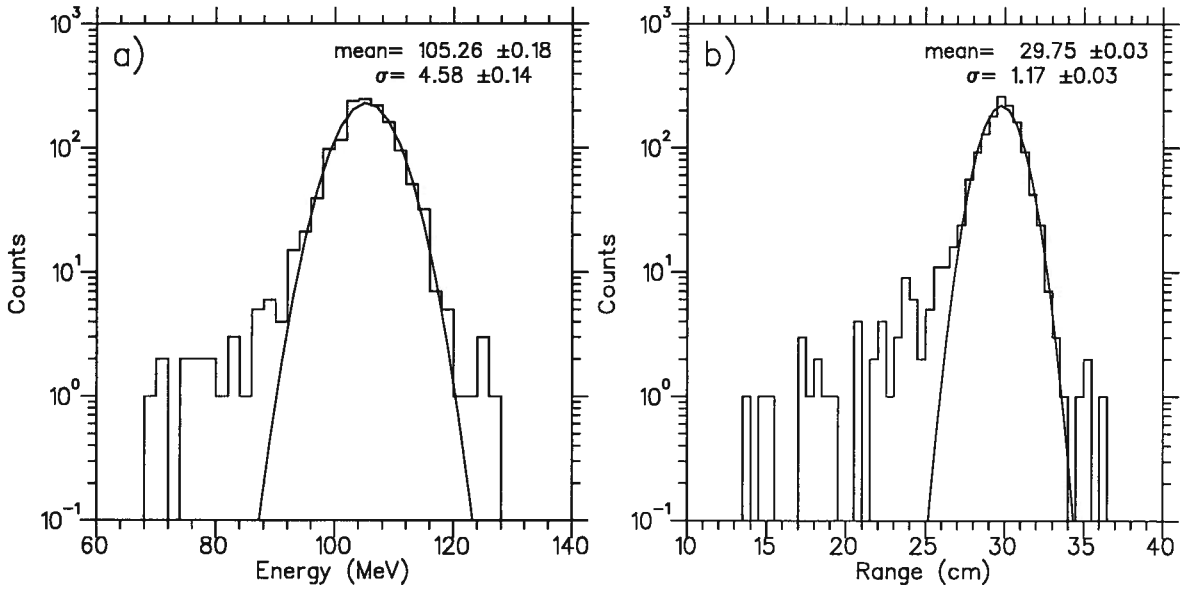

Figure 2.29: Total measured a) energy and b) range distributions for the π^+ from $K_{\pi 2}$ decays. Results of a chi-square minimization fit to a single Gaussian function are also shown.

information in the xy plane. The z axis position information was obtained by measuring the charge induced on the cathode by the ionization in the gas. The cathode was a serpentine-patterned copper trace on the wall of the chamber. The charge was measured at both ends and the end-to-end time difference of the signals was proportional to the z position of the ionization.

The RSPC position information, combined with the drift chamber position information, allowed the correction of the range measured in the range stack for the slope of the track in the $r-z$ plane. Figure 2.29b shows the total range in scintillator for $K_{\pi 2}$ events, obtained by summing the measured range in the target, I-counters and range stack. The nominal value of the $K_{\pi 2}$ range is 30.7 cm. The measured resolution is approximately 1.2 cm. As for the energy distribution, the low side tail is due to inelastic scattering of the π^+ in the range stack. The high side tail is due to reconstruction errors.

2.2.6.1 Transient digitizers (TD)

One of the important tasks in the search for $K^+ \to \pi^+\nu\overline{\nu}$ is the positive identification of the π^+ . As explained in the introduction, one way to do this is to identify the decay sequence of the π^+ . Since the charged particles emitted in the decay of kaons in the target and detected in the fiducial region of the drift chamber come to rest in the range stack, this is where the decay sequence can be identified. In the scintillator counter where the π^+ comes to rest, a first pulse will be observed from the pion itself. It will be followed by a second pulse corresponding to the mono-energetic muon from the $\pi^+ \to \mu^+\nu_\mu$ decay. The kinetic energy of the muon is only 4.12 MeV, which corresponds to a mean range in plastic scintillator of 1.4 mm. Therefore, in most cases the muon will deposit all its kinetic energy in the counter where the π^+ stopped and came to rest. The muon will then decay according to $\mu^+ \to e^+\nu_e\overline{\nu}_\mu$. The positron from this decay can have a kinetic energy between 0 and 53 MeV. Most of the time, it will generate a third pulse in the counter where the π^+ stopped and also deposit some energy in the surrounding counters.

To identify this decay chain, the time evolution of the output pulses of the range stack PMTs was recorded. The mean life of the π^+ and the μ^+, 26 ns and 2.2 μs respectively, the typical

range stack counter pulse width of 30–40 ns and the range of energy deposition in the counter where the π^+ comes to rest, typically 0–30 MeV, defined the operating parameters required of the recording devices. The devices used were custom built transient digitizers (TD) [51], which had a sampling rate of 500 MHz, a dynamic range of 8 bits and a total time range of 10 μs. To reduce the number of such devices, the output pulses from four contiguous sectors of the range stack were multiplexed for each end and all layers, for a total of 180 TD channels. A number of additional TD channels were used to monitor the PMT output of several other sub-detectors, notably the B4 hodoscope, the I-counters and the lead-glass detector. The TD channels were in groups of four on a double-width Fastbus [47] module; eight such modules were housed in a standard Fastbus crate.

The output of discriminators monitoring range stack PMT pulses from each counter was used to provide information on which of the four counters were contributing to the pulse in a given TD channel. This information, digitized as a single bit at a frequency of 250 MHz, was recorded along with the pulse height information; it was referred to as "flags".

Figure 2.30 shows the PMT pulses digitized by TDs from both ends of a range stack counter in which a π^+ came to rest and decayed (stopping counter). Also showed are the digitized pulses from both ends of the counter immediately below the stopping counter; a single pulse is visible, corresponding to the π^+ . On these graphs, X's and O's represent the sampled points, separated in time by 2 ns. Figure 2.31 shows the TD information for the same channels with an expanded time scale, showing the pulse corresponding to the positron from muon decay. The positron deposited energy in several surrounding counters, as showed by the TD information from two additional range stack layers.

In addition to π^+ identification, the TDs were also used for all time measurements in the range stack. The time of a pulse was determined on its leading edge at the interpolated half-height of the pulse. For 1991 data, this time value was then measured in reference to the time of a sharp fiducial pulse ($\sim$10 ns wide, 4 ns rise time), generated by an external circuit and injected in all TD channels near the end of the recorded time range for each event. These fiducial time pulses essentially synchronized all TD channels to an accuracy of better than

30 ps, removed time shifts which can occur in the TD system on an event by event basis and greatly simplified the time calibration. The intrinsic time resolution obtained for range stack counters was $\sigma \simeq 0.35$ ns. This was measured by comparing the time of individual counters that were hit by a charged particle to the average of all other counters hit by the particle.

In 1991, the PMT pulses from layers A, B and C of the range stack passed through an amplifier with a logarithmic transfer function before being input to the TDs. This effectively increased the dynamic range of the TDs for those counters, to match the greater range of energy deposited by a π^+ coming to rest in those thick counters.

2.2.7 Photon veto system

Another important aspect in the search for $K^+ \to \pi^+\nu\overline{\nu}$ is the detection of photons emitted by background processes. Most of the photon detection was done with the photon veto system, consisting of three individual sub-detectors : the barrel assembly and two endcaps. All three were electro-magnetic shower counters made of alternating layers of 5 mm thick plastic scintillator and 1 mm thick lead. The lead was used to convert incident photons into electron–positron pairs and the scintillator detected the ionization energy of electrons and positrons in the shower. The fraction of the total energy of the shower deposited in the scintillator, or visible fraction, was approximately 30%. Because only a portion of the energy deposited in these counters is detected, they are commonly referred to as sampling calorimeters.

There are three primary sources of inefficiency for the photon veto system :

1. Electro-magnetic shower fluctuations
2. Photon escape
3. Photo-nuclear absorption.

The first item led to the choice of thickness for the scintillator and lead layers. Photons can escape detection through gaps in the system or regions where the number of radiation lengths is not as large as others. The geometrical design of the detector was such that there were at least 12 radiation lengths for 79% of 4π sr and at least 2 radiation lengths for 99% of 4π sr.

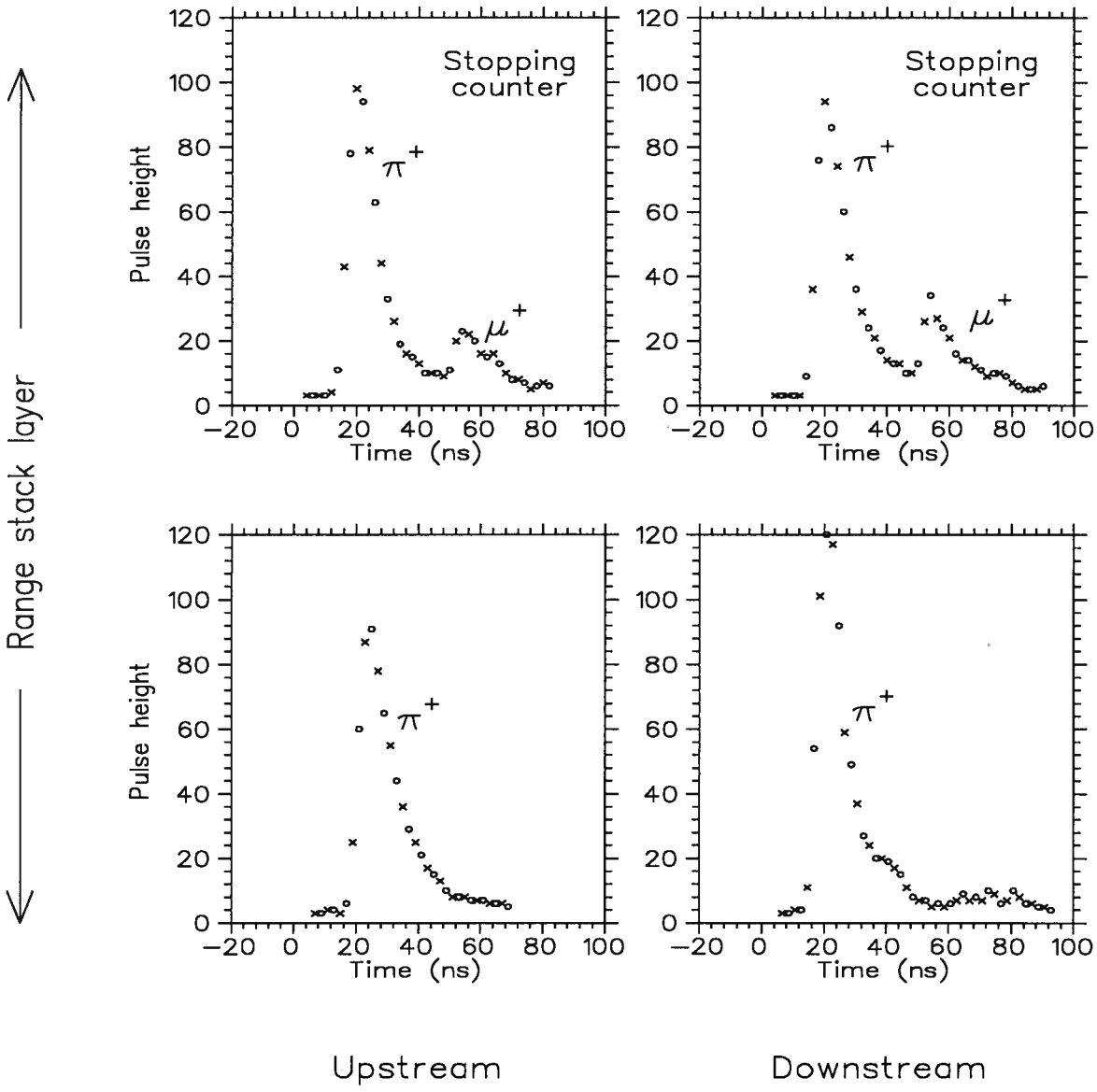

Figure 2.30: Range stack counter pulses recorded with transient digitizers. Information from the stopping counter clearly shows the $\pi^+ \rightarrow \mu^+\nu_\mu$ decay.

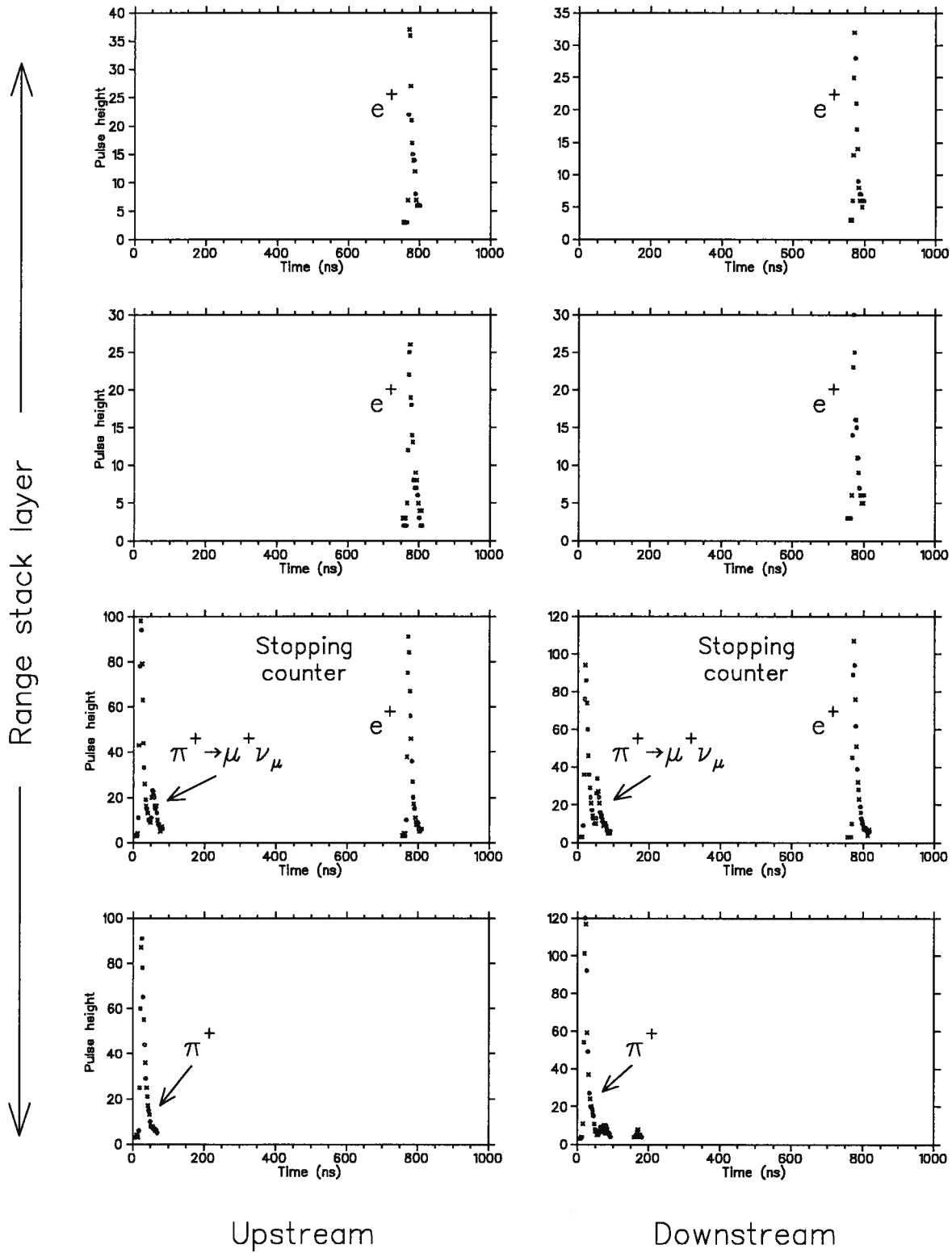

Figure 2.31: TD information for the same event as figure 2.30 but with an expanded time and space scale, showing the positron from muon decay.

Photo-nuclear absorption is dominated by giant dipole resonance excitation for photon energies below 30 MeV. The de-excitation is often by neutron evaporation; some of those slow neutrons can be detected through their interactions in plastic scintillator. For photon energies above 140 MeV, pion production becomes possible; those cases should be easier to detect.

The other important design criteria for the photon veto system used in this experiment was the response time of the detectors. Because of the high beam intensity for this experiment, each detector element was subjected to a large random flux of particles over the duration of the accelerator spills. The rate in each counter was a function of its volume, its proximity to the particle beam and the quantity of energy required to record a hit. For a veto system, the energy threshold had to be balanced against the fact that random particles cause accidental vetoing and result in a loss of acceptance. This can be mitigated by restricting the search for photons to a small coincidence time window. This requires very fast response and is the main reason behind the choice of plastic scintillator for the veto system.

2.2.7.1 Barrel Veto (BV)

The barrel veto consisted of a 1.9 m long cylindrical array surrounding the range stack. It was divided into 48 azimuthal sectors and 4 radial layers, as shown in figures 2.15 and 2.28. All modules were supported by a web-like frame of 1.5 mm thick stainless steel. The azimuthal boundaries were angled with respect to the detector's radial direction such that they did not project back to the target; this limited the effect of gaps and non-active material on photon detection. The modules in a sector consisted of 16, 18, 20 and 21 layers of lead and plastic scintillator, in order of increasing radius, for a total of 14.3 radiation lengths.

As for the range stack counters, scintillation light was collected from both ends of the modules via acrylic light guides. Between the light guides and the modules were 15 cm long acrylic mixer blocks which made light collection uniform. Light was detected outside of the magnet at each end with conventional phototubes. Approximately 10 photo-electrons per MeV deposited in the scintillator were obtained. The analog sum of all signals from barrel veto modules was discriminated at a voltage level equivalent to 5 MeV (visible) to define a barrel

veto signal. The time resolution for photon hits in the barrel veto compared to the time of the charged particle measured in the range stack was $\sigma \simeq 1.4$ ns.

2.2.7.2 Endcaps (EC)

The two endcap detectors, referred to as upstream and downstream endcaps, were positioned on either side of the drift chamber, as shown in figure 2.14. Each was divided in 24 azimuthal modules, with each module consisting of 66 layers of lead and plastic scintillator wedge-shaped plates, for a total of 12.4 radiation lengths. The plates were installed perpendicular to the beam direction so that the path of all photons emitted in the target crossed a significant thickness of lead and had a high probability to initiate an electro-magnetic shower. The inner radius of each endcap was 10.3 cm, surrounding the beam region upstream and the target downstream. The outer radius was 42.7 cm and 40.8 cm for the upstream and downstream endcaps respectively.

The light emitted in the scintillator had to be transported along the z axis to the outside of the magnet where it was detected by phototubes. To accomplish this, the light was collected at the wide end of the modules with a 6.5 mm thick plate of wavelength shifter. This material is essentially an acrylic substrate doped with a fluorescent compound; it absorbs light emitted by scintillator and re-emits it at a longer wavelength. The typical intrinsic efficiency of wavelength shifter to re-emit an absorbed photon is high, 70–95%. However, taking into account the absorption spectrum, the attenuation length in the materials and the geometry involved, a system such as the one here has an efficiency of about 10% to detect light emitted in the scintillator [52]. To maximize this number, the wavelength shifter material was chosen such that its absorption spectrum overlapped as much as possible with the emission spectrum of the scintillator. Another important consideration in the choice of wavelength shifter material was its response time to excitation, which had to be as fast as possible.

Figure 2.32 shows a schematic picture of one endcap module. The wavelength shifter plates were separated from the lead–scintillator modules by a 300 μm thick air gaps which prevented light trapped in the wavelength shifter plate by total internal reflection to re-enter the scintillator plates and be lost. Light was collected at one end of the wavelength shifter plate by an

adiabatic light guide connected to a 1.3 m long cylindrical light guide to reach the phototube outside of the magnet. An average of 8–10 photo-electrons per MeV deposited in the scintillator was obtained from these modules [53]. The energy resolution of individual modules was measured with an electron beam at TRIUMF and determined to be $\sigma(E)/E = 6\%/\sqrt{E}$, where E is the energy measured in GeV.

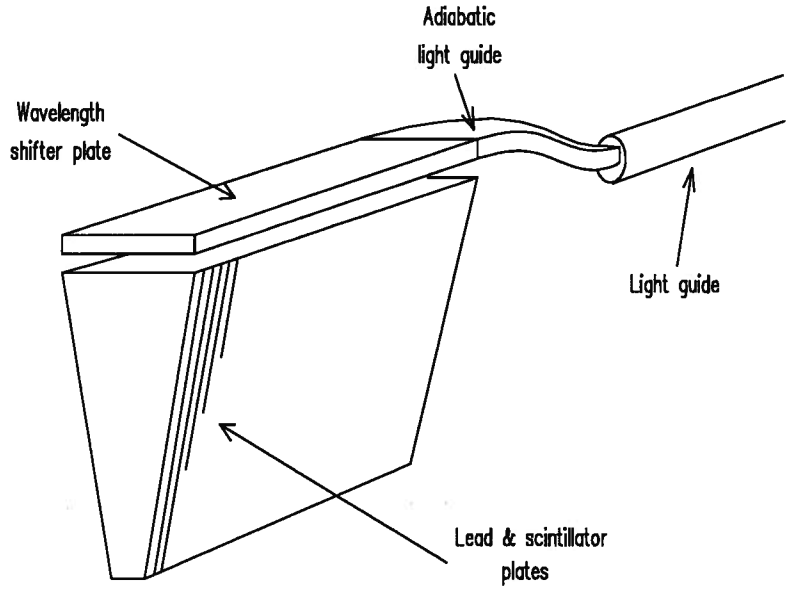

Figure 2.32: Schematic design of one endcap module.

The discriminator threshold voltage for the analog sum of all modules in each endcap was set at a level equivalent to approximately 10 MeV (visible). In 1991, $\times 10$ amplifiers were added before the signals were processed. This allowed a reduction of the voltage required to operate the phototubes, in turn reducing the current drawn by the phototube base and improving the performance and stability of the system. The time resolution for individual modules was $\sigma \simeq 1.7$ ns for hits above 1 MeV.

Chapter 3

Event Selection

This chapter will describe how decays of individual kaons were observed with the help of the detector, and how constraints applied to the digitized information from the detector were used in selecting potential $K^+ \to \pi^+\nu\overline{\nu}$ events among a large background of other processes.

Constraints used to select events were divided in two groups, online and offline. The first refers to initial constraints used to select interesting K^+ decays before the detector information is recorded to a permanent medium. Some of these constraints were applied using electronics techniques while others involved analysis of digitized information by dedicated micro-processors. These constraints were necessary for two main reasons : first, because of the limited rate capability to record the detailed detector information and second, because only a small fraction of the incoming K^+ are interesting in the search for $K^+ \to \pi^+\nu\overline{\nu}$. The events selected online were recorded for further study, usually on magnetic tape. The offline selection refers to all subsequent constraints applied to the recorded data.

3.1 Online selection

The online event selection, or trigger, was designed to reject background events as rapidly as possible while keeping the largest possible acceptance for signal events. The key elements to accomplish this are :

- Stopping K^+ identified
- Delayed decay of the K^+

- Single π^+ stopping in the range stack
- Veto photons

The trigger was arranged in three levels of increasing complexity and execution time. Table 3.2 summarizes the rejection and the execution time of each level for the two data collection periods in 1989 and 1991. A fourth trigger level was installed but not used in event selection; it was used to compress the event information. At each level, a decision was taken as to whether or not to further examine the detector information. Some information processing was required for the trigger decision, and while these tasks were ongoing no other candidate event could be searched for, resulting in "dead time". This was typically of the order of 25–30% of the 1.6 second AGS spill. If at any level of the trigger an event was deemed uninteresting, all current and subsequent operations in reference to the event were stopped and the system started the search for another candidate event at the lowest level of trigger. It was therefore advantageous to regroup the fastest operations at the earliest level of the trigger.

Table 3.2: Trigger levels rejection and execution time.

Level	**Rejection**		**Execution Time**	
	89	**91**	**89**	**91**
0	1080	900	20 ns	
1	3.1	1.8	5 μs	
2	22	13	700 μs	250 μs

Each trigger level will be described below. Also described is the data acquisition system, which retrieved the digitized detector information and transferred it to magnetic tape. Finally, trigger conditions other than the ones used to select $K^+ \to \pi^+\nu\overline{\nu}$ candidate events will be described briefly; these selected low bias events used for detector calibration and background studies.

3.1.1 Level 0

The first trigger level (Level 0) used fast ECL logic circuitry. An event trigger consisted of a coincidence between various detector signals. The requirements for the selection of $K^+ \to \pi^+\nu\overline{\nu}$ candidate events below the $K_{\pi 2}$ peak for the 1989 data set can be represented as

$$\mathrm{KT} \cdot \mathrm{IC} \cdot \mathrm{DC} \cdot (\mathrm{T} \cdot \mathrm{A}) \cdot \mathrm{B_{CT}} \cdot \overline{(12_{\mathrm{CT}} + ... + 18_{\mathrm{CT}})} \cdot \overline{(19 + 20 + 21)} \cdot \overline{(\mathrm{ECM} + \mathrm{ECP} + \mathrm{BV})} \, .$$

The 1991 Level 0 trigger had one minor difference which will be described below. This trigger and the events satisfying its conditions will be referred to as $\pi\nu\overline{\nu}$ in the remainder of this thesis. In the above expression, the $(\cdot)$ represents a logical AND, the $(+)$ a logical OR and a line above an item indicates that it was used as a veto. The individual requirements, to be described in more detail below, are defined as :

KT	$\equiv$	incoming kaon ($\mathrm{KT} \equiv \check{\mathrm{C}}_{\mathrm{K}} \cdot \mathrm{B4} \cdot \mathrm{TG} \cdot \mathrm{spill}$)
$\check{C}_K$	$\equiv$	Kaon Čerenkov counter hit
B4	$\equiv$	B4 hodoscope hit
TG	$\equiv$	target hit
spill	$\equiv$	AGS spill gate
IC	$\equiv$	I-counter hit
DC	$\equiv$	delayed coincidence
$(\mathrm{T} \cdot \mathrm{A})$	$\equiv$	coincidence in first two RS layers
$\mathrm{B_{CT}}$	$\equiv$	particle track reaches RS layer B
$\overline{(12_{\mathrm{CT}} + ... + 18_{\mathrm{CT}})}$	$\equiv$	particle track veto for RS layers 12 to 18 (range veto)
$\overline{(19 + 20 + 21)}$	$\equiv$	veto for RS layers 19, 20 and 21 (muon veto)
$\overline{(\mathrm{ECM} + \mathrm{ECP} + \mathrm{BV})}$	$\equiv$	veto for endcaps and barrel veto

The signal that initiated all events was $(\mathrm{T} \cdot \mathrm{A})$, a coincidence between the first two layers of a given sector of the range stack. Once a $(\mathrm{T} \cdot \mathrm{A})$ coincidence had been identified, all other detector signals were looked at and trigger requirements were examined. Each $(\mathrm{T} \cdot \mathrm{A})$ signal incurred about 20 ns of dead time. The $\pi\nu\overline{\nu}$ trigger required a single $(\mathrm{T} \cdot \mathrm{A})$ coincidence to define the start of a track in the range stack.

The threshold for individual range stack counter hits was approximately 0.5 MeV. Hit modules were considered part of a track if they were in the same sector as a $(T \cdot A)$ coincidence or in the next two sectors over in the direction of a positively charged particle curving in the magnetic field. The minimum range requirement was for the track to reach layer B of the range stack (B_{CT}). A veto was applied for tracks stopping beyond range stack layer 11 (range veto). This eliminated most of the $K_{\mu 2}$ decays as well as part of the $K_{\pi 2}$ decays. For the 1991 data set, this requirement was modified to allow tracks to stop in range stack layer 12, changing the range veto constraint to $\overline{(13_{CT} + ... + 18_{CT})}$. The veto on the last three layers of the range stack was referred to as muon veto because it vetoes the region of the range stack where most muons from $K_{\mu 2}$ decays come to rest. In this trigger, the muon veto primarily rejected photons.

To identify incoming kaons (KT), a coincidence between hits in the kaon Čerenkov counter, B4 hodoscope and target during an AGS spill was required. Approximately 3.5×10^5 kaons per AGS spill satisfied the KT requirement in 1991; in 1989, the rate was typically 15–20% lower. The delayed coincidence (DC) was between a kaon Čerenkov counter signal and any one of the six I-counters. Figure 3.33 shows the fraction of events accepted by this requirement as a function of delay time for 1991 data. As can be seen from the graph, the average delayed coincidence was about 2 ns. The requirement of at least one I-counter hit (IC) was essentially redundant with the delayed coincidence requirement, except for a small difference in energy threshold for the I-counters.

Finally, ECM, ECP and BV represent the upstream and downstream endcaps and the barrel veto signals respectively. Analog sums of the signals from all modules from each of these sub-detectors were formed and then discriminated individually. The threshold was approximately 10 MeV for each endcap and 5 MeV for the barrel veto. As seen in table 3.2, the Level 0 trigger rejection was approximately a factor of 1000. The difference between 1989 and 1991 is simply due to the maximum range requirement in the range stack (layer 12 stops were allowed in 1991).

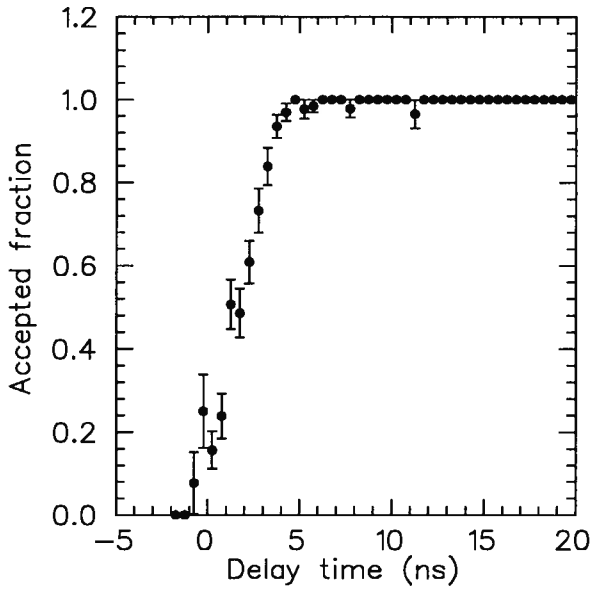

Figure 3.33: Accepted fraction versus delayed time between the incoming kaon and the outgoing charged track for the online delayed coincidence requirement.

3.1.2 Level 1

This trigger level consisted of three requirements for 1989 data. The first one required that the total number of target elements struck at the time of the event be less than 20. This reduced the number of $K^+ \to \pi^+\pi^+\pi^-$ and $K^+ \to \pi^+\pi^- e^+\nu_e$ decays satisfying the $\pi\nu\bar{\nu}$ trigger conditions, as well as photon conversions in the target. For the same purpose, it was required that there be only one cluster of I-counters sectors hit at the time of the event. A cluster was defined as any number of contiguous I-counters with a hit. The third Level 1 requirement was that no more than two range stack hextants could be hit, and if two were hit they had to be adjacent. A range stack hextant was formed of all layers of four adjacent sectors. For example, hextant 1 was the sum of range stack sectors 1 to 4. The threshold for a hextant hit was approximately 10 MeV. This requirement was a form of photon veto, but it was used primarily to determine in which range stack hextant the charged particle came to a stop; this is necessary for the next trigger level.

For 1991 data, only the hextant cut was included in the Level 1 trigger. Although the other two constraints did provide some background rejection at the trigger level, their significant

acceptance loss and the increased data taking rate capability available in 1991 made them unnecessary.

3.1.3 Level 2

This level consisted in a fast π^+ decay search using the TD information. This search was performed by processors which directly accessed the TD information. In 1989, the devices used were the SSPs (SLAC Scanner Processor), which resided in each of the Fastbus crates housing 32 TD channels. In 1991, the search was performed by the Smart Controllers (SC), dedicated processors programmable in C language. These devices significantly reduced execution time of this trigger level, from 700 μs down to 250 μs. The Smart Controllers each handled 16 TD channels and performed a number of other operations on the TD data in addition to the $\pi \rightarrow \mu$ search, before transferring the information to the SSP controlling the Fastbus crate.

The stopping layer and stopping hextant information from Level 0 and Level 1 was passed to all processors involved in the Level 2 trigger. The processor handling the stopping counter then proceeded to retrieve the digitized TD data and performed the π^+ decay search algorithm for each end of that counter in succession. In order to reduce dead time, success of the search for the first end was required before the second end could be examined. This saved typically 200 μs in 1989 and 100 μs in 1991. The search had to succeed for both ends of the stopping counter for the event to be accepted.

Two different cases were handled by the search algorithm : a) two detached pulses and b) a double pulse. In case a) the integrated area of the second pulse was required to be consistent with the energy deposited by a muon from π^+ decay at rest. In case b), use was made of the linear relationship between the maximum height and the area of a pulse from a scintillator counter. For each TD channel, a slope and intercept were determined for this linear relationship using well identified single pulses. The maximum height and integrated area were computed for each π^+ decay candidate pulse. From the pulse maximum, an expected pulse area was calculated using the pre-determined constants and compared with the measured value. If the difference between the measured area and the expected area was greater than a fixed threshold,

the algorithm succeeded. An exception to this arose when the pulse reached the maximum of the TD dynamic range. In this case, the pulse height–pulse area relationship was unreliable, so the event was rejected.

Figure 3.34 shows the TD information for both ends of the stopping counter of two events accepted by level 2. The efficiency of the search increased as a function of the decay time of the π^+ . The average efficiency varied as a function of the range stack stopping layer, from about 70% to nearly 90%. The efficiency was lower in the thicker layers (B and C) because of the larger size of the primary pulse from the stopping π^+ and their lower light collection efficiency resulting in a poorer pulse resolution. The Level 2 trigger constraints were more demanding in 1989 than in 1991, explaining the difference in rejection indicated in table 3.2. Another reason for the difference is the nature of the events reaching Level 2; the different Level 1 trigger conditions in 1989 and 1991 resulted in different emphasis of the various background processes.

3.1.4 Level 3

This trigger level operated in a farm of processors (ACP). Each processor, or node, was programmable in Fortran and could execute the same programs used in the offline selection (see section 3.3). A program executed in a host computer distributed individual events to available ACP nodes. The nodes analyzed the events and signaled the host program upon completion, returning the modified event information and the status of the analysis.

The event rejection capability of this trigger level was not exploited. However, significant operations were performed on the event information. The bulk of the 40 kBytes long events was taken up by the TD information. It was realized that for part of the 10 μs time range covered by the TDs for the range stack channels, a small number of parameters from each pulse, such as leading edge time, pulse height and pulse area, was sufficient information to keep. A fast algorithm was developed to extract this information accurately and store it in an efficient way. The shortest pulses recorded by the TDs occupied four 32-bit words, and very long pulses took up as much as thirty words or more; the algorithm stored the vital information in only two words, regardless of the initial length. This compression was not applied to all range stack TD

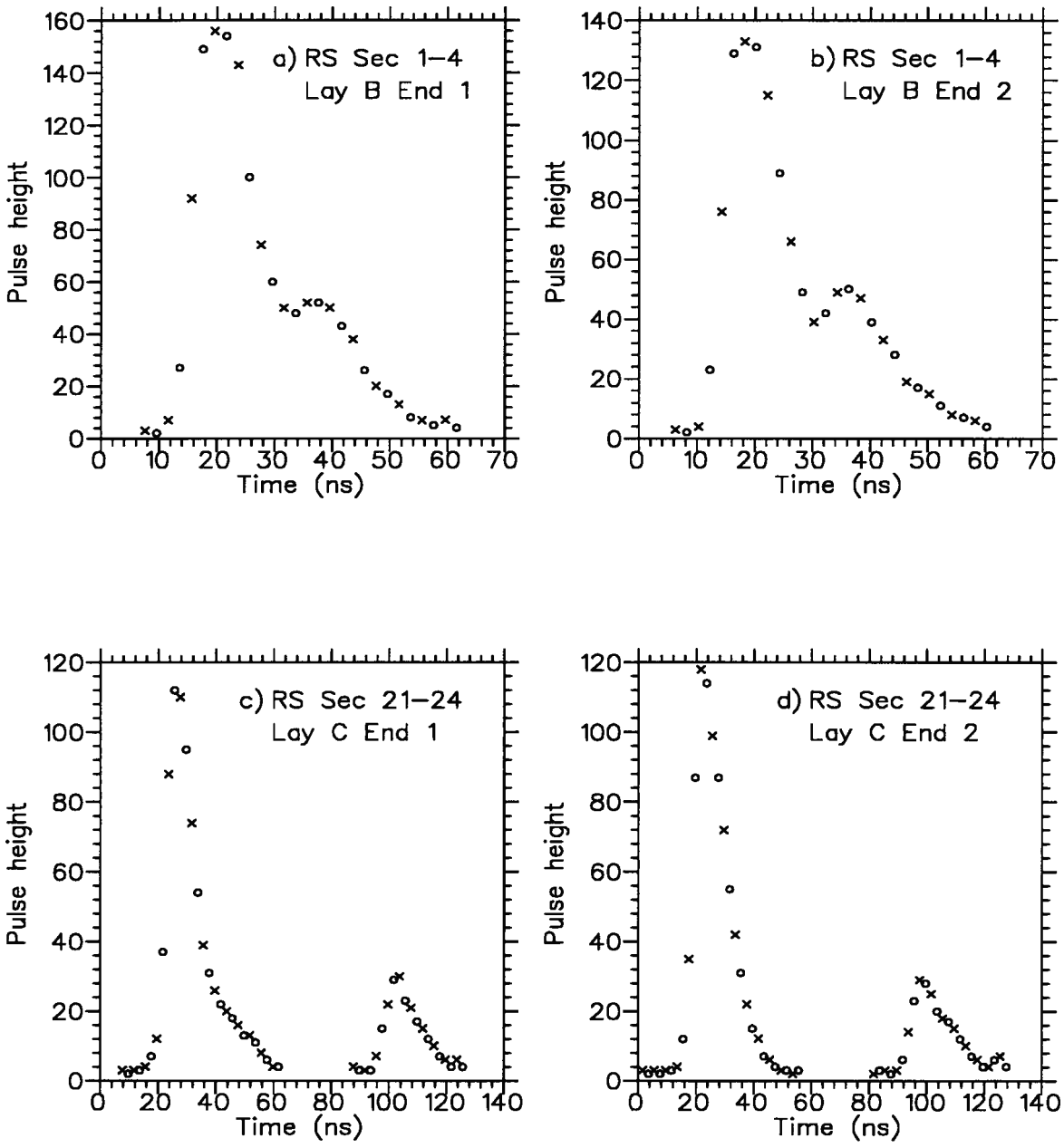

Figure 3.34: TD information for both ends of the stopping counter for events accepted by the online pion decay search for a) and b) double pulse and c) and d) detached pulse.

channels; channels in the stopping hextant (used for trigger Level 2) were exempt. Also, for channels outside of the stopping hextant, pulses in a 320 ns wide time region around the time of the K^+ decay were exempt.

Another operation was performed by this trigger level for 1991 data. An algorithm determined the leading edge time of each of the fiducial time pulses injected in each channel near the end of the TD recording time. This leading edge time was stored in 16 bits. If the leading edge determination was deemed sufficiently accurate, the entire fiducial pulse was removed from the data; otherwise, the full information was kept. The combined effect of the two algorithms, pulse information compression and fiducial time determination, was to reduce the average event size by about a factor of two.

3.1.5 Data Acquisition

The data acquisition system transfered the digitized information from the detector to magnetic tape based on the decisions made by the trigger system. Figure 3.35 shows schematically how the various electronics modules and dedicated processors were linked together and accessed by the computer coordinating the actions of the system in 1991. The main data acquisition program resided on the host computer, a MicroVax II in 1989 and a Vaxstation 3200 in 1991. The primary link from the host computer to the detector was via the CERN Fastbus Interface (CFI). This allowed access to the master SSP located in a Fastbus crate. The master SSP was linked to the secondary SSPs by a cable segment; each secondary SSP controlled one Fastbus crate. One of these SSPs was linked to the trigger system and relayed the Level 0 and Level 1 decisions to the SSPs located in the Fastbus crates housing the TDs. These SSPs then performed the Level 2 algorithm if necessary (or communicated with the Smart Controllers to perform the same task in 1991) and retrieved the digitized information from the TDs. The trigger SSP also recorded the status of all signals used by the trigger. This information was recorded with the data on magnetic tape, and could be used to apply some online constraints during the offline analysis. There were also SSPs in Fastbus crates housing the TDCs. The ADCs were located in CAMAC [54] crates; their information was retrieved via a high speed

bus by the Brookhaven FERA Interface (BFI).

All secondary SSPs stored in memory the information from several events recorded during a spill from the AGS. In the intervening time between spills, the master SSP collected the information from the secondary SSPs and formed the events; typically, this operation took 10 ms per event. The events were then transferred to the ACP system by the Fastbus Branch Bus Interface (FBBI). The ACP host program retrieved the events from the nodes once the level 3 trigger operations were completed. The host computer then transferred the events to magnetic tape. In addition, copies of some events were also transferred via an ethernet line to another computer workstation where the online monitoring program resided. Finally, information concerning the status of the high voltage system was periodically recorded to magnetic tape with the events. The information was provided by a Microvax II which controlled all CAMAC operations.

3.1.6 Monitoring

The data acquisition system made it possible to examine a portion of the events as they were recorded using the offline analysis program. An analysis program verified the integrity of the data and accumulated statistics related to the performance of all sub-detector and their electronics. If any element displayed a behavior outside of some preset tolerance, operators would be notified of the fault.

Another very important aspect of monitoring involved other sets of events selected with different trigger conditions than $\pi\nu\overline{\nu}$ data. These conditions were typically of low bias and were designed primarily to select samples of the most common K^+ decays such as $K_{\pi 2}$ and $K_{\mu 2}$. These events were recorded concurrently with the $\pi\nu\overline{\nu}$ events, hence providing excellent monitoring of the experimental conditions. Because of the large number of events satisfying these simple trigger conditions, their numbers were controlled by applying a pre-scaling factor. The recorded events were analyzed offline to calibrate sub-detectors, estimate background levels and determine the efficiency and acceptance of most of the online and offline constraints.

Table 3.3 gives a description of the monitor triggers used. Note that the requirements for the $\pi\nu\overline{\nu}$ lev0 trigger are slightly different than for the $\pi\nu\overline{\nu}$ trigger described in section 3.1.1;

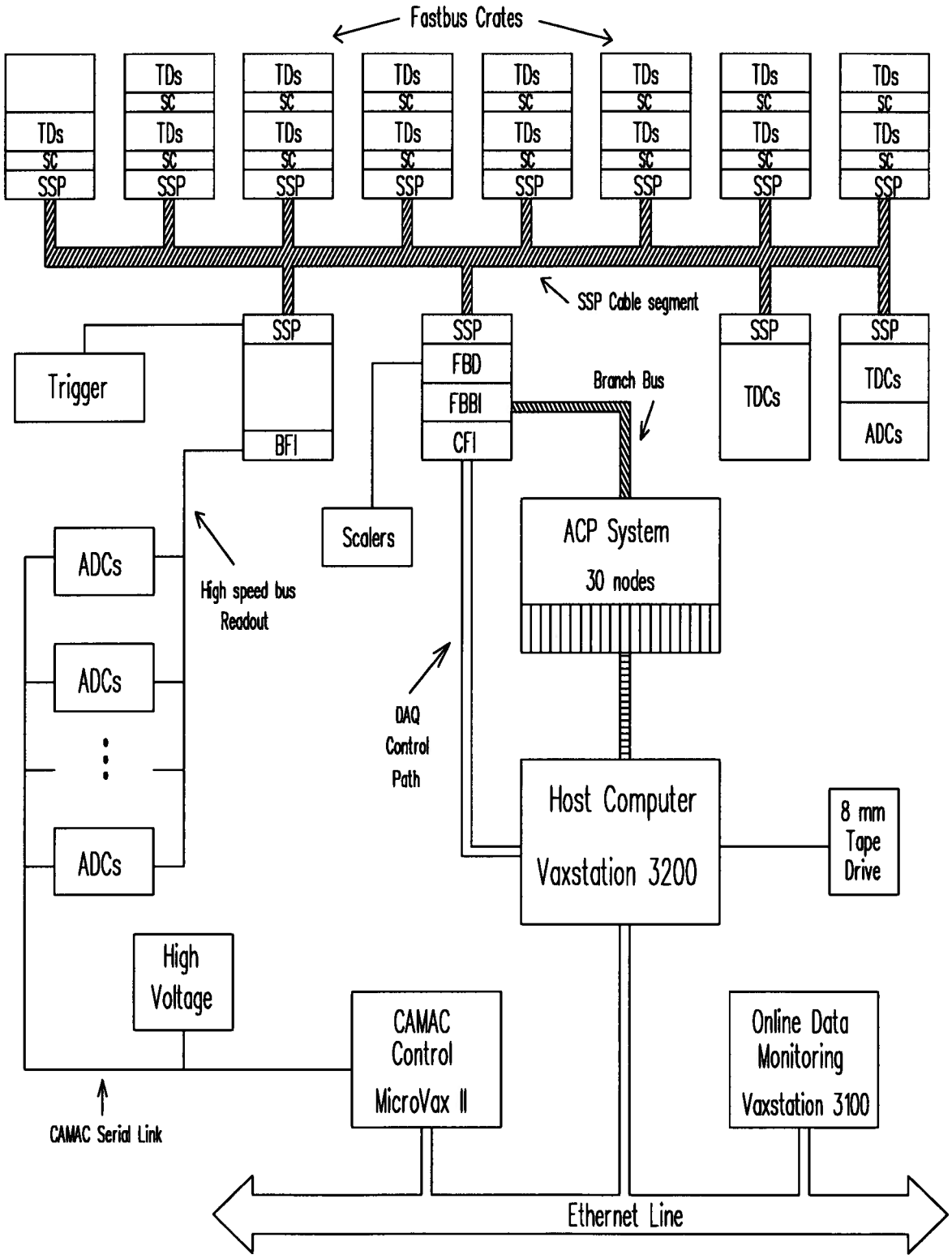

Figure 3.35: Schematic diagram of 1991 data acquisition system.

the former is less restrictive. This is because the $\pi\nu\overline{\nu}$ lev0 trigger is the same as the one used in the search for $K^+ \to \pi^+\nu\overline{\nu}$ above the $K_{\pi 2}$ peak. To obtain a data sample corresponding to the Level 0 trigger conditions used for the $\pi\nu\overline{\nu}$ search below the $K_{\pi 2}$ peak, additional trigger requirements were applied offline based on trigger information recorded with the data.

Table 3.3: Description of Level 0 monitor trigger requirements. Conventions are the same as the ones used in section 3.1.1. These triggers did not use further trigger levels, except π-scat which used Level 1.

Trigger		**Conditions**
Kμ2(1)	$\equiv$	$\mathrm{KT}\cdot(\mathrm{T}\cdot\mathrm{A})\cdot\mathrm{B_{CT}}\cdot(19_{\mathrm{CT}}+20_{\mathrm{CT}}+21_{\mathrm{CT}})$
Kπ2(1)	$\equiv$	$\mathrm{KT}\cdot(\mathrm{T}\cdot\mathrm{A})\cdot\mathrm{B_{CT}}\cdot\overline{(19_{\mathrm{CT}}+20_{\mathrm{CT}}+21_{\mathrm{CT}})}$
$\pi\nu\overline{\nu}$ lev0	$\equiv$	$\mathrm{KT}\cdot\mathrm{IC}\cdot\mathrm{DC}\cdot(\mathrm{T}\cdot\mathrm{A})\cdot\mathrm{B_{CT}}\cdot\overline{(19_{\mathrm{CT}}+20_{\mathrm{CT}}+21_{\mathrm{CT}})}\cdot\overline{(\mathrm{ECM}+\mathrm{ECP}+\mathrm{BV})}$
π-scat	$\equiv$	$\pi_{\mathrm{B}}\cdot\mathrm{E_{TG}}\cdot\overline{\mathrm{DC}}\cdot\mathrm{IC}\cdot(\mathrm{T}\cdot\mathrm{A})\cdot\mathrm{B_{CT}}\cdot\overline{(19_{\mathrm{CT}}+20_{\mathrm{CT}}+21_{\mathrm{CT}})}\cdot\overline{(\mathrm{ECM}+\mathrm{ECP}+\mathrm{BV})}$ with $\pi_{\mathrm{B}}\equiv(\mathrm{B1}\cdot\mathrm{B2})\cdot\check{\mathrm{C}}_{\pi}\cdot\mathrm{B4}\cdot\mathrm{spill}$

3.1.7 Data Samples

Table 3.4 summarizes the data samples collected in 1989 and 1991.

Table 3.4: Summary of the $\pi\nu\overline{\nu}$ data samples.

Year	**Time period (days)**	**# of events**
1989	33	1.4×10^6
1991	59	6.0×10^6

3.2 Calibration

A calibration of the time and energy measurements of the sub-detectors was necessary before offline analysis could proceed. For some of the sub-detectors, the calibration required special data sets or trigger conditions designed specifically for the calibration. In most other cases, use was made of monitor events (see section 3.1.6). This provided for a calibration directly applicable to the experimental conditions of the $\pi\nu\overline{\nu}$ data set. All sub-detectors were calibrated

using events from the common $K_{\mu 2}$ and $K_{\pi 2}$ decays, except for some of the beam counters which were calibrated using beam pions, and the barrel veto energy calibration which was performed using cosmic ray muons. A set of trigger conditions was specifically designed for the latter; data were recorded for each year immediately after the accelerator operations had ceased.

To calibrate the drift chamber, muons from $K_{\mu 2}$ decays were used. Data were taken both with the spectrometer magnet on and off; turning off the magnet removes the complication of the Lorentz angle for the drift electrons' trajectory. The energy calibration of calorimeters and other scintillator counters used well identified kaons, pions or muons. The expected energy deposition by particles in the various detector elements was determined either by Monte Carlo simulation or integration of the Bethe-Bloch formula [17]. These expected values were then used to calibrate the detector response. The energy calibration of a sub-detector was independent of the others.

The time calibration of sub-detectors other than the drift chamber and beam counters proceeded in several steps linking the different sub-detectors. The target, in which both the K^+ and its charged decay products were observed, was calibrated first. The kaons defined time zero. Because the time measurements in the range stack had the best resolution, it was the most important part of the time calibration. Well reconstructed muon tracks from $K_{\mu 2}$ decays were used. Each counter was calibrated with respect to the A-counter in the same sector (or one sector over). The time of the A-counters were aligned by using the average time of the target elements struck by the muon.

Once the range stack time calibration was completed, photons from $K_{\pi 2}$ events were used to calibrate the barrel veto and endcap elements. The π^+ track was reconstructed in the range stack and its time ($T_{\rm rs}$) was determined. The barrel veto and endcap elements struck by photon showers were then calibrated with respect to $T_{\rm rs}$. Finally, the I-counters time calibration was performed using π^+ from $K_{\pi 2}$ decays.

3.3 Offline selection

The events satisfying all trigger requirements were recorded to magnetic tape in YBOS [55] format. Each event was formed of several data banks, each one containing specific information. To retrieve the events from tape and have access to the YBOS data banks, a dedicated program called KOFIA [56] (Kaon OFfline Interactive Analysis) was used. For each event retrieved the main program called a user supplied subroutine which accumulated information about the events and took a decision on whether or not the event should be set aside for further analysis. The user supplied analysis subroutine made use of many other subroutines to retrieve data banks, provide calibrated detector information and perform analysis on the data.

The offline selection requirements were based on the same general criteria as the online requirements. The approach that was followed in the design of these constraints, or "cuts", was different for the two data sets. For 1989 data, the "standard" method typically used in data analysis performed towards the search of rare decays was chosen. In this method, simple cuts are initially applied to the data to reduce the size of the sample. These cuts are usually well established and can be set up with relative ease. Based on examination of the remaining data, more elaborate cuts are designed to reject background events and are then applied to further reduce the sample size. Any number of such iterations can be performed until the set of cuts is deemed final. There is however a problem with this method : if the last steps of the process involve only a small number of events, and they often do, there is a significant danger of biasing the result. Because a large amount of information is available for each event, it is easy to design cuts which reject all events while apparently maintaining a large acceptance for the signal searched for. This could lead to an overestimate of the sensitivity of the experiment. It could also have the unfortunate consequence of preventing the observation of a real signal.

To avoid these pitfalls, for 1991 data the design of all cuts beyond the simple initial set was accomplished using data samples that could not contain potential signal events. In this way, bias was minimized for the final result. However, this method brought the additional difficulty of finding appropriate data samples to prepare the cuts. These samples had to be representative of the background processes that the cuts were designed to reject. The worst scenario would

be a cut which appears very effective when applied to the "background" data sample but turns out to have no rejection at all for true background. Furthermore, some criterion had to be established to determine the effectiveness of a cut. For example, a cut which rejects half of the background sample but has an acceptance of only 50% for the signal would be obviously ineffective. It was decided that the fraction of events rejected by each cut had to be at least twice the fraction of events rejected because of acceptance loss. Obviously, there is some dependence on the data sample used for this test; the data has to be representative of the background being addressed by the cut.

The design of cuts and the estimation of the level of contamination from all background sources was an iterative process. The following section describes all cuts and the next chapter will describe the study of all background sources. In the description that follows, cuts were grouped in several categories : track reconstruction, timing, photon veto, pion identification, beam, target vertex and signal region. Most of these categories contain several different cuts. Each of them was identified by a short word or mnemonic for easy identification later on in the description of the background studies and analysis. A summary of all cuts is given in section 3.3.8.

3.3.1 Event reconstruction

The cuts described in this section pertain to the identification of a stopping kaon in the target and a positively charged particle leaving the target and passing through the I-counters array and the drift chamber and finally coming to rest in the range stack.

3.3.1.1 TARGET

This cut used a set of subroutines to do pattern recognition in the target and attempted to identify target elements hit by a K^+ and ones hit by an outgoing π^+ from kaon decay. Because they travel mostly parallel to the scintillating fibres, kaons typically had large early energy depositions in the target elements. The decay pions tend to travel transversely to the scintillating fibres and therefore had more modest energy losses at later times. The calibrated

ADC and TDC information was used to classify the struck target elements as K^+ or π^+ . To first order, kaon elements had to have a measured time relative to the kaon Čerenkov counter signal between -10.0 and +10.0 ns and an energy greater than 3 MeV, while the pion elements times had to be between -10.0 and +75.0 ns and their energy less than 3 MeV. These initial lists of kaon and pion elements were used to initiate the pattern recognition. Based on their position in the xy plane, neighboring elements were grouped to form clusters, which in turn were used to form the stopping kaon track and the outgoing pion track. For the latter, struck I-counters were also used as a guide to identify the track. During the pattern recognition process, the association of an element as kaon or pion could be changed in order to improve the pattern. This algorithm had a very high efficiency ($\sim 99\%$) in identifying a kaon and its decay charged particle, at the cost of keeping some obviously flawed events. A more restrictive target tracking algorithm, combining information from the drift chamber with the target information, will be described later.

The specific requirements of this cut were simply that a kaon track be successfully reconstructed in the target; no demands were made on the pion track. More restrictive constraints were applied by other cuts which used quantities determined by the target track reconstruction subroutine. This included lists of the identified kaon and pion elements and the energy-weighted time and summed energy of the kaon and pion track.

3.3.1.2 DC-SETUP

One of the primary requirements for a $K^+ \to \pi^+\nu\bar{\nu}$ candidate event is that a single positive track be reconstructed in the drift chamber. In addition to providing the track momentum measurement, the drift chamber tracking information is the key element in identifying the π^+ . The good position resolution helps in linking track segments identified in the target and range stack, where resolution is inherently poorer.

The first step in identifying a track in the drift chamber was to convert the TDC time information from the hit wires into a hit position. A pedestal was subtracted from the raw time value to obtain the drift time of the hit. Using the calibrated value of the drift velocity

the drift time was then converted into a drift distance. From this distance and the calibrated value of the Lorentz angle, two positions in the xy plane were determined for each hit due to the left-right ambiguity. Only in the process of track fitting were mirror hits discarded from the list.

The list of cells from the three axial layers with wire hits was then scanned. In each cell an attempt was made to fit the hit positions to a straight line. The minimum number of hits required was three. The straight line fits in the cells gave a vector position and direction. These vectors were used to identify a crude circular track. The points from the chosen vectors were then used to fit a circle in the xy plane, with the radius of curvature giving the xy component of the track momentum. Other points not initially chosen were included or discarded from the fit on the basis of the change in the chi–square value of the circle fit.

In the event of a successful xy fit, the information was used in combination with the hit positions on the two stereo layers to obtain z-position information. In the turning angle-z position space the track trajectory is a straight line, with the slope giving the z component of the momentum. The minimum number of points required for a successful z fit was three, with at least one in each of the two stereo layers.

The specific requirements for the drift chamber track reconstruction were that one and only one track be identified by the fitting procedure, with successful fits in both the xy and z planes. For 1991 data, other requirements were added. The track had to be positively charged, and there had to be at least one hit in each of the five wire layers. This last requirement ensured that the particle did not exit the drift chamber fiducial volume via one of the end plates, where a large energy loss could go undetected. Finally, as a form of photon veto, the number of hit wires other than the ones used to form the track was limited to be less than or equal to 45. Figure 3.36 shows the distribution for this number for $K_{\mu 2}$ and $\pi\nu\overline{\nu}$ data. For $K_{\mu 2}$ events there should be no activity at the time of the K^+ decay other than the μ^+ , except for accidental particles. For $\pi\nu\overline{\nu}$ data, all background sources are included. This requirement eliminated events in which photon conversions created a large amount of ionization in the drift chamber gas, but did not get reconstructed as tracks. A similar cut was included in the 1989 analysis

but as a separate entry; it appears in the photon veto cuts category (3.3.3).

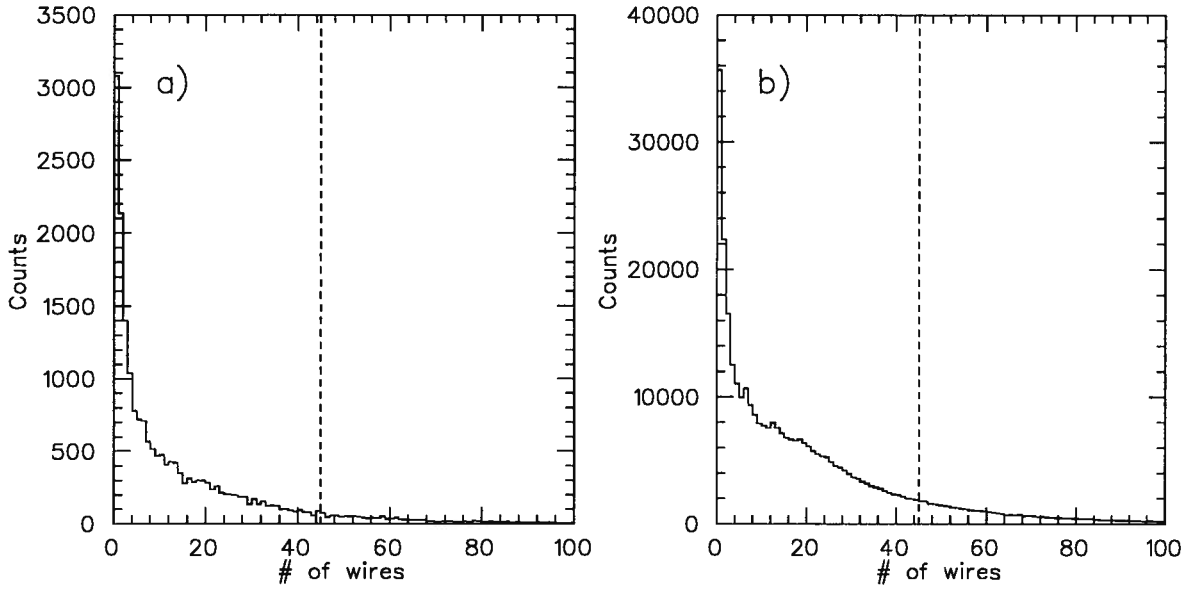

Figure 3.36: Number of struck drift chamber wires outside of the reconstructed track for a) $K_{\mu 2}$ data and b) $\pi\nu\bar{\nu}$ data. The dashed line indicates the cut position.

In 1991, additional tracking information was available from the inner wire chamber (IWC); it was not used in order to identify the track. However, the IWC tracking was performed after the drift chamber track fitting procedure succeeded, and if the chi–square value of the overall fit either in xy or z was improved by the inclusion of IWC information, the results of the combined DC-IWC fit were used for the rest of the event analysis. Therefore, no additional losses of acceptance were incurred by using the IWC, but the analysis benefited from the 10% improvement in z-position resolution (see section 2.2.4).

3.3.1.3 DC-CHI2

In 1989, some events satisfying the basic track fitting criteria had very poor χ^2 probabilities, sometimes identically zero. These cases resulted from unstable fits; hence, a cut was applied to eliminate these events. The drift chamber track fitting algorithm was improved for the 1991 data analysis, and therefore this cut was not necessary.

3.3.1.4 RS-TRACK

To find tracks in the range stack, a list of counters for which the geometrical mean of the calibrated energy at each end of the counter was greater than 0.5 MeV was used. A track was initiated by hits in the T and A counters of a given sector. Each subsequent layer was examined for a hit, first in the same sector as the $T \cdot A$ coincidence and then in the next sector over if no hit was present in the same sector. Both positive and negative track options were considered, with the former being the first choice. Once the charge of the particle had been established the search continued only in that direction, until a layer was found with no hit counter connected to the track.

Each of the tracks thus identified was then compared to the list of drift chamber tracks by determining which T-counter was intersected by each drift chamber track. Only the range stack tracks for which a match was obtained with a drift chamber track were considered for further analysis. The subroutine then summed up the energy deposited by the particle in the range stack and computed its range. For the latter, the drift chamber information was extrapolated to correct for the curvature of the track and the component of the range along the z axis. For the tracks which intersected one or both of the range stack proportional chambers (RSPC), their xy and z position information was used to refine the range measurement.

A correction was needed for the range in the stopping layer. Here, the observed energy in the last layer was used to determine the range, by interpolating an empirical table of range as a function of energy. This implied that a hypothesis had to be made about the particle type. The correction was computed for both a π^+ and a μ^+ hypothesis and both results were made available. In the case of the π^+ hypothesis, since most of the time the pion decay occured within the $\sim$100 ns long ADC integration gate, a value of 4.12 MeV appropriately corrected for saturation [57] was subtracted from the stopping layer energy before the range was determined. One unfortunate consequence of this method for measuring the range is that for tracks stopping in the thicker layers of the range stack the track energy and range are highly correlated. This is particularly important for this analysis because of the high acceptance of range stack layer B for $K^+ \to \pi^+ \nu\bar{\nu}$ events.

This cut required that one and only one track matching the drift chamber track be reconstructed in the range stack. For 1991 data, the stopping layer had to be within layers 3 and 6 (inclusive) and the stopping counter energy had to be greater than 4.0 MeV. This is the minimum expected in the case of a stopping pion decaying to a muon and a neutrino within the ADC gate.

3.3.1.5 RSPC

It is possible for particles to stop in the walls of the proportional chambers (RSPC). The particle might even curl and re-enter the range stack scintillator layer preceding it. To eliminate such possibilities, activity in the RSPC above the stopping counter for tracks stopping in range stack layer C was examined. If hits were recorded by the chamber, the event was rejected. This cut was not applied to 1991 data; no evidence was found for such activity after all other track reconstruction and kinematic cuts were applied.

3.3.1.6 ICOUNTER

In the I-counters, energy is deposited by the charged particle leaving the target. If the particle is a π^+ , it can undergo a nuclear interaction in the I-counter, possibly leaving more energy than expected. It is also possible for kaons, other beam particles or photon conversions to deposit energy. Again, the energy measured in the I-counters will be greater than what is expected. To reject some of these cases, it was required in 1989 data that the total measured energy be less than 5.0 MeV in the I-counter struck by the π^+ track identified in the target.

A subroutine using the drift chamber track fit information determined which of the six I-counters was hit by the charged particle, the range of the particle in that I-counter and estimated the energy deposited, based on the range and assuming the particle was a π^+ . The subroutine had to succeed in finding an intersection between the drift chamber track and the inner and outer faces of the I-counters array. The range was computed as the arc length between the two intersection points, corrected for the component along the z-axis using the drift chamber track information. The estimated energy deposition was then computed, using the π^+ expected rate

of energy loss at the measured momentum. The energy loss rate was computed by interpolation in a table of empirical values.

The expected energy loss was then compared to the measured ADC energy. In the case where the track crossed two adjacent I-counters, the measured energy in both counters was summed. Because of the finite position resolution of the drift chamber, this was also done in the case where the track was close to the boundary between two I-counters. Figure 3.37 defines the geometry for this requirement. For each event, the angle θ between the center (dashed line) of the counter and a vector from the center of the target to the intersection point of the track with the inner face of the counter (CP) was found. If the absolute value of $\sin\theta$ was greater than 0.4, the energy of the adjacent counter was added. The maximum possible value of $|\sin\theta|$ was 0.5, defined by the I-counters geometry. The difference between the measured energy and the estimated energy had to be less than or equal to 2.0 MeV. Figure 3.38 shows this quantity for a sample of $K_{\pi 2}$ events.

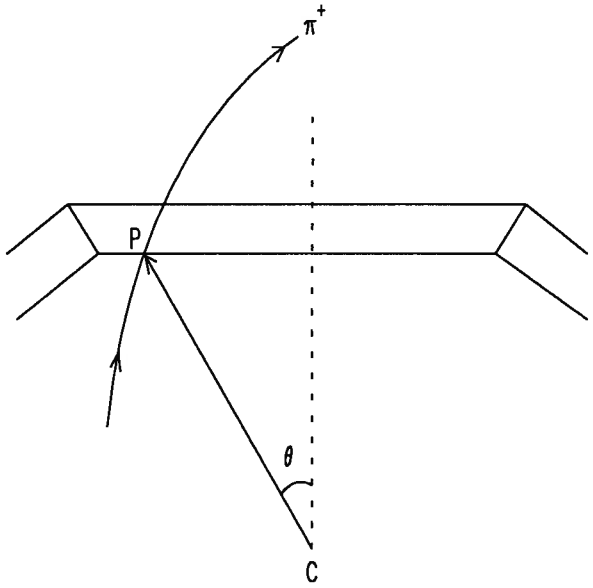

Figure 3.37: Geometry conventions used for ICOUNTER cut.

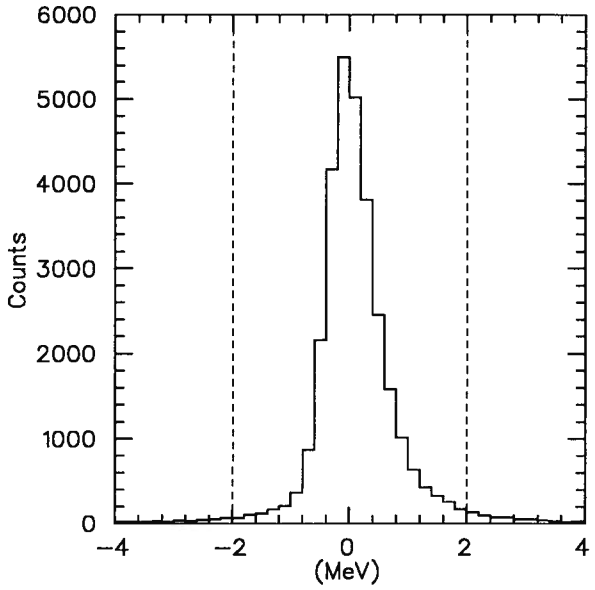

Figure 3.38: Difference between measured and estimated I-counter energy for the π^+ for $K_{\pi 2}$ events. Events outside of the region defined by the dashed lines were rejected.

3.3.1.7 FIDUCIAL

This cut ensured that the K^+ decayed in the fiducial volume of the target and that the charged particle trajectory was contained within the geometrical acceptance of the drift chamber and the T-counters. Two quantities were used : the z position of the kaon decay vertex ($Z_{\rm vtx}$) and the sine of the dip angle of the π^+ trajectory ($\sin\theta_{\rm dip}$), measured at the decay vertex. The dip angle is defined as the angle between the particle track and the xy plane, with positive values in the same direction as the positive z-axis. This angle is equivalent to the directional cosine along the z-axis. $Z_{\rm vtx}$ was determined by extrapolating the DC track in the target and finding the point of closest approach with the position of the decay vertex in the xy plane given by the target track reconstruction routine. The cut positions were set at $|Z_{\rm vtx}| \leq 10$ cm and $|\sin\theta_{\rm dip}| \leq 0.5$; events outside of these limits were rejected. Figure 3.39 shows the distribution of these two variables for a sample of 1991 $K_{\pi 2}$ events.

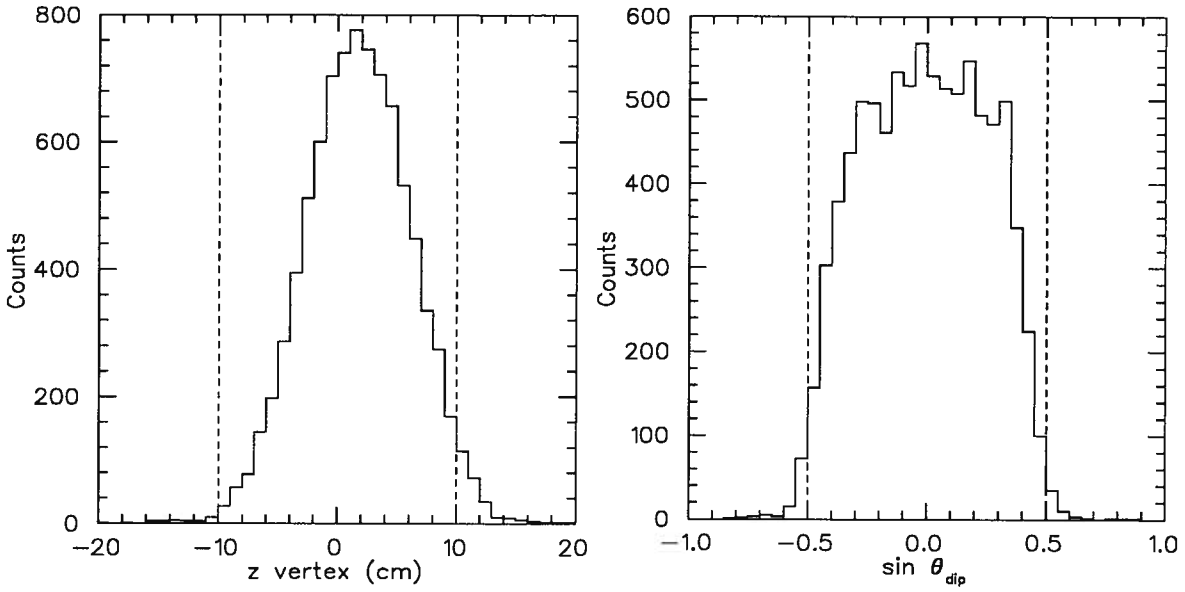

Figure 3.39: Kaon decay vertex z position and π^+ track dip angle for $K_{\pi 2}$ events. Cut positions are indicated by the dashed lines.

3.3.1.8 ZDCTZ

In 1989, it was not required that the track in the drift chamber include hits in all five cell layers. The result of this is that some particles exited the chamber by traversing one of the aluminum end plates, thereby losing some undetermined amount of energy. To remove such events a cut was applied on the position of the track along the z-axis at the outer radius of the drift chamber ($Z_{\rm DC}$); the cut position was $-22.0 < Z_{\rm DC} < 24.0$ cm.

An additional measurement of the track position along the z-axis was obtained by comparing the energy measured at each end of the T-counter struck by the track. The position along the z-axis is given by

$$Z_T = \frac{\lambda}{2}\ln(\frac{E_1}{E_2}) \tag{3.29}$$

where λ is the attenuation length of light in the scintillator counter and E_i is the energy measured at end i. For good tracks, there is a linear relationship between this measurement and $Z_{\rm DC}$. Figure 3.40 shows the distribution of Z_T versus Z_DC for a sample of 1989 $\pi\nu\overline{\nu}$ Pass1 data. The dashed lines show the cut used; also shown are the limits for the cut on Z_{DC}. Note that the scale for Z_T was not calibrated in centimetres.

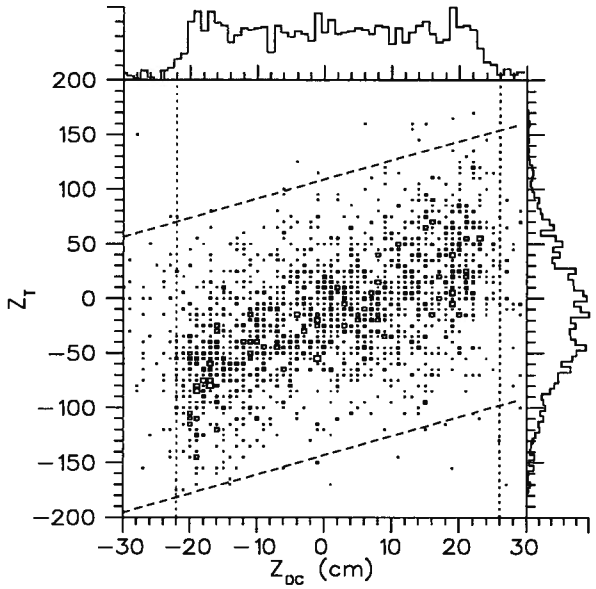

Figure 3.40: Z_T versus Z_{DC} distribution for 1989 $\pi\nu\bar{\nu}$ Pass1 data. The events inside the dashed and dotted lines were accepted.

3.3.2 Timing

3.3.2.1 PROMPT

This cut ensured that the K^+ decayed at rest in the target by requiring a delay between the measured time of the K^+ track in the target (T^K_{tg}) and the measured time of the π^+ track (T^π_{tg}). Each quantity was an energy-weighted average of the time of individual target elements part of the K^+ or π^+ track. The time difference T^π_{tg} -T^K_{tg} was required to be within the bounds $2.0 \leq (T^\pi_{tg}$ -T^K_{tg}) ≤ 50.0 ns. The late time constraint originated from the fact that for late K^+ decays a significant part of the energy deposited by the π^+ could be missed by the ADC integration gate and therefore reduce the total measured track energy. Figure 3.41 shows the distribution of T^π_{tg} -T^K_{tg} for a sample of 1991 $\pi\nu\bar{\nu}$ events. The spectrum is formed of three components : a peak near time zero from K^+ decays in flight, an exponential decay part from K^+ decays at rest and a flat component over the entire spectrum from beam pions. Note that the early part of the exponential spectrum is deformed by the acceptance of the online delayed coincidence (see figure 3.33).

For 1989 data, several other requirements were included in this cut. The time of the charged

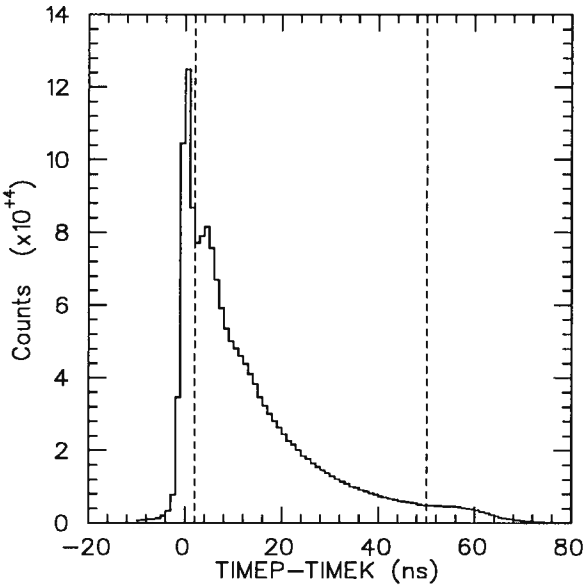

Figure 3.41: T^{π}_{tg} -T^{K}_{tg} distribution for 1991 $\pi\nu\overline{\nu}$ events. Events outside of the region defined by the dashed lines were rejected.

particle track in the range stack (T_{rs}) was determined by taking the mean of the time measured at the two ends of the A-counter struck by the track. The following cuts were applied using this time measurement :

$$T_{rs} > -1.0\,\text{ns}$$
$$T_{rs} - T^{K}_{tg} > 1.0\,\text{ns}$$
$$|T^{\pi}_{tg} - T_{rs}| < 4.5\,\text{ns}\,. \tag{3.30}$$

For 1991 data, additional requirements on the time of the charged particle track were re-grouped in another cut, described next.

3.3.2.2 TRKTIM

This cut was concerned with the time information of the π^+ in 1991 data. The time of the π^+ track in the target (T^{π}_{tg}) was defined earlier. The I-counter time (T_{ic}) was the time of the I-counter identified as part of the track by the ICOUNTER cut. If the information was reliable, the time value as measured by the TDs was used; otherwise the TDC based time was used. In the case where the track crossed two I-counters or was close to the boundary between two

counters, the earliest of the two time measurements was chosen.

The time of the range stack track ($T_{\rm rs}$) was determined by averaging the times of the counters belonging to the track, determined from the leading edge of the TD pulses. For each counter on the track, a list of calibrated times from each end was scanned for end-to-end coincidences. The difference between the times at each end had to be less than 7 ns. A list was made of the average time of the two ends for counters with a coincidence, thereby removing the dependence of the time measurement on the position of the energy deposition in the counter. This list was then scanned to find times within 10 ns of the T-counter time. The overall track time was a weighted average of all counter times found in coincidence with the T-counter, with the weight given by the pre-determined time resolution of the hits.

The three different measurements of the time of the charged particle track were then compared to each other. A χ^2 quantity was formed, using $T_{\rm rs}$ as the reference because of its better resolution :

$$\chi^2 = \frac{(T_{\rm ic} - T_{\rm rs} - \Delta_{\rm ic})^2}{\sigma_{\rm ic}^2} + \frac{(T_{\rm tg}^{\pi} - T_{\rm rs} - \Delta_{\rm tg})^2}{\sigma_{\rm tg}^2}$$

with Δ and σ the measured mean and standard deviation of the $(T_{\rm ic} - T_{\rm rs})$ and $(T_{\rm tg}^{\pi} - T_{\rm rs})$ distributions for $\pi\nu\overline{\nu}$ data. The standard deviation for $(T_{\rm tg}^{\pi} - T_{\rm rs})$ was $\sigma = 0.81$ ns, and for $(T_{\rm ic} - T_{\rm rs})$ it was $\sigma = 1.15$ ns and $\sigma = 0.59$ ns for TDCs and TDs, respectively.

The χ^2 probability $\mathcal{P}(\chi^2)$ was determined for two degrees of freedom. Figure 3.42 shows the distribution of the base 10 logarithm of the χ^2 probability for $K_{\mu 2}$ events. On this graph, all counts below -10.0 are accumulated in the leftmost bin; these are mostly events for which no outgoing track elements were found in the target, hence no $T_{\rm tg}$ value was available. Events with a probability $\mathcal{P}(\chi^2)$ less than 10^{-5} were rejected, as indicated by the dashed line on the figure.

3.3.3 Photon Veto

In the search for $K^+ \to \pi^+\nu\overline{\nu}$ below the $K_{\pi 2}$ peak, most backgrounds involve photons. The high rate environment created by the intense incident beam of kaons and pions makes it difficult to effectively reject photons while keeping accidental vetoing at an acceptable rate. Cuts have

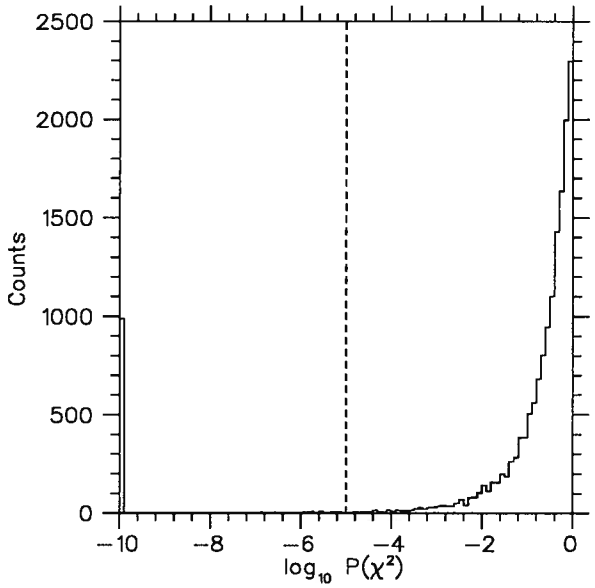

Figure 3.42: Logarithm of the χ^2 probability for the TRKTIM cut for $K_{\mu 2}$ events. Events to the left of the dashed line were rejected.

to be designed to balance these two factors. Some cuts indirectly veto photons, usually because a photon conversion shower perturbs some measurement. This section will describe cuts that are designed specifically to reject events with photons.

The most straightforward approach to photon veto is to search for energy deposition in coincidence with the π^+ detected in the drift chamber and range stack; the search should encompass the entire detector, except for the regions where the identified π^+ deposited energy. A subroutine performed such a search in the electro-magnetic calorimeter (barrel veto and endcaps), the range stack, I-counters and V-counters. Table 3.5 gives the average accidental rate for hits above 1 MeV for the different subsystems (constant background). Note that there is some correlation between the rates; for example, a single random particle can deposit energy in both an endcap and the range stack.

For the barrel veto and the range stack, time and energy information was required from both ends of the counters. Another subroutine handled cases where partial information was available. For 1989 data, a cut was setup for the endcaps and barrel veto (INT_EB) and one for the range stack, I-counters and V-counters (INT_RIV). For 1991 data, a separate cut was setup for the range stack and barrel veto energy depositions found with information from one

Table 3.5: Accidental rates in various detector subsystems for hits above 1 MeV. The endcaps entry is the sum of both the upstream and downstream endcaps.

Subsystem	Rate (MHz)
Range stack	2.6
Barrel Veto	1.1
Endcaps	6.8
I-counters	0.33
V-counters	0.89

end missing (INTSE); all other events with some photon energy were handled by a single cut (INTIME).

3.3.3.1 INTIME

As mentioned above, this cut looked for energy in the detector in coincidence with the charged track, but away from the regions struck by that track. The time of the track measured in the range stack ($T_{\rm rs}$) was taken as the reference time. The leading edge times of hits in all counters in the search regions with measured ADC energy were compared to the reference time. If the time difference was within a pre-determined time window, the energy of that counter was added to a sum. In the case of the barrel veto and the range stack, time and energy information was required from both ends of the counters; the absolute value of the end-to-end time difference in a module had to be less than 30 ns.

Individual energy sums were tallied for each sub-detector, and a cut was applied on each sum. Table 3.6 lists the time windows and energy thresholds used. Figure 3.43 shows the distribution of energy versus time for hits in the various subsystems for $\pi\nu\overline{\nu}$ events. The search windows are indicated on the graphs. For the barrel veto graph, a late tail can be observed. This is attributed to slow neutrons resulting from photo-nuclear interactions. Figure 3.44 shows the same graphs, but for pre-selected $K_{\mu 2}$ events. Since in this case no activity is expected at the time of the μ^+ , it is a measure of the level of accidental vetoing expected in the case of $K^+ \to \pi^+\nu\overline{\nu}$ events; as will be seen in the section describing the acceptance calculation, the loss

is significant. The prompt peak in the range stack plot is due to counters that are part of the charged particle track but have less than 0.5 MeV and to δ-rays emitted by the charged particle. Because of the energy threshold chosen for the cut, only the latter incurs an acceptance loss. There is also a prompt peak in the I-counter plot. There are two contributions to this peak : tracks which hit two adjacent counters at an angle shallow enough to avoid identification as a sector crossing and photon conversions in the target depositing energy in the I-counters. The latter contribution is about twice the former and is probably due to photons radiated by the μ^+. It should be noted that losses due to the I-counters account for only about 2.5% of the total INTIME cut acceptance loss.

Table 3.6: Parameters for INTIME cut (1991 data).

Subsystem	**Time window**	**Threshold**
	[Min,Max] (ns)	(MeV)
RS	[-2.0,+13.0]	0.5
BV	[-5.0,+15.0]	0.4
EC	[-4.5,+4.5]	0.6
IC	[-5.0,+5.0]	0.2
VC	[-6.0,+5.0]	0.1

3.3.3.2 INTSE

It was noted in the description of the previous cut that for the range stack and barrel veto, information from both ends of the counters was required. However, in the case where a photon converts very close to one end of these counters, it is quite possible for the other end to miss the hit completely, especially if the energy deposited is small. Also, hardware or software errors can result in a wrong measurement of the time of a hit at one end. The INTSE cut looked for counters in the range stack and barrel veto for which either the energy or the time information from one end was missing. The hits were categorized according to which information was available, and search parameters similar to the ones for the INTIME cut were determined for each category. Table 3.7 lists the categories that were found to provide some photon rejection and the time windows and thresholds for each. Figures 3.45 and 3.46 show the distributions of

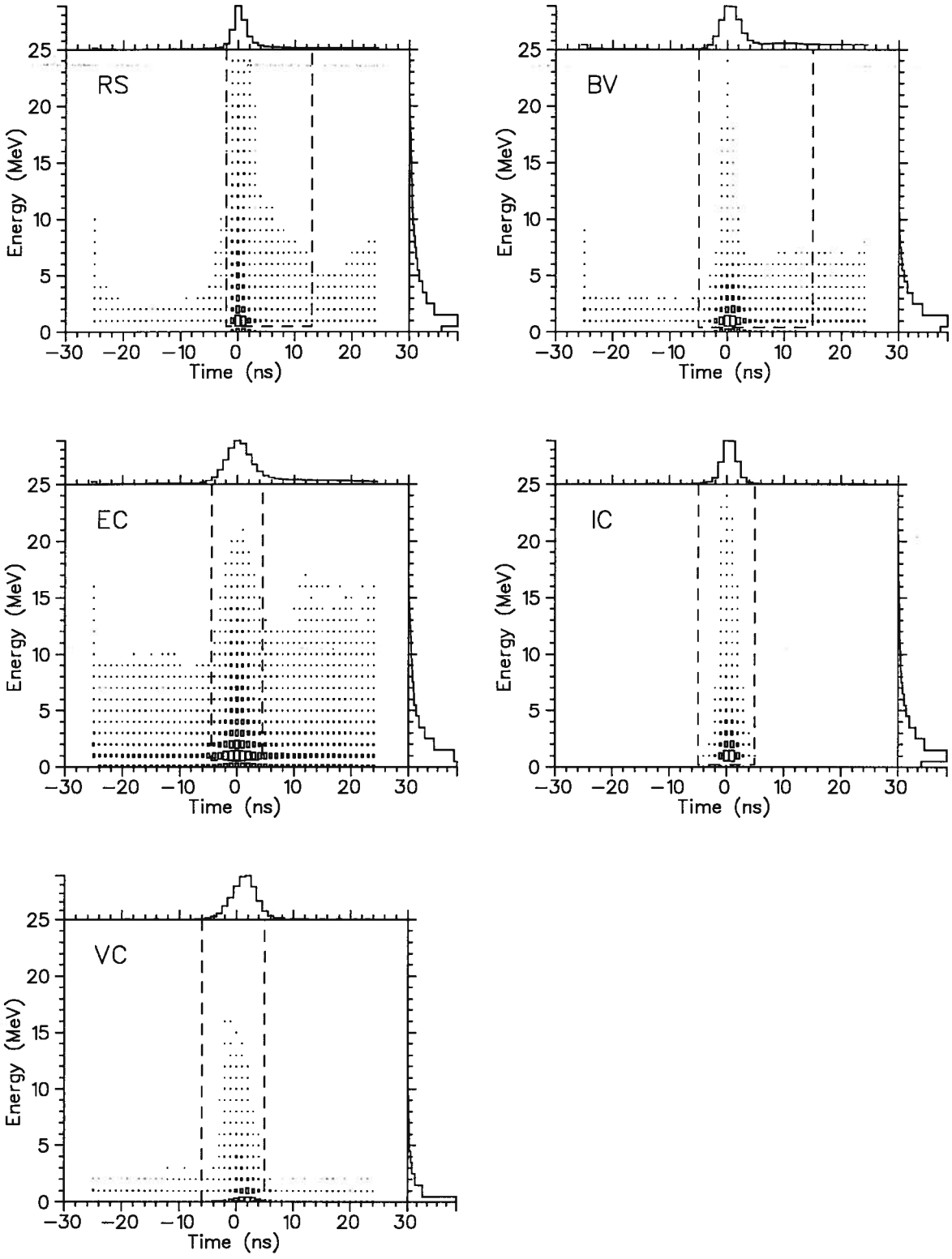

Figure 3.43: Energy versus time distribution of hits in the various subsystems for the INTIME cut for 1991 $\pi\nu\overline{\nu}$ data.

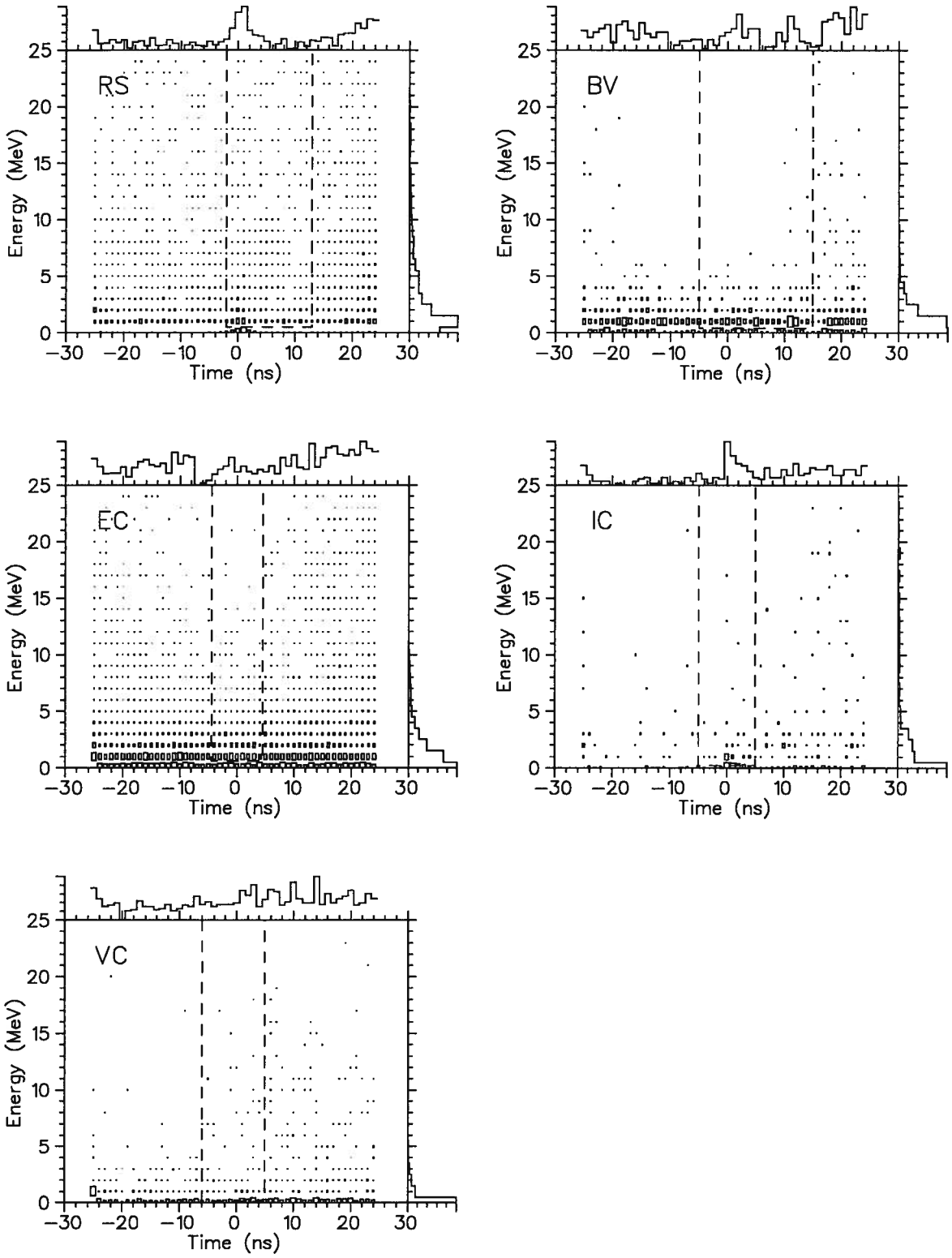

Figure 3.44: Energy versus time distribution of hits in the various subsystems for the INTIME cut for 1991 $K_{\mu 2}$ events.

time versus energy of hits in the different categories for $\pi\nu\overline{\nu}$ and $K_{\mu 2}$ events respectively, after the INTIME cut had been applied.

Table 3.7: Parameters for INTSE cut (1991 data).

Subsystem	**Ends hit**		**Time window**	**Threshold**
	Energy	Time	[Min,Max] (ns)	(MeV)
RS	both	single	[-7.0,+7.0]	0.0
RS	single	both	[-5.0,+5.0]	0.0
RS	single	single	[-10.0,+10.0]	0.6
BV	both	single	[-8.0,+8.0]	0.0
BV	single	single	[-14.0,0.0]	0.5

3.3.3.3 INT_EB

This cut looked for activity in the endcaps and barrel veto for 1989 data. The time windows and energy thresholds are listed in tables 3.8 and 3.9. Included in the single end hits parameters (table 3.9) is an entry referring to the endcaps. This cut requires the number of endcap modules with a time hit within the coincidence window but with no measured energy to be less than two.

Table 3.8: Photon veto cut parameters for 1989 data.

Subsystem	**Time window**	**Threshold**
	[Min,Max] (ns)	(MeV)
RS	[-4.2,+13.8]	0.5
BV	[-4.3,+11.7]	0.3
EC	[-5.9,+6.1]	0.5
IC	[-4.75,+3.25]	1.0
VC	[-6.4,+5.6]	1.0

3.3.3.4 INT_RIV

This cut dealt with the range stack, I-counters and V-counters, and completed the photon veto cuts for 1989 data. Tables 3.8 and 3.9 give the parameters used. In addition, for the IC and VC

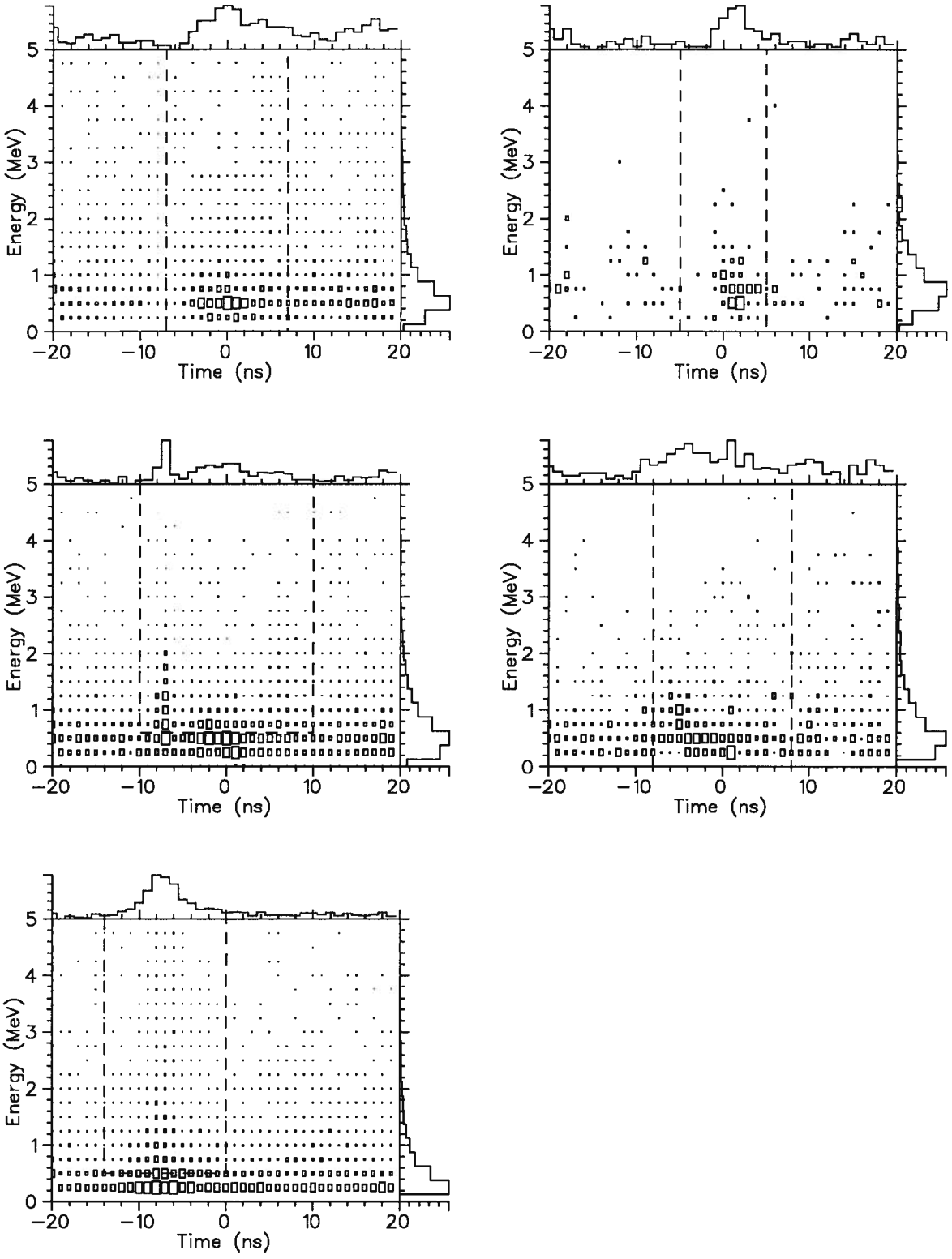

Figure 3.45: Energy versus time distribution of hits for the various INTSE cut categories for 1991 $\pi\nu\overline{\nu}$ data. Going from left to right and top to bottom the graphs correspond to the categories listed in table 3.7.

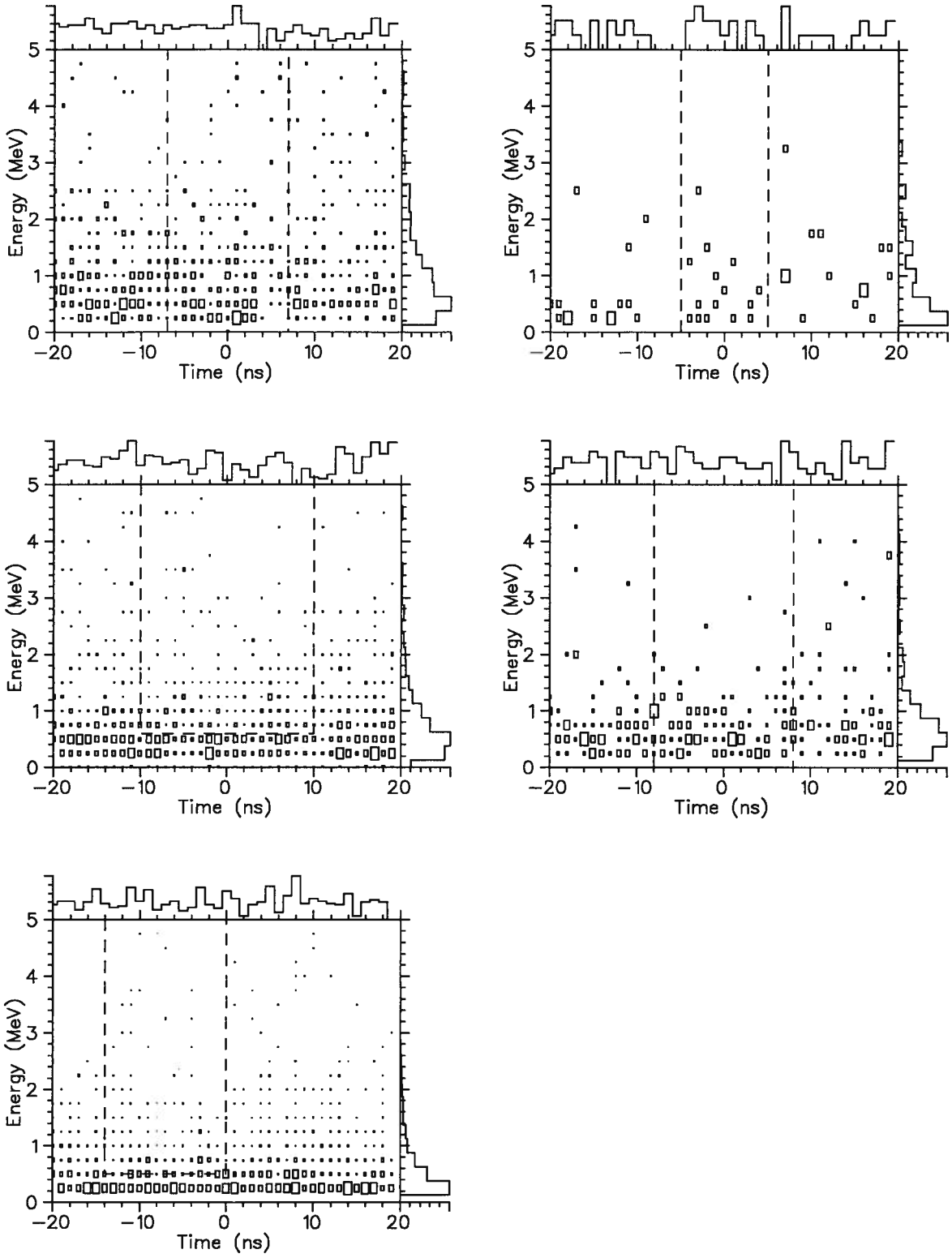

Figure 3.46: Energy versus time distribution of hits for the various INTSE cut categories for 1991 $K_{\mu 2}$ events. The graphs correspond to the same categories as in figure 3.45.

Table 3.9: Photon veto cut parameters for single end hits for 1989 data. Also included is a cut on endcap energy hits with no recorded time.

Subsystem	**Ends hit**		**Time window**	**Threshold**
	Energy	Time	[Min,Max] (ns)	(MeV)
RS	both	single	[-5.0,+5.0]	0.5
RS	single	both	[-6.5,+6.5]	0.5
RS	single	single	[-6.5,+6.5]	0.5
BV	both	single	[-5.0,+5.0]	0.3
BV	single	both	[-11.0,1.0]	0.3
BV	single	single	[-11.0,1.0]	0.3
EC	2 hits	none	[-4.0,12.0]	—

subsystems, cases where there were no time hits found in a ±400 ns time window but energy was measured were rejected.

3.3.3.5 PB-GLASS

As described in section 2.2.1.5, the primary purpose of the lead-glass counter was to detect photons originating from the target and heading in the direction opposite to the K^+ beam close to the beam axis. It was also designed to be sensitive to incoming beam pions, but not to kaons. As was seen in section 2.2.1.5, the kaons sometimes do leave a signal, mostly ascribed to fluorescence in the lead-glass. This made the detection of low energy showers more difficult than expected.

To help in this task, the multiplicity signal from the lead-glass counter recorded by a TD channel was used. For each multiplicity pulse identified, the leading edge time was measured for pulse heights corresponding to each number of phototubes hit. Because of the narrow width of the signals ($\sim$ 15 ns), sometimes a single TD pulse resulted in several time values at a given threshold. Figure 3.47 shows a TD pulse for the multiplicity of the lead-glass counter formed of several hits. The horizontal dotted lines show the pulse height positions at which the time is evaluated for rising portions of the pulse, corresponding to the number of phototubes hit. The list of time values for a given minimum number of phototubes threshold was compared to the time of the track in the range stack ($T_{\rm rs}$). The time value closest to $T_{\rm rs}$ was then

selected as $T_{\rm PbG}$. Figure 3.48 shows the distribution of $T_{\rm PbG} - T_{\rm rs}$ as a function of the delayed coincidence time measured in the target for $\pi\nu\overline{\nu}$ data, for minimum thresholds of one, two and three phototubes. The vertical band identifies the hits due to photons and the diagonal band is due to the incoming kaons; the latter becomes more important as the minimum threshold is lowered.

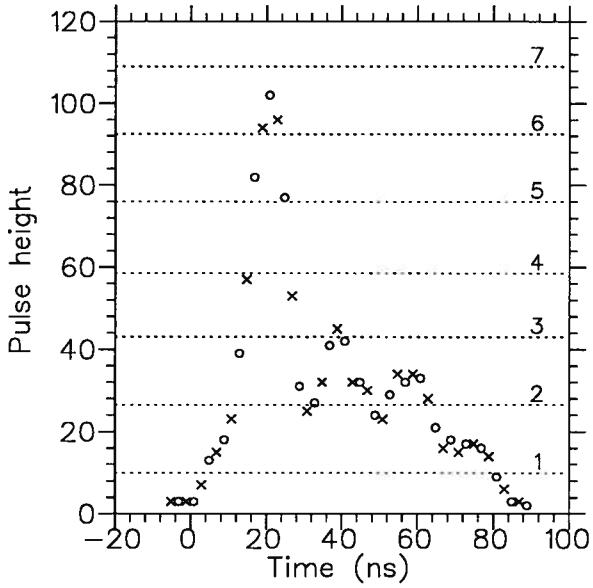

Figure 3.47: TD multiplicity pulse from lead-glass counter. The dotted lines indicate the pulse heights at which the time is evaluated for a rising pulse, corresponding to the number of phototubes hit.

Based on these distributions and similar ones for $K_{\mu 2}$ data, a coincidence time window was set at -6.0 to +8.0 ns. If the delayed coincidence time ($T^{\pi}_{\rm tg}$ -$T^{K}_{\rm tg}$) was greater than 15 ns a minimum threshold of 1 phototube was used; otherwise, a threshold of 3 phototubes was chosen. Note that a single phototube hit corresponded to about 10 MeV deposited in the lead-glass. The presence of a hit in the coincidence time window vetoed the event.

3.3.3.6 B4TD

In 1989 the lead-glass counter was not available. It was possible for photons with a trajectory opposite to the incoming beam to convert in the B4 hodoscope or convert in the degrader with some products from the electro-magnetic shower depositing energy in the B4 hodoscope. For

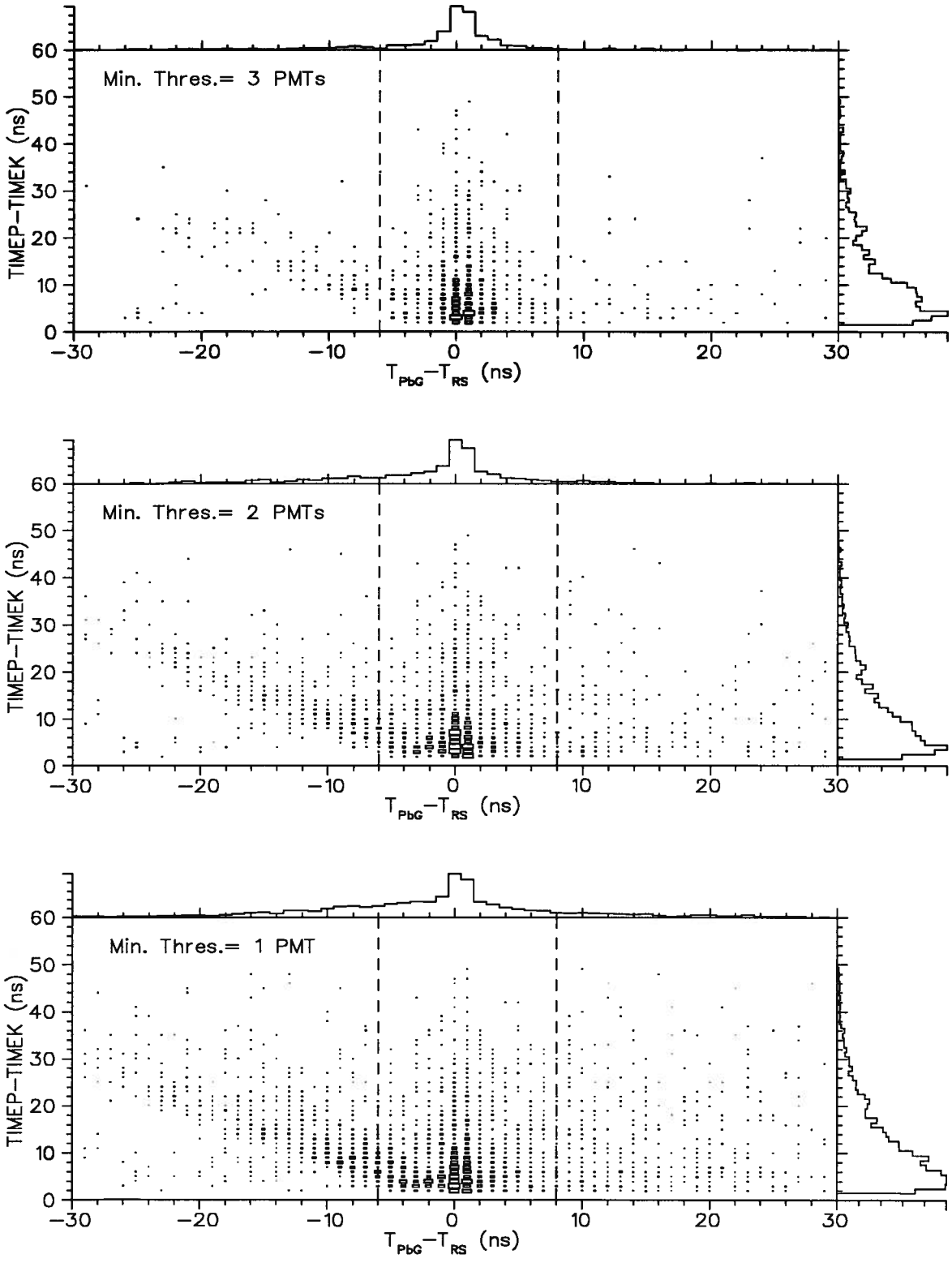

Figure 3.48: Lead-glass detector time versus delayed coincidence time for $\pi\nu\bar{\nu}$ events. The dashed lines indicate the coincidence time window.

1991 data, it was seen in the previous section that the PB-GLASS cut had some limitations for low energy photons, because of the light given off by incoming kaons. Some sensitivity for these low energy showers was obtained by searching for energy deposition in the B4 hodoscope at the time of the K^+ decay.

The output of the B4 hodoscope phototubes was recorded with TD channels. For 1989 data, the output of the B4T counter was used for this cut. In 1991, the sum of the phototube output from the six elements of each of the two B4 hodoscope planes was used. Single and double pulse hypothesis fits (see section 3.3.4.5) were performed independently on the output of each channel. Figure 3.49 shows the time of the second pulse compared to $T_{\rm rs}$ as a function of $\log_{10}\chi_\mu$ for 1991 data. The variable χ_μ is related to the residual of the single pulse fit; a double pulse therefore has a large value of χ_μ . If the value of $\log_{10}\chi_\mu$ was above 1.8 (2.0) and a second pulse was found with a time with respect to $T_{\rm rs}$ within a coincidence window of $\pm$6.0 ns ($\pm$5.0 ns) for 1989 (1991) data, the event was rejected.

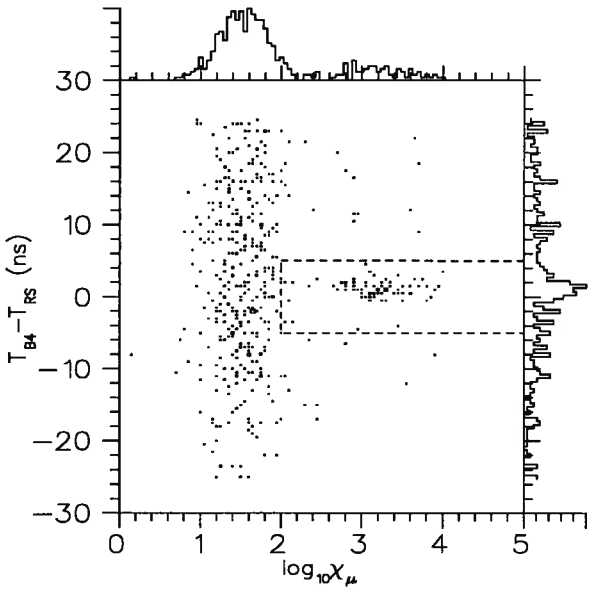

Figure 3.49: $T_{\rm b4} - T_{\rm rs}$ versus $\log_{10}\chi_\mu$ for B4 counter TD fits for 1991 $\pi\nu\overline{\nu}$ data. Events inside the dashed box were rejected.

3.3.3.7 NDC

This cut looked at the total number of hit wires in the drift chamber for each event. In 1991 it was included as part of the DC-SETUP cut, but in 1989 it was an individual cut. Also, in 1989 the hits selected by the track fitting procedure were not excluded from the total. Events with a number of hit wires greater than 50 were rejected.

3.3.3.8 DISENPI

This cut looked at activity in the target at the time of the K^+ decay. The time reference was $T_{\rm rs}$. The energy of all target elements not part of the π^+ or K^+ track with a time within the window [-6.0,+7.0] ns was summed. If the sum exceeded 5.0 MeV the event was rejected. It should be noted that the TGTRACK cut (see section 3.3.6.1) includes essentially the same requirements but with a lower energy threshold. This cut was not used for 1991 data.

3.3.3.9 DISENK

Similarly to the above cut, the energy in target elements not part of the π^+ or the K^+ track but in coincidence with the K^+ track was summed up. The time window chosen was $-4.0 < t - T^K_{\rm tg} < 2.0$ ns, where t is the time of the element considered, and the energy threshold was 5.0 MeV. This was primarily directed at beam pion backgrounds. It was not applied to 1991 data.

3.3.4 Pion identification

This section describes the cuts designed to positively identify π^+ tracks in the range stack. Primarily, these cuts differentiate between π^+ and μ^+ , but they also have a significant contribution in the rejection of π^+ nuclear interactions. Cuts are applied on the kinematic information (range, energy and momentum) from the track, and several cuts relate to the $\pi^+ \rightarrow \mu^+ \rightarrow e^+$ decay chain identification in the range stack using the TDs.

3.3.4.1 RGEMOM

This cut required consistency between the π^+ momentum measured with the drift chamber and the π^+ range measured in the range stack. Based on the momentum, the range of the π^+ in scintillator was inferred from an empirical table. A cut was applied on the difference between the measured range and the expected value. The cut was ± 5 cm for particles stopping in layers B and C and ± 6 cm in layer 11. This cut was only used for 1989 data.

3.3.4.2 MASS

In this cut the consistency between the π^+ momentum measured with the drift chamber and the π^+ energy measured in the range stack was verified. Using those two quantities the mass of the particle can be determined according to the formula :

$$M = \frac{P_{\rm DC}^2 - T_{\rm RS}^2}{2T_{\rm RS}} \tag{3.31}$$

where $P_{\rm DC}$ is the momentum and $T_{\rm RS}$ is the kinetic energy and the speed of light c has been set to 1. If the measured mass was outside of the range $105 < M < 175$ MeV/c^2 the event was rejected. As for RGEMOM, this cut was only used for 1989 data.

3.3.4.3 KINSCORE

For 1991 data, the three independent kinematic quantities (momentum as measured by the drift chamber, range in the range stack and kinetic energy as measured in the range stack) were used for a single cut. In reality, these three quantities were not completely independent. As described in section 3.3.1.4, the range in the last layer of the range stack hit by the track was computed using the measured energy. This computation was made for both a π^+ and a μ^+ hypothesis. Also, a small amount of energy was lost by the charged particle in the drift chamber carbon fibre outer wall. This loss was calculated using the measured momentum, assuming the particle was a π^+ , and was included in the range stack track energy. However, the effect of this correction on the correlation should be negligible.

Any two of the three kinematic quantities available should be sufficient to determine the particle type. However, because of finite resolutions, it was necessary to use all three to obtain

adequate separation. The range stack range was compared to the range expected according to the measured momentum for both a μ^+ and a π^+ hypothesis. The differences between the measured and the expected value for both hypotheses were used. The third quantity used in the cut was the mass of the particle, determined according to equation 3.31.

The three quantities, pion hypothesis range–momentum correlation, muon hypothesis range–momentum correlation and particle mass were combined to form a Fisher discriminant, using multiple discriminant analysis [58]. This type of analysis assumes that the data consists of two distinct populations, and finds the linear combination of the input variables (Fisher discriminant) which provides the maximum separation between the two populations, in this case pions and muons. The coefficients needed to form the Fisher discriminant were determined using training samples, well identified groups of events belonging almost entirely to one of the two populations. The muon training sample was taken from $\pi\nu\overline{\nu}$ lev 0 monitor data and the pion training sample from π-scat monitor data. Figure 3.50 shows the distribution of the Fisher discriminant for the two training samples. To avoid systematic effects due to the average range and energy of pions stopping in different range stack layers, the linear coefficients and cut positions were determined for individual range stack stopping layers. The cut positions for each range stack layer are indicated in figure 3.50; events within the dashed lines were accepted.

3.3.4.4 DEDXRS

This cut looked more closely at the charged particle energy deposition in the range stack. Based on the track position and momentum measured with the drift chamber, the energy deposition in each range stack counter struck by the track was computed by summing the estimated energy loss in small steps. The radius and the center of curvature of the track (and therefore the momentum) were re-calculated at each step. The energy deposition of each step was calculated based on the step size and the energy loss rate (dE/dx) in plastic scintillator obtained from a table of empirical values, assuming the particle was a π^+ . This computation was performed for RS layers A, B and C; it followed the particle until either its kinetic energy was 1.0 MeV or less or it exited range stack layer C. This estimated energy deposition in each range stack

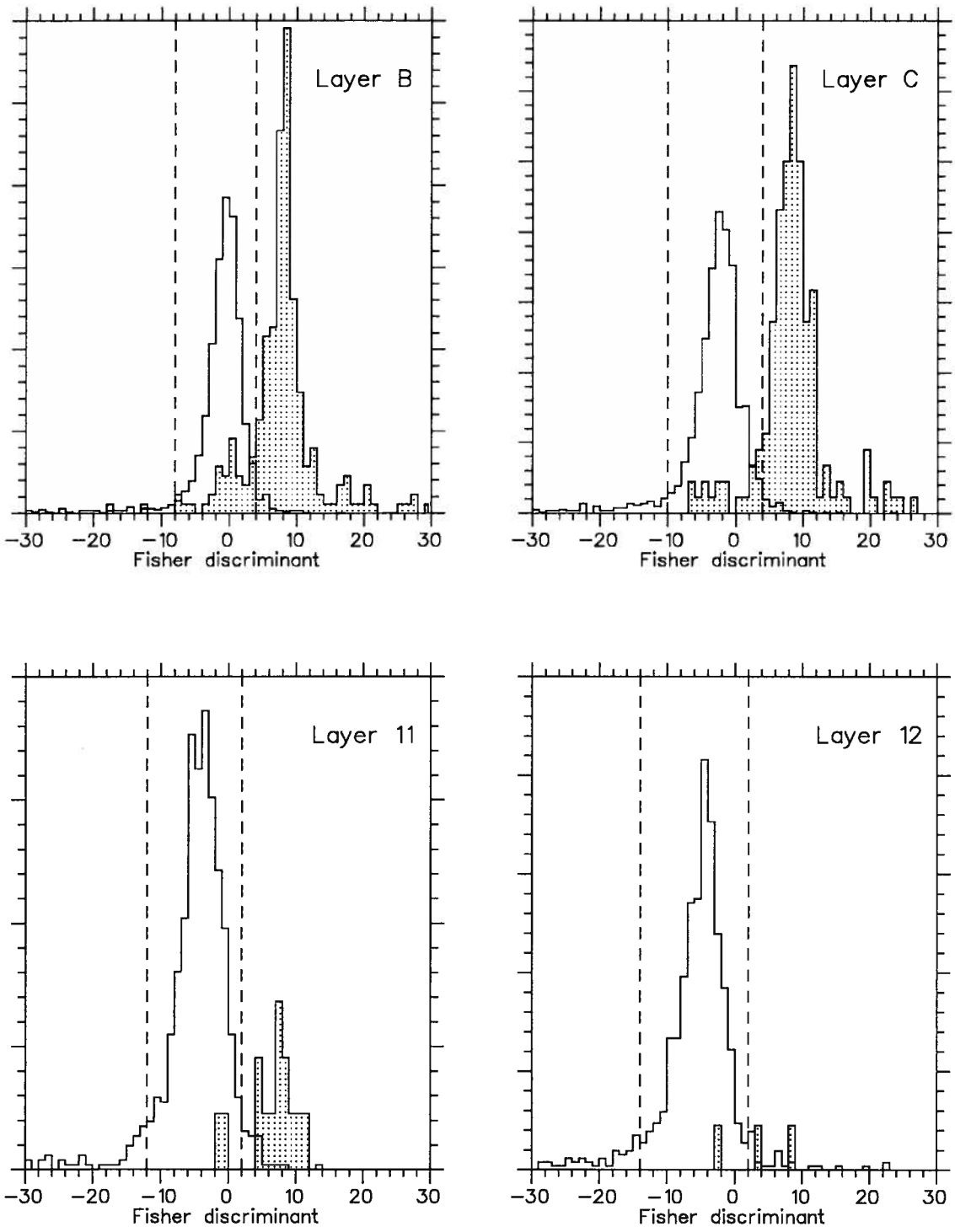

Figure 3.50: KINSCORE results for pre-selected samples of pions (open histograms) and muons (shaded histograms) for the different stopping layers. The individual histograms were normalized to the total sample size for each particle type.

layer struck by the π^+ , except for the layer in which it came to a stop, was compared to the energy measured with the ADCs. Figure 3.51 shows the distribution of measured energy minus expected energy for each range stack layer for 1989 Pass1 data. Events outside of the region defined by dashed lines were rejected.

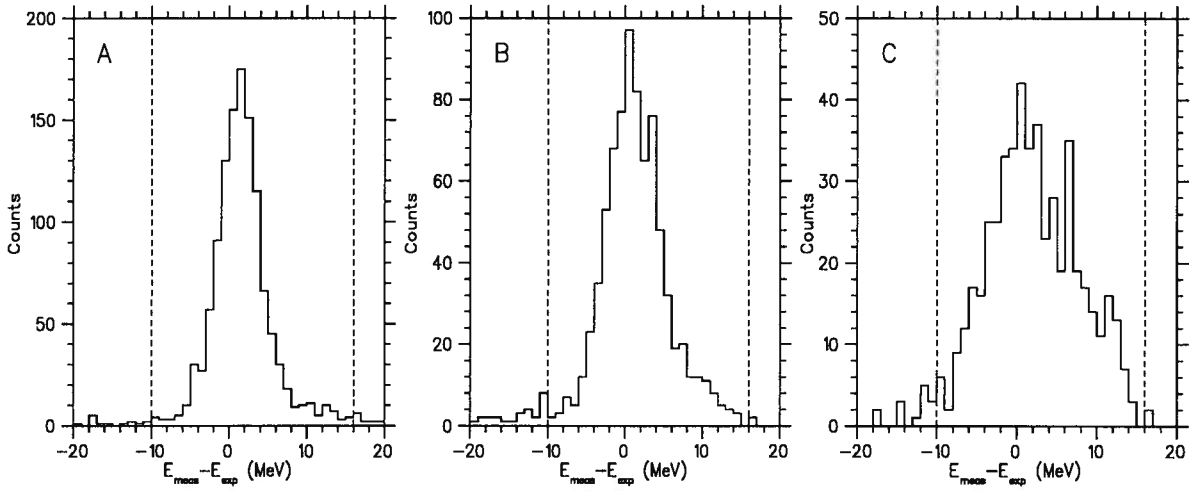

Figure 3.51: Measured minus expected energy in range stack layers A, B and C for 1989 $\pi\nu\overline{\nu}$ data (DEDXRS cut). Events outside of the regions defined by dashed lines were rejected.

The effect of this cut was to reject muons, pions which undergo nuclear interactions in the range stack and photons which converted on top of the track in the range stack. It was not used for 1991 data; the background studies indicated that no significant gains in background rejection could be made by including it in the data analysis. Other cuts addressing the same potential background processes provided adequate rejection.

3.3.4.5 FASFITPI and FITPI

These two cuts made use of a subroutine designed to perform single and double pulse fits on the TD information from both ends of the range stack counter in which the charged particle came to a stop. The pulses recorded by the TDs in a time window 100 ns before and 150 ns after the time of the charged track were examined by the subroutine. Using pre-determined single pulse shapes, the data was fit with the CERN MINUIT minimization program [59] for both a single and double pulse hypothesis. For a single pulse, the two fit parameters were a

time offset for the beginning of the pulse and a scale factor for the pulse height. For the double pulse hypothesis, the fit used four parameters : the time offset of the first pulse, the time delay between the first and second pulse and a scale factor for each pulse. Figure 3.52 shows the fit results for both ends of the stopping counter for a π^+ .

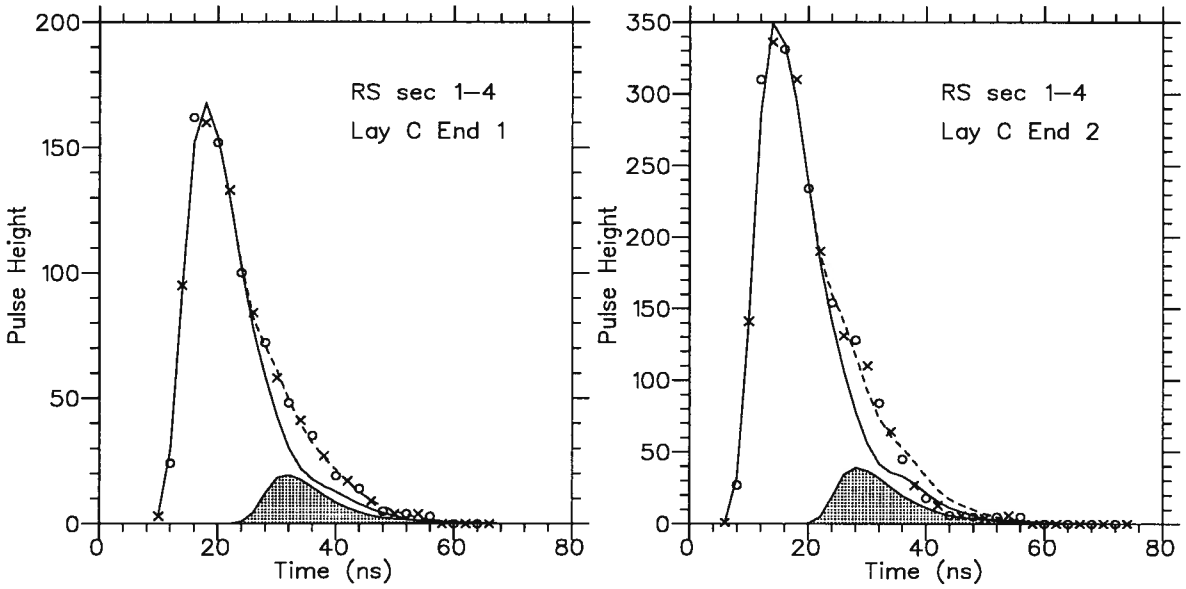

Figure 3.52: TD information and fit results for a π^+ candidate for both ends of the stopping counter. The dashed line indicates the double pulse fit result; the full line and the shaded area indicate the first and second pulse respectively.

Listed below are quantities obtained from the fits that are used to constrain the results.

$C_\mu(i)$: single pulse hypothesis residual for end i

χ_μ : $0.5 \times \log_{10}(C_\mu(1) \times C_\mu(2))$

$C_\pi(i)$: double pulse hypothesis residual for end i

$C_{\mu\pi}(i)$: $C_\mu(i)$ / $C_\pi(i)$

$P_{\mu\pi}$: $C_{\mu\pi}(1) \times C_{\mu\pi}(2)$

$E_\mu(i)$: second pulse area for end i

$\overline{E_\mu}$: $\sqrt{E_\mu(1) \times E_\mu(2)}$

$T_\mu(i)$: time delay between first and second pulse for end i

ΔT_μ : $T_\mu(1) - T_\mu(2)$

$\overline{T_\mu}$: $0.5 \times (T_\mu(1) + T_\mu(2))$

The FASFITPI cut was a quick version of the cut in which only a single pulse hypothesis fit was performed. Cuts were applied on $C_\mu(i)$ and χ_μ . The FITPI cut compared the results of the single and double pulse fits; cuts were applied on $C_{\mu\pi}(i)$, $P_{\mu\pi}$, $E_\mu(i)$, $\overline{E_\mu}$ and ΔT_μ . The latter quantity was a measure of the distance separating the point of origin of the two pulses along the z-axis in the range stack counter. Figure 3.53 shows the distribution of $\overline{E_\mu}$ and ΔT_μ for a pre-selected sample of pions. Note that the default cuts were already applied to this sample. The rms resolution for $\overline{E_\mu}$ was approximately 30 counts, corresponding to 0.6 MeV. ΔT_μ is proportional to the difference between the z-axis position of the energy deposition of the first and second pulse; the resolution was 1.4 ns, corresponding to approximately 20 cm.

To further constrain the result for 1989 data, tighter cuts were applied on some quantities obtained from the fits : $|\Delta T_\mu| < 3.5$ ns, $P_{\mu\pi} > 20$ and $9 < \overline{T_\mu} < 60$ ns. For 1991 data, several quantities were combined in a chi-square quantity, defined by

$$\chi^2 = \sum_{i=1}^{n} \frac{(x_i - \overline{x_i})^2}{\sigma_{x_i}^2}$$

where the x_i were χ_μ , $\log_{10} P_{\mu\pi}$, $\overline{E_\mu}$, ΔT_μ and $\min(E_\mu(1), E_\mu(2))$, and $\overline{x_i}$ and σ_{x_i} were the mean and standard deviations of each quantity, determined from a sample of pre-selected π^+ . Because the difference in counter thickness influences the resolution for fit results, parameters were determined individually for layers B, C and 11+12. The probability for the χ^2 value obtained

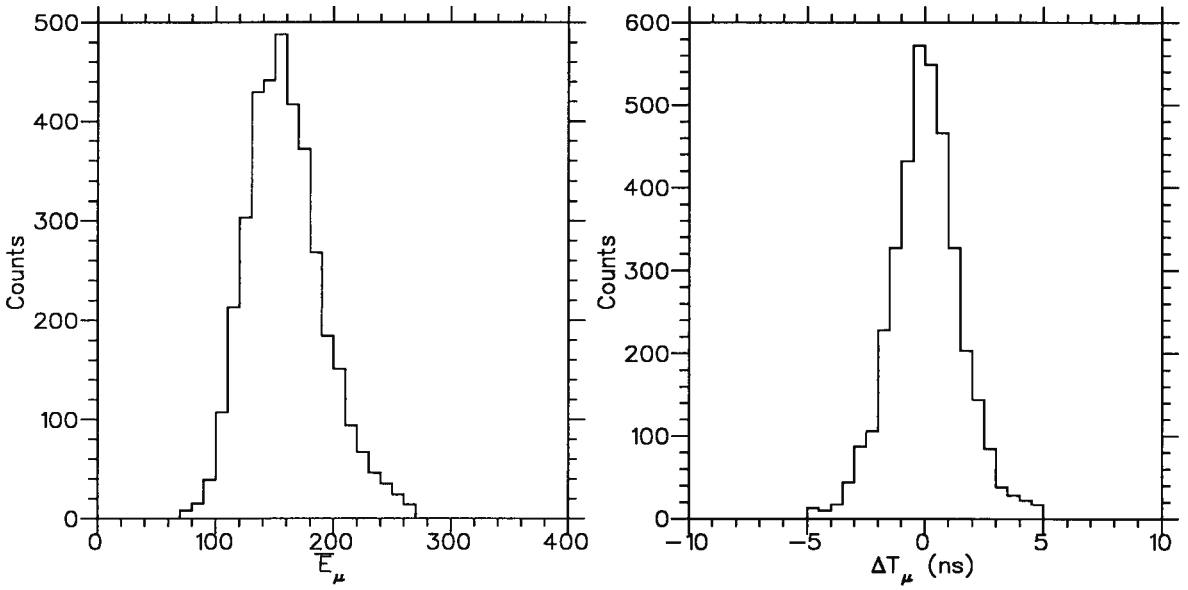

Figure 3.53: $\overline{E_\mu}$ and ΔT_μ variables from FITPI cut for pre-selected π^+ .

was determined for the appropriate number of degrees of freedom; events with a probability less than 0.01 were rejected. Figure 3.54 shows the base 10 logarithm of the probability distribution for samples of pre-selected π^+ and μ^+ .

3.3.4.6 TD_MDA

The five quantities combined to form a χ^2 value in the FITPI cut for 1991 data were also combined to form a Fisher discriminant (see section 3.3.4.3), along with E_{last}, the energy deposited in the last range stack layer struck by the charged particle track. To determine the linear coefficients necessary for this cut, a muon training sample was selected kinematically out of the $\pi\nu\bar{\nu}$ data sample using the KINSCORE cut; in this case, the cut position was chosen to select muons instead of pions. The pion training sample was taken from π-scat monitor data. This cut was designed to primarily reject cases where a fluctuation in a large single pulse was mistaken for a double pulse. This effect was greater for early delay times; therefore, the cut was applied only if $\overline{T_\mu}$ was less than 26 ns for tracks stopping in layers B and C and less than 40 ns for tracks stopping in layers 11 and 12. Events with a Fisher discriminant greater than 0.0 in layers B and C and 0.3 in layers 11 and 12 were rejected. Figure 3.55 shows the distribution of

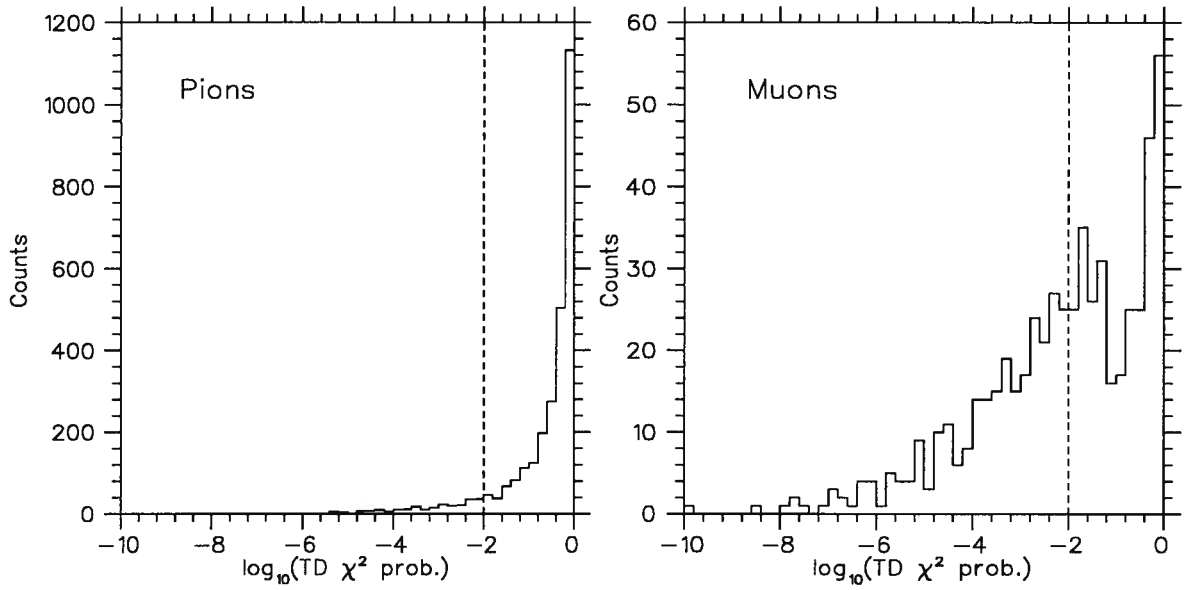

Figure 3.54: Base 10 logarithm of the pion probability distribution for samples of pre-selected π^+ and μ^+ for 1991 data. Events to the left of the dashed line were rejected (probability < 0.01).

the Fisher discriminant for π^+ and μ^+ samples. The dashed lines indicate the cut positions.

3.3.4.7 ELVETO

A significant fraction of the muon background surviving the two-pulse constraints in the stopping counter originated from accidental hits providing the second pulse or from early μ^+ decays. In both cases, it was possible for the particle responsible for the second pulse to also deposit some energy in the area surrounding the stopping range stack counter. The ELVETO cut looked at time hits in coincidence with the time of the "muon" pulse in a search region surrounding the stopping range stack counter. The region covered three sectors on either side of the stopping counter and the minimum number of layers forming a thickness of at least 3.9 cm above and below the stopping counter. Any time hit found at least 5 ns after the π^+ track time and within 5 ns of $\overline{T_\mu}$ rejected the event.

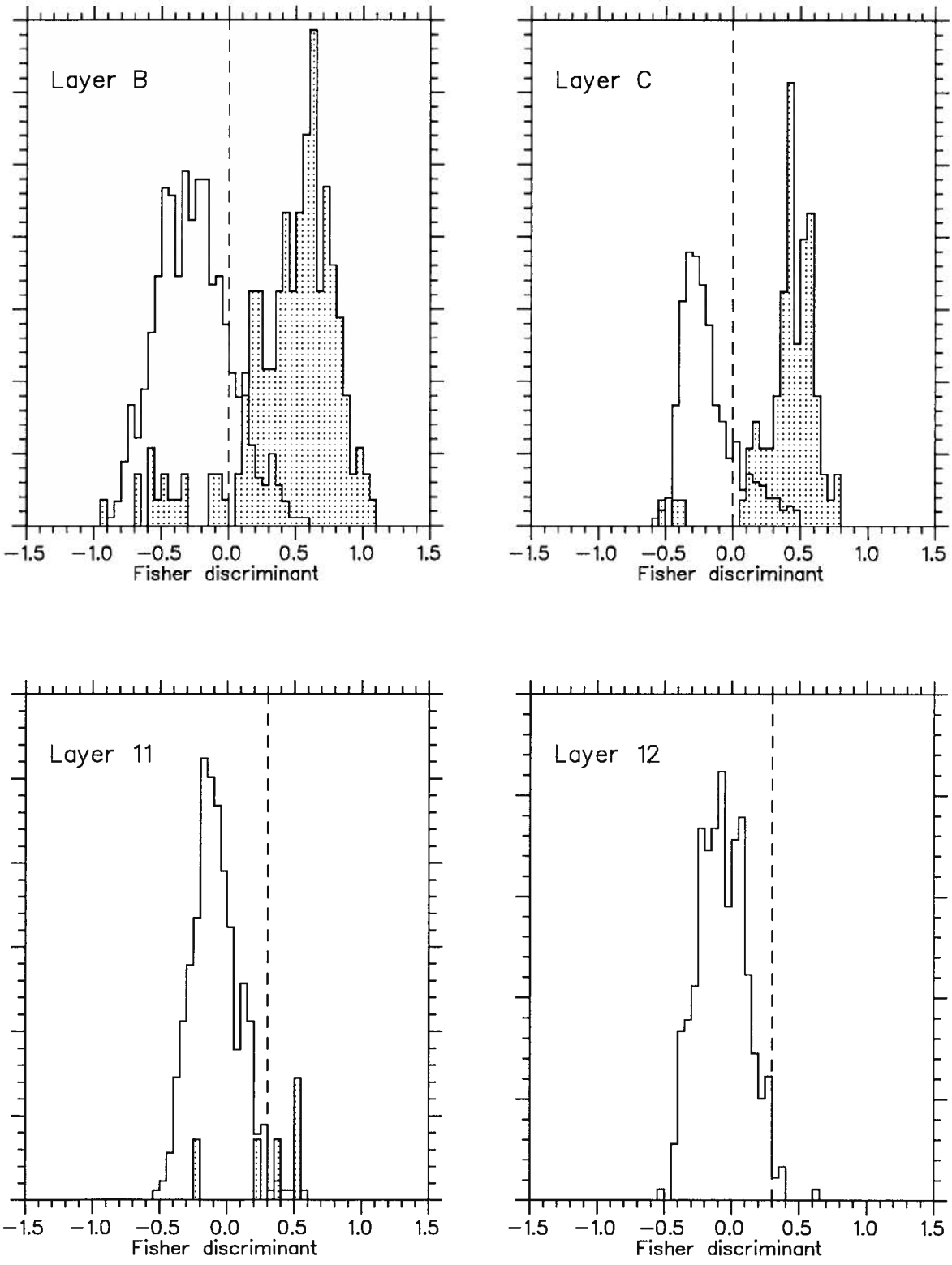

Figure 3.55: TD_MDA results for pre-selected samples of π^+ (open histograms) and μ^+ (shaded histograms) for the different stopping layers. The individual histograms are normalized to the total sample size for each particle type.

3.3.4.8 TDFOOL

The range stack time hits used by the ELVETO cut were derived from the leading edge of pulses recorded by the transient digitizers. For the range stack layer immediately preceding the stopping layer, a second pulse in coincidence with the one in the stopping counter could be obscured by the pulse corresponding to the passage of the stopping charged particle. For this reason, a double pulse fit identical to the one performed in the stopping counter was performed in the preceding layer. In the cases where a hextant crossing occured in that layer, both hextants were examined. For successful double pulse fits, if the time of the second pulse was within 3 ns of the one in the stopping counter, the event was rejected. This cut was only used for 1991 data.

3.3.4.9 ELECTRON

The final step in π^+ identification was to identify a positron from the $\pi^+ \rightarrow \mu^+ \rightarrow e^+$ decay chain. Positron candidates were searched for in the range stack in a region ± 1 sector and ± 2 layers from the stopping counter. The electro-magnetic shower from a positron can deposit energy in several range stack counters. Time measurements from the two ends of counters in the search region were scanned for coincidences; the mean and difference time for each was recorded, as well as the mean pulse height. Groups of counters with a mean time within 5 ns of each other were selected; a minimum of two counters was required to form a group. A group was selected as a positron candidate if the average time of the counters in the group was at least 20 ns later than the π^+ decay time, at least one counter had a pulse height greater than 100 counts ($\sim$ 2.5 MeV) at each end, the total pulse height for the group was greater than 750 counts and the average end-to-end time difference was within 3.5 ns of the $\pi \rightarrow \mu$ time difference (ΔT_μ). Finally, the summed area of all range stack pulses with a time within 5 ns of the positron candidate time had to be less than 7000 counts. This considerably reduced fake positron signals due to accidental tracks.

3.3.5 Beam cuts

Because of the trigger requirement for a kaon Čerenkov signal, and the target track reconstruction constraints, specific offline requirements for an incoming K^+ were not necessary. However, the identification and rejection of beam pions scattering into the range stack was very important. Several detector elements were used for this purpose.

3.3.5.1 CERENKOV

The time values of the pion Čerenkov counter multiplicity signal pulses, measured with a TDC, were compared to the measured time of the charged particle track in the range stack ($T_{\rm rs}$). The time value closest to $T_{\rm rs}$ was selected as the pion Čerenkov time ($T_{\check{C}_\pi}$). A cut on $|T_{\check{C}_\pi} - T_{\rm rs}|$ was set at 6.0 ns (5.0 ns) for 1989 (1991) data; events within those bounds were rejected. Figure 3.56 shows the $T_{\check{C}_\pi} - T_{\rm rs}$ distribution for 1991 $\pi\nu\overline{\nu}$ events. This requirement provided most of the beam pion background rejection.

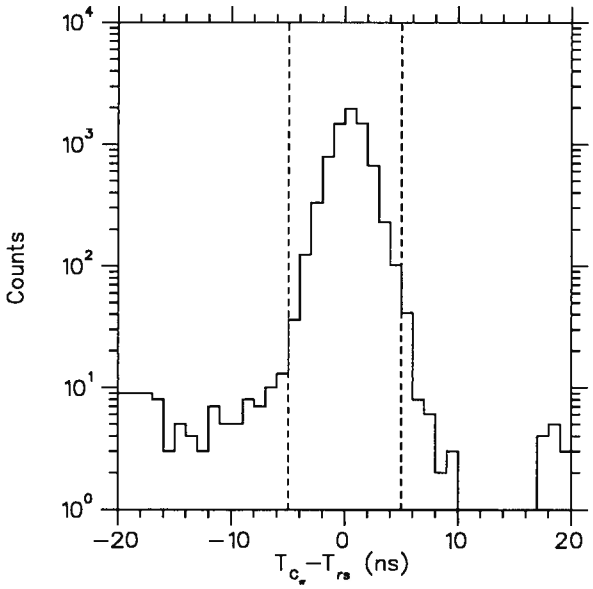

Figure 3.56: Time of pion Čerenkov hits with reference to $T_{\rm rs}$ for 1991 $\pi\nu\overline{\nu}$ events. Events inside the dashed lines were rejected.

3.3.5.2 BWPC

The pion Čerenkov counter has a limited efficiency in detecting beam pions, as well as limited geometrical coverage. The radiator only covers a circular region 15 cm in diameter, which can be exceeded by the beam pion halo. The multi-wire proportional chamber (BWPC) provides a wider geometrical coverage for beam pions. Hits in at least two of the three planes of the chamber were required to identify a particle; however, nearly 99% of the time a hit was found in all three planes. The measured time of a particle in the chamber was the average of the calibrated times of the individual hits. A subroutine searched for time hits near zero identifying a K^+ , and then looked for later hits which would indicate the presence of another beam particle. The list of hits was compared to $T_{\rm rs}$ and the closest one was chosen as $T_{\rm bw}$. Events for which $-4.0 < T_{\rm bw} - T_{\rm rs} < 12.0$ ns were rejected. Figure 3.57 shows the time distribution for $\pi\nu\bar{\nu}$ events. This cut was only used for 1991 data.

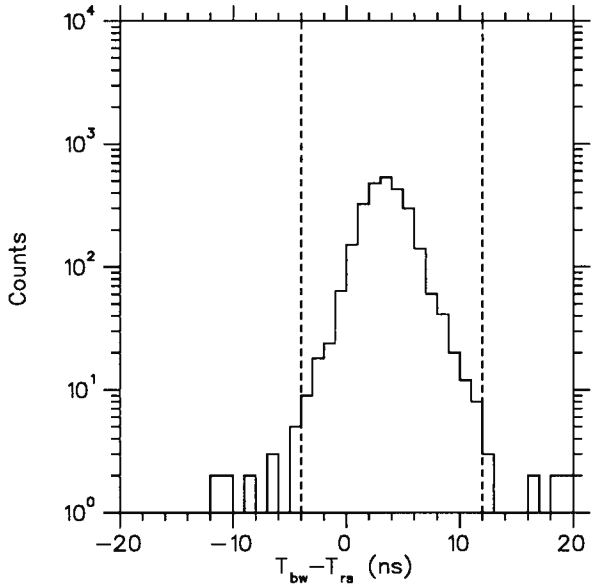

Figure 3.57: Time of BWPC hits with reference to $T_{\rm rs}$ for 1991 $\pi\nu\bar{\nu}$ events. Events inside the dashed lines were rejected.

3.3.5.3 BM_HOLE

The beam hole counter was described in section 2.2.1.1. As mentioned above, the halo of beam pions tends to be wider than the K^+ beam, due to the beam line optics. The entire K^+ beam should be well within the acceptance region of the hole counter. Beam pions can strike the scintillator counters forming the hole. For 1991 events in which a beam hole counter ADC hit of more than 10 counts was recorded, the list of TDC times was scanned and compared to $T_{\rm rs}$. The beam hole counter time closest to $T_{\rm rs}$ was chosen as $T_{\rm bh}$. Events with $|T_{\rm bh} - T_{\rm rs}|$ less than 5.0 ns were rejected.

In 1989, the BM_HOLE counter cut was used for a different purpose. It was used to detect charged particles which might originate from photon conversions in the degrader. The TDC time scale of the beam hole counter was calibrated such that the time of a beam particle with respect to $T_{\rm rs}$ was zero. Particles resulting from a photon conversion related to the decay of a K^+ in the target would appear with a delay corresponding to the time of flight of the K^+ to the target and the photon traveling towards the beam hole counter, approximately 20 ns. Events with a beam hole counter ADC energy greater than 50 counts and a time with respect to $T_{\rm rs}$ within a [-16.0,+24.0] ns window were rejected. No evidence was found for such hits in 1991 data.

3.3.5.4 B4_CNTR

This cut required that the energy deposited in the B4 hodoscope be consistent with that expected from a slow K^+ about to enter the target. It was only used for 1991 data. The calibrated ADC values of the energy deposition in each of the six fingers of the two B4 hodoscope planes was summed. The average of the sum from each plane was taken as $E_{\rm B4}$. Figure 3.58 shows the distribution of $E_{\rm B4}$ for $K_{\mu 2}$ events and beam pion-scattering events, where it is clear that a faster moving π^+ deposits much less energy than a stopping K^+ . Events with $E_{\rm B4}$ less than 1.8 MeV were rejected. This constraint was particularly effective against events in which a K^+ passed through the Čerenkov counter and subsequently decayed in flight to a π^+ which scattered in the target and stopped in the range stack.

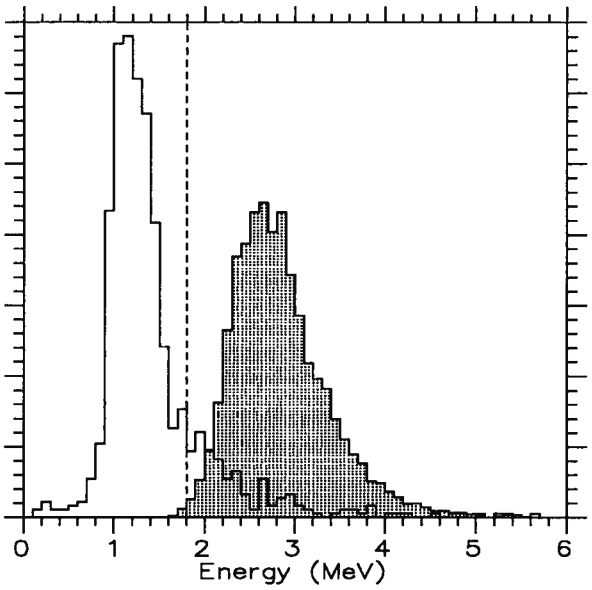

Figure 3.58: Energy measured in the B4 hodoscope for beam K^+ (shaded histogram) and π^+ (open histogram). Events to the left of the dashed line were rejected.

3.3.6 Vertex Cuts

The cuts described in this section are concerned with the quality of the K^+ decay vertex in the target. Any anomalous energy deposition must be identified in order to reject π^+ nuclear interactions or additional K^+ decay products. Information from the drift chamber and the B4 hodoscope supplemented the target information to improve the background rejection capability.

3.3.6.1 TGTRACK

This cut used the drift chamber track information to define a track in the target. Target elements with ADC information were categorized as pion or kaon hits according to their measured time. The list of kaon and pion elements as provided by the target track reconstruction subroutine (see section 3.3.1.1), which used primarily energy information to categorize hits, was used as a starting point. To be considered part of the pion track, an element had to have a measured time within 5 ns of $T_{\rm rs}$ and closer to $T_{\rm rs}$ than $T_{\rm tg}^K$. A cut was placed on the number of kaon (N_K) and pion (N_π) elements at $1 \leq N_K \leq 10$ and $1 \leq N_\pi \leq 30$. A 0.8 cm wide swath centered on the extrapolated drift chamber track defined the π^+ trajectory in the target. Using the center

of curvature of the drift chamber track in the xy plane and an axis parallel to the x-axis as a reference, a rotation angle was found for each kaon and pion element based on a vector between the center of curvature and the center of the target elements. The rotation angle decreased as the particle exited the target. Figure 3.59 shows the geometry conventions used. Using this information, the following cuts were applied :

1. At least one kaon element was on the swath.
2. The maximum pion rotation angle was less than or equal to the maximum kaon rotation angle ($\phi_\pi^{\max} \leq \phi_K^{\max}$).
3. If $\phi_\pi^{\max} > \phi_K^{\min}$, the pion element with $\phi_\pi^{\max}$ had at least one pion element neighbor.
4. Groups of kaon elements not on the swath could not have elements on both sides of the DC track. This removed events where the pion originated from the middle of the kaon cluster.
5. The maximum pion element energy, corrected for the dip angle of the π^+ trajectory, had be less than or equal to 3.5 MeV.
6. Pion elements on the swath could not have a neighboring pion element off the swath.
7. The energy of pion elements off the swath and disconnected from other elements was summed up (E_π^{disc}). A cut was placed at $E_\pi^{\text{disc}} \leq 1.5$ MeV.
8. The minimum distance between the pion element with $\phi_\pi^{\max}$ and the kaon elements (MINDIS) was computed. A cut was placed at MINDIS ≤ 2.0 cm.
9. The distance covered by the extrapolated drift chamber track in the kaon elements was computed (DPATHK). A cut was placed at DPATHK ≤ 1.2 cm.

This cut eliminated a large number of pion interactions in the target, as well as photon conversions. Figures 3.60, 3.61 and 3.62 show examples of events rejected by the TGTRACK cut.

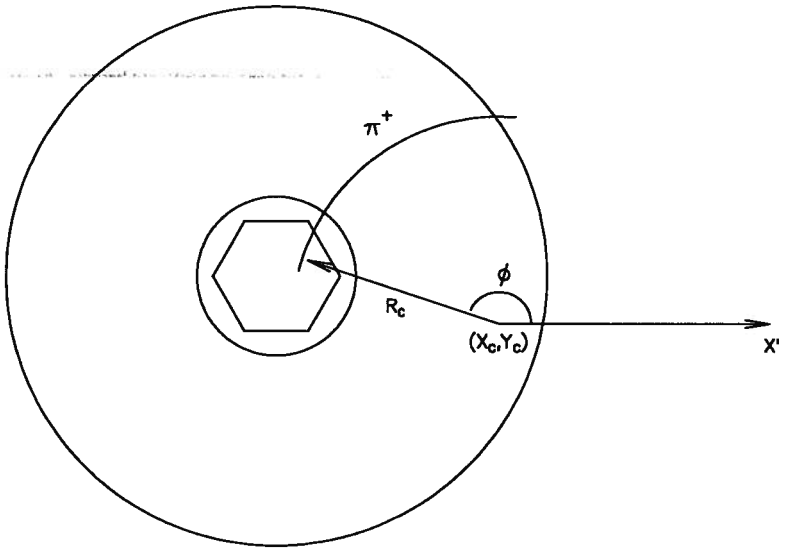

Figure 3.59: Geometry conventions for TGTRACK cut. An angle ϕ was determined for each target element on the swath defined by the π^+ track.

3.3.6.2 NK

This cut required the total number of target elements struck by the K^+ to be less than 10. The TGTRACK cut described above restricted this number to be less than 11, and therefore this cut had little impact. It was only applied to 1989 data.

3.3.6.3 TGFIT

This cut used transient digitizers to identify large energy depositions at the time of the K^+ decay in the target elements struck by the K^+ . In the element where the K^+ comes to rest, only a few MeV are expected at the time of the K^+ decay from the outgoing π^+ . However, if the π^+ undergoes a nuclear interaction or travels a significant distance along the z axis before scattering towards the range stack, more energy will be deposited. Also, the π^+ could travel in the target elements struck by the K^+ in a way that makes part of its path undetected.

Three TD channels were used in 1991 to view the target phototubes' output. Each TD channel covered one third of the target elements, distributed in a random but known fashion. Unconstrained single and double pulse hypothesis fits, similar to the ones performed on the range stack information for the $\pi \rightarrow \mu$ decay search, were performed independently in each

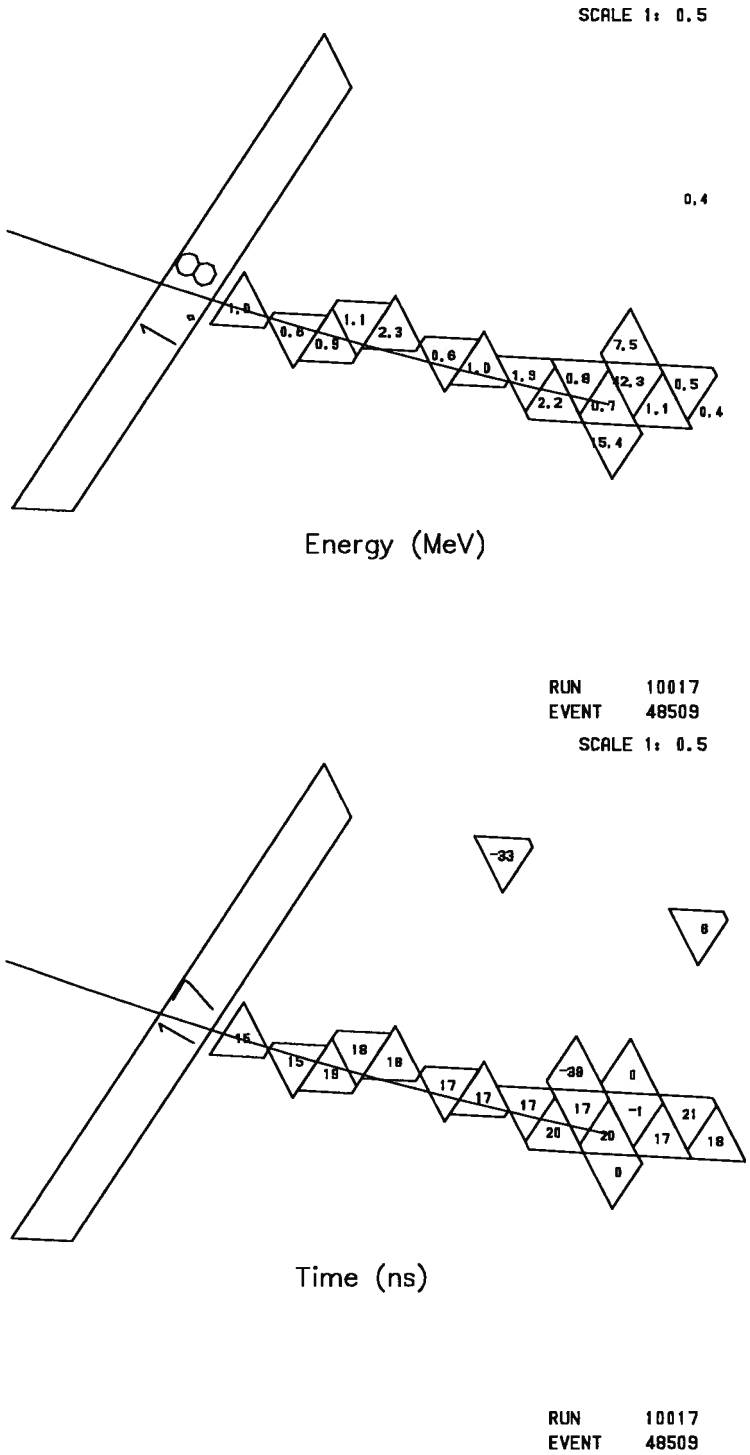

Figure 3.60: Large angle scatter event rejected by the TGTRACK cut. The top display gives the energy information (MeV) and the bottom display give the corresponding time information (ns). The extrapolated DC track trajectory is also indicated.

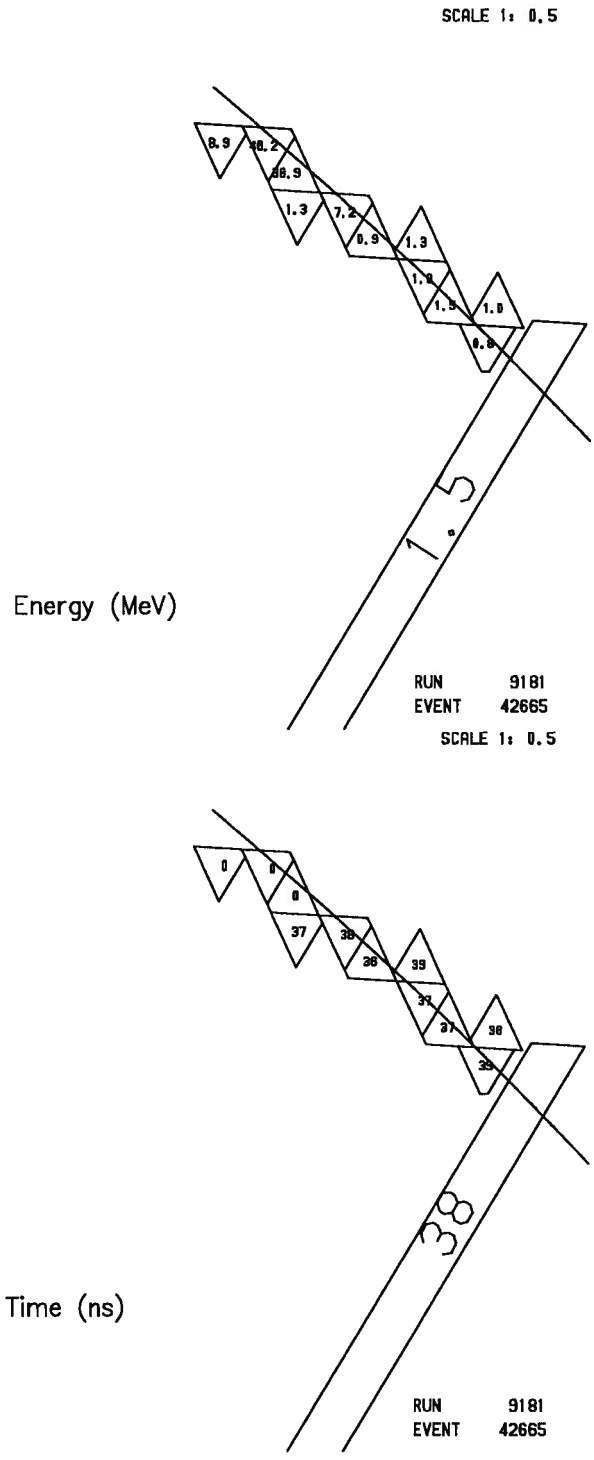

Figure 3.61: Large energy deposition by a π^+ rejected by the TGTRACK cut. The displays are as in figure 3.60. Note the energy deposition of 7.2 MeV in a single π^+ target element.

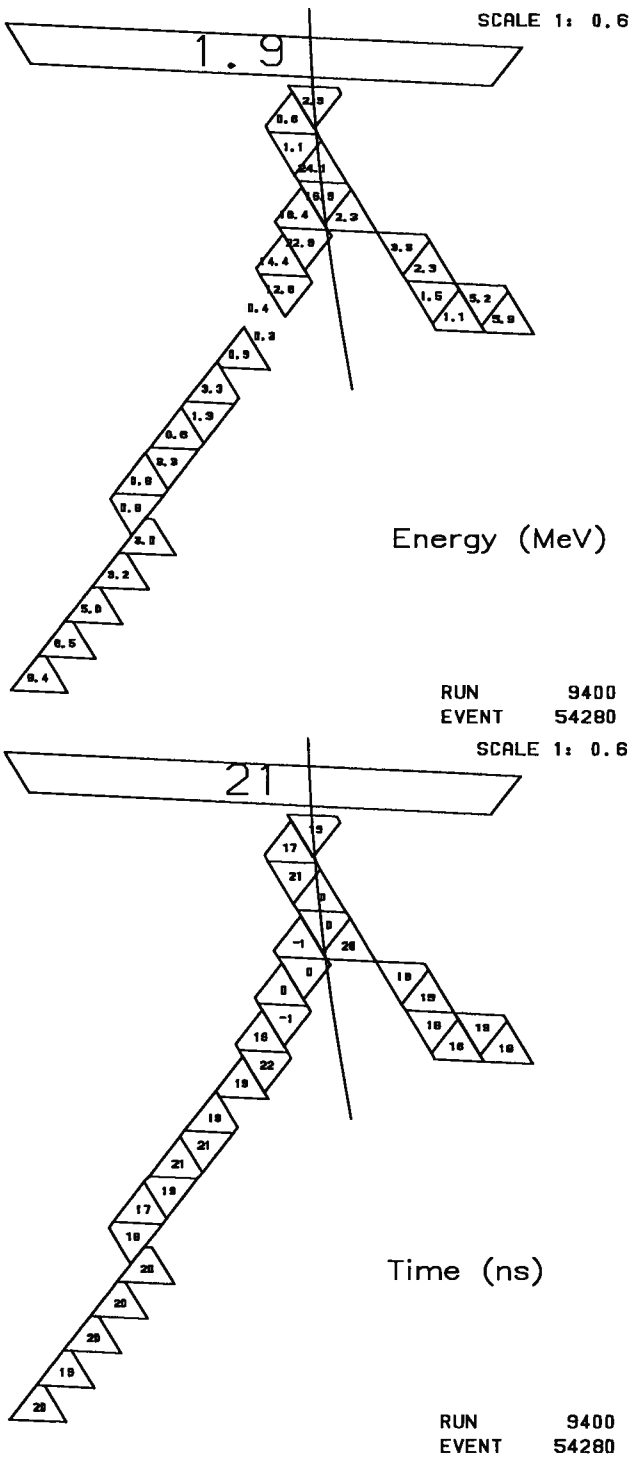

Figure 3.62: Photon conversion or multiple charged track K^+ decay rejected by the TGTRACK cut. Displays are as in the previous two figures.

of the three channels. The overall time scale of each channel was calibrated such that the stopping K^+ time was zero. The pulse area in each channel was also calibrated. For the fit, pulse information was considered up to only 35 ns beyond the known π^+ time in the target (T^{π}_{tg}), obtained from the target track reconstruction subroutine. This prevented late accidental hits from disrupting the fits. The quality of the single and double pulse fits was compared; if the single pulse fit was the best and the time of the pulse was within 5 ns of T^{π}_{tg} the energy was assigned to the pion. If the double pulse fit was the best, the time of both the first and second pulse was compared to T^{π}_{tg}. If the time was within 5 ns of T^{π}_{tg}, the energy was assigned to the pion.

From the list of pion elements and the known assignment of target elements to TD channels, the pion energy expected in each TD channel measured with the ADCs was summed up. This number was compared to the energy measured with the TDs for the cases where a successful fit occured. For the individual channels, if the energy measured with the TDs exceeded the energy measured with the ADCs by 3 MeV or more, the event was rejected. A cut was also placed at 3 MeV on the sum of the differences between TD and ADC measured energy for the three channels. Figure 3.63 shows the distribution of this sum for $K_{\pi 2}$ background events, both from the $K_{\pi 2}$ kinematic peak region and from the $K^+ \rightarrow \pi^+ \nu \overline{\nu}$ kinematic search region. The excess of events in the high side tail in plot b) identifies events in which the π^+ lost a significant amount of energy in the target elements struck by the K^+. Figure 3.64 shows the TD information as well as the fit results for the three TD channels of an event rejected by the TGFIT cut. There is a very large energy deposition at the time of the K^+ decay in channel # 2. The single pulse fit for channel # 3 is not very good. This is most likely due to the fact that the pulse shape used for the fit is an average for all target elements included in each TD channel and is expected to be less accurate for some target PMTs. The rejection of the TGFIT cut was limited by the double pulse resolution of the fits. Pulse shape accuracy is one of the factors contributing to this limitation.

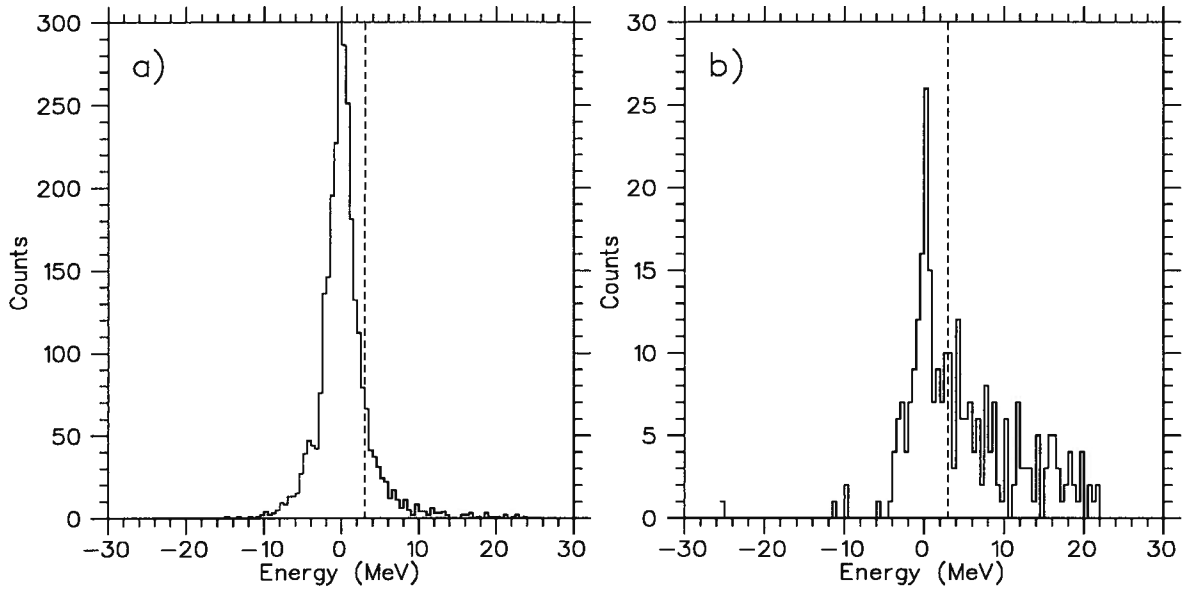

Figure 3.63: Energy deposited by the π^+ in the target as measured by the TDs minus the values measured by the ADCs. The TD energy value is the sum of the three channels (see text). Both plots are for $K_{\pi 2}$ events recorded in the $\pi\nu\overline{\nu}$ data. Figure a) is for events in the $K_{\pi 2}$ peak and figure b) is for events in the $\pi\nu\overline{\nu}$ signal region.

3.3.6.4 VTX_PCA

As for the previous cut, the VTX_PCA cut was designed to reject events in which a large energy loss by the π^+ was hidden in the K^+ track. The method consisted in comparing three different measurements of the energy assigned to the K^+ in the target. The first measurement was the direct measurement of the K^+ energy in the target, i.e. the sum of the measured energy in all elements identified as belonging to the K^+ track. The second energy measurement was derived from the measured range of the K^+ in the target. It was determined by extrapolating the drift chamber track back to the decay vertex to obtain the range along the z-axis and combining it with the range in the xy plane as measured by the target track reconstruction subroutine. A table of energy as a function of range for K^+ was then interpolated to obtain an estimate of the K^+ energy deposition based on the measured range.

The third energy measurement was obtained from the K^+ energy loss rate (dE/dx) in the B4 hodoscope, given by dividing the measured energy deposition by the known counter

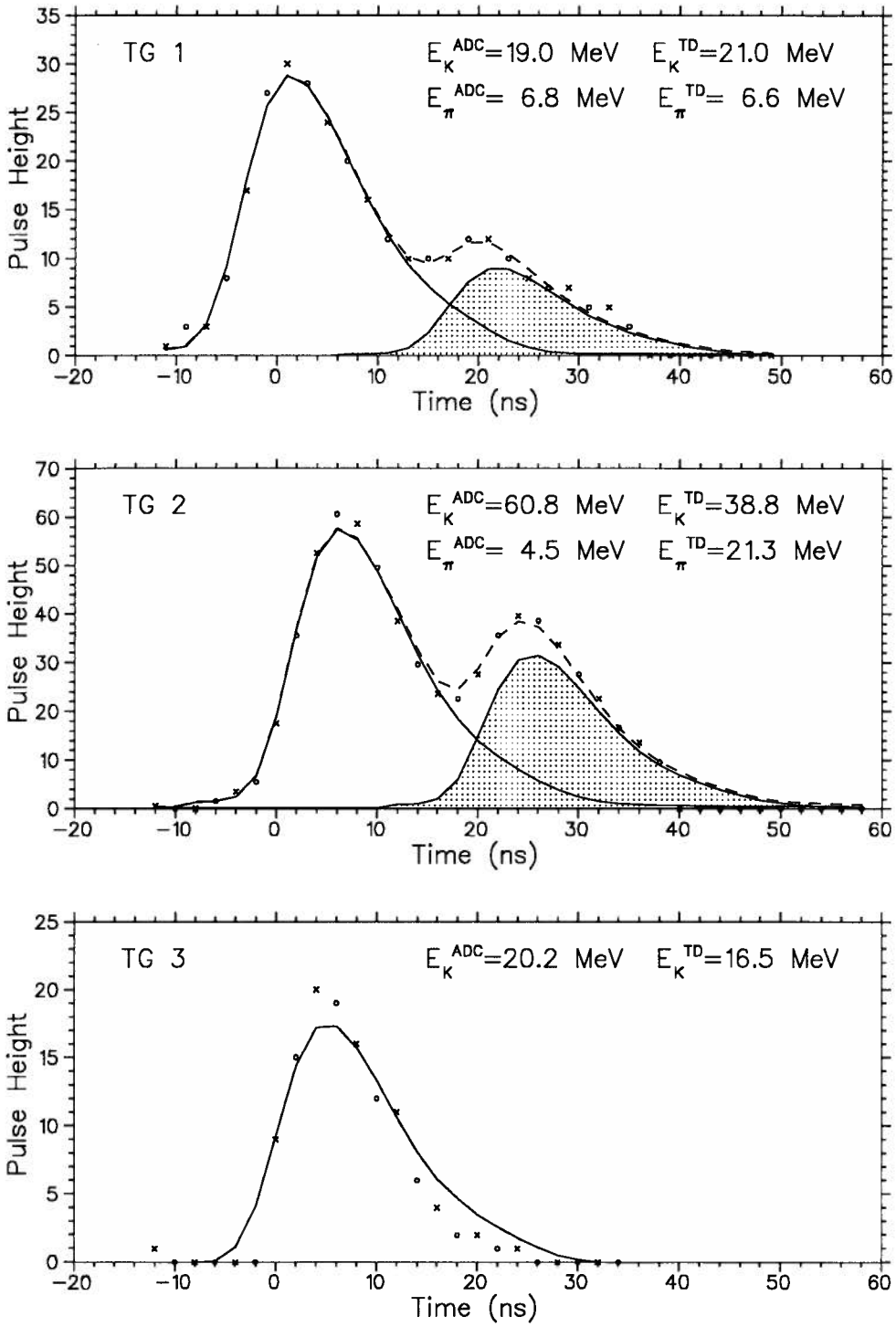

Figure 3.64: Target TD information and fit results for an event rejected by the TGFIT cut. The dashed line shows the double pulse fit, the full line shows the first pulse and the shaded area indicates the second pulse. For channel # 3 only a single pulse fit is shown.

thickness. A table of K^+ energy as a function of energy loss rate was interpolated to obtain the estimated K^+ energy deposition. The values of the difference between the direct measurement and the two expected values of the K^+ energy deposition were then combined in a principal component analysis [58]. In this type of multi-variate analysis, new variables are formed as linear combinations of the input variables. The coefficients are chosen such that the output variables are uncorrelated and have maximum variance. The output variables are then rescaled such that their variance is unity. For n input variables, there will be n output variables, corresponding to the principal components. For VTX_PCA, a cut was applied in the space defined by the two resulting normalized variables. Figure 3.65 shows the distribution in this space for two samples of $K_{\pi 2}$ background events; the events identified as "peak" are from the $K_{\pi 2}$ kinematic peak region and the ones identified as "tail" are from the $K^+ \to \pi^+ \nu\bar{\nu}$ kinematic search region.

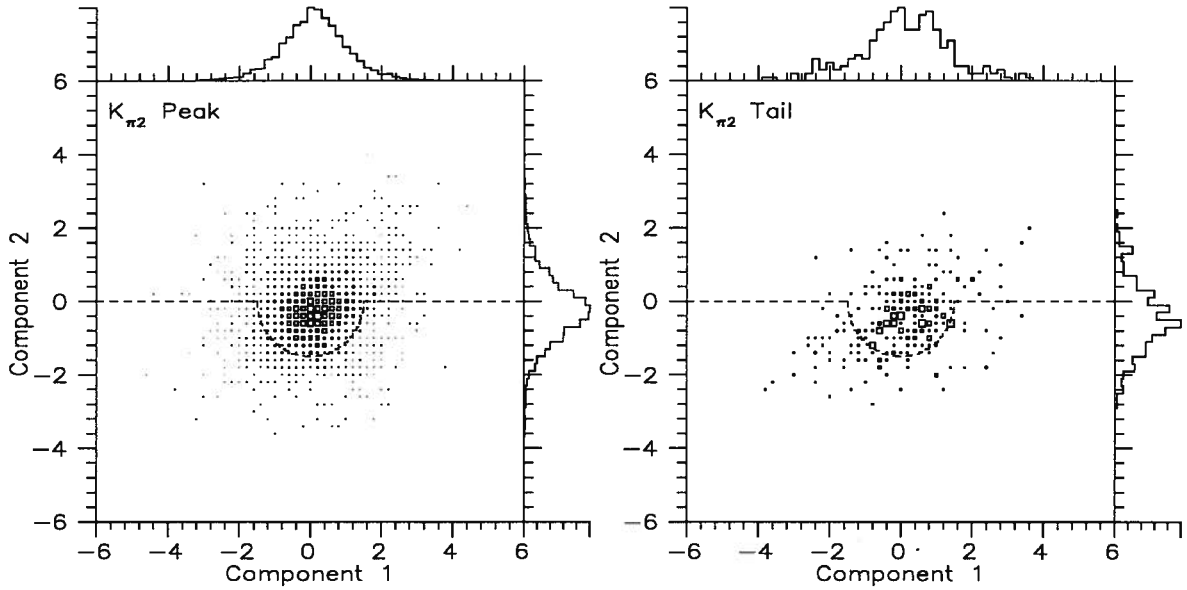

Figure 3.65: VTX_PCA components for $K_{\pi 2}$ events. Events below the dashed line were rejected.

This cut was used for 1991 data only. For 1989 data, cuts were applied individually on the consistency of the extrapolated K^+ decay vertex position with the K^+ energy and the B4 hodoscope energy with the K^+ energy. These cuts are described below.

3.3.6.5 ZK_EK

This cut was based on the relationship between the position of the K^+ decay vertex along the z axis ($Z_{\rm vtx}$) and the measured K^+ energy in the target (E_K). Events not satisfying the relation

$$(Z_{\rm vtx} + 10.0) < (\frac{E_K}{50})^3 \tag{3.32}$$

were rejected. Figure 3.66a shows the relationship between E_K and $Z_{\rm vtx}$ for 1989 $\pi\nu\overline{\nu}$ Pass1 data; the events to the right of the dashed line were rejected.

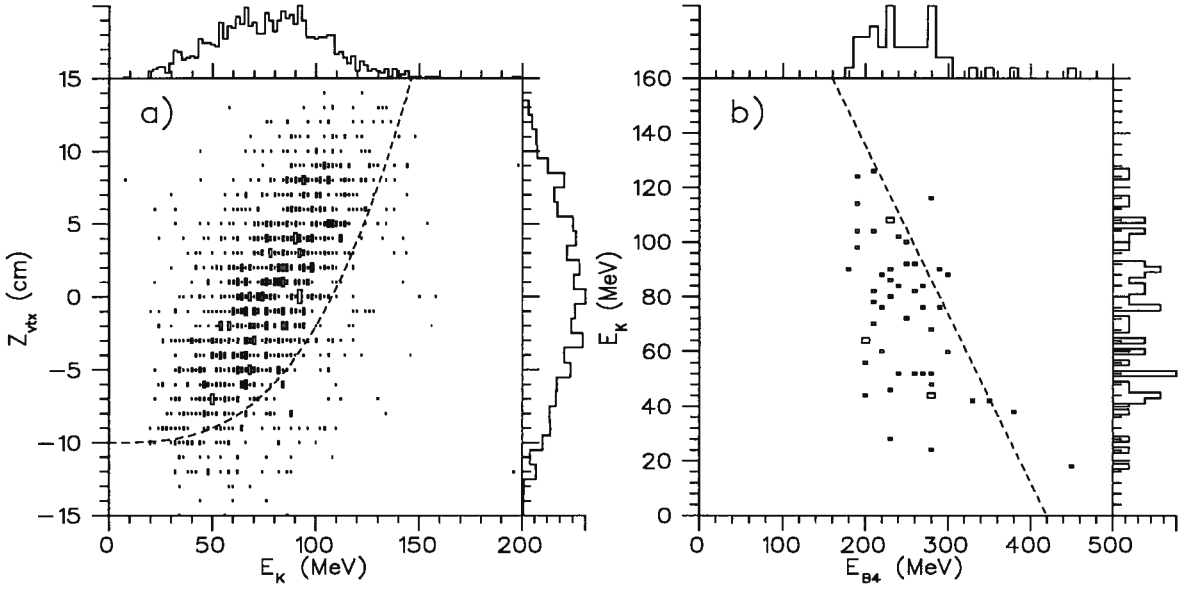

Figure 3.66: Relationship between $Z_{\rm vtx}$, E_K and E_{B4} for 1989 $\pi\nu\overline{\nu}$ data. a) shows $Z_{\rm vtx}$ versus E_K and b) shows E_K versus E_{B4}. The dashed lines indicate the cut positions. See text for details.

3.3.6.6 EB4_EK

Similarly to the previous cut, consistency was demanded between the K^+ energy in the target and the energy deposited in the B4 hodoscope by the K^+ . Figure 3.66b shows the distribution of E_K versus E_{B4} for 1989 Pass2 data (see section 5.1.1.1); the events above the dashed line were rejected.

3.3.7 Kinematic search region (KINCUT)

This cut selected the π^+ kinematic region where $K^+ \to \pi^+\nu\overline{\nu}$ candidates were searched for. This region excluded the $K_{\pi 2}$ peak region where background events were expected due to the limited π^0 rejection. The three quantities used, total range, total momentum and total energy, were determined as follows : the total range was the sum

$$R_{\rm tot} = R_{TG} + R_{IC} + R_{iw} + R_{ow} + R_{RS} \tag{3.33}$$

where R_{TG} is the measured π^+ range in the target, R_{IC} the range in the I-counters, R_{iw} and R_{ow} the range in the inner and outer radius drift chamber carbon fibre walls respectively and R_{RS} is the range in the range stack. The range in the target is the path length in the xy plane determined from the target elements struck by the π^+ , corrected for the dip angle of the π^+ trajectory determined by the drift chamber. The determination of the I-counters range was described in section 2.2.3. The range in the drift chamber walls was based on the known thickness of the walls and the measured particle trajectory. The measurement of the range stack range was described in section 2.2.6.

To obtain the total momentum, the measured drift chamber momentum had to be corrected for the energy lost by the π^+ before entering the chamber. This was done by first converting the measured drift chamber momentum to a range (R_{DC}), by interpolation in a table of empirical values relating momentum and range in scintillator for a π^+ . This range value was summed with the π^+ range before the drift chamber

$$R'_{DC} = R_{TG} + R_{IC} + R_{iw} + R_{DC} \tag{3.34}$$

and R'_{DC} was re-converted to a momentum value ($P_{\rm tot}$) using the same empirical range versus momentum table.

The total π^+ energy was given by

$$E_{\rm tot} = E_{TG} + E_{IC} + E_{iw} + E_{ow} + E_{RS} \tag{3.35}$$

where E_{TG} is the measured π^+ energy in the target, E_{IC} the energy measured in the I-counters, E_{iw} and E_{ow} the energy deposited in the drift chamber walls and E_{RS} the energy measured in

the range stack. The energy deposition in the drift chamber walls was determined by converting the measured range to an energy using the known energy loss rate for a π^+ in carbon fibre.

Each of the three kinematic quantities were constrained independently. The three are also directly related; therefore, the cut position on one quantity could be fixed and the other two adjusted accordingly. For 1989 data, the total energy cut was fixed based on the distribution of $K_{\pi 2}$ background events. The total momentum and total energy cut positions were then adjusted by requiring that the ratio of acceptance for $K^+ \to \pi^+\nu\overline{\nu}$ events and rejection for $K_{\pi 2}$ events be the same as for the total range cut. For $K^+ \to \pi^+\nu\overline{\nu}$, Monte Carlo generated events were used, while real data was used for $K_{\pi 2}$.

For 1991 data, the total range cut was set first, at the same position as for 1989 data. This was to ensure some level of consistency between the accepted regions for the two data sets. The total range cut was chosen because of its stability, due mainly to its geometric nature. The total momentum and energy are more susceptible to calibration variations; their cut positions were set to the same ratio of acceptance versus rejection as the range cut. The final cut positions for the two data sets are given in table 3.10. Figure 3.67 shows the distributions used to set the 1991 cuts.

Table 3.10: Upper bound set for the $K^+ \to \pi^+\nu\overline{\nu}$ kinematic search region.

Quantity	**Year**	
	1989	**1991**
Total energy (MeV)	98.0	99.0
Total range (cm)	27.0	27.0
Total momentum (MeV/c)	190.0	195.0

The cut at the lower end of the spectrum was determined implicitly by the minimum range requirement of the $\pi\nu\overline{\nu}$ trigger. Based on the Monte Carlo $K^+ \to \pi^+\nu\overline{\nu}$ distribution in figure 3.67, we see that this roughly corresponds to $R_{\rm tot}$ = 11 cm, $E_{\rm tot}$ = 52 MeV and $P_{\rm tot}$ = 140 MeV/c.

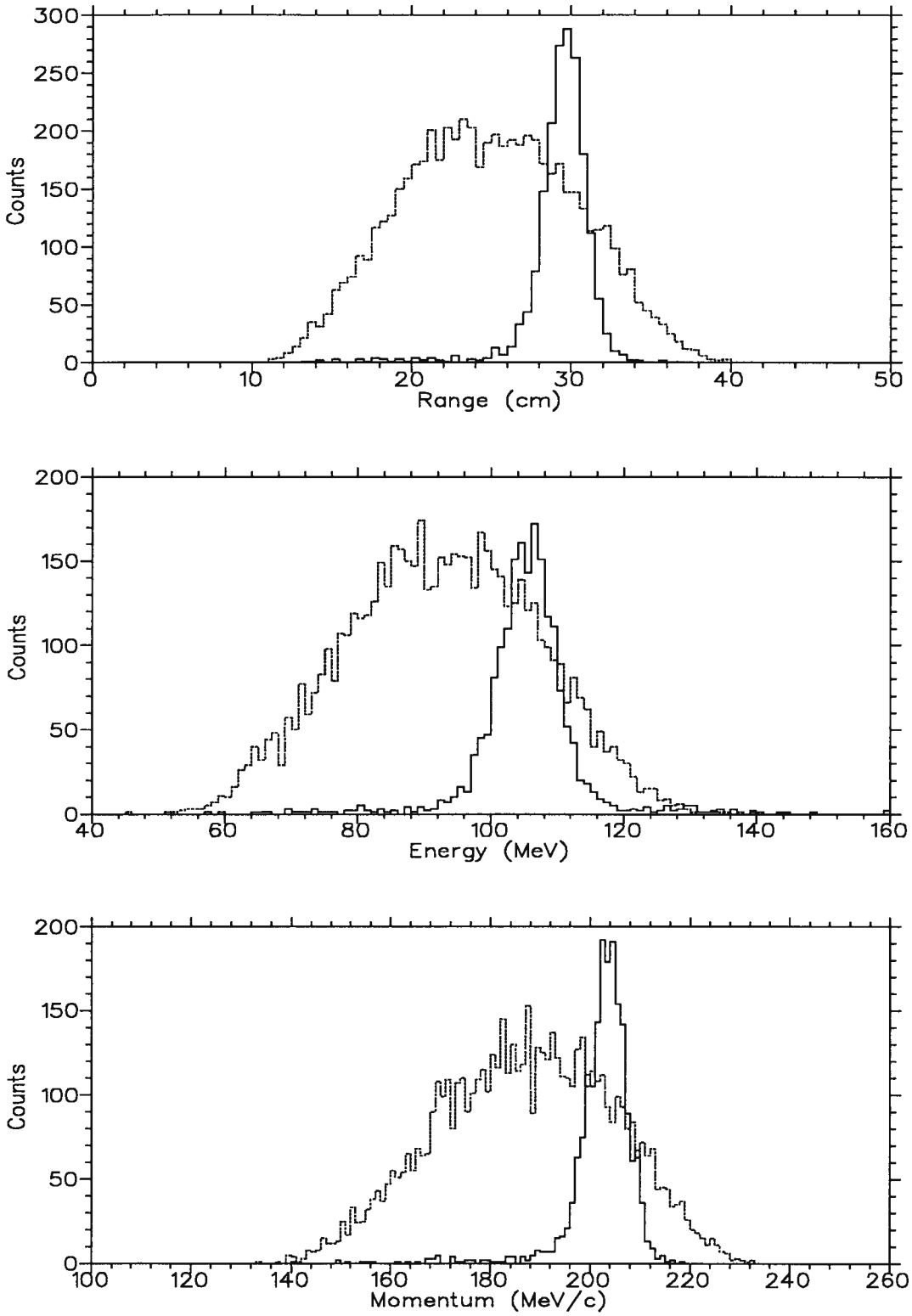

Figure 3.67: Total range, energy and momentum of the π^+ for $K_{\pi 2}$ background (solid line) and $K^+ \to \pi^+ \nu\bar{\nu}$ Monte Carlo (dashed line) events. The number of Monte Carlo events in the histograms is arbitrary.

3.3.8 Offline cuts summary

Tables 3.11 and 3.12 list all the offline analysis cuts used and a brief description for each.

3.4 First Analysis Pass

The offline event selection proceeded in several stages, or "passes". The first one (Pass1), consisted of a subset of the cuts described in the previous section. The cuts chosen had high acceptance for signal events and reduced the size of the data sample for subsequent analysis. Because the resulting sample was used in studies of the possible background sources for 1991 data, which will be described in Chapter 4, the results of Pass1 will be given here. Results of further analysis passes will be described in Chapter 5.

Several of the cuts were less stringent at Pass1 than the final versions described in section 3.3. In particular, the photon veto time windows and energy thresholds were different than for the final cut. Table 3.13 lists the photon veto parameters used at Pass1 for 1989 and 1991 data. Also, the PROMPT cut only required T^{π}_{tg} -$T^{K}_{tg} > 1.5$ ns for both 1989 and 1991 data.

Tables 3.14 and 3.15 give detailed statistics for the various cuts; for 1991 data, statistics are for approximately one third of the data sample. Note that the cuts in 1991 were more restrictive than in 1989, by about a factor of 7. In these tables, as well as all other tables describing data analysis in this thesis, the number indicated next to the entry identifying each cut represents the number of events satisfying the cut requirements. In many cases, the rejection (R) or acceptance (A) of each cut will also be indicated, as is the case here. The rejection is defined as

$$R = \frac{N_e}{N_p} \tag{3.36}$$

where N_e is the number of events examined by the cut and N_p is the number of events passing the cut requirements. The acceptance is simply the inverse of the rejection.

Table 3.11: Summary of all offline analysis cuts.

Cut	**Description**
Event reconstruction	
TARGET	K^+ and π^+ track reconstruction in target
DC-SETUP	Drift chamber track reconstruction
DC-CHI2	Drift chamber track fit chi-square
RS-TRACK	Range stack track reconstruction
RSPC	Activity in RSPC if RS stopping layer = 11
ICOUNTER	π^+ I-counter energy and range
FIDUCIAL	K^+ decay vertex along z axis, π^+ trajectory dip angle
ZDCTZ	π^+ track position along z axis at outer DC radius
Timing	
PROMPT	Time delay between K^+ and π^+ in target
TRKTIM	Consistency of π^+ track time in TG,IC and RS
Photon Veto	
INTIME	Photon veto in RS, BV (both ends) and EC, IC, VC
INTSE	Photon veto in RS, BV (single ends)
INT_EB	Photon veto in EC and BV
INT_RIV	Photon veto in RS, IC, VC
PB-GLASS	Lead-glass detector hits in coincidence with π^+
B4TD	Second pulse in B4 in coincidence with π^+ in RS
NDC	Number of DC wires hit
DISENPI	Energy in target outside of π^+ and K^+ tracks at time of π^+
DISENK	Energy in target outside of π^+ and K^+ tracks at time of K^+
Pion identification	
RGEMOM	RS range and DC momentum correlation
MASS	RS range and energy correlation
KINSCORE	RS range, RS energy and DC momentum correlation
DEDXRS	Energy deposition pattern in RS
FASFITPI	Single pulse hypothesis TD fit ($\pi \to \mu$ search)
FITPI	Comparison of single and double pulse hypothesis TD fit
TD_MDA	Multiple discriminant analysis of TD fit results
ELVETO	Veto in RS at $\pi \to \mu$ time
TDFOOL	TD double pulse fit in RS layer previous to stop
ELECTRON	Search for positron from $\pi \to \mu \to e$ decay chain
Beam cuts	
CERENKOV	Pion Čerenkov counter veto
BWPC	Beam wire chamber veto at time of π^+ in RS
BM_HOLE	Beam hole counter veto
B4_CNTR	Energy deposition in B4 hodoscope

Table 3.12: Summary of all offline analysis cuts (continued).

Cut	Description
Vertex cuts	
TGTRACK	Refined track reconstruction in target
NK	Total number of target elements struck by K^+
TGFIT	Double pulse fit of target TD information
VTX_PCA	Correlation of TG K^+ energy, TG K^+ range and B4 energy
ZK_EK	Correlation of target K^+ range and energy
EB4_EK	Correlation of B4 energy and K^+ target energy
Kinematic search region	
KINCUT	Total range, energy and momentum cut

Table 3.13: Parameters for Pass1 photon veto cuts. The time column refers to the coincidence time window.

Subsystem	1989		1991	
	Time (ns)	Threshold (MeV)	Time (ns)	Threshold (MeV)
RS	[-4.3,3.7]	1.0	[-1.0,1.0]	2.0
BV	[-5.2,4.8]	1.0	[-3.0,3.0]	2.0
EC	[-4.9,5.1]	1.0	[-2.0,2.0]	5.0
IC	[-4.75,3.25]	1.0	—	—
VC	[-6.4,5.6]	1.0	—	—

Table 3.14: 1989 Pass1 results. The number of events showed next to each cut is the number satisfying the cut requirements.

Cut	# events	Rejection
	1382868	
TARGET	1270154	1.08874 ± 0.00028
PROMPT	780919	1.6265 ± 0.0011
DISENPI	649167	1.20296 ± 0.00061
INT_EB	324314	2.0017 ± 0.0025
DC-SETUP	176448	1.8380 ± 0.0030
RS-TRACK	160763	1.09756 ± 0.00082
INT_RIV	87215	1.8433 ± 0.0042
FASFITPI	34901	2.499 ± 0.010
FITPI	15911	2.194 ± 0.013
ELVETO	12554	1.2674 ± 0.0052
Total		110.15 ± 0.98

Table 3.15: 1991 Pass1 results for one third of the data sample.

Cut	**# events**	**Rejection**
	2062081	
TARGET	1988477	1.0370 ± 0.0001
PROMPT	1363512	1.4583 ± 0.0007
DC-SETUP	834914	1.633 ± 0.001
RS-TRACK	802423	1.0405 ± 0.0002
TRKTIM	800332	1.00261 ± 0.00006
INTIME	460984	1.736 ± 0.002
FASFITPI	362892	1.270 ± 0.001
FITPI	131113	2.768 ± 0.006
Total		15.73 ± 0.04

Chapter 4

Background Studies

The most difficult task in the search for $K^+ \rightarrow \pi^+\nu\overline{\nu}$ is the rejection of the large number of background processes that can mimic it. In the search for rare processes, the possibility always exists that a signal could be observed, regardless of the theoretical predictions. To have confidence in the final result, the expected contributions from background processes have to be determined. Since it is expected in the case of this experiment that background contributions will be relatively small, the estimation of the expected levels of background is likely to require an extrapolation beyond the sensitivity to the process $K^+ \rightarrow \pi^+\nu\overline{\nu}$. This can make the reliability of the estimates difficult to ascertain.

Background levels can be estimated in two ways : using Monte Carlo simulations and using real data. The former involves lengthy simulations which can necessitate days or weeks of computer usage. This can limit the usefulness of this method, although the introduction in the last few years of inexpensive and powerful computer workstations somewhat mitigated this problem. A more important limitation of the Monte Carlo method is the reliability of the simulation of the various physical processes involved. For $K^+ \rightarrow \pi^+\nu\overline{\nu}$ background processes, uncertainties in nuclear and photo-nuclear total and differential cross-sections can lead to large uncertainties when extrapolating to sensitivities of the order of $10^{-8} - 10^{-9}$. Nevertheless, in some cases this method is the only one available.

For these reasons, real data was used whenever possible to determine background levels. This has the advantage that any instrumental effect not properly reproduced in a Monte Carlo simulation is taken into account. Both the $\pi\nu\overline{\nu}$ and monitor data samples are suitable for such

studies, although the $\pi\nu\overline{\nu}$ data sample is generally preferable since it is the one with the largest intrinsic sensitivity to all background processes. To study a particular background, cuts can be applied to a data sample to select a sub-sample dominated by this background. Other cuts can then be designed and their effectiveness studied.

A useful way to select a background data sample is to invert one of the cuts designed to reject it, i.e. select the events which fail the cut. This has the advantage that none of the events used in the background study could be a candidate event, and is of great importance in eliminating potential bias in the search for a $K^+ \to \pi^+\nu\overline{\nu}$ signal. Assuming that the rejection of the inverted cut is independent of the others, the expected number of background events from the source studied is then :

$$N_{\rm bgd} = N_K^{\rm tot} \times \frac{N_{\rm evt}}{N_K} \times \frac{1}{\epsilon} \times \frac{1}{R} \tag{4.37}$$

where $N_K^{\rm tot}$ and N_K are the number of kaons (or some other suitable normalization) in the $\pi\nu\overline{\nu}$ data sample and in the background study sample, respectively, $N_{\rm evt}$ is the number of events remaining after all cuts are applied to the sample selected by inverting a cut, ϵ is the efficiency of the inverted cut to select the background events and R is the rejection of the inverted cut. The last two quantities have to be determined with an independent data sample.

Equation 4.37 is quite general. In practice, the data sample used to study the background is often the $\pi\nu\overline{\nu}$ sample; in this case, $N_K^{\rm tot}$ and N_K are equal. Also, the selection criteria of the inverted cut are often the same as the ones used in the final analysis. In this case the efficiency of selecting background events (ϵ) is simply related to the rejection of the cut :

$$\epsilon = 1 - \frac{1}{R} = \frac{R-1}{R} \,. \tag{4.38}$$

Taking both of these cases into consideration, we can rewrite equation 4.37 as

$$N_{\rm bgd} = \frac{N_{\rm evt}}{R-1} \,. \tag{4.39}$$

Finally, in some cases some of the cuts applied to the sample selected by inverting a cut are known to be independent of each other. Their rejection can be determined separately and then

factored out in order to increase the statistical power of the procedure. We would then have

$$N_{\mathrm{bgd}} = \frac{N'_{\mathrm{evt}}}{R-1} \times \prod_{i=1}^{n} \frac{1}{R_i} \tag{4.40}$$

where R_i is the rejection of the ith of n cuts factored out of the analysis, and N'_{evt} is the number of events left after applying all cuts to the sample selected by inverting a cut, except the cuts whose rejection is factored out in the expression. By factoring out several cuts with large rejection, it becomes possible to reach levels of background sensitivity that would not otherwise be attainable.

The success of this method depends on two points :

1. the rejection of the inverted cut and the others designed to reject the background of interest are independent.

2. the rejection of the inverted cut can be reliably estimated by using another data sample.

To demonstrate this, consider the following simple example, in which a single background source is present, there are no signal events and we have three cuts (or groups of cuts) designated A, B, and C. Figure 4.68 illustrates this situation; there is a total of N_{tot} events, the number of events which pass all cuts is N_0 and the terms N_i in each region represent the number of events rejected by cut i. We now wish to estimate the number of background events, $\tilde{N}_0$, before we perform the final analysis which will result in N_0 events. We can select a sample of background events by inverting cut A, and then apply cuts B and C which results in N_A events. Following the method described above, we have

$$\tilde{N}_0 = \frac{N_A}{\tilde{R}_A - 1} \tag{4.41}$$

where $\tilde{R}_A$ is an estimate of the rejection of cut A. For this, we can select a different sample by inverting cut B and then apply cut A. We then have

$$\tilde{R}_A = \frac{N_{ABC} + N_{AB} + N_{BC} + N_B}{N_{BC} + N_B} \,. \tag{4.42}$$

Substituting this back in equation 4.41, we get

$$\tilde{N}_0 = N_A \times \frac{N_{BC} + N_B}{N_{ABC} + N_{AB}} \,. \tag{4.43}$$

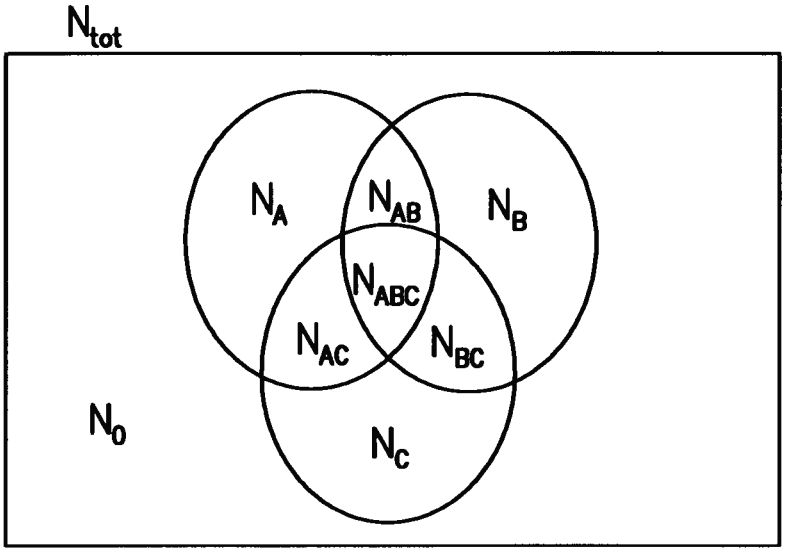

Figure 4.68: Example of background estimation. See text for explanations.

We see from this that to validate the method, we need

$$\frac{N_{BC} + N_B}{N_{ABC} + N_{AB}} \simeq \frac{N_0}{N_A} \tag{4.44}$$

which expresses the fact that the fraction of events accepted over rejected by cut A is independent of the sample chosen, which means that the rejection of cut A has to be independent of the other cuts.

A variation of this generic method makes use of the fact that $K^+ \to \pi^+\nu\overline{\nu}$ events are searched for in a specific region of phase space. Events falling outside of this region can be examined extensively without introducing bias for the events inside the search region. A cut can be inverted to enhance a particular background source as described above, but here the ratio of events seen inside and outside of the search region is exploited. The assumption is made that the ratio of the number of events outside of the search region to the number inside is the same for the sample selected by inverting a cut as for the data remaining after all cuts. This is expressed as

$$\frac{N_{\rm out}^{\rm inv}}{N_{\rm in}^{\rm inv}} \simeq \frac{N_{\rm out}}{N_{\rm in}} \tag{4.45}$$

where the subscripts "in" and "out" refer to the number of events inside and outside of the search region respectively, and the superscript "inv" refers to the events selected by inverting

a cut. The factor $N_{\rm out}$ can be obtained by applying all cuts to the events outside of the search region. The estimate for the number of background events can then be calculated :

$$N_{\rm bgd} = N_{\rm in} = N_{\rm out} \times \frac{N_{\rm in}^{\rm inv}}{N_{\rm out}^{\rm inv}} \,. \tag{4.46}$$

Equation 4.45 can be rearranged to give

$$\frac{N_{\rm in}}{N_{\rm in}^{\rm inv}} \simeq \frac{N_{\rm out}}{N_{\rm out}^{\rm inv}} \tag{4.47}$$

which simply expresses the fact that the rejection of the cut used to select the background must be the same for the events inside and outside of the search region. The categorization of the events in two kinematic regions is effectively a cut; what is expressed above is equivalent to saying that the rejection of the two cuts considered must be independent. A correlation between the two can significantly affect the result obtained in the background estimation.

The following sections describe in detail the studies of the various background sources for the search for $K^+ \to \pi^+\nu\overline{\nu}$, performed using the methods just described. For 1989 data, the studies were not very extensive and were performed after the final analysis was completed. This is because the analysis method used (see section 3.3) did not require *a priori* background studies. The background was studied as the analysis cuts were prepared and the overall level was estimated afterwards. It was subsequently realized that this method could lead to bias in the final result. Therefore, for 1991 data detailed estimates for each possible background source were made before the final analysis was performed.

4.1 1989 Background studies

4.1.1 $K^+ \to \pi^+\pi^0$

This decay is the primary source of background for this search. For $K_{\pi 2}$ decays to be mistaken for $K^+ \to \pi^+\nu\overline{\nu}$ decays, the photons from π^0 decays have to be missed (or one photon and an e^+e^- pair from π^0 Dalitz decays). The π^0 rejection inefficiency of the detector for π^0 's from $K_{\pi 2}$ decays has been measured to be $\approx 1 \times 10^{-6}$ [60]. We can therefore expect some $K_{\pi 2}$ events to remain in the data sample after applying all the photon veto cuts. The kinematic search

region for $K^+ \to \pi^+\nu\bar{\nu}$ was chosen such that most of the remaining $K_{\pi 2}$ events are rejected (see section 3.3.7). The background comes from the low energy tail of the π^+ distribution. One component of the tail comes from resolution effects and measurement errors. In this case, all three kinematic quantities have to be mis-measured in a correlated way since a cut is applied on the consistency of the three quantities with a π^+ hypothesis. The other more serious component to the low energy tail comes from π^+ nuclear interactions. The interaction can occur either in the target, I-counters or in the range stack. The latter case is not as serious since the momentum measurement is not affected. However, if the interaction occurs in the target close to the K^+ decay vertex, the energy loss will have occured before the π^+ kinematic quantities are measured. The rejection of $K_{\pi 2}$ background therefore relies heavily on the ability to detect π^+ nuclear interactions in the target.

One other possibility is decay in flight of the pion, with the resulting μ^+ from $\pi^+ \to \mu^+\nu_\mu$ continuing more or less in the direction of the initial π^+ . The time of flight in the detector of a π^+ from $K_{\pi 2}$ decay is only a few nanoseconds, compared to its mean life of $\tau_{\pi^+} = 26$ ns. A simple Monte Carlo simulation showed that of those $K_{\pi 2}$ decays which satisfied the track reconstruction requirements, only about 2% had decayed in flight. Because the kinetic energy available for the final state particles in this π^+ decay is so small, and the direction of the μ^+ is essentially the same as the initial π^+ to satisfy the track reconstruction requirements, the energy of the charged particle track is most of the time about equal to that expected from $K_{\pi 2}$ decay. Also, an accidental hit in the stopping counter is required to satisfy the $\pi^+ \to \mu^+ \to e^+$ decay chain requirement. A more complete Monte Carlo simulation showed that the decay in flight background is at least a factor of 50 less than the case where the π^+ undergoes a nuclear interaction. Therefore, this contribution to $K_{\pi 2}$ background was considered negligible.

In plastic scintillator, the π^+ can interact either with a hydrogen (single proton) or a carbon nucleus. In the energy regime of this experiment, $\pi^+ - p$ interactions are entirely elastic, with a maximum energy loss for the π^+ of about 58 MeV; the cross section is approximately 70 mb at 108 MeV. Interactions with carbon nuclei are more complex, since several inelastic channels are open [61]. The total $\pi^+ - {}^{12}C$ interaction cross section of nearly 600 mb at 108 MeV can be

divided into three parts : elastic, inelastic and absorption, with each part contributing about one third of the cross section [62]. The absorption part includes "true" absorption and also charge exchange ($\pi^+ \, ^{12}C \rightarrow \pi^0 p \, ^{11}C$), which contributes about 20% of the absorption cross section. Since there is no π^+ in the final state for absorption, it does not contribute to this background unless the interaction is in the range stack, in which case two accidental pulses must be present in the stopping counter to fake the π^+ decay chain. The maximum energy loss in an elastic collision with a carbon nucleus is about 7 MeV, implying that the contribution to the low energy tail of the $K_{\pi 2}$ peak from π^+ –C elastic collisions is small.

In inelastic collisions, the simplest interaction is the case where the carbon nucleus is left in an excited state and returns to ground state via gamma or alpha emission. If gamma emission occurs, the probability of detecting the interaction increases substantially. Typical excitation energies are 4.4 MeV, 7.7 MeV, 9.6 MeV and 12.7 MeV, but many higher energy states also exist [63]. The energy levels with the largest share of the cross section are the 4.4 MeV and 9.6 MeV levels [61]. The first one decays exclusively by gamma emission, while the second decays almost exclusively via alpha emission. In the case of alpha emission, the ^8Be residual nucleus decays to two alpha particles with a half-life of about 0.07 fs. The rest mass of ^8Be is only about 90 keV higher than the summed rest mass of two alpha particles, resulting in very little kinetic energy for the decay products. Therefore, the probability of detecting this interaction in the target is very small.

If the energy transferred to the carbon nucleus by the π^+ is sufficiently large, it becomes possible to knock out a nucleon from the nucleus, leaving either a ^{11}B or ^{11}C nucleus, possibly in an excited state. The thresholds are 16.1 and 18.7 MeV for proton and neutron emission respectively. If the emitted nucleon is a proton, the probability of detecting the interaction increases significantly, but strongly depends on the energy and direction of the emitted proton. Neutrons knocked out or emitted through evaporation of an excited nucleus can also be detected if they collide with protons in scintillator, as long as the interaction occurs within the coincidence time window of the INTIME or INTSE cuts; this will not necessarily be the case since some of the neutrons will be emitted at very low energy and therefore will move slowly through the

detector.

Since the two important effects in $K_{\pi 2}$ background are photon and nuclear interaction detection, they are obvious choices for cuts used in selecting data samples to be used in a background study, especially since naively the two types of cuts should be independent. In reality, the correlation between the two is quite large. This is related to the non-uniformity of the photon veto coverage of the detector and is illustrated in figure 4.69. In this figure, the π^+ from $K_{\pi 2}$ decay initially travels in the direction of the beam axis and scatters in the target towards the range stack through a nuclear interaction, satisfying all the particle tracking requirements of the analysis. The energy deposited by the π^+ before it scatters towards the range stack overlaps with the energy deposition of the incident K^+ , making its detection difficult. The π^0 is emitted back-to-back with the π^+ and promptly decays to two photons. The most likely angle for the decay photons is along the direction of the π^0 , which in this case points back to the beam hole, the region with the least number of radiation lengths in the detector. For $K_{\pi 2}$ decays in which the π^+ does not scatter in the target, the photons tend to be emitted in the direction of the barrel veto, where coverage is maximal. As can be seen, this effect will strongly correlate nuclear interactions and photon detection. This was the primary reason for the installation of the lead-glass detector in 1991.

The $K_{\pi 2}$ background contribution was estimated by making use of the ratio of events inside and outside of the $K^+ \to \pi^+ \nu \overline{\nu}$ kinematic search region. This method is the second background estimation technique described in the introduction to this chapter. In what follows, since they are dominated by the $K_{\pi 2}$ peak, the events outside of the $K^+ \to \pi^+ \nu \overline{\nu}$ kinematic search region will be referred to as "peak" events; the events inside will be referred to as "tail" events. The ratio of the two numbers will be designated by η:

$$\eta = \frac{\#\text{Peak events}}{\#\text{Tail events}} \,. \tag{4.48}$$

To measure η, use was made of a monitor data sample collected using special trigger conditions. The EC and BV veto requirements were removed from the $\pi\nu\overline{\nu}$ Level 0 trigger, and all other trigger requirements the same as for $\pi\nu\overline{\nu}$; this considerably enhanced the number of $K_{\pi 2}$ decays recorded. A total of 15523 events were available for further analysis. All offline cuts

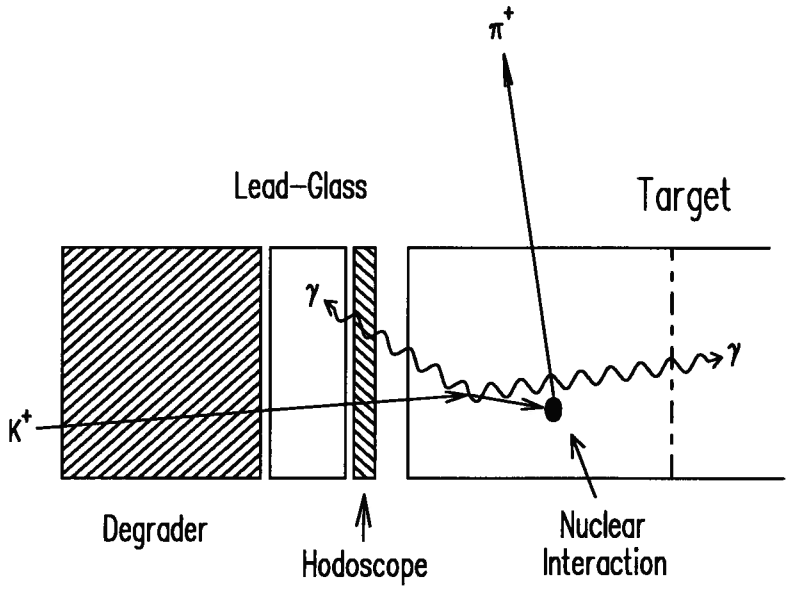

Figure 4.69: Correlation between nuclear interactions and photon veto in $K_{\pi 2}$ background.

except direct photon veto cuts and the final kinematic cut were applied to this data sample; a total of 2451 events survived all cuts, of which 14 were in the $K^+ \to \pi^+\nu\overline{\nu}$ search region. This resulted in

$$\eta = \frac{2437}{14} = 174 \pm 47 \tag{4.49}$$

where the error is statistical. As will be described in section 5.1.1.2, application of all cuts to the events outside of the $K^+ \to \pi^+\nu\overline{\nu}$ search region resulted in 49 events. Assuming that the ratio η remains the same after application of photon veto cuts, we can estimate the $K_{\pi 2}$ background contribution :

$$N_{\rm bgd} = \frac{49 \pm 7}{174 \pm 47} = 0.282 \pm 0.086\,. \tag{4.50}$$

However, we just saw that we can expect a correlation between the photon veto cuts and the final kinematic cut, namely that the photon veto cuts are not expected to be as effective for the tail events as they are for the peak events. Therefore, this estimate is not expected to be correct.

To estimate the effect of this correlation, a Monte Carlo simulation was used (see appendix C). First, the angular and energy dependence of the inefficiency of the photon veto

system was determined by simulating a large number of photons with a uniform distribution in energy (0–250 MeV) and direction ($-1.0 \leq \cos\theta_\gamma \leq 1.0$), where $\cos\theta_\gamma$ is the z-axis directional cosine of the photon. The distribution was also uniform in the xy plane. The point of origin of these photons was in the target and chosen according to the distribution of K^+ stopping positions determined experimentally. A simulated photon was considered to be missed if less than 1.0 MeV of energy was deposited in the active regions of the detector.

Using this information as a lookup table, the detection inefficiency for neutral pions with a total energy of 245 MeV, as in $K_{\pi 2}$ decays, was determined. Again, the angular distribution was uniform and the point of origin of the π^0 in the target was chosen according to the real K^+ stopping distribution. The π^0 was allowed to decay and based on the direction and energy of the two decay photons the probability of not detecting the π^0 was calculated. Table 4.16 gives the inefficiency for different parts of the angular distribution. Because in $K_{\pi 2}$ decays the π^0 is emitted back-to-back with the π^+ , the range $-0.5 \leq \cos\theta_{\pi^0} \leq 0.5$ corresponds to the fiducial region accepted by the $\pi\nu\bar{\nu}$ trigger. Note the large differences observed between the different angular ranges, which simply reflects the non-uniformity of the photon detection system.

Table 4.16: π^0 detection inefficiency. The angle θ_{π^0} is the angle between the π^0 direction and the z-axis.

Angular range	**Inefficiency**
$-1.0 \leq \cos\theta_{\pi^0} \leq -0.9$	55×10^{-5}
$-0.5 \leq \cos\theta_{\pi^0} \leq 0.5$	1.5×10^{-5}
$0.9 \leq \cos\theta_{\pi^0} \leq 1.0$	41×10^{-5}
$-1.0 \leq \cos\theta_{\pi^0} \leq 1.0$	6.9×10^{-5}

The final step was the simulation of $K_{\pi 2}$ decays satisfying the $\pi\nu\bar{\nu}$ trigger requirements. As for the real data sample described above, the online photon veto requirements were not included, but the rest of the Level 0 and Level 1 $\pi\nu\bar{\nu}$ trigger requirements were simulated. The simulation included nuclear interactions and decay of the π^+ , but the π^0 was not allowed to decay to save computer time. All offline analysis cuts that could be applied to the simulated

events were applied. At this stage, the ratio of events in the $K_{\pi 2}$ peak region to the events in the tail region was consistent with what was observed in real data. The π^0 angular distribution for the remaining events in the peak region was almost entirely in the $-0.5 \leq \cos\theta_{\pi^0} \leq 0.5$ range, as could be expected. For the events in the tail, the distribution was more or less flat in $\cos\theta_{\pi^0}$. All of the tail events had undergone a nuclear interaction in the target, indicating the strong correlation expected. Using the information obtained on the π^0 detection inefficiency to weight the $K_{\pi 2}$ simulated events remaining after all cuts, the effect of the correlation was determined. The correlation factor measured was 3.7 ± 0.5, where the error is statistical only.

If we correct the estimate for the number of $K_{\pi 2}$ background events expected for this correlation factor, we get

$$N_{\rm bgd} = (0.282 \pm 0.086) \times (3.7 \pm 0.5) = 1.04 \pm 0.35 \,. \tag{4.51}$$

The study of the simulated $K_{\pi 2}$ events remaining after all cuts and located in the $K^+ \to \pi^+\nu\overline{\nu}$ kinematic search region indicated that additional rejection could be expected for this background from the BM_HOLE and EB4_EK cuts. These were not included in this study because the B4 hodoscope and the beam hole counters are not simulated properly by the Monte Carlo program. However, it was clear that additional rejection could be expected from those cuts. Therefore, it was concluded that the number of $K_{\pi 2}$ background events was less than one.

4.1.2 Muons

The muon background involves two different kaon decay modes : $K^+ \to \mu^+\nu_\mu\gamma$ ($K_{\mu\nu\gamma}$) and $K^+ \to \pi^0\mu^+\nu_\mu$ ($K_{\mu 3}$). These are the only two direct sources of muon background in the kinematic region considered in this search. Another possible source would be $K_{\mu 2}$ decays. However, a muon from such a decay would have to suffer an undetected energy loss of at least 50 MeV in order to be a background; the probability for such an occurrence is extremely remote. This study also includes a portion of the pion decay in flight background, which was briefly discussed in section 4.1.1.

For $K_{\mu\nu\gamma}$ and $K_{\mu 3}$ decays to be backgrounds to $K^+ \to \pi^+\nu\overline{\nu}$, the μ^+ has to be misidentified as a π^+ and photons have to escape detection. Therefore, there are three groups of independent cuts that can be used to select and study muon background : particle identification cuts, which include kinematic and TD cuts, and photon veto cuts. This study used the first two groups.

The first step in the study was to apply all cuts except TD and kinematic cuts to the Pass1 data sample. Only 22 events remained after application of those cuts. One reason for such low statistics is that at Pass1 FASFITPI, FITPI (without tighter constraints on ΔT_μ , $P_{\mu\pi}$ and $\overline{T_\mu}$) and ELVETO were applied, which reduced muon background contamination considerably. The sample of 22 events should contain mostly muon background events. Table 4.17 shows the effect of the remaining cuts on this sample. The first observation from this table is that the TD cuts appear to be far more effective than the kinematic cuts. Examination of the remaining events shows that for all three events satisfying the TD cuts the π^+ stopped in RS layer C, while for 9 of the 11 events satisfying the kinematic cuts the π^+ stopped in layer B. The distribution of particle mass for the latter shows that most of them are more likely to be pions than muons. One explanation is that they are pions which underwent a nuclear interaction in the range stack. The requirement by the TD cuts for a complete $\pi^+ \to \mu^+ \to e^+$ decay chain is very effective against such events. Therefore, the rejection of the kinematic cuts was determined using only events with a π^+ stop in RS layer C, resulting in $R_{\rm kin} = 3.5 \pm 2.1$.

Table 4.17: Effect of kinematic and TD cuts on 1989 muon background. At this stage the FITPI cut did not include a cut on $\overline{T_\mu}$.

Kinematic cuts	**# events**
	22
RGEMOM	14
DEDXRS	12
MASS	11
TD cuts	**# events**
	22
FITPI	9
ELECTRON	3

For the FITPI cut applied in table 4.17 there were no specific requirements on $\overline{T_\mu}$, the

average of the time delay between the first and second pulse in the stopping range stack layer (see section 3.3.4.5). The decision to apply the requirement $9 < \overline{T_\mu} < 60$ ns was based on examination of a different sample of muon background. In this case, cuts on the range–momentum correlation and the mass of the charged particle were used to select muons in the Pass1 data sample. Beyond Pass1, only the RSPC, TGTRACK and KINCUT cuts were applied to this sample in order to increase the number of events available. Despite this precaution, only 7 events remained after application of the TD cuts used in table 4.17. However, the muon background was concentrated at early and late $\overline{T_\mu}$ values. The cut on $\overline{T_\mu}$ provided an estimated additional rejection of $R_{\overline{T_\mu}} = 3.5 \pm 2.1$.

The estimate for the number of muon background events was based on the three events remaining after TD cuts in table 4.17 and the estimates for $R_{\rm kin}$ and $R_{\overline{T_\mu}}$:

$$N_{\rm bgd} = (3.0 \pm 1.7) \times \frac{1}{(3.5 \pm 2.1)} \times \frac{1}{(3.5 \pm 2.1)} = 0.24 \pm 0.24 \qquad (4.52)$$

where the error is statistical only. Obviously this estimate suffers from low statistics. However, the very fact that so few muon background events could be extracted from the $\pi\nu\overline{\nu}$ data sample was an indication that the contribution from muon background was not very large. Because of possible contamination by pion background, the estimate was probably conservative and therefore judged acceptable.

4.1.3 Beam pions

The large π^+ content of the particle beam used for this experiment can be a source of background when a π^+ scatters inelastically in the target. The trigger requirements that an incoming K^+ be identified and that there be a delay between the incoming and outgoing particles in the target significantly reduced the contribution from this source. Nevertheless, it was necessary to design additional offline constraints to further reduce this potential background. The main assumption made in this study was that a potential background event occured only if the beam π^+ scattered in the active target and was the particle of choice in the drift chamber and range stack. Cases for example of a π^+ emerging from the degrader and stopping in the range stack without hitting the target were assumed to be negligible after all analysis cuts are applied.

Beam pions come from three sources : primary production by proton–Pt target collisions, decay in flight of a kaon, and nuclear interaction of a kaon, primarily in the degrader. There is also the possibility of protons in the secondary beam line interacting in the degrader and producing pions. However, a proton with a momentum of 800 MeV/c is just about at threshold for π^+ production, and therefore this contribution can be neglected. The particle identification capability of the Čerenkov counter allowed the classification of the beam pion background into two groups :

A) Two particle background. This group can be divided in two subgroups :

   1. A K^+ and a π^+ crossed the Čerenkov counter.
   2. Two K^+ crossed the Čerenkov counter. One of the two decayed or interacted resulting in a π^+ .

B) Single particle background. In this case, a single K^+ crossed the Čerenkov counter and decayed or interacted resulting in a π^+ track which scattered in the target.

In each case the trigger conditions can be satisfied; in case B, a fluctuation due to finite time resolution is required for the event to pass the delayed coincidence requirement. The beam pion background study performed for 1989 data only considered case A-1; the other cases were considered to be negligible. A sample of $\pi\nu\overline{\nu}$ events which satisfied the Pass1 requirements, failed the CERENKOV cut and were located in the $K^+ \rightarrow \pi^+\nu\overline{\nu}$ kinematic search region were selected. This sample of 3005 events was dominated by beam pion background. All other cuts were then applied to these events; the analysis ran out of events before all cuts could be applied. Full results of this analysis are given in table B.65.

To estimate the beam pion background contribution, the rejection of the CERENKOV cut had to be measured. A sample of beam pion background was selected out of the $\pi\nu\overline{\nu}$ data by requiring that two particles be identified in the beam wire chamber and that the energy deposition in the B4 counter be consistent with a single π^+ . Using this sample, the rejection of the CERENKOV cut was determined to be $R_{\check{C}} = 11.6 \pm 1.3$.

Because no events remained after analysis of the sample of events which failed the CERENKOV cut, an upper limit on the number of background events was set. From Poisson statistics, if the observed number of events is 0, the 90% confidence level upper limit on the mean number of events is 2.3. Therefore,

$$\begin{aligned} N_{\rm bgd} &< \frac{2.3}{R_{\check{C}} - 1} \\ &< \frac{2.3}{10.6} \\ &< 0.22 \ (90\% \text{ C.L.}). \end{aligned} \tag{4.53}$$

4.1.4 $K^+ \to \pi^+\pi^-e^+\nu_e$ (K_{e4})

The decay K_{e4} , a four body decay with three charged tracks and with a branching ratio of 3.9×10^{-5}, may appear at first to be rather benign as a background to $K^+ \to \pi^+\nu\overline{\nu}$. However, it is kinematically possible for both the π^- and the e^+ to be emitted with a very small amount of energy. Both of them can conceivably hide in the active target in the region where the K^+ stopped; in particular, a low energy π^- coming to rest in plastic scintillator will be captured with almost 100% probability by a carbon nucleus. The end point of the kinematic spectrum for π^+ from K_{e4} is 203 MeV/c, just below the $K_{\pi 2}$ peak, resulting in a large kinematic acceptance for the π^+ by this search.

A slightly different scenario for this background is the case where the π^- is absorbed in the target in flight, instead of coming to rest and be captured by a carbon nucleus. The true absorption cross section for π^- on ^{12}C is $\sim$ 100 mb for a π^- momentum of 170 MeV/c. For K_{e4} decays in which the π^+ momentum is in the $\pi\nu\overline{\nu}$ search region, the momentum of the π^- is almost always below 170 MeV/c, peaking around 80 MeV/c. To go undetected, the interaction should take place within a short distance from the decay vertex, say 2 cm. The probability of π^- absorption in plastic scintillator at 170 MeV/c within 2 cm is about 1%. Therefore, the portion of K_{e4} background in which the π^- was absorbed in flight is quite small compared to the case where the π^- interacts at rest, and can be neglected. Note that at 80 MeV/c, a charged pion has a range of about 2 cm in plastic scintillator.

The signature of K_{e4} decays as a potential background to $K^+ \to \pi^+\nu\bar{\nu}$ is essentially identical to $K_{\pi 2}$ decays in which the π^+ undergoes a nuclear interaction in the target and the photons from the π^0 decay were not detected. Energy deposited in the K^+ target elements by K_{e4} charged decay products other than the π^+ must be identified. Techniques to do this were developed for $K_{\pi 2}$ background. What is needed here is to determine how often K_{e4} decays have this decay pattern in the target. Note that for most K_{e4} decays, multiple tracks will be identifiable in the target and cuts such as TGTRACK will reject these events very effectively.

To select a sample of K_{e4} background events, all cuts were applied to Pass2 data (see section 5.1.1.1) with the exception of TGTRACK and ZK_EK. A total of 51 events were left. Inspection of these events indicated that many were likely to be K_{e4} decays, although it was not possible to clearly distinguish K_{e4} background from $K_{\pi 2}$ events with a π^+ undergoing a nuclear interaction in the target. The assumption was made that most of the events in the sample were K_{e4} decays. The remaining task was to determine the rejection of the two cuts not applied to the sample. To determine the rejection of the TGTRACK cut, a large number of K_{e4} decays were simulated with a Monte Carlo program. The matrix element used to weigh the kinematics of K_{e4} decay in the simulation was as described in references [67] and [68]. A complete simulation of π^- interactions in scintillator was not available; therefore, only the ionization energy loss was taken into account for the π^- . Cuts simulating the ones applied to the real data were applied to the simulated events. A total of 670 events remained before application of TGTRACK. All but three events were rejected by the cut, resulting in a rejection of $R_{\mathrm{TGTRACK}} = 223 \pm 129$.

After application of TGTRACK on the simulated events, the ones remaining had a very low energy π^- stopping in the target. The ZK_EK cut should be reasonably efficient at detecting the energy released by the capture of a π^- at rest in the target. But since π^- nuclear interactions were not simulated by the Monte Carlo program, another method was needed to determine the rejection of ZK_EK. Based on studies of π^- interactions in carbon described in the literature [69, 70], the rejection was estimated to be $R_{\mathrm{ZK\_EK}} = 2.0 \pm 0.5$. More detailed studies of π^- interactions performed for 1991 background estimates confirmed that this number

was appropriate.

The estimate for the number of K_{e4} background events was then calculated to be

$$\begin{aligned} N_{\rm bgd} &= \frac{51 \pm 7.1}{R_{\rm TGTRACK}\, R_{ZK\_EK}} \\ &= \frac{51 \pm 7.1}{(223 \pm 129)(2.0 \pm 0.5)} \\ &= 0.114 \pm 0.074 \end{aligned} \tag{4.54}$$

where the error is statistical only.

4.1.5 1989 Background summary

Table 4.18 summarizes the estimates for the background sources studied. Errors given are statistical only; systematic errors on these numbers were not very well known, particularly for $K_{\pi 2}$ background. Based on these results, it was estimated that the sum of all contributions was one event or less. Other potential background sources discussed in section 1.3.1 and not studied here were considered negligible.

Table 4.18: Summary of 1989 background estimates.

Background	Estimate (# events)
$K^+ \to \pi^+\pi^0$ ($K_{\pi 2}$)	< 1.0
Muons ($K_{\mu 3}$, $K_{\mu 2\gamma}$)	0.25 ± 0.25
Beam pions	< 0.22 (90% C.L.)
$K^+ \to \pi^+\pi^- e^+\nu_e$ (K_{e4})	0.114 ± 0.074

4.2 1991 Background studies

4.2.1 $K^+ \to \pi^+\pi^0$

Two different methods were developed to estimate the $K_{\pi 2}$ background contribution in 1991 data. Each used the $\pi\nu\overline{\nu}$ data sample, but systematic effects were very different for the two methods. No Monte Carlo simulations were used.

4.2.1.1 Method 1

This method is essentially the same as the one used for 1989 data. First, the ratio of $K_{\pi 2}$ events found outside of the $K^+ \to \pi^+ \nu\bar{\nu}$ kinematic search region to the number inside (η) was determined. The background sample was selected by inverting the photon veto cuts applied after Pass1; all other cuts were then studied, particularly cuts which reject nuclear interactions in the target, and η was measured. In a separate analysis, all cuts were applied to the peak events from the entire $\pi\nu\bar{\nu}$ data sample. From the number of remaining events, and assuming the measured value of η applies to the case where all cuts are used, the number of $K_{\pi 2}$ background events inside the kinematic search region could be estimated.

The data sample selection started with the Pass1 data sample. Note that this means that the INTIME cut was partially applied. All cuts were applied except the cuts specifically designed to reject interactions in the target, namely TGTRACK, TGFIT, VTX_PCA, PB-GLASS and B4TD, KINCUT and the photon veto cuts (INTIME and INTSE). The latter were inverted, i.e. all events which failed either of these two cuts were selected. Inverting the photon veto cuts after the Pass1 cuts were applied resulted in a sample of events for which only a small amount of energy was visible outside of the π^+ track, which is very close to the full analysis without actually performing it. A total of 27512 events were selected; full details are given in table B.66. Table 4.19 shows the effect of the remaining cuts on this sample, separated in peak and tail events, as well as the value of η at each step. The value of η after all cuts is 30.8 ± 3.5. Figure 4.70 shows the π^+ momentum spectrum for the events in the first and last lines of table 4.19, highlighting the effectiveness of the cuts applied at reducing the tail events relative to the peak. This can also be seen quantitatively in table 4.19 : the value of η increases with the application of every cut. It should be noted however that the open histogram sample in figure 4.70 contains a number of events from K_{e4} decays, which are heavily suppressed by the TGTRACK cut (see section 4.2.5).

The number of peak events remaining after all cuts for the entire $\pi\nu\bar{\nu}$ data sample was 159. Details of this analysis are given in table B.67. Based on this result, the expected number of

Table 4.19: Final analysis to determine η for $K_{\pi 2}$ background estimation (Method 1).

Cut	**Peak**		**Tail**		η
	#	**Rejection**	**#**	**Rejection**	
Selected	21119		6393		3.3
TGTRACK	3876	5.45 ± 0.08	419	15.3 ± 0.7	9.25
TGFIT	3485	1.112 ± 0.006	250	1.68 ± 0.07	13.9
VTX_PCA	3057	1.140 ± 0.007	191	1.31 ± 0.05	16.0
PB-GLASS	2259	1.35 ± 0.02	78	2.4 ± 0.2	29.0
B4TD	2191	1.031 ± 0.004	71	1.10 ± 0.04	30.8

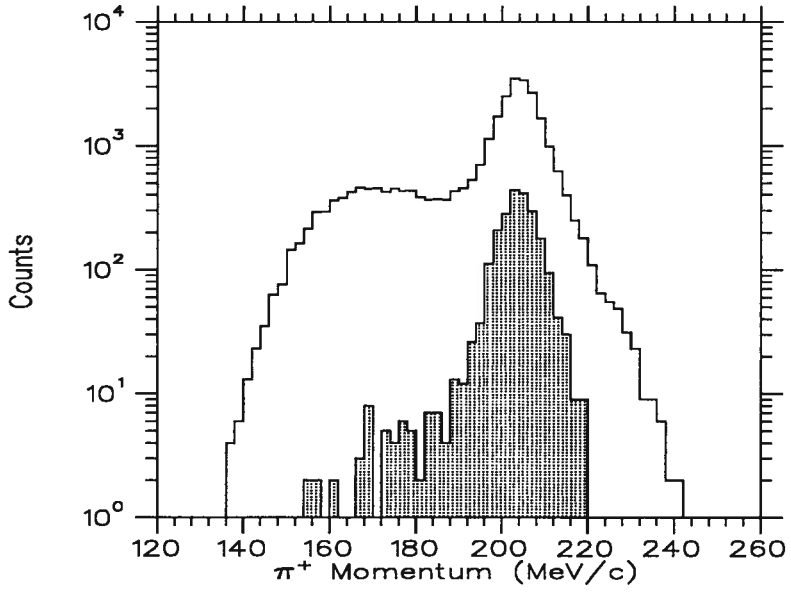

Figure 4.70: $K_{\pi 2}$ background data sample with inverted photon veto cuts before application of remaining cuts (open histogram) and after (shaded histogram).

background events from $K_{\pi 2}$ decays was

$$N_{\rm bgd} = \frac{N_{\rm peak}}{\eta} = \frac{159 \pm 13}{30.8 \pm 3.5} = 5.16 \pm 0.72 \tag{4.55}$$

where the error is statistical only. This number is quite large and seems to indicate that the analysis cuts are not sufficient at removing background events.

Further studies of the ratio η offered a possible explanation for this large number of background events. The ratio was determined for two other levels of photon veto. Table 4.20 summarizes the results. The first line comes from analysis of Kπ2(1) monitor data to which all $\pi\nu\overline{\nu}$ trigger conditions were applied, except the photon veto. All offline cuts were also applied, with the exception of direct photon veto cuts. This resulted in a very large value of η, and is the value that could be expected if there was no correlation between photon veto and nuclear interactions, since in this case there are almost no constraints on the photons from π^0 decay. The second entry gives the value of η measured after only online photon veto cuts were applied. These cuts correspond to a threshold of approximately 5 and 10 MeV in the barrel veto and the endcaps respectively. The data sample consisted of about 4% of the full data sample. It can be seen that η is almost the same as for the data sample selected after Pass1 photon veto cuts discussed above and displayed as the third entry in the table. These results clearly demonstrate the strong correlation between photon veto and nuclear interactions. It could be argued that since the value of η appears to be constant after online photon veto cuts have been applied, the extrapolation can be made to the level at which no prompt energy is visible. However, the very large correlation makes this extrapolation somewhat uncertain. Furthermore, it is possible that by requiring detection of a small amount of photon energy, the number of tail events is enhanced compared to the case where nothing can be seen, since in many nuclear interactions low energy photons are emitted by excited nuclei. For these reasons, the background estimate from this method was considered unreliable.

4.2.1.2 Method 2

This method was based on the assumption that the most important component of the $K_{\pi 2}$ background came from events in which a nuclear interaction occured in the target and interaction products

Table 4.20: $K_{\pi 2}$ peak to tail event ratio for various levels of photon veto.

Condition	Peak	Tail	η
No photon veto	3815	9	424 ± 141
Online photon veto	485	16	30.3 ± 7.5
Pass1 photon veto	2189	71	30.8 ± 3.6

were hidden by the K^+ track in the target. In order to select such background events, the TGFIT cut was inverted. The first step in the event selection was the application of all cuts to the Pass1 data sample, except TGTRACK, VTX_PCA, PB-GLASS, B4TD, TGFIT and KINCUT. This corresponds to the events passing the BWPC cut in table B.67, a total of 1464 events. Of these, 745 failed TGFIT and were used to study the other cuts. Table 4.21 shows the analysis results. As can be seen, all the events in the $K^+ \to \pi^+ \nu\overline{\nu}$ search region (or tail) were rejected before the last cut was applied. The rejection of B4TD was estimated by applying it to the 9 tail events passing the TGTRACK cut. Only one event was rejected, giving a rejection of $R_{\mathrm{B4TD}} = 1.12 \pm 0.13$.

Table 4.21: Analysis results for $K_{\pi 2}$ background sample (Method 2).

Cut	Peak		Tail	
	#	Rejection	#	Rejection
Selected	1202		262	
Fail TGFIT	599		146	
TGTRACK	26	23.0 ± 4.4	9	16.2 ± 5.2
VTX_PCA	21	1.24 ± 0.12	5	1.80 ± 0.54
PB-GLASS	10	2.10 ± 0.48	0	—
B4TD	10	1.00 ± 0.00	0	—

The last factor needed for the background estimation was the rejection of the TGFIT cut, which was used to select the background sample. For this, a data sample representative of the $K_{\pi 2}$ background was needed, but selected in a different way than the one used above. The VTX_PCA cut was designed to reject the same kind of background as TGFIT, and so should be appropriate for the selection. The primary limitation of TGFIT is the double pulse resolution

of the TDs covering the target. Therefore, its efficiency is a strong function of the K^+ decay time; the later the decay, the better the chance of identifying the π^+ pulse. VTX_PCA, on the other hand, only uses summed energy and geometric quantities and is limited by the resolution of the measurement of these quantities. By using a sample of events which fail the VTX_PCA cut, we should be able to measure the rejection of TGFIT in a reasonably accurate way.

The application of VTX_PCA and TGFIT only really makes sense after TGTRACK has been applied. The sample of events after TGTRACK in table 4.21 would be appropriate, but there are only 9 events available in the $K^+ \to \pi^+\nu\overline{\nu}$ search region. Removing the photon veto cuts beyond Pass1 increased the statistics. The events satisfying the BWPC cut requirements in table B.66 were used for this purpose. Table 4.22 describes the additional cuts applied for the sample selection. The TGFIT cut was then applied, and 60 events survived, for a rejection of

$$R_{\mathrm{TGFIT}} = \frac{121}{60} = 2.02 \pm 0.18\,. \tag{4.56}$$

From this, the measured value of R_{B4TD} and the fact that no events which failed TGFIT survived the full analysis, we can set a 90% C.L. upper limit on the number of background events expected from this source :

$$N_{\mathrm{bgd}} < \frac{2.3}{R_{\mathrm{TGFIT}} - 1} \times \frac{1}{R_{\mathrm{B4TD}}} = 2.0 \tag{4.57}$$

where the factor of 2.3 corresponds to the 90% confidence level upper limit for a Poisson statistical process in which no events were observed.

Table 4.22: Event selection for data sample used to determine the rejection of the TGFIT cut.

Cut	# events	Rejection
Selected	28522	
TGTRACK	4501	6.336 ± 0.087
KINCUT	432	10.42 ± 0.48
Failed VTX_PCA	121	—

This result, indicating that the background from $K_{\pi 2}$ decays is less than two events at the 90% confidence level, is not consistent with the result obtained with Method 1. The two

methods used different techniques and different data samples, and therefore should be sensitive to different systematic effects. Method 2 is obviously limited by statistics. This cannot be remedied as the entire $\pi\nu\bar{\nu}$ data sample was used.

Two assumptions have to be validated to make the estimate from Method 2 correct :

1. The potential $K_{\pi 2}$ background consists of events in which the energy lost by the π^+ in a nuclear interaction in the target overlaps with the energy deposited by the K^+ .

2. The rejection of the TGFIT cut for this type of background can be correctly measured using a data sample selected by inverting the VTX_PCA cut.

If there is a significant component to the $K_{\pi 2}$ background for which a nuclear interaction in the target leaves no visible energy, then both assumptions will be invalid. These assumptions appeared reasonable, and therefore the estimate from Method 2 was believed to more accurately represent the actual expected background from $K_{\pi 2}$ decays.

4.2.2 Radiative $K_{\pi 2}$

The radiative decay $K^+ \to \pi^+\pi^0\gamma$ ($K_{\pi 2\gamma}$) provides a simple mechanism for the π^+ to lose energy compared to the non-radiative $K_{\pi 2}$ decay : emission of a photon. The most important contribution is from inner bremsstrahlung, in which the photon is emitted by the π^+ . There is also the possibility of direct photon emission, in which the photon is emitted by an intermediate state particle. This contribution to the decay rate has been measured and is about 15 times less than the inner bremsstrahlung part [17].

The signature of $K_{\pi 2\gamma}$ background is practically the same as $K_{\pi 2}$ decays with nuclear interactions. It is therefore very difficult to disentangle the two components in the real data. Considering the $K_{\pi 2\gamma}$ branching ratio and the presence of another photon compared to $K_{\pi 2}$, it can reasonably be expected that the contribution of $K_{\pi 2\gamma}$ will be smaller than $K_{\pi 2}$. To prove this, a Monte Carlo simulation was used. The method consisted in the determination of the expected number of $K_{\pi 2\gamma}$ events in the $K^+ \to \pi^+\nu\bar{\nu}$ kinematic search region as a function of the number of $K_{\pi 2}$ peak events observed outside of the search region.

In order to normalize the number of $K_{\pi 2\gamma}$ events to the number of $K_{\pi 2}$ peak events, it is necessary to know the branching ratio for each decay. The branching ratio for $K_{\pi 2\gamma}$ is a function of the region of phase space considered. In fact, most of the $K_{\pi 2\gamma}$ branching fraction for very low photon energy is included in the $K_{\pi 2}$ branching fraction. Experimental measurements of the $K_{\pi 2\gamma}$ branching ratio have been made using the region of π^+ kinetic energy between 55 and 90 MeV [64, 65], significantly below the $K_{\pi 2}$ peak energy of 108.5 MeV. Figure 4.71 shows the π^+ energy spectrum for 10^5 decays generated with a Monte Carlo program. The correct matrix element, including a direct emission contribution, was used to weigh the events generated. A cutoff on the π^+ kinetic energy was placed at 106 MeV. The ratio of the integral of the spectrum in figure 4.71 for the ranges 55–90 MeV and 0–106 MeV gave the correction factor for the effective $K_{\pi 2\gamma}$ branching ratio for the full energy range up to the cutoff :

$$\mathrm{BR}(K_{\pi 2\gamma}) = \frac{\int_0^{106} dN}{\int_{55}^{90} dN} \times (2.93 \pm 0.16) \times 10^{-4} = (1.11 \pm 0.06) \times 10^{-3} \qquad (4.58)$$

where the sum of the accepted values for the inner bremsstrahlung and the direct emission parts of the branching ratio in the energy region 55–90 MeV has been used [17].

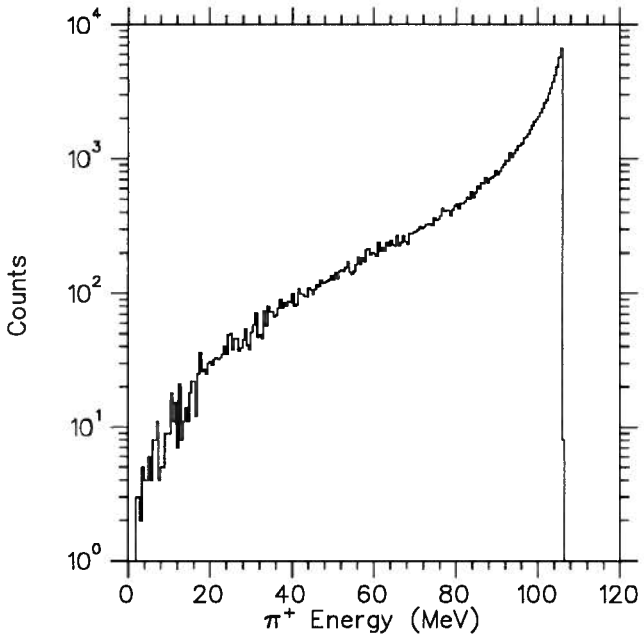

Figure 4.71: Kinetic energy spectrum of π^+ from $K_{\pi 2\gamma}$ decays simulated by Monte Carlo. A total of 10^5 decays were generated.

$K_{\pi 2}$ and $K_{\pi 2\gamma}$ events were generated with the Monte Carlo program. The photon veto requirements were not included in the $\pi\nu\overline{\nu}$ trigger simulation since the overall π^0 rejection of order 10^5–10^6 would force the simulation of a prohibitive number of events. The simulation primarily determined the relative acceptance of the analysis for the π^+ for the two decays.

Table 4.23 summarizes the results of the simulation and subsequent analysis for both decays. The number of events was normalized to the number of stopped kaons. From these numbers and the branching ratio for each decay, the ratio κ of $K_{\pi 2}$ events in the kinematic peak over $K_{\pi 2\gamma}$ events in the $K^+ \to \pi^+\nu\overline{\nu}$ search region was determined :

$$\begin{aligned} \kappa &= \frac{\#K_{\pi 2}}{\#K_{\pi 2\gamma}} \times \frac{\mathrm{B}(K_{\pi 2})}{\mathrm{B}(K_{\pi 2\gamma})} \times \frac{N^{\gamma}_{KT}}{N_{KT}} \\ &= \frac{1976 \pm 44}{776 \pm 28} \times \frac{0.2117 \pm 0.0016}{(1.11 \pm 0.06) \times 10^{-3}} \times \frac{71312}{67941} \\ &= 510 \pm 35 \end{aligned} \tag{4.59}$$

where N^{γ}_{KT} and N_{KT} are the number of kaons satisfying the KT trigger requirement in the $K_{\pi 2\gamma}$ and the $K_{\pi 2}$ simulation respectively.

Table 4.23: Event simulation and analysis results for $K_{\pi 2\gamma}$ background.

Requirement	$K_{\pi 2}$	$K_{\pi 2\gamma}$
KT (stopped kaon decay)	67941	71312
Passed trigger simulation	5209	4890
Passed offline analysis	1976	776

Figure 4.72 shows the energy versus directional cosine along the z-axis for the photons from π^0 decay for simulated $K_{\pi 2}$ and $K_{\pi 2\gamma}$ events satisfying all offline analysis cuts. The distributions are clearly very similar; therefore, it was assumed that the π^0 rejection of the photon veto system is the same for both decays. For $K_{\pi 2\gamma}$ decays, the presence of an additional photon increases the rejection. The single photon detection inefficiency of the detector has been measured as a function of energy and angular distribution [66]. From these measurements, and the energy distribution of the extra photon for the 776 Monte Carlo $K_{\pi 2\gamma}$ events satisfying all the analysis requirements, the photon veto inefficiency was estimated to be $\overline{\epsilon}_{\gamma} = (7.83 \pm 0.78) \times 10^{-2}$, from

which the rejection due to the detection of the radiated photon was determined :

$$R_\gamma = \frac{1}{\bar{\epsilon}_\gamma} = 12.8 \pm 1.3 \,. \tag{4.60}$$

Finally, from the known number of $K_{\pi 2}$ peak events remaining after all cuts were applied to the $\pi\nu\bar{\nu}$ data sample (table B.67), we can estimate the number of background events from $K_{\pi 2\gamma}$ decays :

$$\begin{aligned} N_{\rm bgd} &= \frac{N_{K_{\pi 2}}}{\kappa} \times \frac{1}{R_\gamma} \\ &= \frac{159 \pm 13}{510 \pm 35} \times \frac{1}{12.8 \pm 1.3} \\ &= 0.0244 \pm 0.0036 \end{aligned} \tag{4.61}$$

where the error is statistical only. This estimate is significantly less than the expectation from $K_{\pi 2}$ background, justifying the initial hypothesis.

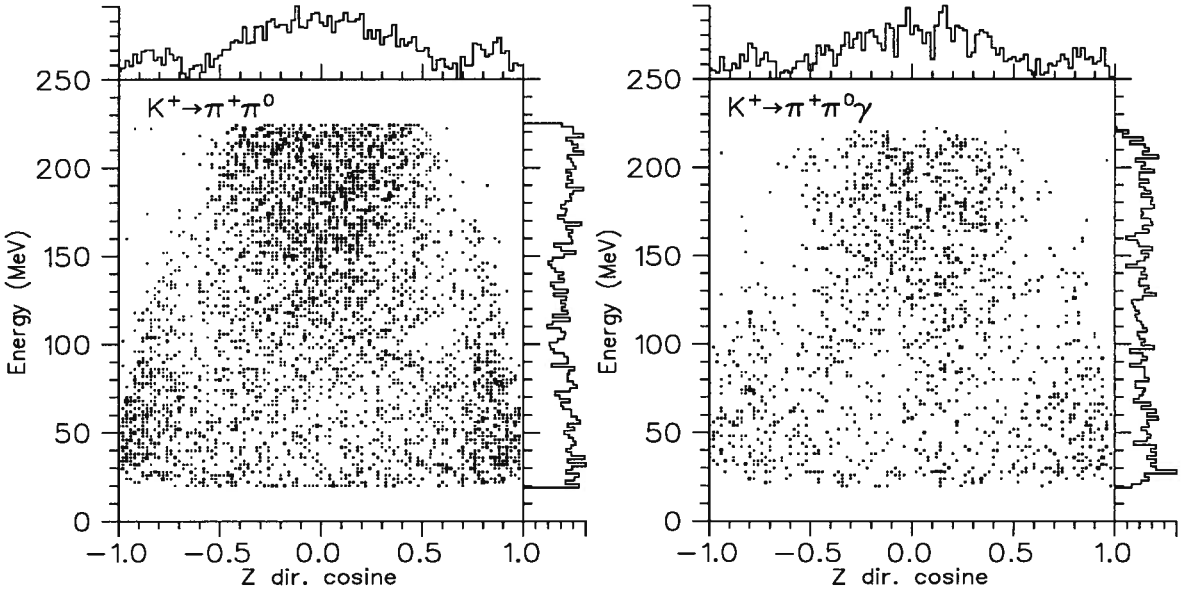

Figure 4.72: Energy versus z-axis directional cosine for photons from π^0 decay in simulated $K_{\pi 2}$ and $K_{\pi 2\gamma}$ events.

4.2.3 Muons

This study of muon background was similar to the one performed for 1989 data. However, it was done in a more systematic fashion. The kinematic cuts were studied first, using monitor data.

A sample of muon events was then selected out of $\pi\nu\overline{\nu}$ Pass1 data using inverted kinematic cuts; this sample was used to study TD cuts. The photon veto cuts were factored out of this study to improve the statistical power. The muon background was then estimated by combining the result of the TD cuts study and the estimated rejection of the kinematics and photon veto cuts.

The effect of correlation between the cuts involved in this study was considered. The selection criteria for the data samples used could have resulted in biasing of the relative importance of the two decay modes involved; for instance, the photon veto cuts should affect $K_{\mu\nu\gamma}$ and $K_{\mu 3}$ in a different way. Examination of the phase space distribution of the data samples used showed that the differences between the samples were minor and therefore correlations should not be very important in this study.

4.2.3.1 Kinematic Cuts

Samples of muons suitable for a study of kinematic cuts were obtained from monitor data. In the absence of any cuts placing requirements on the $\pi^+ \rightarrow \mu^+ \rightarrow e^+$ decay chain, the kinematic region below the $K_{\pi 2}$ peak is rich in muon background events. Two different types of monitor data were used to select muon samples : $\pi\nu\overline{\nu}$ lev0 data and Kπ2(1) (see section 3.1.6). The $\pi\nu\overline{\nu}$ lev0 data sample was the one used to prepare the kinematic cuts. All requirements of the $\pi\nu\overline{\nu}$ Level 0 trigger were applied to this data, based on the trigger information recorded with the events. Also applied were track reconstruction cuts in the target, drift chamber and range stack, TRKTIM, PROMPT and KINCUT. Full details are given in table B.68. Only 219 events satisfied all these requirements. Figure 4.73 shows the distribution of total range versus total momentum prior to the final cut for this sample. This shows that the sample is dominated overall by $K_{\pi 2}$ events but that in the kinematic region selected the sample is dominated by a clear band of muons.

This sample, and a sample of pions selected from π-scat monitor data by applying TD cuts, were used to determine the parameters of the KINSCORE cut. As described in section 3.3.4.3, this cut combined the independent measurements of the momentum, range and kinetic energy

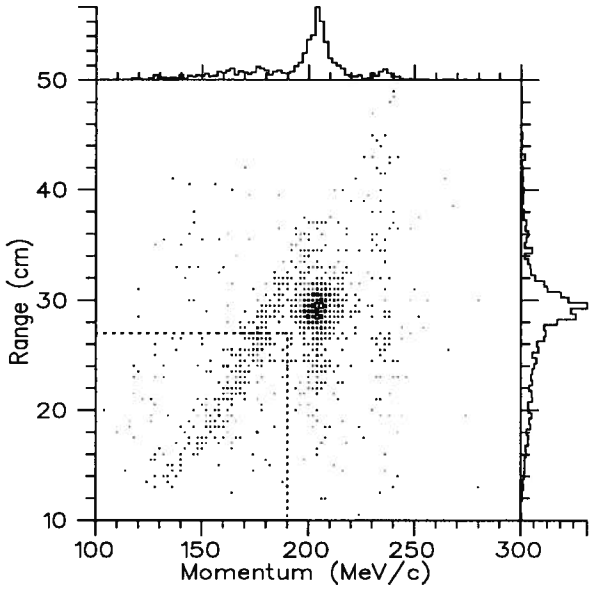

Figure 4.73: Total range versus total momentum for muon sample from $\pi\nu\overline{\nu}$ lev0 data. The events below the dotted line were selected.

to identify the particle type. Because of the small number of muon events available, the parameters and cut position were determined for all range stack stopping layers combined. After examination of a larger sample of pions, the cut positions were re-adjusted to the values given in section 3.3.4.3.

To measure the rejection of the KINSCORE cut, another sample of muons was selected. This time the Kπ2(1) monitor data was used. A total of 440 events were selected; table B.69 gives the details of the selection. The main difference between the sample selected from $\pi\nu\overline{\nu}$ lev0 data and this one is that there were no direct photon veto cuts for the latter; this should enhance the presence of $K_{\mu\nu\gamma}$ and $K_{\mu 3}$ decays, but also enhance the number of $K_{\pi 2}$ decays as well. By applying the TGTRACK cut, the number of π^+ from $K_{\pi 2}$ decays in the $K^+ \to \pi^+\nu\overline{\nu}$ kinematic search region should be significantly reduced. The shaded histograms in figure 3.50 are from this data sample; it is clearly dominated by muons.

Applying the KINSCORE cut to this sample resulted in 59 events, for a rejection of $R_{\rm kin} = 7.46 \pm 0.90$. However, even though the sample was dominated by muons before the application of the KINSCORE cut, a small pion contamination could dominate the sample after the cut was applied and significantly affect the value of $R_{\rm kin}$. Therefore, an estimate of the pion

contents of the sample was required. TD based pion identification cuts (FITPI, ELVETO and ELECTRON) were applied to the 440 events; nine events survived. This number had to be corrected for the acceptance loss of the TD cuts used, and then corrected for the acceptance loss of KINSCORE to estimate the number of pions remaining. The acceptance was taken from sections 5.2.3.1 and 5.2.3.2. Table 4.24 summarizes the estimation of the pion contamination; as can be seen, the effect is significant.

Table 4.24: Estimate of pion contamination in muon sample for muon background kinematic studies. $A_{\rm TD}$ is the combined acceptance of the FITPI, ELVETO and ELECTRON cuts and $A_{\rm kin}$ is the acceptance of the KINSCORE cut.

Layer	**# events**	$A_{\rm TD}$	**# pions**	$A_{\rm kin}$	**# pions**
B	5	0.360 ± 0.015	13.1 ± 6.1	0.8498 ± 0.0074	11.8 ± 5.2
C	3	0.445 ± 0.020	6.7 ± 3.8	0.8286 ± 0.0094	5.6 ± 3.2
11+12	1	0.509 ± 0.019	2.0 ± 2.0	0.8354 ± 0.0093	1.7 ± 1.7
Total	9		22.6 ± 7.4		19.1 ± 6.3

Based on these numbers, the kinematic rejection for muons was measured to be

$$R_{\rm kin} = \frac{(440 \pm 21) - (22.6 \pm 7.4)}{(59 \pm 7.7) - (19.1 \pm 6.3)} = 10.5 \pm 2.7 \tag{4.62}$$

where the error is statistical.

4.2.3.2 TD cuts

To study the effect of the TD cuts on the muon background, muons were selected out of the $\pi\nu\overline{\nu}$ Pass1 data sample based on kinematics. The selection used the Fisher variable from KINSCORE; the cut position was [5.0,+15.0]. Using the second muon data sample described in the previous section, the efficiency of this muon selection was measured. Out of 440 events, 328 were accepted. This had to be corrected for the pion contamination, both before and after the selection. In the previous section, the pion contamination before the cut was estimated to be 22.6 ± 7.4 events. Based on the large pion rejection of the muon selection cut (50–200), the pion contamination after the muon selection was negligible. Therefore, the muon selection

efficiency was

$$\epsilon_\mu = \frac{328 \pm 18}{(440 \pm 21) - (22.6 \pm 7.4)} = 0.786 \pm 0.060 \tag{4.63}$$

Other cuts were also applied in the selection to eliminate other backgrounds that might contaminate the sample. All cuts except TD cuts, the 4.0 MeV minimum energy requirement in the stopping counter and explicit photon veto cuts (INTIME, INTSE, PB-GLASS and B4TD) were applied; this included the signal region cut on total momentum, range and energy. A total of 575 events were selected. Figure 4.74 shows the $\overline{T_\mu}$ distribution for those events, clearly not consistent with the exponential distribution expected from π^+ decay.

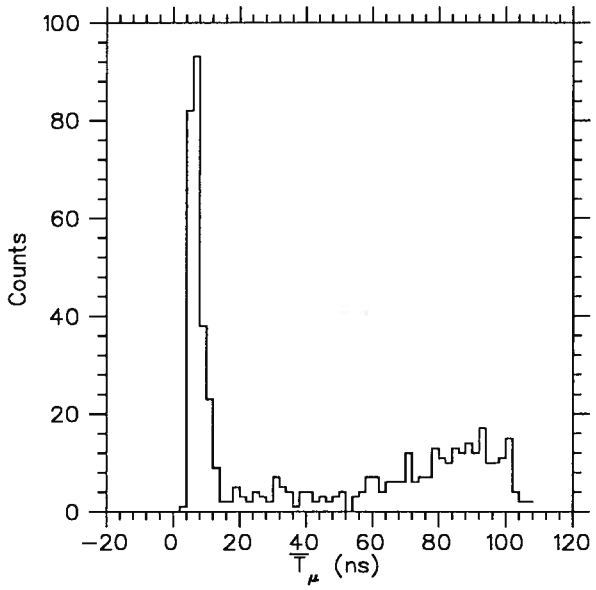

Figure 4.74: $\overline{T_\mu}$ distribution for muon background.

Three components can be identified in this time spectrum: a large group concentrated at small $\overline{T_\mu}$ values, a flat component and a rise of the flat component at late values of $\overline{T_\mu}$. The first group corresponds to cases where fluctuations of the primary pulse were mistaken for a second pulse. These are rejected by tightening constraints on the results of the double pulse fits. The second component corresponds to accidental hits providing the second pulse in the stopping counter and early μ^+ decays. These can be rejected by searching for other related activity in the detector at the same time or by demanding that the z-axis position of the second pulse be consistent with the z position of the primary pulse. For the case where the second

pulse originates from the early decay of the μ^+ , a large rejection is obtained by demanding a third pulse consistent with the $\pi^+ \to \mu^+ \to e^+$ chain. Finally, the rise in the flat component at late times is attributed to the edge of the ADC integration gate (about 75 ns) for the range stack. For earlier times, the presence of an accidental hit can disrupt the range stack track reconstruction, and therefore more of these events are rejected.

This sample of events was used to develop the various TD based cuts other than FASFITPI and FITPI described in section 3.3.4. Table 4.25 shows the effect of these TD cuts on the muon sample. In this table, the RS-TRACK cut only includes the 4.0 MeV requirement in the stopping counter, and the FITPI cut only includes the χ^2 cut on the fit results; the other requirements for these two cuts were already applied at Pass1.

Table 4.25: TD rejection of muon background.

Cut	# events	Rejection
Muons	575	
RS-TRACK	540	1.065 ± 0.011
FITPI	280	1.929 ± 0.080
TD_MDA	221	1.267 ± 0.039
TDFOOL	138	1.601 ± 0.084
ELVETO	30	4.60 ± 0.74
ELECTRON	15	2.00 ± 0.36
R_{TD}		38.3 ± 9.8

As was noted earlier, explicit photon veto cuts were not applied to this sample in order to increase the statistical power of the study. In fact, the photon veto cuts reject all 15 events remaining after application of the TD cuts. The rejection of the photon veto cuts for the muon background can be measured by applying them to the entire muon sample. Table 4.26 shows the effect of these cuts.

It should be emphasized that the rejection measured here for the TD cuts and the photon veto cuts only includes the effect of the cuts applied after Pass1. The total rejection of the TD and photon veto cuts was effectively much higher since a large background rejection occurs at the trigger level and at Pass1.

Table 4.26: Photon veto rejection of muon background.

Cut	# events	Rejection
Muons	575	
INTIME	143	4.02 ± 0.29
INTSE	95	1.505 ± 0.089
PB-GLASS	58	1.64 ± 0.13
B4TD	57	1.018 ± 0.018
$R_{\overline{\gamma}}$		10.1 ± 1.3

4.2.3.3 Muon background estimate

The estimate for the total number of events expected from muon sources for the 1991 data sample is then

$$\begin{aligned} N_{\text{bgd}} &= \frac{N_{\text{evt}}}{\epsilon_\mu} \times \frac{1}{R_{\text{kin}}} \times \frac{1}{R_{\overline{\gamma}}} \\ &= \frac{15 \pm 3.9}{0.786 \pm 0.060} \times \frac{1}{10.5 \pm 2.7} \times \frac{1}{10.1 \pm 1.3} \\ &= 0.180 \pm 0.071 \end{aligned} \tag{4.64}$$

where N_{evt} is the number of events remaining in the kinematically selected muon sample after all cuts except explicit photon veto cuts. The error quoted is statistical only.

4.2.4 Beam pions

The various sources of beam pion background were described in section 4.1.3. In this study, none of the cases listed were considered negligible. Events matching the characteristics of each category were selected out of the $\pi\nu\overline{\nu}$ Pass1 data sample and studied separately. As a first step, all cuts except the ones specifically directed at beam pion backgrounds and the $K^+ \to \pi^+\nu\overline{\nu}$ kinematic search region cut were applied to the Pass1 $\pi\nu\overline{\nu}$ data sample. This provided a sample of 12818 events, dominated by beam pion background. Table B.70 gives the details of the selection.

4.2.4.1 Two particle background

The multi-wire proportional chamber was the ideal device to select the two beam particle background. It was equally sensitive to K^+ and π^+ , was located immediately next to the Čerenkov counter and had large acceptance for both the focused kaons and the more diffuse pions. Out of the data sample described in table B.70, events which failed the BWPC cut were selected. To remove a possible contamination from $K_{\pi 2}$ decays with an accidental hit in the BWPC, the kinematic search region cut (KINCUT) was also applied; a total of 3284 events were selected. Applying the remainder of the cuts resulted in no events. A large part of the rejection was provided by the TGTRACK cut. Therefore, to improve the sensitivity of the background estimate, the target vertex cuts (TGTRACK, TGFIT and VTX_PCA) were removed from the analysis and their rejection estimated separately. Table 4.27 shows the result of the analysis without these cuts.

Table 4.27: Two beam particle background analysis.

Cut	# events	Rejection
Two particle bgd	3284	
PROMPT	2590	1.268 ± 0.011
ICOUNTER	1821	1.422 ± 0.018
TRKTIM	453	4.02 ± 0.16
FIDUCIAL	353	1.283 ± 0.032
BM_HOLE	328	1.076 ± 0.016
B4_CNTR	282	1.163 ± 0.026
CERENKOV	33	8.5 ± 1.4
PB-GLASS	10	3.30 ± 0.87
B4TD	5	2.00 ± 0.63
Total		657 ± 294

Using the same sample of two beam particle background, the rejection of the cuts left out was measured. Here, care had to be taken to avoid over-estimating the rejection. Even though the intrinsic rejection of the cuts constraining the track in the target and the rejection of all other cuts are independent of each other, in practice there is some overlap in the rejection

of some of those cuts. For this reason, the TRKTIM and FIDUCIAL cuts were applied before measuring the combined rejection of TGTRACK, TGFIT and VTX_PCA. The measured combined rejection was

$$R_{\rm TG} = \frac{671}{5} = 134 \pm 60\,, \tag{4.65}$$

dominated by the TGTRACK cut.

The final piece of information that was needed was the rejection of the BWPC cut. To measure this, a sample of events with a hit in the pion Čerenkov counter as well as a hit in the lead-glass counter at the time of the track in the range stack was selected. This sample was extracted from the sample described in table B.70 ; a total of 7822 events were selected, and the BWPC cut was applied to these events. This resulted in a measured rejection of

$$R_{\rm BWPC} = \frac{7822}{521} = 15.0 \pm 0.6\,. \tag{4.66}$$

The estimate for the number of background events from two beam particle sources after all cuts in the $\pi\nu\overline{\nu}$ analysis was then

$$\begin{aligned} N_{\rm bgd} &= N_{\rm evt} \times \frac{1}{R_{\rm BWPC} - 1} \times \frac{1}{R_{\rm TG}} \\ &= (5.0 \pm 2.2) \times \frac{1}{(15.0 \pm 0.6) - 1} \times \frac{1}{(134 \pm 60)} \\ &= 0.0027 \pm 0.0017\,. \end{aligned} \tag{4.67}$$

4.2.4.2 Single particle background

This type of background occurs when a single K^+ , already identified in the Čerenkov counter, decays or interacts resulting in a π^+ before reaching the target. The simplest way to select this type of background was to identify a single π^+ in the B4 hodoscope. Figure 3.58 showed the energy distribution of π^+ and K^+ in the B4 counter; there is clear separation between the two particle types. Using the sample described in table B.70, single pions were selected by inverting the B4_CNTR cut. To remove background events involving two beam particles, the CERENKOV and BWPC cuts were applied as well. Only 93 events out of the entire $\pi\nu\overline{\nu}$ Pass1 data sample satisfied all the analysis criteria. Table 4.28 describes the analysis of this sample using the remaining cuts.

Table 4.28: Single beam particle background analysis.

Cut	# events	Rejection
Single particle bgd	93	
PROMPT	74	1.257 ± 0.066
ICOUNTER	39	1.90 ± 0.21
TRKTIM	15	2.60 ± 0.53
FIDUCIAL	10	1.50 ± 0.27
TGTRACK	0	—
TGFIT	0	—
BM_HOLE	0	—
VTX_PCA	0	—
PB-GLASS	0	—
B4TD	0	—
KINCUT	0	—

Obviously, this measurement suffers from low statistics. The main reason for this is that the online delayed coincidence as well as the offline PROMPT cut applied at Pass1 had a very large rejection for the background studied here. In order to increase the sensitivity of the estimate, it was necessary to determine the rejection of the cuts which were not necessary in table 4.28. Of these, the only cuts that can be expected to provide a large rejection factor are PB-GLASS and KINCUT. For the former, the beam pion can be identified as it passes through the lead-glass degrader. For the latter, figure 4.75 shows the total range versus total momentum distribution for the selected sample of single beam particle background. The distribution is clearly uniform, with no significant contamination from $K_{\pi 2}$ events; only the part of the distribution in the search region will contribute to the background. The rejection of PB-GLASS and KINCUT was measured using the selected sample :

$$R_{\mathrm{PbG}} = \frac{93}{33} = 2.82 \pm 0.39 \tag{4.68}$$

$$R_{\mathrm{KINCUT}} = \frac{93}{29} = 3.21 \pm 0.49\,. \tag{4.69}$$

The rejection of the B4_CNTR cut, which was used to select the background sample, was determined using a sample of π-scat monitor data. For this data sample, a beam pion was identified in the Čerenkov counter, ensuring that only a π^+ entered the target passing through

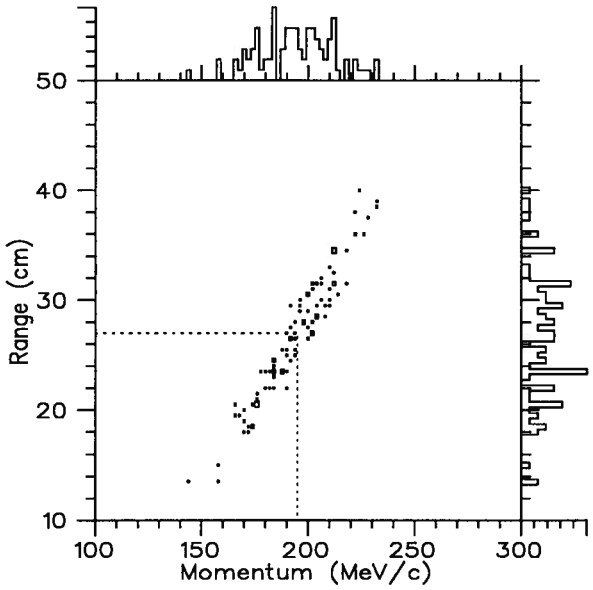

Figure 4.75: Total range versus total momentum for single beam particle background data sample. Events above the dotted lines were rejected by the KINCUT cut.

the B4 counter. The rejection was measured to be

$$R_{\mathrm{B4}} = \frac{1000}{176} = 5.68 \pm 0.39 \,. \tag{4.70}$$

Neglecting the rejection of other unnecessary cuts in table 4.28, the background from single beam particles was estimated as

$$N_{\mathrm{bgd}} = N_{\mathrm{evt}} \times \frac{1}{R_{\mathrm{B4}} - 1} \times \frac{1}{R_{\mathrm{PbG}}} \times \frac{1}{R_{\mathrm{KINCUT}}} \,. \tag{4.71}$$

Because in this case no events were observed after applying the remaining cuts to the selected sample (table 4.28), an upper limit was set :

$$N_{\mathrm{bgd}} < 2.3 \times \frac{1}{(5.68 - 1)} \times \frac{1}{2.82} \times \frac{1}{3.21} = 0.05 \ \ (90\%\mathrm{C.L.}) \tag{4.72}$$

Obviously, this component of the beam pion background dominates. However, it is clear that the estimate is conservative and is also limited by statistics. It is possible that the rejection of the TGTRACK cut was significantly more than what can be estimated from reducing 10 events to none. Nonetheless, the estimate is at a comfortable level for this analysis, ensuring that the probability of observing a background event from beam pion background was sufficiently low, and in reality was probably much lower.

4.2.5 $K^+ \rightarrow \pi^+\pi^-e^+\nu_e$ (K_{e4})

As was seen in the 1989 study of K_{e4} background, because of the similarity between the signatures of the K_{e4} and $K_{\pi 2}$ backgrounds, it is very difficult to extract a sample of events from the available real data that is unambiguously dominated by K_{e4} . It is however reasonable to expect that the K_{e4} background contribution should be small, at least compared to $K_{\pi 2}$. For these reasons, a more detailed Monte Carlo simulation was used to estimate the level of background from K_{e4} decays in 1991 data; no real data were used.

K_{e4} decays satisfying the $\pi\nu\overline{\nu}$ trigger conditions were simulated with the Monte Carlo program. Since only a portion of the K_{e4} phase space is of any interest for this study, immediately after the K^+ decay the kinematic variables of the decay products were examined. Several conditions had to be met for the simulation of the event to proceed further :

1. π^+ momentum $P_{\pi+} > 140$ MeV/c
2. π^+ z-axis directional cosine $w_{\pi+} < 0.6$
3. π^- kinetic energy $T_{\pi-} < 50$ MeV
4. If $20 < T_{\pi-} < 50$ MeV, $w_{\pi-} > 0.5$
5. e^+ kinetic energy $T_{e+} < 80$ MeV

These conditions saved a large amount of computer time and did not bias the result of the study, as will be shown below. As for the simulation used for 1989 data (section 4.1.4), nuclear interactions for the π^- were not simulated. Their effect was taken into account separately.

A total of 1×10^7 K_{e4} decays were simulated. Offline cuts applied were event reconstruction cuts, INTIME, TGTRACK and KINCUT. Details of the simulation and analysis are given in table B.71; a total of 19 events satisfied all criteria. Figure 4.76 shows the total range versus total momentum for these events. As can be seen, they are confined to the lower part of the $K^+ \rightarrow \pi^+\nu\overline{\nu}$ kinematic search region; this was caused by the constraints imposed by the trigger and the analysis. Figure 4.77 shows the kinetic energy distribution of the π^- and e^+ immediately after the K^+ decay for the remaining events. Clearly, the constraints applied at

simulation time did not bias the distributions; all remaining events are well below the cutoffs of 20 and 80 MeV for the π^- and the e^+ respectively.

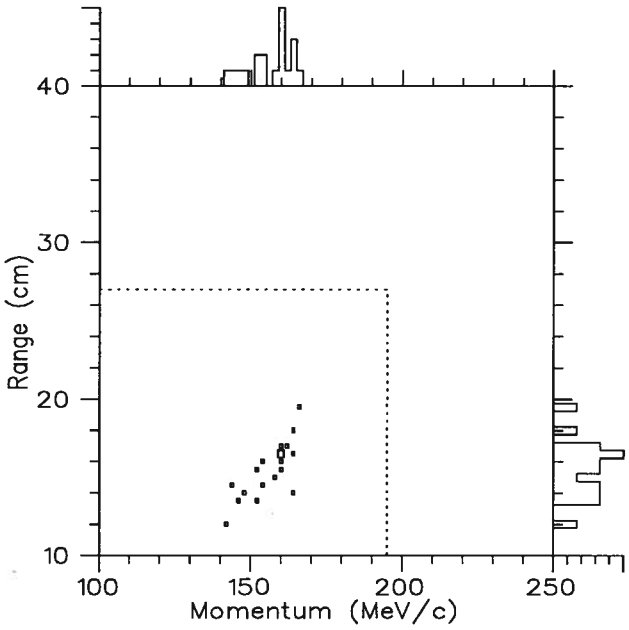

Figure 4.76: Total range versus total momentum for K_{e4} simulated background. All events are found in the search region (inside the dotted line).

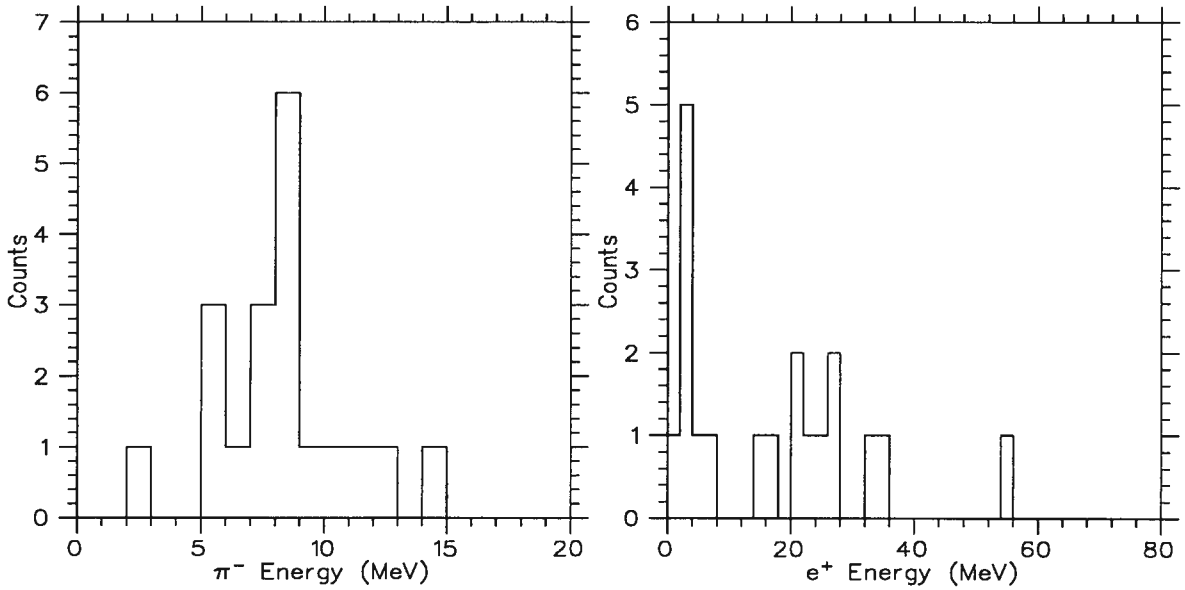

Figure 4.77: Kinetic energy at birth of the π^- and e^+ for simulated K_{e4} events passing all analysis criteria.

To estimate the expected number of background events from this source after analysis of all data, several other factors were required. The number of background events was expressed as :

$$N_{\rm bgd} = \frac{N_p}{N_{\rm gen}} \times B(K_{e4}) \times A_{\rm anal} \times \frac{1}{R_{\pi^-}} \times N_K \times \frac{f_s^D}{f_s^{\rm MC}} \tag{4.73}$$

where N_p is the number of simulated events satisfying all analysis criteria, $N_{\rm gen}$ is the number of events generated in the simulation, $B(K_{e4})$ is the K_{e4} branching ratio, $A_{\rm anal}$ is a correction taking into account the real data acceptance and the acceptance loss of cuts not applied in this analysis, R_{π^-} is the rejection due to nuclear interactions of the stopping π^- , N_K is the total number of K^+ observed in the real data analysis and $f_s^{\rm MC}$ and f_s^D are the fraction of incident K^+ that stopped in the target for the Monte Carlo simulation and the real data respectively. From the analysis of Monte Carlo generated data described above, we have $N_{\rm evt} = 19$ and $N_{\rm gen} = 1 \times 10^7$. The accepted value of the branching ratio is $B(K_{e4}) = 3.9 \times 10^{-5}$ [17]. $A_{\rm anal}$ was calculated from the measured acceptance of the individual cuts for real data (see section 5.2.5) and corrected for the intrinsic acceptance of cuts applied to Monte Carlo data. A value of $A_{\rm anal} = 0.0390 \pm 0.0021$ was obtained. From data analysis of the $\pi\nu\bar{\nu}$ sample, $N_K = 1.436 \times 10^{11}$ (section 5.5.1). From section 5.3, $f_s^D = 0.6422 \pm 0.0085$, and from Monte Carlo event generation we have $f_s^{MC} = 0.9059 \pm 0.0011$.

The rejection due to stopping negative pions was more difficult to determine. Negative pions can interact in flight in the same manner as π^+ 's, but the most significant effect is their capture at rest by nuclei. As a result of the interaction at rest of a negative pion with a carbon nucleus, a large variety of fragments can be produced [69, 70]; this is commonly referred to as a "π^- star". Table 4.29 gives the multiplicity and average energy of stopped π^- interaction products. There will also be gamma rays produced as a result of the de-excitation of the heavier nuclear fragments or from absorption of neutrons by carbon nuclei.

Data were obtained from a TRIUMF test experiment which measured the energy deposited by 20 MeV negative pions stopping in a block of plastic scintillator [71]. The block was 4 cm high, 4 cm wide and 3 cm thick and viewed by a single photomultiplier tube. Figure 4.78 shows the energy distribution observed. The primary peak at 20 MeV corresponds to π^- absorption with no detectable reaction products; the smaller peak around 14 MeV is due to negative muons

Table 4.29: Interaction products multiplicity and average energy for π^- stopping in carbon. Entries for charged decay products are from reference [69] and for neutrons from reference [70].

Particle	**Multiplicity** (particles/π^-)	**Average energy** (MeV)
proton	0.45 ± 0.04	10.4 ± 1.8
deuteron	0.33 ± 0.03	6.3 ± 1.1
triton	0.22 ± 0.02	3.0 ± 0.5
^3He	0.03 ± 0.005	0.5 ± 0.2
^4He	0.62 ± 0.06	5.5 ± 1.0
Li	0.13 ± 0.02	1.2 ± 0.3
neutron	2.44 ± 0.18	31.8 ± 3.1

which contaminated the beam.

In this setup, the probability of interaction for neutrons or gamma rays is not very large. The mean free path of a 30 MeV neutron in scintillator is about 19 cm. It was assumed that the large energy tail in figure 4.78 is from charged particles. There are therefore two contributions to R_{π^-} :

$$R_{\pi^-} = R_{\text{chg}} \times R_{n,\gamma} \tag{4.74}$$

where R_{chg} is the rejection from charged particles and $R_{n,\gamma}$ is the rejection from neutrons and gamma rays. We assume that the two factors are independent.

For R_{chg}, the assumption was made that it was necessary to get at least 10 MeV from the π^- absorption in order to detect the interaction and reject the event, with cuts such as TGTRACK, TGFIT and VTX_PCA. Based on the data shown in figure 4.78, the additional rejection from π^- nuclear interaction is $R_{\text{chg}} = 1.776 \pm 0.016$, where the error is statistical only.

To estimate $R_{n,\gamma}$, neutrons with an appropriate energy distribution were simulated in the detector. The visible energy deposited in the detector within a time coincidence window corresponding to the INTIME cut parameters was summed, to simulate the effect of the INTIME cut. It was found that the probability of detecting the presence of a neutron from π^- absorption was 0.1961 ± 0.0040, where the error is statistical only. According to table 4.29, the mean number of neutrons emitted in π^- absorption in carbon is 2.44; therefore, the rejection expected

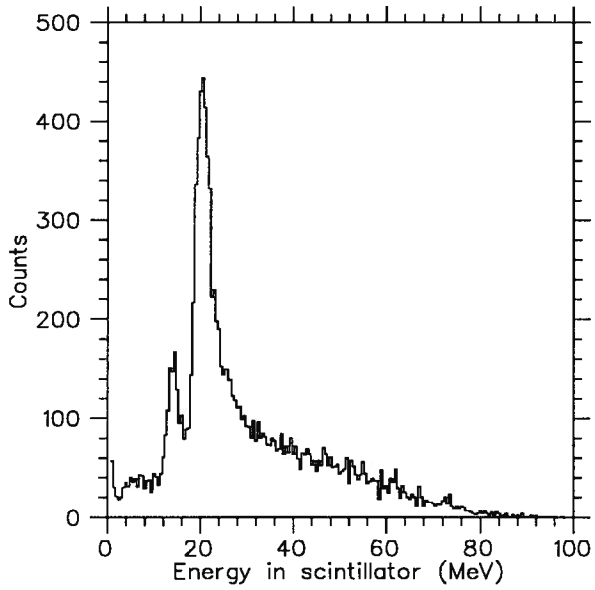

Figure 4.78: Energy deposited in scintillator by stopping π^- . The small peak at 14 MeV is due to μ^- contamination in the test beam.

due to neutrons is $R_{n,\gamma} = 1.638 \pm 0.018$. It is possible that residual nuclei emitting gamma rays contribute to the rejection; due to the complicated nature of these excitations and lack of a proper simulation program, this contribution was neglected. Hence, the total rejection due to the absorption of negative pions in the target was estimated to be

$$R_{\pi^-} = (1.776 \pm 0.016) \times (1.638 \pm 0.018) = 2.909 \pm 0.041 \,. \tag{4.75}$$

Finally, substituting this value and the ones for all other factors in equation 4.73, we obtain the total number of background events expected from K_{e4} decays :

$$\begin{aligned} N_{\rm bgd} &= \frac{19 \pm 4.4}{1 \times 10^7} \times (3.91 \pm 0.17) \times 10^{-5} \times (0.0390 \pm 0.0021) \times \frac{1}{(2.909 \pm 0.041)} \times \\ &\quad \times (1.436 \times 10^{11}) \times \frac{0.6422 \pm 0.0085}{0.9059 \pm 0.0011} \\ &= 0.101 \pm 0.024 \,. \end{aligned} \tag{4.76}$$

4.2.6 Charge exchange

Kaons interact via the strong force when they propagate through matter. One possible interaction for a charged kaon is charge exchange, in which it interacts with a nucleon, resulting in

a neutral kaon and a nucleon. In the case of a positively charged kaon, the reaction is

$$K^+ n \rightarrow K^0 p \,. \tag{4.77}$$

The neutron will obviously be bound in a nucleus. In the case of this experiment, if the interaction occurs in the active target, the energy loss from the proton can easily overlap with the energy loss from the incident K^+ and be missed. The neutral kaon is a superposition of the two mass eigenstates K_L^0 (K-long, mean life 51.7 ns) and K_S^0 (K-short, mean life $8.92 \times 10^{-11} s$). The K-short decays essentially 100% of the time to two pions, with a small amount of radiative two pion decay. The three pion decay mode of the K-short has yet to be observed, with branching ratio upper limits of a few times 10^{-5}. On the other hand, about 65% of the K-long's decay semi-leptonically ($K_L^0 \rightarrow \pi^{\pm} \ell^{\mp} \nu_\ell$). Since this is a three body decay, the lepton in the final state can have very little energy and be difficult to detect if the K-long decays before exiting the target. Both the muonic and electronic branch contribute to this potential background :

$$K_L^0 \rightarrow \pi^+ \mu^- \overline{\nu}_\mu \quad BR = 13.5\% \tag{4.78}$$

$$K_L^0 \rightarrow \pi^+ e^- \overline{\nu}_e \quad BR = 19.35\% \,. \tag{4.79}$$

Just as was the case with $K^+ \rightarrow \pi^+ \pi^- e^+ \nu_e$, this background is indistinguishable from $K_{\pi 2}$ background : a single π^+ originates from the target and the energy deposited by the proton and the decay lepton in the target overlaps with the energy deposited by the incident K^+ . If the lepton has a significant amount of energy it will easily be detected. The estimate of the background contribution from this source hinges on the determination of the rate at which particles other than the K^+ and the π^+ remain hidden. Because of their very different masses, the energy loss behavior of electrons and muons is quite different. For a given energy, it will be easier to detect an electron, so we can expect the muonic branch to contribute more to the overall background rate. In addition, the kinematic end point of the muonic branch is lower than the electronic branch, resulting in a larger kinematic acceptance by the $\pi\nu\overline{\nu}$ trigger.

No reliable way of selecting data samples representative of this background was found, and the estimate had to rely on a Monte Carlo simulation. The first step in setting up the

simulation was to obtain the charge exchange cross section as a function of energy. This is not trivial since no measurement exists of this cross section at the relatively low energies involved in this experiment, except for a nuclear emulsion measurement averaged over C, N and O nuclei for a K^+ energy of 60 MeV [72]. A few measurements exist of the charge exchange cross section for K^+ on deuterium at low energy [73, 74]. The assumption was made that the cross section for ^{12}C is six times that of deuterium, appropriately corrected for nuclear shadowing and electro-magnetic effects. The cross section is typically a few mb, which results in an average probability of interaction of 1.5×10^{-3} for K^+ incident on the target.

The reliability of the cross-section used in the Monte Carlo simulation was checked using a special data set [75]. Trigger conditions were arranged to select K-short decays to two charged pions. This study unequivocally demonstrated the presence of neutral kaons in the target. The fraction of observed K-short per incident K^+ was determined for both the real data and the Monte Carlo. The ratio of the two numbers gives a correction factor for the charge exchange rate :

$$\xi = \frac{\text{Monte Carlo}}{\text{Real Data}} = 2.44 \pm 0.98 \tag{4.80}$$

The simulation for the study of charge exchange as a $K^+ \rightarrow \pi^+\nu\overline{\nu}$ background started with a K^+ at the front face of the scintillator target. The total probability of charge exchange interaction for each event was calculated based on the K^+ energy at the start of the event and recorded in a data bank. The energy at which the interaction occurred was chosen based on the theoretical distribution calculated from the charge exchange cross section and the kaon energy loss energy dependence. The K^+ was then allowed to propagate in the target and when its energy dropped below the pre-selected value, the charge exchange reaction was forced, with a K-long being produced. The two semi-leptonic decay channels of the K-long were studied separately.

In most cases, the K-long was produced with an energy large enough for it to leave the target before it decays. For example, a K-long with a kinetic energy of only 10 MeV has a velocity of 6 cm/ns ; considering the K-long lifetime of 51.7 ns, the probability is small that it will decay within the active target. Therefore, the K-long was forced to decay within the target

and the probability for this to occur was recorded for each event. Forcing every K^+ simulated to undergo charge exchange and each K-long produced to decay within the target significantly improved the efficiency of the simulation.

The events satisfying the simulated $\pi\nu\overline{\nu}$ trigger were analyzed with the same program used for the real data. The number of background events expected from this source in the real data was expressed as

$$N_{\rm bgd} = \frac{N_{\rm pass}}{N_{K_{\rm inc}}} \times \frac{1}{\xi} \times f_{K_L^0} \times {\rm BR} \times A_{\rm anal} \times \frac{1}{R_{\rm others}} \times N_{KT} \times f_{K_{\rm inc}} \qquad (4.81)$$

where $N_{\rm pass}$ is the weighted number of events surviving the analysis, $N_{K_{\rm inc}}$ is the number of kaons started at the front face of the target which satisfy the KT trigger requirement, ξ is as defined above by equation 4.80, $f_{K_L^0}$ is the fraction of the K^0's produced in strong interactions that are K-longs, BR is the branching ratio of the K-long decay mode studied, $A_{\rm anal}$ is as defined in section 4.2.5, $R_{\rm others}$ is the additional rejection expected from cuts not applied, N_{KT} is the total number of events satisfying the KT trigger requirement in the data and $f_{K_{\rm inc}}$ is the fraction of counts recorded as KT in the real data that are actual K^+ incident on the front face of the target. The latter was determined by a Monte Carlo simulation to be $f_{K_{\rm inc}} = 0.8742 \pm 0.0023$; losses come from a K^+ either decaying in flight or interacting in the degrader and still satisfying the KT requirement. As mentioned in the previous section, $N_{KT} = 1.436 \times 10^{11}$. $A_{\rm anal}$ was calculated in the same way as for K_{e4} background; the value obtained was $A_{\rm anal} = 0.0458 \pm 0.0081$. $f_{K_L^0} = 0.5$ since a K^0 is a superposition of the two mass eigenstates K-long and K-short, each with equal probability.

$R_{\rm others}$ is dominated by the VTX_PCA cut. It might be expected that TGFIT would also provide a significant rejection factor; however, as will be seen below, π^+ tracks from charge exchange background emerge from the target typically a few nanoseconds from the arrival time of the K^+ , which renders the TGFIT cut essentially ineffective. The VTX_PCA cut was not applied to the simulated data because the B4 hodoscope is not simulated properly by the Monte Carlo program. By inspecting the distribution of K^+ energy in the target as a function of the decay vertex position extrapolated from the drift chamber track, the rejection expected was estimated to be $R_{\rm others} = 2.0 \pm 0.5$. Substituting for the known values in equation 4.81, we

obtain

$$N_{\rm bgd} = \frac{N_{\rm pass}}{N_{K_{\rm inc}}} \times {\rm BR} \times (5.9 \pm 3.0) \times 10^8 \ . \tag{4.82}$$

4.2.6.1 $K_L^0 \to \pi^+ \mu^- \overline{\nu}_\mu$

A total of 2.0×10^6 events were simulated for $K_L^0 \to \pi^+ \mu^- \overline{\nu}_\mu$; of these, 1993776 satisfied the KT trigger requirements. The offline cuts applied were the same as for the K_{e4} background study. Table B.72 gives the details of the simulation and analysis; 37 events remained after all cuts were applied. Each event had a weight given by the product of three probabilities :

1. Probability of K^+ charge exchange
2. Probability of decay of the K_L^0 in the target
3. Probability of satisfying the online delayed coincidence.

The third item was calculated based on the measured value of $T_{\rm tg}^{\pi}$ -$T_{\rm tg}^{K}$ and the distribution shown in figure 3.33. The sum for the 37 events was 4.96×10^{-3}. Figure 4.79 shows the $T_{\rm tg}^{\pi}$ - $T_{\rm tg}^{K}$ distribution before the PROMPT and KINCUT cuts were applied; note that each event was weighed appropriately in the histogram. The large count in the bin near 4 ns is dominated by a single event with a very low energy K-long, which has a high probability of decay in the target.

Using equation 4.82, the numbers from table B.72 and BR($K_L^0 \to \pi^+ \mu^- \overline{\nu}_\mu$) = 0.135 ± 0.002 [17], the background contribution was estimated :

$$\begin{aligned} N_{\rm bgd} &= \frac{4.96 \times 10^{-3}}{1993776} \times (0.135 \pm 0.002) \times (5.9 \pm 3.0) \times 10^8 \\ &= 0.20 \pm 0.10 \end{aligned} \tag{4.83}$$

where the error is statistical only. This background is obviously non-negligible.

4.2.6.2 $K_L^0 \to \pi^+ e^- \overline{\nu}_e$

The simulation and analysis for the decay $K_L^0 \to \pi^+ e^- \overline{\nu}_e$ proceeded in exactly the same way as for $K_L^0 \to \pi^+ \mu^- \overline{\nu}_\mu$. A total of 6×10^5 events were simulated, of which 598053 satisfied the

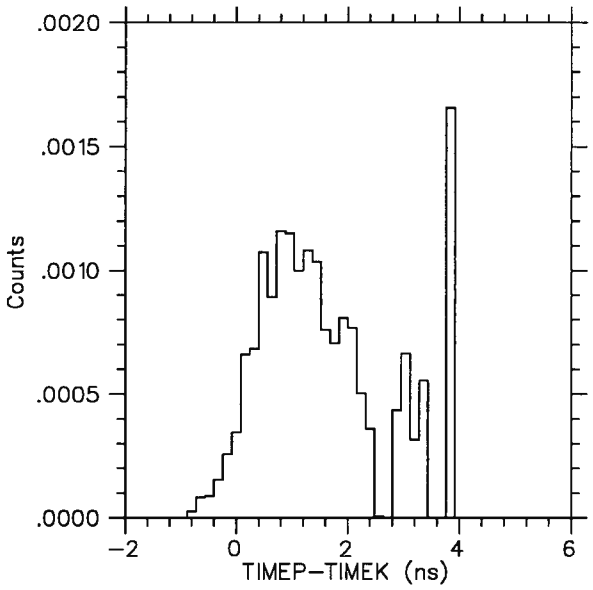

Figure 4.79: T^{π}_{tg} -T^{K}_{tg} distribution for $K^0_L \to \pi^+\mu^-\overline{\nu}_\mu$ decays from charge exchange background.

KT trigger requirements; only 6 events remained after offline cuts were applied, with a summed weight of 1.04×10^{-4}. Details are given in table B.73. When compared to $K^0_L \to \pi^+\mu^-\overline{\nu}_\mu$, the obvious difference between the two analyses was with respect to the trigger acceptance, which is a factor of 3.7 times less for $K^0_L \to \pi^+e^-\overline{\nu}_e$. The electron from $K^0_L \to \pi^+e^-\overline{\nu}_e$ is more easily detected than the muon in $K^0_L \to \pi^+\mu^-\overline{\nu}_\mu$. This is also reflected in the rest of the analysis, with the INTIME cut having a much greater rejection. The other important point is that the PROMPT cut was not applied in this analysis. If it had been applied, all the events would have been rejected. To avoid the time consuming task of generating perhaps an order of magnitude more events for a background process which was obviously less significant than $K^0_L \to \pi^+\mu^-\overline{\nu}_\mu$, use was made of the results of the study of the latter process to estimate the rejection of the PROMPT cut. The time delay in the target should be independent of the K^0_L decay mode, and hence no systematic effect should be introduced.

Of the 901 events passing the TGTRACK cut in table B.72, 596 were found in the search region. The weighted sum of these events was 1.38×10^{-2}. Therefore, the rejection of the

PROMPT cut was estimated to be

$$R_{\text{PROMPT}} = \frac{1.38 \times 10^{-2}}{4.96 \times 10^{-3}} = 2.78\,. \tag{4.84}$$

To determine the background contribution, equation 4.82 was modified to take into account the rejection of the PROMPT cut :

$$N_{\text{bgd}} = \frac{N_{\text{pass}}}{N_{K_{\text{inc}}}} \times \frac{1}{R_{\text{PROMPT}}} \times \text{BR} \times (5.9 \pm 3.0) \times 10^8\,. \tag{4.85}$$

Substituting the appropriate numerical values, it followed that

$$\begin{aligned} N_{\text{bgd}} &= \frac{1.04 \times 10^{-4}}{598053} \times \frac{1}{2.78} \times (0.1935 \pm 0.0025) \times (5.9 \pm 3.0) \times 10^8 \\ &= 0.0071 \pm 0.0036 \end{aligned} \tag{4.86}$$

where the accepted value of the $K_L^0 \to \pi^+ e^- \overline{\nu}_e$ branching ratio was used [17]. The error is once again statistical only. This background contribution is nearly 30 times less than the one determined for $K_L^0 \to \pi^+ \mu^- \overline{\nu}_\mu$ decay.

4.2.7 Hyperon production

Semi-leptonic decay is not the only possible $K^+ \to \pi^+ \nu \overline{\nu}$ background process for a neutral kaon produced via K^+ charge exchange. Through the well known process of oscillation, the K^0 produced in a nuclear interaction has a time dependent probability of being a $\overline{K^0}$ [76]. Since it contains a strange quark as opposed to a strange anti-quark, the $\overline{K^0}$ can interact with a nucleon and produce a strange baryon through the reaction

$$\overline{K^0} N \to Y \pi \tag{4.87}$$

where N is either a proton or neutron and Y is a Σ or Λ hyperon; the latter can in turn decay to a charged pion and a nucleon. For the specific case of this experiment, interactions on the single proton of hydrogen nuclei in scintillator can be neglected since the likelihood of detecting both interaction products or their decay daughters is very large. For nucleons bound in carbon nuclei, there is a significant probability that one of the interaction products will be immediately absorbed by the carbon nucleus, and therefore be difficult to detect.

The process which *a priori* appeared to be the most significant was studied with a Monte Carlo simulation. The first part of the simulation was identical to the simulation of K^+ charge exchange background. Instead of allowing the neutral kaon to decay, it was forced to interact in the target via the reaction

$$\overline{K^0}N \rightarrow \Sigma^+\pi \tag{4.88}$$

assuming it had evolved in a $\overline{K^0}$. The probability for this was calculated based on the K^0 time evolution and stored in a data bank. The total cross section for the interaction of K_L^0 with carbon and hydrogen has been measured for relatively low incident energies [77]. By combining these data, the total interaction cross section of K_L^0 in scintillator was determined. The cross section for equation 4.88 has not been explicitly measured however. To estimate it, use was made of the $K^-p \rightarrow \Sigma\pi$ cross section [78], which should be similar except for some isospin differences and electro-magnetic effects. Based on this information, an energy independent cross section of 50 mb/nucleon was assumed, corrected by a factor of 0.5 for the nucleon screening effect in carbon nuclei. From this cross section, the probability for the $\overline{K^0}$ to interact was calculated and stored. The pion in the final state was assumed to have been absorbed by the carbon nucleus, and therefore was not tracked in the event simulation. This was corrected for, as will be described below. The distribution of the cosine of the angle of the interaction products with respect to the direction of the $\overline{K^0}$ was assumed to be flat in the center of momentum frame.

After the interaction, it was assumed that the Σ hyperon escaped the carbon nucleus, propagated in the target and decayed via the process

$$\Sigma^+ \rightarrow \pi^+ n\,. \tag{4.89}$$

This decay has a branching ratio of 48%. In the rest frame of the Σ^+, the π^+ and neutron momentum is 185 MeV/c ; for the neutron, this corresponds to a kinetic energy of 18 MeV, making its detection difficult. Because of its large rest mass of 1189 MeV/c^2, the Σ particle typically has a very short range in the target. The kinematic acceptance for the decay π^+ is very large, even taking into account that some of the Σ's decay in flight. The mean life of the Σ^+ is $(0.799 \pm 0.004) \times 10^{-10}$ ns ; this implies that π^+ tracks from this background process will appear more or less prompt, as for the charge exchange background.

A total of 2×10^5 events were simulated. Of these, 193105 satisfied the KT requirement and 81 remained after all cuts had been applied. Table B.74 gives detailed results. The weight for each event was the product of four factors :

1. Probability of K^+ charge exchange
2. Probability of $K^0 \rightarrow \overline{K^0}$
3. $\overline{K^0}$ interaction probability
4. Online delayed coincidence probability

The sum of the weights for the remaining events was 3.15×10^{-3}.

If we compare the results of table B.74 to the ones obtained for charge exchange background, it is clear that the acceptance is much larger for this process. The probability of $\overline{K^0}$ interaction and the probability of detection of the interaction products determine the importance of this background relative to the charge exchange background. The number of background events from this source was estimated with the following formula :

$$N_{\rm bgd} = \frac{N_{\rm pass}}{N_{K_{\rm inc}}} \times \frac{1}{\xi} \times f_{K_L^0} \times \mathcal{P}^{\Sigma_{\rm esc}} \times \mathcal{P}^{\pi_{\rm abs}} \times A_{\rm anal} \times \frac{1}{R_\pi} \times B(\Sigma \rightarrow \pi n) \times N_{KT} \times f_{K_{\rm inc}} \quad (4.90)$$

Many of the factors in this equation are the same as for the charge exchange background : ξ, $f_{K_L^0}$, $A_{\rm anal}$, N_{KT} and $f_{K_{\rm inc}}$. The accepted value of the branching ratio is $B(\Sigma \rightarrow \pi n) = 0.4830 \pm 0.0030$ [17]. The factor $R_{\rm others}$ we had for the charge exchange background has been replaced by R_π. Inspection of the extrapolated z-vertex as a function of K^+ energy in the target showed that no significant additional rejection could be obtained from cuts such as VTX_PCA. However, the pion produced in the interaction is absorbed by the carbon nucleus, but is not simulated. As calculated for K_{e4} background, we can expect an additional rejection of $R_\pi = 2.91 \pm 0.04$ from neutrons and other interaction products from π^- absorption.

Appropriate values for the two remaining factors, $\mathcal{P}^{\Sigma_{\rm esc}}$ and $\mathcal{P}^{\pi_{\rm abs}}$ are not obvious. Fortunately, a bubble chamber experiment investigated $K^- p$ interactions and reported values for these factors [79]. They determined $\mathcal{P}^{\Sigma_{\rm esc}} = 0.52 \pm 0.10$ and $\mathcal{P}^{\pi_{\rm abs}} = 0.10$; no error was quoted for the latter. With $N_{\rm pass} = 3.15 \times 10^{-3}$ and $N_{K_{\rm inc}} = 193105$, and substituting all the other

factors, we obtain the estimate for the number of background events from this source using equation 4.90 :

$$N_{\rm bgd} = 0.33 \pm 0.16 \, . \tag{4.91}$$

This number is quite large, and raised serious concern. Inspection of the simulated events satisfying all analysis criteria showed that about one third of them had a large gap in the xy plane in the target between the elements struck by the K^+ and the elements struck by the Σ^+. The target track reconstruction algorithm assigned the elements struck by the Σ^+ to the "kaon", and ignored the elements struck by the K^+ . Such a signature was looked for in several real data samples, but no evidence was found. The other main characteristics of this background are early times in the target and a π^+ momentum peaked around 185 MeV/c; again, no clear evidence was found in various data samples chosen to enhance these characteristics. This is in contrast with K_{e4} background for which even though the background estimate relied upon a Monte Carlo simulation, such events could be identified by scanning events at various stages of background studies using real data. For charge exchange, the independent study by other E787 collaborators clearly identified the presence of K^0_S particles in the target. There is therefore no doubt that K^0_L particles are also produced; their decay can be reliably simulated by the Monte Carlo program. In the case of hyperon production following K^+ charge exchange, the interaction cross section is not very well known, and the simulation relied on necessarily crude assumptions. For all these reasons, it was concluded that this background contribution, even though it cannot be ruled out, is likely overestimated by the simulation.

4.2.8 1991 Background summary

Estimates for all the background sources for 1991 data are summarized in table 4.30. Because some of the estimates are given as an upper limit, it is difficult to add all of them to obtain a total background estimate. If we neglect the one particle beam pion background, the sum for all background sources other than $K_{\pi 2}$ is 0.84 ± 0.20 events. According to the Poisson probability distribution, the probability of observing one event if the mean of the distribution is 0.84 is $\mathcal{P} = 0.36$ and the probability of observing no events is $\mathcal{P} = 0.43$. This means that there was a

non-negligible probability of observing at least one background event after analysis of the entire data sample, particularly considering the estimate for the $K_{\pi 2}$ background. However, upon careful examination of the background data samples available, no additional constraints could be found that reduced the background expectation significantly while satisfying the rejection versus acceptance loss criterion of effectiveness.

Table 4.30: Summary of 1991 background estimates.

Background	**Estimate (# events)**
$K^+ \to \pi^+\pi^0$ ($K_{\pi 2}$)	< 2.0 (90% C.L.)
$K^+ \to \pi^+\pi^0\gamma$ ($K_{\pi 2\gamma}$)	0.0244 ± 0.0036
Muons ($K_{\mu 3}$,$K_{\mu 2\gamma}$)	0.180 ± 0.071
Beam pions (two part.)	$(2.7 \pm 1.7) \times 10^{-3}$
Beam pions (one part.)	< 0.05 (90% C.L.)
$K^+ \to \pi^+\pi^- e^+\nu_e$ (K_{e4})	0.101 ± 0.024
Charge exchange ($K_L^0 \to \pi^+\mu^-\overline{\nu}_\mu$)	0.20 ± 0.10
Charge exchange ($K_L^0 \to \pi^+ e^-\overline{\nu}_e$)	0.0071 ± 0.0036
Hyperon production	0.33 ± 0.16

Chapter 5

Data Analysis and Results

This chapter describes the analysis steps beyond the first pass, the determination of the acceptance for $K^+ \rightarrow \pi^+\nu\overline{\nu}$ and $K^+ \rightarrow \pi^+X^0$, the determination of the total integrated kaon flux and the final results. A discussion of these results will be deferred until the next chapter.

5.1 Final Analysis

5.1.1 1989 Data

The final stage of the 1989 data analysis proceeded in two steps, Pass2 and Pass3. Details of each step are given in the sections below.

5.1.1.1 1989 Pass2

The second analysis pass on 1989 data consisted in five cuts applied to the events satisfying all Pass1 requirements. The cuts were the CERENKOV cut, the remainder of the PROMPT cut requirements except for T^{π}_{tg} -$T^{K}_{tg} < 50$ ns, the ELECTRON cut, the RGEMOM cut and the MASS cut. For the latter, the calculated particle mass had to be within the range 100–180 MeV/c^2, which is slightly less restrictive than the final cut. Table 5.31 gives the detailed statistics of this analysis pass. The remaining data sample contained a mixture of most background event types.

Table 5.31: 1989 Pass2 results.

Cut	# events	Rejection
Pass1	12554	
CERENKOV	9459	1.3272 ± 0.0068
PROMPT	4042	2.340 ± 0.028
ELECTRON	1889	2.140 ± 0.036
RGEMOM	1258	1.502 ± 0.024
MASS	1160	1.0844 ± 0.0089
Total		10.82 ± 0.30

5.1.1.2 1989 Pass3

For Pass3, the remaining cuts and final versions of cuts partially applied in earlier passes were applied to the Pass2 data sample. Table 5.32 gives the detailed statistics of this analysis. No events remained after all cuts were applied. Figure 5.80 shows the kinematic distribution for the events before the application of the last cut (KINCUT). The group of events above the $K^+ \to \pi^+\nu\bar{\nu}$ search region corresponds to $K_{\pi 2}$ decays in which the photons from π^0 decay were not detected.

5.1.2 1991 Data

The 1991 data analysis beyond Pass1 proceeded in three steps, Pass2 to Pass4. Pass3 consisted of two separate steps, each involving analysis of a portion of the events satisfying Pass2 requirements. Details for each pass are given below.

5.1.2.1 1991 Pass2

For the second pass of the 1991 analysis, all cuts except the ones expected to have the largest effect on the most serious background sources, namely TGTRACK, TGFIT, VTX_PCA, PBGLASS, B4FIT, were applied to the Pass1 data sample. Several of the cuts applied were the full versions of cuts partially applied at Pass1. Table 5.33 gives the result for each cut applied in succession. Of the remaining 1464 events, a total of 262 were in the $K^+ \to \pi^+\nu\bar{\nu}$ kinematic search region. Figure 5.81 shows the π^+ range versus momentum distribution for the remaining

Table 5.32: 1989 Pass3 results.

Cut	# events	Rejection
Pass1	1160	
BM_HOLE	1140	1.0175 ± 0.0040
B4TD	1036	1.100 ± 0.010
NK	1025	1.0107 ± 0.0033
PROMPT	1002	1.0230 ± 0.0048
DISENPI	989	1.0131 ± 0.0037
DISENK	976	1.0133 ± 0.0037
INT_EB	527	1.852 ± 0.055
NDC	470	1.121 ± 0.017
DC-CHI2	451	1.0421 ± 0.0099
ICOUNTER	400	1.128 ± 0.019
RSPC	399	1.0025 ± 0.0025
INT_RIV	293	1.362 ± 0.041
FITPI	203	1.443 ± 0.056
TGTRACK	88	2.307 ± 0.018
FIDUCIAL	70	1.257 ± 0.068
ZDCTZ	64	1.094 ± 0.040
ZK_EK	59	1.085 ± 0.039
EB4_EK	52	1.135 ± 0.054
DEDXRS	50	1.040 ± 0.029
MASS	49	1.020 ± 0.021
KINCUT	0	—

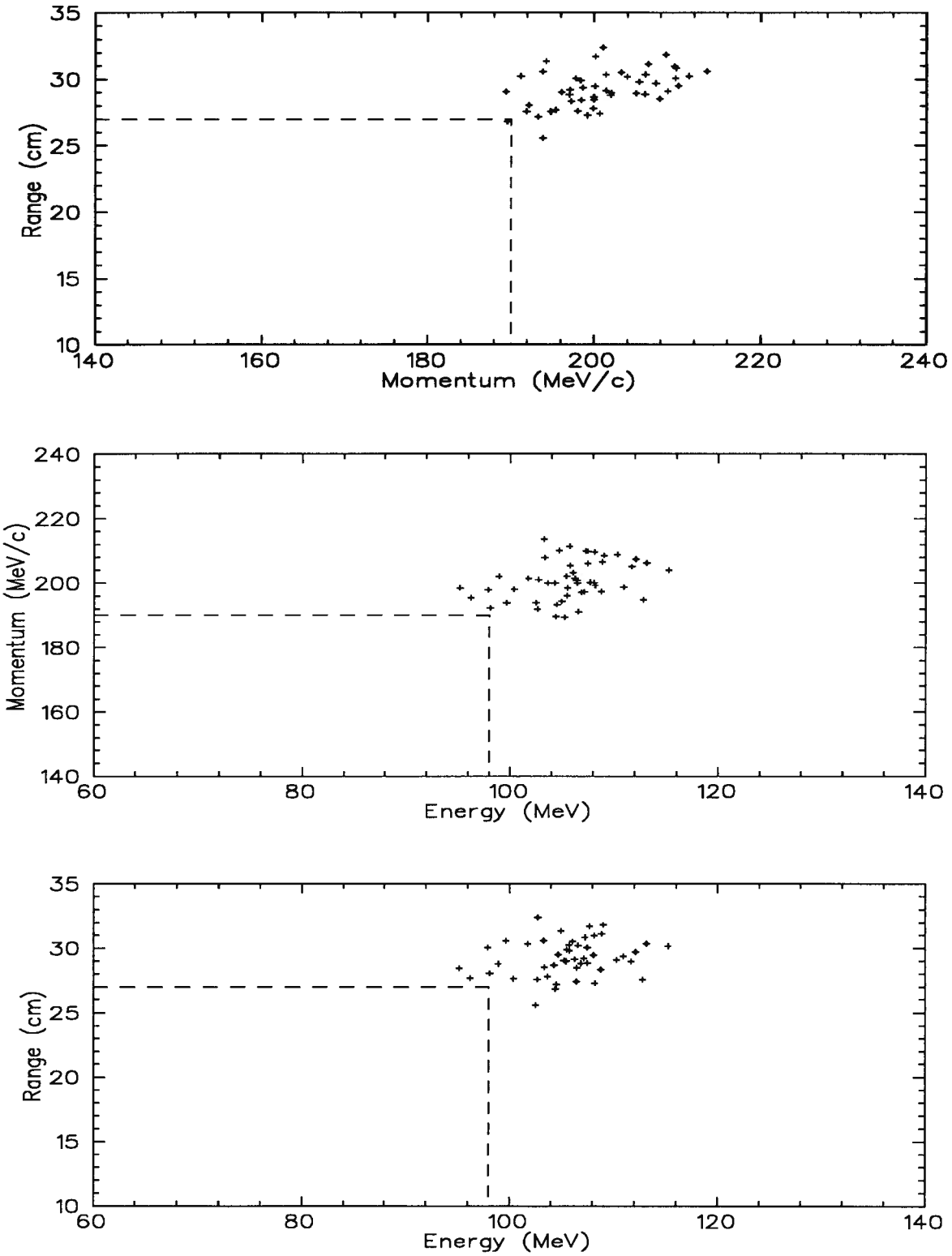

Figure 5.80: Kinematic distributions for 1989 events before the final cut. The dashed lines indicate the upper limits of the $K^+ \to \pi^+\nu\overline{\nu}$ search region.

events. A clear peak from $K_{\pi 2}$ events can be observed, as well as a flat low energy tail in the $K^+ \to \pi^+ \nu\bar{\nu}$ search region.

Table 5.33: 1991 Pass2 results for the entire data sample.

Cut	# events	Rejection
Pass1	399958	
PROMPT	348794	1.14669 ± 0.00069
DC-SETUP	260033	1.3413 ± 0.0013
RS-TRACK	239065	1.08771 ± 0.00063
ICOUNTER	165311	1.4462 ± 0.0020
TRKTIM	100537	1.6443 ± 0.0032
INTIME	18952	5.305 ± 0.035
INTSE	14677	1.2913 ± 0.0051
FITPI	10255	1.4312 ± 0.0078
TD_MDA	9366	1.0949 ± 0.0033
TDFOOL	7113	1.3167 ± 0.0076
ELVETO	5219	1.3629 ± 0.0097
ELECTRON	3991	1.308 ± 0.010
FIDUCIAL	3199	1.2475 ± 0.0098
KINSCORE	2813	1.1372 ± 0.0074
BM_HOLE	2700	1.0418 ± 0.0040
B4_CNTR	2544	1.0613 ± 0.0051
CERENKOV	1604	1.586 ± 0.024
BWPC	1464	1.0956 ± 0.0084
Total		273 ± 7

5.1.2.2 1991 Pass3

Pass3 consisted in the application of the remaining cuts to the events satisfying the Pass2 requirements. Because of the large uncertainties in the background estimates, it was decided to initially perform Pass3 on 30% of the data sample. If any events remained, they could be investigated and appropriate action taken before the remainder of the data was analyzed. In this way, if a certain feature of the background had been overlooked, improvements could be made that would potentially benefit the remaining 70% of the data sample without bias.

Table 5.34 shows the results of the analysis of 30% of the Pass2 sample with all cuts. Separate statistics are given for the kinematic search region events (tail) and events outside of

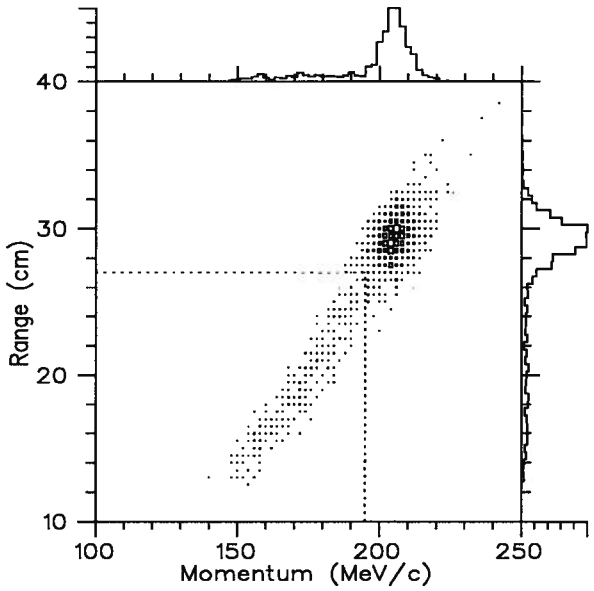

Figure 5.81: Total π^+ range versus total momentum for 1991 events satisfying all Pass2 requirements. The dashed line indicates the upper limit of the $K^+ \to \pi^+\nu\bar{\nu}$ search region.

that region (peak), as well as the overall total. As can be seen, two events satisfied all analysis criteria.

Table 5.34: Results of full analysis for 30% of the 1991 Pass2 sample.

Cut	# Events	Peak		Tail	
		#	Rejection	#	Rejection
Pass2	420	351		69	
TGTRACK	89	80	4.39 ± 0.43	9	7.7 ± 2.4
TGFIT	79	73	1.096 ± 0.038	6	1.50 ± 0.35
VTX_PCA	71	65	1.123 ± 0.046	6	1.00 ± 0.00
PB-GLASS	49	46	1.41 ± 0.11	3	2.00 ± 0.82
B4TD	47	45	1.022 ± 0.022	2	1.50 ± 0.61
KINCUT	2	0	—	2	1.00 ± 0.00

The two events were carefully examined for any obvious flaw that might have been missed by the analysis procedure; none was found. The possibility of software errors was also considered, but all aspects of the events had been correctly analyzed. Table 5.35 lists some important characteristics of the events. The first observation is that the momentum of the π^+ for the

two events is similar and relatively high. In both cases the π^+ energy is lower than what could be expected based on the momentum; this is reflected in the high calculated rest mass. The same can be said of the total range. The total energy and total range match very well. This is not unexpected however, since the range in the last range stack layer struck by the π^+ track is determined using the measured energy in that layer. It should also be noted that both events are well within the $K^+ \to \pi^+\nu\bar{\nu}$ kinematic search region. They are at least 3.5 standard deviations below the $K_{\pi 2}$ peak position in all three kinematic quantities.

Table 5.35: Characteristics of the remaining events after full analysis of 30% of the 1991 data sample.

Quantity	**Event 1**	**Event 2**
RS stopping layer	3	4
RS stopping sector	21	24
Total π^+ momentum (MeV/c)	188.8	189.1
Total π^+ energy (MeV)	87.0	90.8
Total π^+ range (cm)	22.6	24.6
Rest mass (MeV/c^2)	147.5	143.6
K^+ decay time (ns)	2.7	4.9
π^+ decay time (ns)	47.2	55.8

The π^+ momentum for both events is close to the value expected for Σ^+ decay (185 MeV/c at rest). The relatively early K^+ decay time in the target is also somewhat suggestive. Event 1 had a 0.58 MeV energy deposition in one endcap module within the time window of the INTIME cut. This is just below the cut position of 0.6 MeV. No other activity was observed at the time of the π^+ track. Finally, the π^+ decay time in the stopping range stack counter is quite late. This might be expected if the "muon" pulse was a random hit, as opposed to a true muon from pion decay. However, the evidence is rather slim. The estimate of the background from muon sources was quite firm and did not support this hypothesis. All other background sources were revised, and the only possible background explanations were $K_{\pi 2}$, charge exchange and hyperon production.

All cuts were re-examined to determine if additional rejection could be obtained. Only the offline photon veto cuts INTIME and INTSE and the cut on the summed energy of pion

time target elements not connected to the π^+ track (part of TGTRACK) could be tightened to reduce the background by a factor of two above the reduction due to acceptance loss. No particular feature of the background samples allowed the design of new cuts. It was therefore decided to complete Pass3 on the entire data sample with the existing cuts, and apply the tighter cuts as Pass4. Details about those cuts and their effect on the Pass3 data sample will be given in the next section.

Table 5.36 shows the results of the final analysis, including the 30% discussed above. An additional five events satisfied all analysis criteria, bringing the total to seven events. This is entirely consistent with the two events observed in 30% of the sample, but inconsistent with the background estimates. Table 5.37 lists the characteristics of all seven events; in this table, events B and F were events 1 and 2 in the 30% initially analyzed.

Table 5.36: Results of full analysis for the entire 1991 Pass2 sample.

Cut	**Events**	**Peak**		**Tail**	
		#	**Rejection**	**#**	**Rejection**
Pass2	1464	1202		262	
TGTRACK	306	279	4.31 ± 0.23	27	9.7 ± 1.8
TGFIT	272	254	1.098 ± 0.021	18	1.50 ± 0.20
VTX_PCA	246	231	1.100 ± 0.022	15	1.20 ± 0.13
PB-GLASS	174	165	1.400 ± 0.058	9	1.67 ± 0.35
B4TD	166	159	1.038 ± 0.016	7	1.28 ± 0.23
KINCUT	7	0	—	7	1.00 ± 0.00

The delayed coincidence time distribution is consistent with the K^+ mean life. The π^+ decay time for these events still appears somewhat stretched out, but not excessively so. Contrary to the first two events observed, the additional events are spread out in the kinematic space. Figure 5.82 shows the kinematic distribution of the events before the final cut was applied. The large group of events immediately above the $K^+ \to \pi^+\nu\overline{\nu}$ search region is again due to $K_{\pi 2}$ peak events for which the photons from π^0 decay were not detected. The smaller group about 20 MeV higher in energy than the $K_{\pi 2}$ peak corresponds to $K_{\pi 2}$ events in which a low energy photon ($\sim$ 20 MeV) from π^0 decay converted in the range stack on top of the π^+ track. Such events were

Table 5.37: Characteristics of the remaining 1991 events after full analysis of the entire $\pi\nu\overline{\nu}$ data sample.

Quantity	Event						
	A	B	C	D	E	F	G
RS stopping layer	4	3	3	3	4	4	4
RS stopping sector	11	21	21	10	10	24	16
Total π^+ momentum (MeV/c)	174.0	188.8	176.6	164.2	184.6	189.1	186.9
Total π^+ energy (MeV)	85.3	87.0	86.0	73.2	92.2	90.8	93.5
Total π^+ range (cm)	21.6	22.6	22.6	16.6	24.3	24.6	25.8
Rest mass (MeV/c^2)	133.1	147.5	142.0	153.6	137.4	143.6	135.5
K^+ decay time (ns)	14.7	2.7	21.3	10.0	12.3	4.9	2.1
π^+ decay time (ns)	28.6	47.2	28.9	13.9	58.6	55.8	15.2

not observed in the 1989 data sample because of the application of the DEDXRS cut, which rejected events with an anomalous energy deposition pattern for the track in the range stack. Background studies in 1991 showed that such a cut would have no effect other than acceptance loss on the background events in the $K^+ \to \pi^+\nu\overline{\nu}$ search region. Indeed, the application of such a cut to the Pass3 sample rejected almost all the events in the satellite peak above the $K^+ \to \pi^+\nu\overline{\nu}$ search region but none of the events in the search region.

Figure 5.83 shows the same distributions as in figure 5.82 for a large number of $K^+ \to \pi^+\nu\overline{\nu}$ Monte Carlo events satisfying the simulated $\pi\nu\overline{\nu}$ trigger and the offline analysis cuts, indicating the shape of the signal from $K^+ \to \pi^+\nu\overline{\nu}$ assuming a V-A weak interaction coupling.

5.1.2.3 1991 Pass4

As mentioned above, after analyzing 30% of the Pass2 data sample using all cuts and finding two candidate events, the offline cuts were re-examined. Based on the available background samples, it was found that the INTIME, INTSE and TGTRACK cuts could be made more restrictive while satisfying the condition that the rejected fraction be at least a factor of two larger than the acceptance loss. Tables 5.38 and 5.39 list the new parameters for the INTIME and INTSE cuts respectively, to be compared to tables 3.6 and 3.7. For the INTIME cut, in addition to widening the coincidence time window and lowering the energy threshold, a cut was

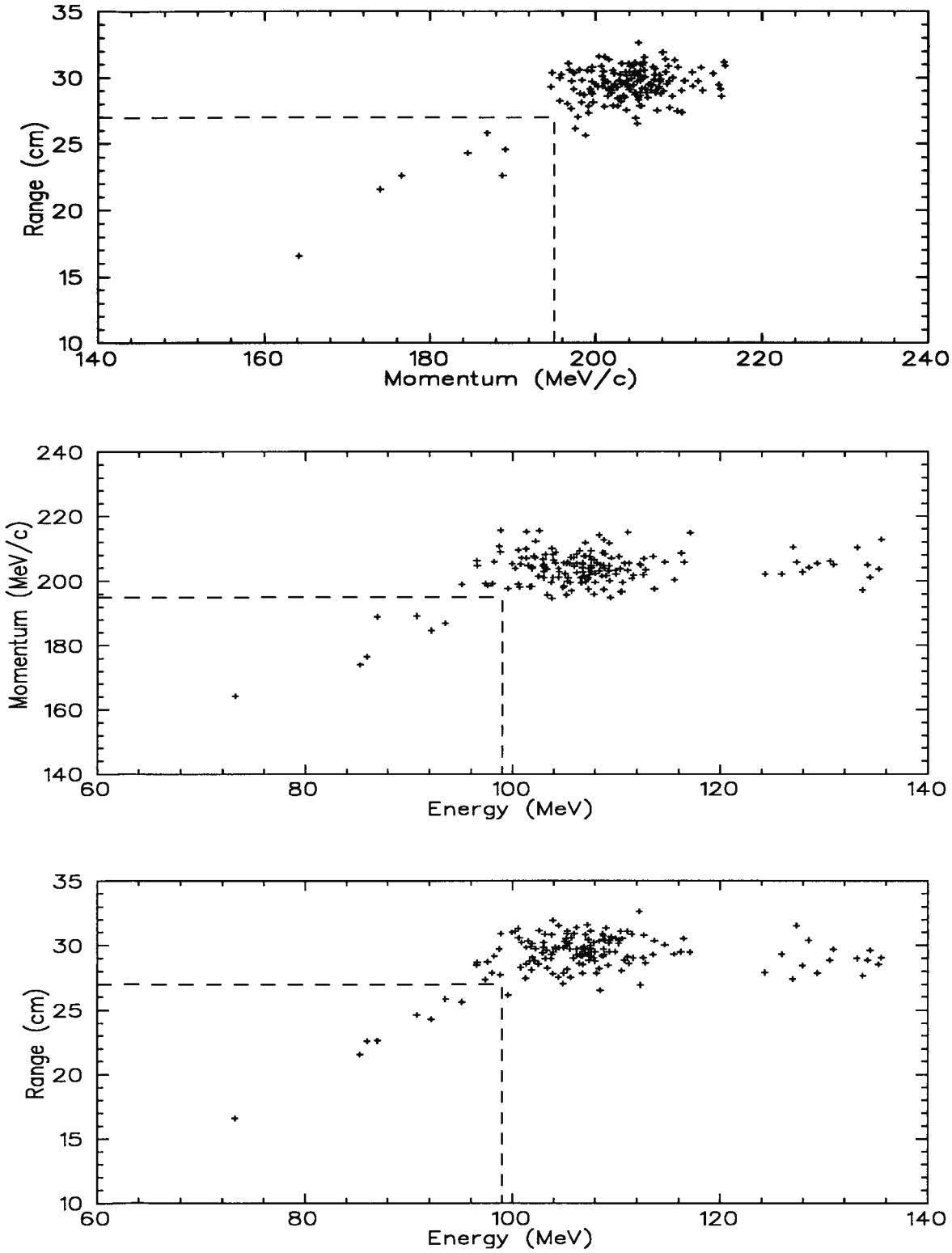

Figure 5.82: Kinematic distributions for 1991 events before the final Pass3 cut. The dashed lines indicate the upper limits of the $K^+ \to \pi^+ \nu\bar{\nu}$ search region.

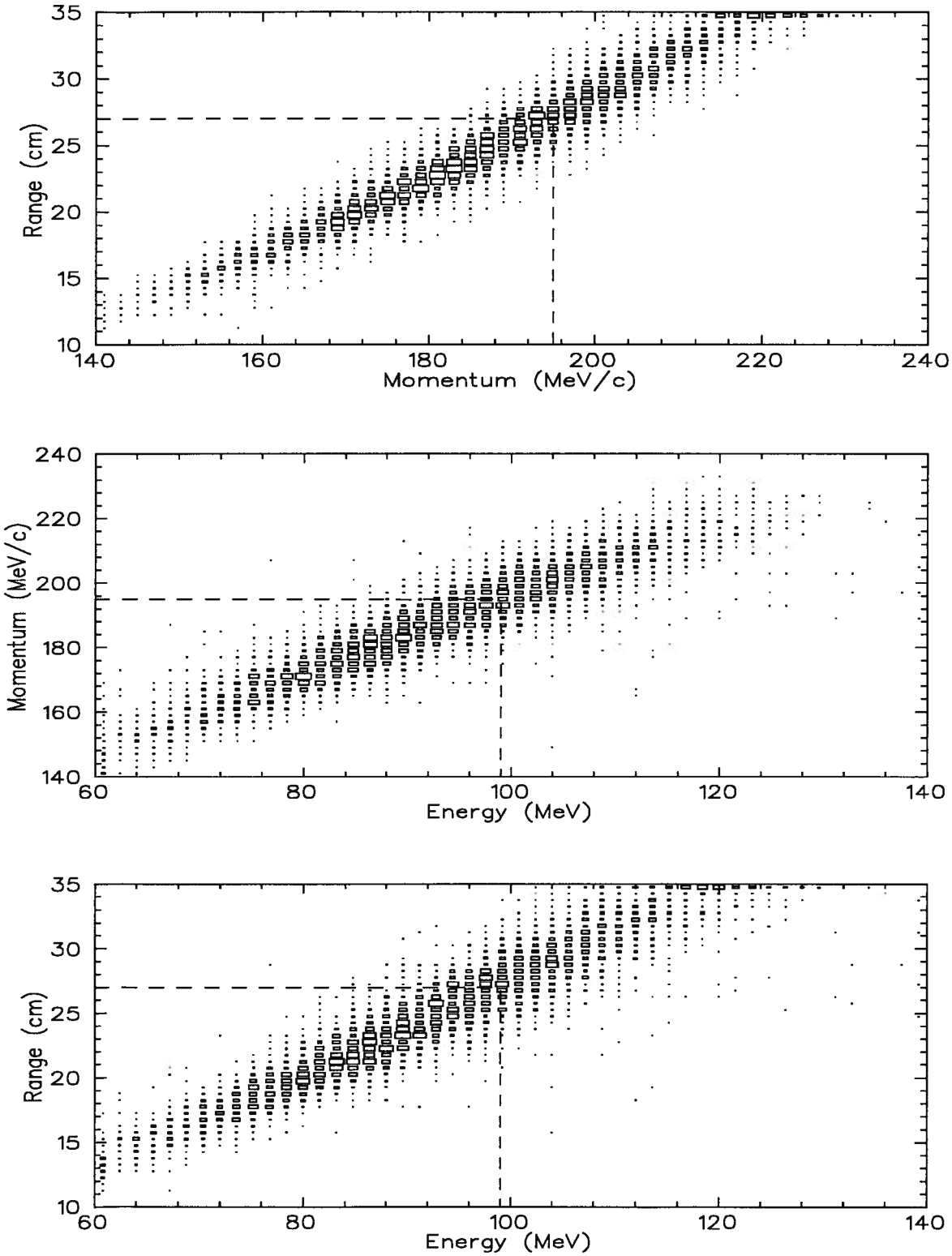

Figure 5.83: Kinematic distributions for $K^+ \to \pi^+\nu\overline{\nu}$ Monte Carlo events before the final cut. The dashed lines indicate the upper limits of the $K^+ \to \pi^+\nu\overline{\nu}$ search region.

placed on the energy in the V-counters measured by the ADCs for cases where no time value was recorded in the TDCs for the same module in the range [-400,+200] ns. For INTSE, some windows and thresholds were changed and new categories were added : barrel veto single end ADC hits with TDC hits at both ends, barrel veto single end ADC hits with no TDC hits and endcap time hits with no energy measured with the ADCs. For the latter, at least two modules with time hits within the coincidence time window are required.

Table 5.38: Parameters for tighter 1991 INTIME cut, to be compared to table 3.6.

Subsystem	**Time window**	**Threshold**
	[Min,Max] (ns)	(MeV)
RS	[-2.0,+16.0]	0.5
BV	[-8.0,+15.0]	0.4
EC	[-4.5,+8.0]	0.0
IC	[-6.0,+6.0]	0.2
VC	[-6.0,+5.0]	0.1
VC	No time	0.8

Table 5.39: Parameters for tighter 1991 INTSE cut to be compared to table 3.7.

Subsystem	**Ends hit**		**Time window**	**Threshold**
	Energy	Time	[Min,Max] (ns)	(MeV)
RS	both	single	[-10.0,+10.0]	0.0
RS	single	both	[-5.0,+5.0]	0.0
RS	single	single	[-10.0,+10.0]	0.25
BV	both	single	[-12.0,+8.0]	0.0
BV	single	both	[-6.0,+12.0]	0.0
BV	single	single	[-14.0,0.0]	0.4
BV	single	none	—	1.0
EC	none	2 hits	[-2.0,+10.0]	1.0

The parameters for these two cuts were adjusted by examining the events remaining after the cuts were applied with the previous set of parameters. For the rejection, a sample of $\pi\nu\bar{\nu}$ events failing the TGTRACK cut and located in the $K^+ \to \pi^+\nu\bar{\nu}$ signal region was used, while for the acceptance a sample of $K_{\mu 2}$ events was used.

For TGTRACK, the cut position for $E_\pi^{\rm disc}$ was moved from 1.5 MeV to 1.0 MeV. $E_\pi^{\rm disc}$ is the energy sum for the target elements off the swath defined by the drift chamber track and not connected to the other track elements but in coincidence with the time of the track. This is a form of photon veto. The sample used to adjust the cut was the sample of events failing the photon veto cuts beyond Pass1 and located in the $K^+ \to \pi^+\nu\bar{\nu}$ kinematic search region (see table 4.19). Of the 71 events in the sample, 3 were rejected by tightening the TGTRACK cut.

The tighter cuts described here gave an additional rejection factor of 1.58, primarily against $K_{\pi 2}$ background, with an acceptance relative to the Pass3 cuts of 0.83. They also affected the background estimates. In most cases the change was small and came primarily from the acceptance loss of the additional cuts. For $K_{\pi 2}$ background, the estimate from Method 1 changed significantly. The value of the peak/tail ratio was updated to

$$\eta = \frac{2231}{74} = 30.1 \pm 3.5 \,. \tag{5.92}$$

As will be seen below, the number of events remaining in the $K_{\pi 2}$ peak region after all cuts is 117. Therefore, the $K_{\pi 2}$ background estimate using Method 1 becomes

$$N_{\rm bgd} = \frac{117 \pm 11}{30.1 \pm 3.5} = 3.89 \pm 0.58 \,. \tag{5.93}$$

The change in the $K_{\pi 2}$ background estimate from Method 2 is more difficult to assess, since no events remained after Pass3 cuts were applied to the selected background sample. If we assume that the estimated additional rejection factor of $R_{\rm Pass4} = 1.58$ applies fully to $K_{\pi 2}$ background, we can then calculate the background estimate as

$$N_{\rm bgd} < \frac{2.3}{R_{\rm TGFIT} - 1} \times \frac{1}{R_{\rm B4TD}} \times \frac{1}{R_{\rm Pass4}} = 1.3 \tag{5.94}$$

where we modified equation 4.57.

The application of these tighter cuts on the events satisfying all Pass3 requirements resulted in the rejection of three of the seven events in the $K^+ \to \pi^+\nu\bar{\nu}$ search region. Outside of the search region 117 of the 159 events analyzed satisfied all requirements. Figure 5.84 shows the kinematic distributions of the events before the final cut.

Referring back to the designation of table 5.37, the three events rejected were events B, C and D. Event B, as mentioned before, had a 0.58 MeV energy deposition in one endcap

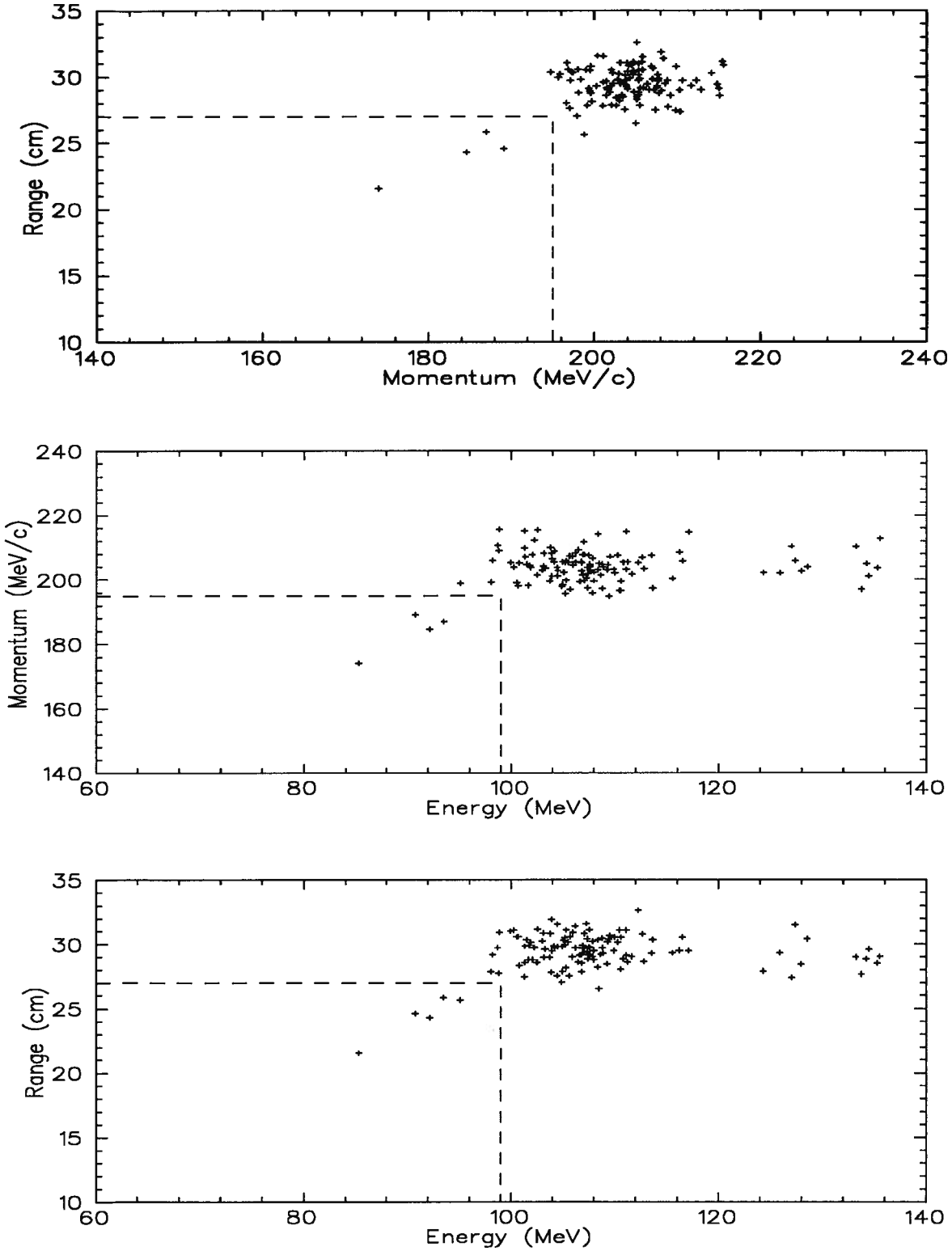

Figure 5.84: Kinematic distributions for remaining 1991 events before the final cut for Pass4 analysis. The dashed lines indicate the upper limits of the $K^+ \to \pi^+ \nu\bar{\nu}$ signal region.

module with a time within the coincidence window. It might be argued that rejecting this event somewhat biased the analysis since the endcap energy deposition had been observed before the cut was adjusted. However, the energy threshold of the endcap cut was not adjusted based on this event but rather by looking at the background sample. All other INTIME and INTSE energy thresholds and time windows were re-adjusted in order to tighten the photon veto cuts as much as possible. Therefore, the bias introduced by rejecting this event is most likely negligible. Event C failed the TGTRACK cut with $E_{\pi}^{\rm disc} = 1.25$ MeV. Event D had two endcap TDC hits within the coincidence time window but with no measured ADC energy. Further discussion about the result and the nature of the remaining events will be reserved for chapter 6.

5.2 Acceptance

The combined acceptance of the detector, trigger and offline analysis must be determined in order to calculate a branching ratio. The calculation relied as much as possible on real data to take into account all the experimental conditions. The low bias monitor data were well suited to this task, since they were collected in the same conditions as the $\pi\nu\overline{\nu}$ data sets. Some acceptance factors, such as the detector geometrical acceptance and the effects of π^+ nuclear interactions cannot be determined using real data; for those items a Monte Carlo simulation was used.

Three monitor data samples were used to measure the acceptance factors : $K\mu 2(1)$, $K\pi 2(1)$ and π-scat. A description of the trigger requirements for these data sets was given in table 3.3. As their designation would suggest, these data sets contained primarily $K_{\mu 2}$, $K_{\pi 2}$ and beam pions respectively. The following sections describe the analysis of each of those data sets and the acceptance factors derived from each. As much as possible, cuts were applied in the same order as in the final analysis, particularly for groups of cuts which address the same backgrounds. This method should minimize systematic effects and possible double counting of acceptance losses.

5.2.1 $K_{\mu 2}$ measurements

By their nature, $K_{\mu 2}$ decays are ideal for measurements that require a single charged track and no other particles, one of the important features of $K^+ \to \pi^+ \nu\overline{\nu}$ decays. The drawbacks of $K_{\mu 2}$ decays are the high momentum of the charged particle, which is substantially higher than the upper limit of the accepted region of kinematics for this search, and the fact that the charged particle is a μ^+ as opposed to a π^+ . Nonetheless, the acceptance of several cuts was measured with a sample of $K_{\mu 2}$ decays. They are well suited for measuring the acceptance of cuts affected mainly by accidental losses, such as photon veto, beam and reconstruction cuts. The $K\mu 2(1)$ trigger is very efficient at selecting $K_{\mu 2}$ decays. Therefore, with minimal additional constraints clean samples were selected.

5.2.1.1 1989 $K_{\mu 2}$ measurements

Two separate samples of $K_{\mu 2}$ events were selected out of the $K\mu 2(1)$ monitor data sample. The first was selected by requiring that the events satisfy the online delayed coincidence cut and that there be a single track in the range stack, identified without the use of drift chamber tracking information. The delayed coincidence is not part of the $K\mu 2(1)$ trigger, and so it was required offline by looking at the trigger information recorded in the data. This sample was used to determine the acceptance of target and drift chamber track reconstruction cuts, as well as Level 1 trigger cuts and some beam counters cuts. After the target and drift chamber track reconstruction cuts had been applied, a $\pm 1.5\sigma$ cut on the total range, kinetic energy and momentum of the μ^+ was applied to improve the purity of the sample. The values of the mean and width (σ) of the $K_{\mu 2}$ kinematic peak were from fits to a Gaussian function plus a flat background component for all three quantities. Table 5.40 gives the details of the analysis as well as the acceptance of each cut considered.

Further explanations are necessary for the DC-SETUP cut. The low value of the acceptance is the result of a broken wire in the drift chamber. The wire broke about 65% into the 1989 data taking period. Because of the significant amount of time needed for a repair, it was decided to postpone it until data collection was complete for the year. Since the broken wire could have

Table 5.40: Acceptance of reconstruction cuts for 1989 data measured with $K_{\mu 2}$ decays.

Cut	# events	Acceptance
	24686	
TARGET	24108	0.97658 ±0.00096
DC-SETUP	17084	0.7086 ±0.0029
$R_{\rm tot}$, $E_{\rm tot}$, $P_{\rm tot}$ cut	8666	—
Level 1 $N_{TG} < 20$	6992	0.8068 ±0.0042
Level 1 IC, Hextant cut	6813	0.9744 ±0.0019
CERENKOV	6649	0.9759 ±0.0018
BM_HOLE	6551	0.9853 ±0.0015
B4TD	6476	0.9886 ±0.0013

curled around several other wires, the high voltage was turned off for a section covering one third of the drift chamber active volume, resulting in the low acceptance of the track reconstruction cut. Furthermore, the acceptance obtained here is for charged particles with a momentum of 236 MeV/c, which is significantly higher than the momentum in the $K^+ \to \pi^+\nu\bar{\nu}$ kinematic search region. A correction based on the ratio of the DC-SETUP cut acceptance for $K_{\mu 2}$ and $K^+ \to \pi^+\nu\bar{\nu}$ events simulated with a Monte Carlo program was applied to the number given in table 5.40. The corrected value was $A_{\rm DC-SETUP} = 0.672 \pm 0.003$.

The second sample of $K_{\mu 2}$ decays was selected by applying the target and drift chamber track reconstruction cuts, the CERENKOV and B4TD cuts to reduce beam pion contamination and by requiring that the track not reach the outermost layer of the range stack. The latter requirement was applied using the trigger information recorded with the events and was to ensure that the muon did not deposit energy in the barrel veto, since this sample was used to determine the acceptance of all photon veto cuts. Also determined with this sample were the acceptance of the range stack and other track reconstruction cuts not determined with the other $K_{\mu 2}$ sample, as well as timing cuts and vertex cuts. A total of 8011 events were selected. Table 5.41 gives details of the analysis and the acceptance of each cut. Cuts applied to the other sample of $K_{\mu 2}$ events were also applied here to minimize possible double counting of acceptance losses.

Table 5.41: Acceptance of photon veto, event reconstruction, timing and vertex cuts measured with $K_{\mu 2}$ decays. The values used in the final $K^+ \to \pi^+ \nu\overline{\nu}$ acceptance calculation are indicated by a check mark. For the others, the acceptance was measured by other means.

Cut	**# events**	**Acceptance**	**Used**
Events selected	8011		
ICOUNTER ($E_{\rm IC} < 5$ MeV)	7765	0.9693 $\pm$0.0019	
RS-TRACK	7731	0.99562 $\pm$0.00075	$\surd$
$R_{\rm tot}$, $E_{\rm tot}$, $P_{\rm tot}$ cut	4917	—	
Level 0 Del. coinc.	4081	0.8300 $\pm$0.0054	$\surd$
Level 0 Photon veto	3899	0.9554 $\pm$0.0032	$\surd$
Level 1 $N_{TG} < 20$	3069	0.7871 $\pm$0.0066	
Level 1 IC, Hextant cut	3006	0.9795 $\pm$0.0026	
BM_HOLE	2955	0.9830 $\pm$0.0024	
NK	2946	0.9970 $\pm$0.0010	$\surd$
PROMPT	2512	0.8527 $\pm$0.0065	$\surd$
DISENPI	2496	0.9936 $\pm$0.0016	$\surd$
DISENK	2475	0.9916 $\pm$0.0018	$\surd$
INT_EB	1995	0.8061 $\pm$0.0079	$\surd$
NDC	1881	0.9429 $\pm$0.0052	$\surd$
DC-CHI2	1825	0.9702 $\pm$0.0039	$\surd$
ICOUNTER	1795	0.9836 $\pm$0.0030	
INT_RIV	1574	0.8769 $\pm$0.0078	$\surd$
TGTRACK	1223	0.777 $\pm$0.010	$\surd$
FIDUCIAL	1169	0.9558 $\pm$0.0059	
ZDCTZ	1126	0.9632 $\pm$0.0055	$\surd$
ZK_EK	1106	0.9822 $\pm$0.0039	$\surd$
EB4_EK	1060	0.9584 $\pm$0.0060	$\surd$

Because of the dependence of energy deposition on particle type and momentum, the ICOUNTER cut acceptance measured here was not used; it was rather determined with a sample of $K_{\pi 2}$ decays (see section 5.2.2). Also, a correction was necessary for the cut on the maximum energy deposition in target elements struck by the outgoing charged particle (part of the TGTRACK cut). This correction amounted to 0.962 ± 0.003, resulting in $A_{\mathrm{TGTRACK}} = 0.747 \pm 0.010$. The acceptance of the FIDUCIAL and ZDCTG cuts was corrected for the momentum dependence of the charged particle track in the same way that the DC-SETUP cut was corrected. The values obtained were $A_{\mathrm{FIDUCIAL}} = 0.932 \pm 0.004$ and $A_{\mathrm{ZDCTG}} = 0.923 \pm 0.006$.

Finally, the acceptance of the RSPC cut was determined by counting the number of events with a hit in the chamber located in the sector diametrically opposite to the sector in which the muon from $K_{\mu 2}$ decay came to a stop. The value measured was $A_{\mathrm{RSPC}} = 0.98321 \pm 0.00097$.

5.2.1.2 1991 $K_{\mu 2}$ measurements

A sample of $K_{\mu 2}$ events was selected by applying the online delayed coincidence cut, based on the trigger information recorded with the events. This selected K^+ decays and ensured that a charged particle passed through one of the I-counters and was contained in the DC/RS fiducial region. Since the data sample was to be used to measure the acceptance of the photon veto cuts, muons that reached the last layer of the range stack were rejected using the trigger information.

Table 5.42 gives the statistics of the sample selection and shows the results of the application of the track reconstruction cuts, along with the value of the acceptance for each cut. Note that for the RS-TRACK cut, the minimum energy deposition requirement of 4 MeV in the last counter of the track was not included; only the track reconstruction part of the cut was used. Because of a possible dependence on the momentum of the track, the acceptance of the DC-SETUP, RS-TRACK and ICOUNTER cuts was not taken from this analysis. It was rather measured with π^+ tracks from $K_{\pi 2}$ decays, which have a momentum closer to the one of π^+ from $K^+ \to \pi^+ \nu \overline{\nu}$ decays accepted in this analysis; this will be described in next section 5.2.2.

In principle, the acceptance of the TRKTIM cut could be taken directly from this analysis,

Table 5.42: Acceptance of event reconstruction cuts for 1991 data measured with $K_{\mu 2}$ decays. Only the value of the acceptance for the TARGET cut was ultimately used in the final acceptance calculation.

Cut	# events	Acceptance
	73766	
Online del. coinc.	49198	—
Online RS layer 21 veto	20360	—
	20360	—
TARGET	20107	0.98757 ± 0.00078
DC-SETUP	17127	0.8518 ± 0.0025
RS-TRACK	17051	0.99556 ± 0.00051
ICOUNTER	16105	0.9445 ± 0.0018
TRKTIM	15027	0.9331 ± 0.0020

but there is one caveat. Because this cut requires consistency between the time of the track measured in the target, I-counter and range stack, events which have no pion element in the target will be rejected by it. By selecting muon tracks which do not reach the last layer of the range stack, the K^+ decay vertex distribution of the events selected was biased towards the center of the target in the xy plane. This implied that the number of events rejected because there were no target elements struck by the muon track was less, thereby increasing the acceptance of the TRKTIM cut. The $K\mu 2(1)$ monitor events were re-analyzed in the same way as in table 5.42, but this time without rejecting the events reaching the last layer of the range stack. From this analysis, the acceptance of the TRKTIM cut was obtained :

$$A_{TRKTIM} = \frac{32810}{37183} = 0.8824 \pm 0.0017 \,. \tag{5.95}$$

The acceptance of the other event reconstruction cuts was the same as in table 5.42 within statistical errors.

The next step was to determine the acceptance of photon veto cuts and beam cuts. Before proceeding, the data sample satisfying all cuts in table 5.46 was purified by applying a cut on the total momentum, range and energy of the μ^+ . The cut was applied at $\pm 2\sigma$ for each quantity, based on Gaussian fits of the distributions. Table 5.43 shows the results of the analysis. As in the case of event the reconstruction cuts, the acceptance of cuts that might depend on

particle type or momentum of the charged particle was not taken from this analysis, but rather from analysis of a sample of $K_{\pi 2}$ decays. This included FIDUCIAL, TGTRACK, TGFIT and VTX_PCA. Also, the acceptance of the PROMPT cut was not measured with this sample, but rather was measured along with the acceptance of the online delayed coincidence cut, which was used to select this sample. All cuts were nonetheless applied, even if their acceptance was not being measured, to avoid possible double counting of acceptance losses.

Table 5.43: Acceptance of photon veto and beam cuts measured with $K_{\mu 2}$ decays for 1991 data. The values used in the final $K^+ \to \pi^+ \nu\overline{\nu}$ acceptance calculation are indicated by a check mark.

Cut	# events	Acceptance	Used
Events selected	10646		
Online EC & BV veto	9654	0.9068 ± 0.0028	√
Hextant cut	9448	0.9787 ± 0.0015	√
PROMPT	8836	0.9352 ± 0.0025	
INTIME	6008	0.6799 ± 0.0050	√
INTSE	4824	0.8029 ± 0.0051	√
FIDUCIAL	4604	0.9544 ± 0.0030	
TGTRACK	3318	0.7207 ± 0.0066	
TGFIT	3060	0.9222 ± 0.0046	
BM_HOLE	3021	0.9872 ± 0.0020	√
B4_CNTR	3011	0.9967 ± 0.0010	√
VTX_PCA	2735	0.9083 ± 0.0053	
CERENKOV	2729	0.99781 ± 0.00089	√
BWPC	2633	0.9648 ± 0.0035	√
PB-GLASS	2330	0.8849 ± 0.0062	√
B4TD	2243	0.9627 ± 0.0039	√

The acceptance of the delayed coincidence, both online and offline, was also measured with $K_{\mu 2}$ decays. A series of cuts not including the delayed coincidence requirement were applied to the $K\mu 2(1)$ monitor data sample to select a clean sample of $K_{\mu 2}$ events; the delayed coincidence cuts were subsequently applied to determine their acceptance. The cuts used to select the data sample were : online RS layer 21 veto, TARGET, DC-SETUP, RS-TRACK, ICOUNTER, TRKTIM, FIDUCIAL and a $\pm 2\sigma$ cut on the total range, momentum and energy as in table 5.43. Out of the total of 73766 events analyzed, 12363 satisfied all selection criteria. Table 5.44 gives

the measured acceptance for the online and offline delayed coincidence cuts. Also measured with this sample is the acceptance of the online IC requirement, which in principle should be redundant with the delayed coincidence. However, because of slightly different discriminator thresholds for the two requirements there is a small additional acceptance loss from the IC requirement.

Table 5.44: Acceptance of delayed coincidence cuts and IC trigger cut measured with $K_{\mu 2}$ decays for 1991 data.

Cut	# events	Acceptance
Events selected	12363	
Online del. coinc.	10052	0.8131 ± 0.0035
Online IC cut	10003	0.99512 ± 0.00069
PROMPT	9336	0.9333 ± 0.0025

The acceptance loss due to accidental hits of two other trigger cuts, $\overline{(13_{CT} + ... + 18_{CT})}$ (range veto) and $\overline{(19 + 20 + 21)}$ (muon veto), were also determined with $K\mu 2(1)$ monitor data. These factors could not be determined directly based on the trigger information recorded with the data since all μ^+ tracks from $K\mu 2(1)$ triggers reach at least layer 19 of the range stack. The ± 20 ns coincidence time window of the trigger had to be simulated using the range stack information from the ADCs and TDs. A region seven sectors wide centered on the stopping range stack sector was excluded from the search in order to avoid hits related to the μ^+ track. Acceptance losses from both cuts overlap with acceptance losses from the INTIME and INTSE cuts. Therefore, the measurement was made with the $K_{\mu 2}$ data sample after all photon veto cuts were applied. The events satisfying all cuts in table 5.43 were used.

For the muon veto cut, the measurement was done by simply counting the number of events with a hit in either layer 19, 20 or 21 of the range stack in the region away from the μ^+ track. This number was corrected for the fact that 7 sectors out of 24 were excluded from the search. The measured acceptance was

$$A_{\mathrm{muveto}} = 0.9877 \pm 0.0025 \,. \tag{5.96}$$

For the range veto, losses occured when accidental hits appeared in layers 13 to 18 in the

sector with the $T \cdot A$ hit or up to two sectors over from the $T \cdot A$ sector in the direction of a curling positively charged particle. For the events remaining after application of the muon veto cut above, layers 13 to 18 of the range stack were scanned for hits in a region three sectors wide diametrically opposite to the μ^+ track. The measured acceptance was

$$A_{\rm rgeveto} = 0.99848 \pm 0.00076 \, . \tag{5.97}$$

5.2.2 $K_{\pi 2}$ measurements

5.2.2.1 1989 $K_{\pi 2}$ measurements

For 1989 data, the only cut whose acceptance was measured with $K_{\pi 2}$ decays selected out of $K\pi 2(1)$ monitor data was the ICOUNTER cut. The value obtained was $A_{\rm ICOUNTER} = 0.943 \pm 0.002$. Many more measurements were done with $K_{\pi 2}$ decays for 1991 data; these are described in the next section.

5.2.2.2 1991 $K_{\pi 2}$ measurements

$K_{\pi 2}$ decays have two advantages compared to $K_{\mu 2}$ decays for the determination of $K^+ \to \pi^+ \nu\overline{\nu}$ acceptance factors : the charged particle is a pion, and its momentum is reasonably close to the values allowed in the search for $K^+ \to \pi^+ \nu\overline{\nu}$. The drawback is of course the presence of photons from π^0 decay. This can be remedied by requiring that both photons from π^0 decay be detected in the barrel veto, essentially "pulling" them away from the central region of the detector. In this way, acceptance measurements can be made using the clean π^+ track.

$K\pi 2(1)$ monitor data were used. This trigger is not as efficient at selecting $K_{\pi 2}$ decays as the $K\mu 2(1)$ trigger is at selecting $K_{\mu 2}$ decays, primarily because of the large number of $K_{\mu 2}$ decays that can stop in range stack layers below 19. However, requiring the presence of two clearly identified clusters of energy in the barrel veto consistent with a π^0 from $K_{\pi 2}$ decay selected a fairly pure sample of $K_{\pi 2}$ events. The TARGET and PROMPT cuts were also applied to improve the purity of the sample. Table 5.45 shows the results of the selection; a total of 9882 $K_{\pi 2}$ events were selected out of the entire $K\pi 2(1)$ monitor data sample.

Table 5.45: $K_{\pi 2}$ event selection from 1991 $K\pi 2(1)$ monitor data.

Cut	# events	Rejection
$K\pi 2(1)$ monitor events	166726	
TARGET	163048	1.02256 ± 0.00038
PROMPT	97428	1.6735 ± 0.0034
π^0 photons in BV	9882	9.859 ± 0.094

The sample was then used to determine the acceptance of event reconstruction cuts and some vertex cuts. Table 5.46 shows the results of the analysis. Note that for the RS-TRACK cut, the 4 MeV minimum requirement in the last counter was not included; it was accounted for together with the TD cuts acceptance factors.

Table 5.46: Acceptance of event reconstruction cuts measured with $K_{\pi 2}$ decays for 1991 data. Numbers used in the final $K^+ \to \pi^+ \nu\overline{\nu}$ acceptance calculation are indicated by a check mark.

Cut	# events	Acceptance	Used
	9882		
DC-SETUP	8573	0.8675 ± 0.0034	$\surd$
RS-TRACK	8559	0.99837 ± 0.00044	$\surd$
ICOUNTER	7948	0.9286 ± 0.0028	$\surd$
TRKTIM	7587	0.9546 ± 0.0023	
FIDUCIAL	7158	0.9435 ± 0.0026	$\surd$
TGTRACK	4458	0.6228 ± 0.0057	$\surd$
TGFIT	4087	0.9168 ± 0.0041	$\surd$
VTX_PCA	3636	0.8896 ± 0.0049	$\surd$

The π^+ momentum spectrum for $K^+ \to \pi^+ \nu\overline{\nu}$ events accepted by this experiment is not the same as that for $K_{\pi 2}$ events. The possibility that a correction was required to take into account this momentum dependence was investigated. Use was made of Monte Carlo simulated events for both $K^+ \to \pi^+ \nu\overline{\nu}$ and $K_{\pi 2}$ decays. The ratio of the acceptance of each cut as measured with Monte Carlo events for the two types of data should give the appropriate correction. It was found that some cuts needed a downward correction while others needed an upward correction. The overall correction was consistent with unity, so this effect was neglected in the acceptance

calculation.

5.2.3 π-scat measurements

The π-scat trigger is a good source of isolated pions of various momenta emerging from the target and stopping in the range stack. With minimal event reconstruction cuts, a relatively pure sample of pions can be selected and then used to determine the acceptance of $\pi^+ \rightarrow \mu^+ \rightarrow e^+$ (TD) and kinematic cuts.

5.2.3.1 TD cuts

Simple event reconstruction cuts were applied to π-scat monitor events to select beam pions stopping in the range stack. In principle, the combined acceptance of FASFITPI and FITPI could simply be obtained by taking the ratio of events passed to events analyzed. However, even if kinematic cuts are applied to π-scat data it is very difficult to obtain a pure sample of stopped π^+ . In many cases the π^+ is absorbed in a nuclear interaction at the very end of its trajectory in the range stack and hence satisfies all kinematic requirements. Losses due to nuclear interactions are taken into account separately; we do not want to include them here as well.

An alternative method, based on the fact that most of the acceptance losses for the FITPI cut are due to early decays of the π^+ , was used to determine the acceptance. The time resolution of the TDs coupled with the finite rise and decay time of the scintillator pulses limited the ability to separate the decay muon pulse from the primary π^+ pulse. Therefore, by fitting the late part of the distribution of π^+ decay times measured by FITPI, where the acceptance should be very high, and extrapolating the fitted curve to the early time region, the acceptance loss could be estimated. Losses not due to early decays were taken into account by individually scanning a portion of the failed events and estimating the fraction of events that should have been accepted.

Both FITPI and FASFITPI were applied to the selected sample of pions. [1] The resulting

[1] Note that here the FITPI cut does not include tighter requirements on $\overline{T_\mu}$, $P_{\mu\pi}$, etc.

π^+ decay time spectra was used to perform the fits. Individual measurements were made for range stack layers B, C and 11; because of their different thicknesses, it can be expected that the acceptance will differ in each layer. For 1991 data, the acceptance of layer 12 was determined together with layer 11. Figure 5.85 shows the fit results for 1991 data. The depletion of events at early times can be clearly seen. The data was fit using a χ^2 minimization method to the function $y = Ae^{-t/\tau}$, where y is the number of counts in a bin, t is the time value of a bin, A is the normalization factor and τ is the mean life of the π^+ . The value of A is also the extrapolated number of events for the entire time range. The time range used for the fit was the one giving the best χ^2 per degree of freedom and resulting in a π^+ mean life consistent with the accepted value of $\tau_{\pi^+} = 26.030 \pm 0.024$ ns [17]. For example, the values obtained for the graphs in figure 5.85 were 26.83 ± 0.97 ns, 26.4 ± 1.0 ns and 26.1 ± 1.1 ns for layers B, C and 11–12 respectively. Adding a constant term to the function used for the fit did not improve the results. To determine the value of A, the fits were one parameter fits with τ fixed to the accepted value.

A pre-scaled sample of events failed by FITPI was hand scanned to correct for other losses. Since it is difficult to judge early decays, only events with a decay time of at least one π^+ lifetime were considered; therefore the number observed had to be corrected by $e^{1.0}$. The acceptance for a given layer was expressed as

$$A_{\text{FITPI}} = \frac{N_P}{N_E + \frac{N_{PH}}{N_{HS}} \times N_F \times e} \tag{5.98}$$

where N_P is the number of events passing the FITPI cut, N_E is the extrapolated number of events based on the fit, N_F is the number of events which failed the FITPI cut, N_{HS} is the number of failed events hand scanned and N_{PH} is the number of hand scanned events that should have been accepted by FITPI. Table 5.47 gives the final calculated value of the acceptance for each layer for 1989 and 1991 data. There are two reasons for the lower acceptance in 1991 compared to 1989 : first, the higher beam rate in 1991 caused more mistakes by the fitting procedure due to random activity in the stopping counter. The effect increases with proximity of the stopping counter to the beam area. And second, the use of logarithmic amplifiers for range stack layers B and C is likely to have worsened the double pulse resolution.

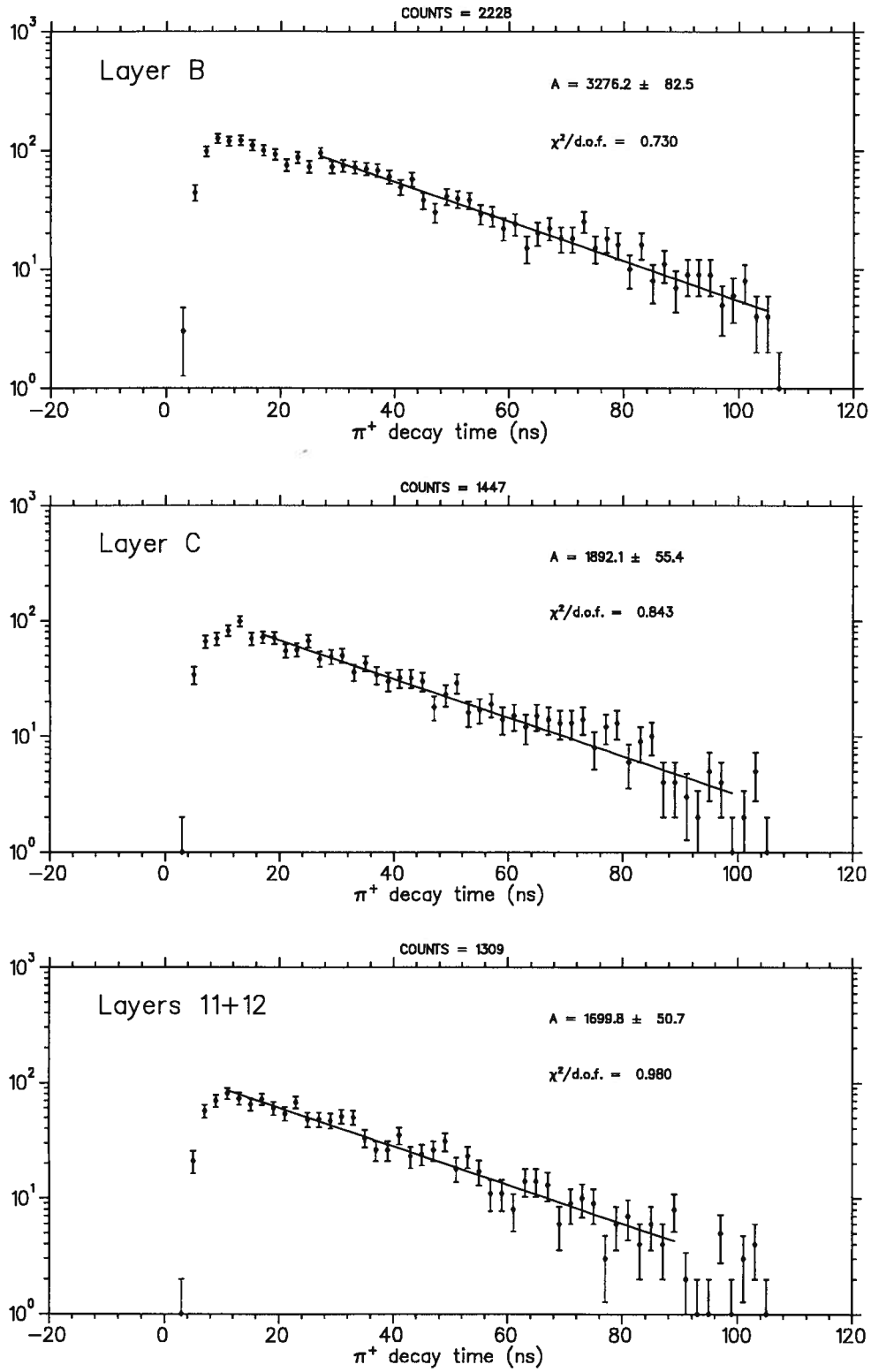

Figure 5.85: Pion decay time distribution used to determine the acceptance of the FITPI and FASFITPI cuts (1991 data).

Table 5.47: Acceptance of FITPI and FASFITPI cuts for each range stack layer, calculated according to equation 5.98.

Year	Layer		
	B	C	11+12
1989	0.764 ± 0.025	0.767 ± 0.025	0.771 ± 0.023
1991	0.581 ± 0.022	0.667 ± 0.028	0.712 ± 0.024

Once the FITPI cut had been applied, the purity of the data sample was very high. Therefore, the acceptance of all other TD cuts was determined simply by applying the cuts to the data sample in succession and taking the ratio of events passed over events analyzed. Tables 5.48 and 5.49 show the results of the analysis for individual range stack stopping layers and gives the overall acceptance for all TD cuts except FITPI and FASFITPI.

Table 5.48: Acceptance of 1989 TD cuts other than FASFITPI and FITPI for each range stack layer.

Cut	Layer		
	B	C	11
Selected pions	513	302	187
Online $\pi \rightarrow \mu$ cut	0.793 ± 0.018	0.679 ± 0.027	0.850 ± 0.026
FITPI (ΔT_μ ,$P_{\mu\pi}$)	0.744 ± 0.022	0.810 ± 0.027	0.887 ± 0.025
ELECTRON	0.739 ± 0.025	0.741 ± 0.034	0.858 ± 0.029
ELVETO	0.978 ± 0.010	1.000 ± 0.000	1.000 ± 0.000
FITPI ($\overline{T_\mu}$)	0.879 ± 0.022	0.860 ± 0.031	0.848 ± 0.032
Total	0.375 ± 0.021	0.350 ± 0.027	0.549 ± 0.036

One additional acceptance factor had to be accounted for. There is a finite probability that the muon from π^+ decay will leave the counter in which the π^+ came to rest. For a rectangular counter of length ℓ, width w and thickness t, the probability for a particle traveling a distance d ($d < t < w < \ell$) to exit the counter is

$$\mathcal{P} = \frac{d}{2}(\frac{1}{t} + \frac{1}{w} + \frac{1}{\ell}) \tag{5.99}$$

where higher order terms were neglected. For the case of range stack counters, the $1/\ell$ term can be neglected. The $1/w$ term represents the fraction of muons leaving from the side of the

Table 5.49: Acceptance of 1991 TD cuts other than FASFITPI and FITPI for each range stack layer.

Cut	Layer		
	B	**C**	**11+12**
Selected pions	2228	1447	1309
Online $\pi \rightarrow \mu$ cut	0.6934 ± 0.0098	0.770 ± 0.011	0.8732 ± 0.0092
4 MeV in last RS counter	0.9683 ± 0.0044	0.9767 ± 0.0045	0.9904 ± 0.0029
FITPI χ^2	0.9044 ± 0.0076	0.9237 ± 0.0080	0.9037 ± 0.0088
TD_MDA	0.9298 ± 0.0069	0.9094 ± 0.0090	0.9883 ± 0.0034
TDFOOL	0.9594 ± 0.0056	0.9617 ± 0.0063	0.9693 ± 0.0054
ELVETO	0.8956 ± 0.0088	0.9135 ± 0.0095	0.9837 ± 0.0040
ELECTRON	0.765 ± 0.013	0.8082 ± 0.014	0.850 ± 0.012
Total	0.371 ± 0.010	0.448 ± 0.013	0.626 ± 0.013

counter. This is only a loss if the stopping counter is at the boundary between two range stack hextants, since the TDs digitize the signals from a whole hextant and no flag information was required for the muon pulse. Therefore, the muon escape probability is

$$\mathcal{P}' = \frac{d}{2}(\frac{1}{t} + \frac{1}{4w}) \,. \tag{5.100}$$

The minimum energy deposition required by the FITPI cut for the muon is approximately 2 MeV, which translates into a range $d = 1.37$ mm. Table 5.50 summarizes the calculation of the correction for muon escape.

Table 5.50: Muon escape correction.

Layer	t (cm)	w (cm)	$\mathcal{P}'(\%)$	Correction
B	5.85	14.4	1.29	0.9871
C	3.90	15.7	1.86	0.9814
11+12	1.95	17.0	3.61	0.9639

The TD acceptance for individual range stack layers is the product of the FASFITPI+FITPI acceptance, the acceptance of all other TD based cuts and the muon escape correction. The final acceptance was obtained by taking a weighted sum of the acceptance for individual layers. The weights were obtained from the range stack stopping layer distribution for $K^+ \rightarrow \pi^+\nu\bar{\nu}$ Monte

Carlo events. Tables 5.51 and 5.52 summarize the calculation of the overall TD acceptance for the $K^+ \to \pi^+\nu\overline{\nu}$ analysis.

Table 5.51: Overall TD acceptance for 1989 data.

Quantity	**Layer**		
	B	**C**	**11**
FASFITPI + FITPI acceptance	0.764 ± 0.025	0.767 ± 0.025	0.771 ± 0.023
Other TD cuts acceptance	0.375 ± 0.021	0.350 ± 0.027	0.549 ± 0.036
Muon escape correction	0.9871	0.9814	0.9639
Total acceptance	0.283 ± 0.018	0.263 ± 0.022	0.408 ± 0.029
Stopping fraction	0.6798 ± 0.0075	0.2561 ± 0.0070	0.0641 ± 0.0041
Final TD acceptance	0.285 ± 0.014		

Table 5.52: Overall TD acceptance for 1991 data.

Quantity	**Layer**		
	B	**C**	**11+12**
FASFITPI + FITPI acceptance	0.581 ± 0.022	0.667 ± 0.028	0.712 ± 0.024
Other TD cuts acceptance	0.371 ± 0.010	0.448 ± 0.013	0.626 ± 0.013
Muon escape correction	0.9871	0.9814	0.9639
Total acceptance	0.213 ± 0.010	0.293 ± 0.015	0.430 ± 0.017
Stopping fraction	0.6381 ± 0.0076	0.3046 ± 0.0073	0.0573 ± 0.0037
Final TD acceptance	0.2498 ± 0.0085		

5.2.3.2 Kinematic cuts

Using a sample of π-scat monitor data selected with TD cuts, it was straightforward to determine the acceptance of the kinematic cuts by simply counting the number of events passing each cut. As for the TD cuts acceptance, the measurements were made for individual range stack stopping layers. Tables 5.53 and 5.54 describe the results of the application of the kinematic cuts on the selected samples, and the calculation of the acceptance for 1989 and 1991 data respectively. As in the case of the TD acceptance, the final result is the weighted sum of the acceptance for each RS layer. The weights were obtained by taking the weights used in the TD

acceptance calculation and correcting them for the TD acceptance of each layer. This is to take into account the fact that the final stopping distribution is different than the one determined by the Monte Carlo after the application of the TD cuts.

Table 5.53: Acceptance of kinematic cuts for 1989 data.

Quantity	**Layer**		
	B	**C**	**11**
Events selected	571	334	265
RGEMOM	0.9685 ± 0.0073	0.949 ± 0.012	0.955 ± 0.013
DEDXRS	0.9620 ± 0.0081	0.946 ± 0.013	0.9921 ± 0.0056
MASS	0.942 ± 0.010	0.967 ± 0.010	0.9880 ± 0.0068
Acceptance	0.877 ± 0.014	0.868 ± 0.018	0.936 ± 0.015
Stopping fraction	0.674 ± 0.042	0.235 ± 0.021	0.091 ± 0.009
Final acceptance	0.880 ± 0.043		

Table 5.54: KINSCORE cut acceptance for 1991 data.

Quantity	**Layer**		
	B	**C**	**11+12**
Events selected	2331	1616	1574
Pass KINSCORE	1981	1339	1315
Acceptance	0.8498 ± 0.0074	0.8286 ± 0.0094	0.8354 ± 0.0093
Stopping fraction	0.543 ± 0.026	0.351 ± 0.020	0.106 ± 0.008
Final acceptance	0.841 ± 0.029		

5.2.4 Monte Carlo measurements

The geometrical and phase space acceptance, as well as the acceptance loss due to nuclear interactions and decay-in-flight of the π^+ were determined with a Monte Carlo simulation. The first two factors were determined by simulating $K^+ \to \pi^+\nu\bar{\nu}$ decays without π^+ decay and π^+ nuclear interactions. A comparison of this simulation with another in which π^+ decay and nuclear interactions were turned on allowed the determination of the acceptance loss from the latter two effects. In both cases the $\pi\nu\bar{\nu}$ trigger was simulated and the offline analysis applied

to the events satisfying the trigger cuts. Table B.75 shows the results for both simulations for 1991 data; similar numbers were obtained for 1989 data. Differences between the two were due to the different K^+ decay vertex distribution in the target and the different momentum resolution for the two years.

Table 5.55 summarizes the acceptance factors obtained from Monte Carlo simulation. The geometrical acceptance ($A_{\rm geom}$) is simply the fraction of events passing the $T \cdot A$ requirement for the sample simulated without π^+ nuclear interactions and π^+ decay. The phase space acceptance ($A_{\rm ph.sp.}$) is the product of several factors : the acceptance of the $B_{\rm CT}$ and range veto ($A_{\rm rgeveto}$) trigger requirements (see section 3.1.1), and the acceptance of the KINCUT cut (total energy, range and momentum) :

$$A_{\rm ph.sp.} = A_{B_{\rm CT}} \times A_{\rm rgeveto} \times A_{KINCUT} \tag{5.101}$$

The acceptance factor taking into account losses from π^+ decay and nuclear interactions ($A_{\rm nuc.}$) is simply the ratio of the combined trigger and analysis acceptance for the simulations with and without π^+ decay and nuclear interactions.

Table 5.55: Acceptance factors determined with Monte Carlo simulation.

Factor	**Year**	
	1989	**1991**
$A_{\rm geom}$	0.4199 ± 0.0018	0.4086 ± 0.0022
$A_{\rm ph.sp.}$	0.3008 ± 0.0035	0.3003 ± 0.0038
$A_{\rm nuc.}$	0.721 ± 0.018	0.706 ± 0.017

5.2.5 Final Acceptance

Tables 5.57 and 5.56 list all the acceptance factors used in calculating the overall $K^+ \to \pi^+\nu\overline{\nu}$ acceptance for 1989 and 1991 data respectively. All errors quoted in the tables are statistical only. The final values for the overall acceptance are

$$A^{89}_{\pi\nu\overline{\nu}} = (2.57 \pm 0.20) \times 10^{-3} \tag{5.102}$$

$$A^{91}_{\pi\nu\overline{\nu}} = (1.77 \pm 0.11) \times 10^{-3} \, . \tag{5.103}$$

Table 5.56: Final $K^+ \to \pi^+\nu\bar{\nu}$ acceptance table for 1989 analysis.

Cut	**Method**	**Acceptance**
Geometry	MC	0.4199 ± 0.0018
Phase space	MC	0.3008 ± 0.0035
Nuclear interactions & π^+ decay	MC	0.693 ± 0.018
Trigger		
Muon veto	$K_{\mu 2}$	0.989 ± 0.003
Delayed coincidence	$K_{\mu 2}$	0.8300 ± 0.0054
Barrel and endcap veto	$K_{\mu 2}$	0.9554 ± 0.0032
Level 1 $N_{TG} < 20$	$K_{\mu 2}$	0.8068 ± 0.0042
Level 1 IC, Hextant cut	$K_{\mu 2}$	0.9795 ± 0.0026
Event reconstruction		
TARGET	$K_{\mu 2}$	0.97658 ± 0.00096
DC-SETUP	$K_{\mu 2}$,MC	0.672 ± 0.003
DC-CHI2	$K_{\mu 2}$	0.9702 ± 0.0039
RS-TRACK	$K_{\mu 2}$	0.99562 ± 0.00075
RSPC	$K_{\mu 2}$	0.98321 ± 0.00097
ICOUNTER	$K_{\pi 2}$	0.943 ± 0.002
FIDUCIAL	$K_{\mu 2}$,MC	0.932 ± 0.004
ZDCTZ	$K_{\mu 2}$,MC	0.923 ± 0.006
Timing		
PROMPT	$K_{\mu 2}$	0.8527 ± 0.0065
Photon veto		
INT_EB	$K_{\mu 2}$	0.8061 ± 0.0079
INT_RIV	$K_{\mu 2}$	0.8769 ± 0.0078
B4TD	$K_{\mu 2}$	0.9886 ± 0.0013
NDC	$K_{\mu 2}$	0.9429 ± 0.0052
DISENPI	$K_{\mu 2}$	0.9936 ± 0.0016
DISENK	$K_{\mu 2}$	0.9916 ± 0.0018
Pion identification		
Transient Digitizers	π-scat	0.285 ± 0.014
Kinematic cuts	π-scat	0.880 ± 0.043
Vertex cuts		
TGTRACK	$K_{\mu 2}$	0.747 ± 0.010
NK	$K_{\mu 2}$	0.9970 ± 0.0010
ZK_EK	$K_{\mu 2}$	0.9822 ± 0.0039
EB4_EK	$K_{\mu 2}$	0.9584 ± 0.0060
Beam cuts		
CERENKOV	$K_{\mu 2}$	0.9759 ± 0.0018
BM_HOLE	$K_{\mu 2}$	0.9853 ± 0.0015
Total acceptance		$(2.57 \pm 0.20) \times 10^{-3}$

Table 5.57: Final $K^+ \to \pi^+\nu\overline{\nu}$ acceptance table for 1991 analysis.

Cut	Method	Acceptance
Geometry, phase space, physics		
Geometry	MC	0.4086 ± 0.0022
Phase space	MC	0.3003 ± 0.0038
Nuclear interactions & π^+ decay	MC	0.706 ± 0.017
Trigger		
Range veto	$K_{\mu 2}$	0.99931 ± 0.00070
Muon veto	$K_{\mu 2}$	0.9837 ± 0.0029
Delayed coincidence	$K_{\mu 2}$	0.8131 ± 0.0035
I-counter	$K_{\mu 2}$	0.99512 ± 0.00069
Barrel and endcap veto	$K_{\mu 2}$	0.9068 ± 0.0028
Hextant cut	$K_{\mu 2}$	0.9787 ± 0.0015
Event reconstruction		
TARGET	$K_{\mu 2}$	0.98757 ± 0.00078
DC-SETUP	$K_{\pi 2}$	0.8675 ± 0.0035
RS-TRACK	$K_{\pi 2}$	0.99837 ± 0.00044
ICOUNTER	$K_{\pi 2}$	0.9286 ± 0.0028
FIDUCIAL	$K_{\pi 2}$	0.9435 ± 0.0026
Timing		
PROMPT	$K_{\mu 2}$	0.9333 ± 0.0025
TRKTIM	$K_{\mu 2}$	0.8824 ± 0.0017
Photon veto		
INTIME	$K_{\mu 2}$	0.6799 ± 0.0050
INTSE	$K_{\mu 2}$	0.8029 ± 0.0051
PB-GLASS	$K_{\mu 2}$	0.8849 ± 0.0062
B4TD	$K_{\mu 2}$	0.9627 ± 0.0039
Pion identification		
Transient Digitizers	π-scat	0.2498 ± 0.0085
KINSCORE	π-scat	0.841 ± 0.029
Vertex cuts		
TGTRACK	$K_{\pi 2}$	0.6228 ± 0.0057
TGFIT	$K_{\pi 2}$	0.9168 ± 0.0041
VTX_PCA	$K_{\pi 2}$	0.8896 ± 0.0049
Beam cuts		
BM_HOLE	$K_{\mu 2}$	0.9872 ± 0.0020
B4_CNTR	$K_{\mu 2}$	0.9967 ± 0.0010
CERENKOV	$K_{\mu 2}$	0.99781 ± 0.00089
BWPC	$K_{\mu 2}$	0.9648 ± 0.0035
Total acceptance		$(1.77 \pm 0.11) \times 10^{-3}$

5.2.5.1 Scalar and tensor interactions

The acceptance for non-Standard Model $K^+ \to \pi^+\nu\overline{\nu}$ mediated by scalar or tensor interactions was obtained using a Monte Carlo simulation. Events with the appropriate kinematic distribution were generated; the $\pi\nu\overline{\nu}$ trigger was simulated and offline analysis cuts were applied. The first order acceptance relative to $A_{\pi\nu\overline{\nu}}$ was obtained for each process by taking the ratio of the number of surviving events to the number of surviving events from an identical simulation in which the kinematic distribution was based on the Standard Model (V-A). The number of events was normalized to the number of stopped K^+ in each simulation.

This acceptance had to be corrected for the fact that the π^+ stopping layer distribution in the range stack is different for each process. The distribution can have a significant effect on the TD acceptance (see section 5.2.3.1). The correction was calculated for each process for 1989 and 1991 data; it typically reduced the acceptance by a few percent. Table 5.58 gives the final calculated acceptances.

Table 5.58: Final calculated acceptance for $K^+ \to \pi^+\nu\overline{\nu}$ via scalar and tensor interactions.

Interaction	**Year**	
	1989	**1991**
Scalar	$(1.95 \pm 0.15) \times 10^{-3}$	$(1.299 \pm 0.081) \times 10^{-3}$
Tensor	$(3.14 \pm 0.24) \times 10^{-3}$	$(2.11 \pm 0.13) \times 10^{-3}$

5.2.5.2 $K^+ \to \pi^+ X^0$

The acceptance for $K^+ \to \pi^+ X^0$ was calculated in the same manner as scalar and tensor interaction $K^+ \to \pi^+\nu\overline{\nu}$, but had to be calculated as a function of M_{X^0}, the mass of the recoiling system. In this case, the effect of the π^+ stopping distribution in the range stack was more significant, as much 25%, and increased or decreased the acceptance, depending on M_{X^0}. The acceptance was calculated assuming that the particles (or system of particles) represented by X^0 are stable. Figure 5.86 shows the total acceptance for 1989 data in the range where it is significant, $150 < M_{X^0} < 260$ MeV/c^2. A similar curve was obtained for 1991 data.

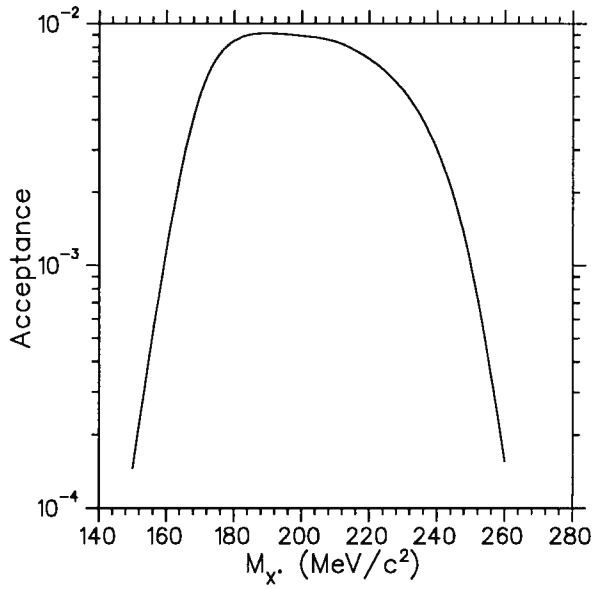

Figure 5.86: Acceptance for $K^+ \to \pi^+ X^0$ as a function of M_{X^0} (1989 data).

5.3 Integrated kaon flux

The other important ingredient needed to determine a branching ratio is the total number of K^+ observed by the detector. In principle, this number would simply be the total number of counts accumulated for the KT trigger requirement, which defines the presence of a K^+ in the detector. This sum should only be accumulated when the data acquisition system was "live" and not busy analyzing or transferring to tape the digital information from an event satisfying trigger conditions.

However, there are several ways in which an incoming K^+ can satisfy all KT trigger requirements without decaying at rest in the target. The K^+ could interact or decay in flight in the degrader and its products pass through the B4 counter and the target. The K^+ could also scatter in the target and decay elsewhere in the detector. These types of events should not be counted, since what we want is the total number of K^+ which decayed at rest in the target. Hence, a correction factor must be determined to take into account the incoming K^+ which do not stop and decay in the target.

To determine this important correction, use was made of the $K\mu 2(1)$ monitor data, out of which can be selected $K_{\mu 2}$ events with relatively few offline requirements. If we wanted to

measure the $K_{\mu 2}$ branching ratio with such an analysis, we would use the following expression:

$$B_{K_{\mu 2}} = \frac{N_p}{f_s \, N_{KT} \, A_{K_{\mu 2}}} \tag{5.104}$$

where N_p is the number of events satisfying all the analysis criteria, N_{KT} is the total KT count, f_s is the fraction of counts in N_{KT} which are stopped kaons in the target, and $A_{K_{\mu 2}}$ is the combined acceptance of online and offline cuts for $K_{\mu 2}$ events. If we can measure the latter, we see that by using the known value of $B_{K_{\mu 2}}$, the value of the correction f_s can be determined easily.

The acceptance $A_{K_{\mu 2}}$ was determined with a Monte Carlo simulation, and was corrected for various effects due to experimental conditions; it was therefore expressed as

$$A_{K_{\mu 2}} = A_{MC} \times A_{\rm cor} \, . \tag{5.105}$$

Results of the analysis of $K\mu 2(1)$ monitor data and $K\mu 2(1)$ simulated events for 1989 and 1991 are given in tables B.76 and B.77 respectively. Event reconstruction cuts were applied, as well as a cut on the total μ^+ range ($43 < R_{\rm tot} < 61$ cm) for 1989 data and on the total μ^+ range and momentum ($46 < R_{\rm tot} < 61$ cm , $215 < P_{\rm tot} < 255$ MeV/c) for 1991 data. For real data, the online and offline delayed coincidence cuts were also applied, as well as the CERENKOV cut. A total of 13801 and 27531 events remained after analysis of real data, for 1989 and 1991 data respectively. For the Monte Carlo simulation, there were a total of 47924 and 28529 stopped kaons for 1989 and 1991 data, respectively, before application of the simulated trigger requirements. Therefore, the uncorrected acceptance was

$$A^{89}_{MC} = \frac{15107}{47924} = 0.3152 \pm 0.0021 \tag{5.106}$$

$$A^{91}_{MC} = \frac{9118}{28529} = 0.3196 \pm 0.0028 \, . \tag{5.107}$$

The acceptance correction for the 1991 analysis was expressed as

$$A_{\rm cor} = A^D_{\rm L0Delc} \times \frac{A^D_{TG}}{A^M_{TG}} \times A^D_{\rm Delc} \times \frac{A^D_{DC}}{A^M_{DC}} \times \frac{A^D_{RS}}{A^M_{RS}} \times \frac{A^D_{IC}}{A^M_{IC}} \times \frac{A^D_{TRK}}{A^M_{TRK}} \times \frac{A^D_{FID}}{A^M_{FID}} \times A^D_{C_\pi} \tag{5.108}$$

where the superscripts D and M refer to real data and Monte Carlo events acceptance respectively, and the subscripts refer to the different cuts. A similar expression was used for the

1989 analysis. The values of the various acceptance factors used to compute the acceptance correction for 1989 and 1991 data are given in tables B.78 and B.79. Table 5.59 summarizes the calculation of the f_s factor for both 1989 and 1991 data. Use was made of equations 5.104 and 5.105, as well as the accepted value of $B_{K_{\mu 2}} = 0.6351 \pm 0.0019$ [17].

Table 5.59: Calculation of f_s for 1989 and 1991 data. Refer to equations 5.104 and 5.105 and the text for a description of the terms in the table.

Quantity	**1989**	**1991**
N_p	13801 ± 117	27531 ± 166
N_{KT}	220357	367963
A_{MC}	0.3152 ± 0.0021	0.3196 ± 0.0028
$A_{\rm cor}$	0.4962 ± 0.0058	0.5740 ± 0.0042
f_s	0.630 ± 0.010	0.6422 ± 0.0085

5.4 $K_{\pi 2}$ branching ratio measurement

As a partial check of the acceptance calculations and integrated kaon flux measurement, a measurement of the $K_{\pi 2}$ branching ratio was made using $K\pi 2(1)$ monitor data. A minimal set of cuts was applied in order to select $K_{\pi 2}$ events : event reconstruction cuts, delayed coincidence, TD cuts, and the CERENKOV beam cut to eliminate any residual beam pion contamination. The branching ratio was obtained using the formula

$$B_{K_{\pi 2}} = \frac{N_p}{f_s \, N_{KT} \, A_{K_{\pi 2}}} \tag{5.109}$$

where N_p is the number of events satisfying all analysis requirements and $A_{K_{\pi 2}}$ is the acceptance of the online and offline cuts for $K_{\pi 2}$ decays. The other factors in the equation were defined in the previous section. The acceptance was again determined by a combination of Monte Carlo simulation and corrections taking into account experimental conditions; it was defined as

$$A_{K_{\pi 2}} = A_{MC} \times A_{\rm cor} \, . \tag{5.110}$$

For the analysis of both real and simulated data, event reconstruction cuts were applied, as well as a cut on the total π^+ range. For real data, the online and offline delayed coincidence

cuts were also applied, as well as the CERENKOV cut and TD cuts. Furthermore, for both 1991 real and Monte Carlo data, the RS-TRACK cut included a restriction on the range stack stopping layer to $3 \leq$ Stop lay. ≤ 6. This explains the smaller acceptance for $K_{\pi 2}$ decays of the 1991 analysis.Tables B.80 and B.81 give detailed analysis results for 1989 and 1991 data respectively.

For the Monte Carlo simulated data, there were a total of 28586 and 14535 events satisfying the KT (stopped K^+) requirement for 1989 and 1991 data respectively. This resulted in uncorrected acceptances of

$$A_{MC}^{89} = \frac{2567}{14535} = 0.1766 \pm 0.0032 \tag{5.111}$$

$$A_{MC}^{91} = \frac{4099}{28586} = 0.1434 \pm 0.0021\,. \tag{5.112}$$

The acceptance correction was analogous to the one used in the calculation of f_s (see equation 5.108). For the TD acceptance, the calculation of section 5.2.3.1 was re-done to take into account the different stopping layer distribution of the π^+ from $K_{\pi 2}$ decays compared to $K^+ \to \pi^+ \nu\overline{\nu}$ decays. The values obtained for the corrections were :

$$A_{\rm cor}^{89} = 0.265 \pm 0.013 \tag{5.113}$$

$$A_{\rm cor}^{91} = 0.312 \pm 0.010\,. \tag{5.114}$$

Table 5.60 summarizes the calculation of the $K_{\pi 2}$ branching ratio for 1989 and 1991 data based on equations 5.109 and 5.110. The errors given are statistical only. Both measurements are consistent with the accepted value of 0.2117 ± 0.0016 [17]. This result gives some confidence in the simulation of the detector geometric acceptance and of π^+ nuclear interactions, as well as in the measurement of the acceptance of TD, delayed coincidence and event reconstruction cuts.

Table 5.60: Calculation of $K_{\pi 2}$ branching ratio for 1989 and 1991 data. Refer to equations 5.109 and 5.110 and the text for a description of the terms in the table.

Quantity	**1989**	**1991**
N_p	1748 ± 42	6830 ± 83
N_{KT}	282057	1103889
A_{MC}	0.1766 ± 0.0032	0.1434 ± 0.0021
$A_{\rm cor}$	0.265 ± 0.013	0.312 ± 0.010
f_s	0.630 ± 0.010	0.6422 ± 0.0085
$K_{\pi 2}$ branching ratio	0.210 ± 0.012	0.2153 ± 0.0085

5.5 Final results

5.5.1 $K^+ \to \pi^+ \nu\overline{\nu}$

Using the calculated values of the acceptance and the total integrated kaon flux, the branching ratio can be calculated. It is expressed as

$$B_{K^+ \to \pi^+ \nu\overline{\nu}} = \frac{N_{\pi\nu\overline{\nu}}}{f_s \, N_{KT} \, A_{\pi\nu\overline{\nu}}} \tag{5.115}$$

where $N_{\pi\nu\overline{\nu}}$ is the number of events selected by the analysis, N_{KT} is the total KT count, f_s is the fraction of counts in N_{KT} which are stopped kaons that decayed in the target (see section 5.3) and $A_{\pi\nu\overline{\nu}}$ is the combined acceptance of the trigger and analysis for $K^+ \to \pi^+\nu\overline{\nu}$ events (see section 5.2). The inverse of the product of f_s, N_{KT} and $A_{\pi\nu\overline{\nu}}$ is defined as the sensitivity (or single event sensitivity).

The observation of the number of events satisfying all analysis criteria is a Poisson statistical process. After the analysis of the 1989 data, no event was found. For 1991 data, the uncertainty in the background estimates precluded the assignment of the 4 events observed as $K^+ \to \pi^+\nu\overline{\nu}$ decays. Hence, an upper limit on the number of $K^+ \to \pi^+\nu\overline{\nu}$ events was set based on the observed number for both data sets. The Poisson probability distribution is defined as

$$f(n,\mu) = \frac{\mu^n e^{-\mu}}{n!} \quad n = 0, 1, 2, ... \tag{5.116}$$

with n the observed number of events and μ the mean of the distribution. We are looking for the mean N such that the probability is at least $1 - \alpha$ (confidence level) that the outcome of

another similar experiment will yield a number of events greater than the number observed, defined as n_0. Therefore,

$$1 - \alpha = \sum_{n=n_0+1}^{\infty} f(n, N) \tag{5.117}$$

or equivalently

$$\alpha = \sum_{n=0}^{n_0} f(n, N) \,. \tag{5.118}$$

For a 90% confidence level upper limit (or $\alpha = 10\%$) and $n_0 = 0$, the solution is $N = 2.3$; for $n_0 = 4$ the solution is $N = 7.99$.

The error on the result of each analysis is dominated by statistical fluctuations. However, the overall error on the sensitivity should be included in the result. The relative statistical error is 6–8% for the overall acceptance and only about 1.5% for f_s. The measured value of the $K_{\pi 2}$ branching ratio agreed with the accepted value within the statistical error for both analyses; however, this is not in itself proof that the systematic error is small. Because of uncertainties in the K^+ stopping distribution and the simulation of nuclear interactions, it is believed that a conservative figure of 10% for the systematic error is more appropriate. A formal way of incorporating the systematic error in an upper limit can be found in the literature [81]. The upper limit is then given by

$$N' = N\{1 + [1 - \sqrt{1 - \sigma_s^2 (N - n_0)^2}]/N\} \tag{5.119}$$

where N and n_0 are as defined above and σ_s is the relative error on the sensitivity.

The branching ratio upper limit for the process $K^+ \to \pi^+ \nu\overline{\nu}$ can then be calculated according to the formula

$$B(K^+ \to \pi^+ \nu\overline{\nu}) < \frac{N'}{f_s \, N_{KT} \, A_{\pi\nu\overline{\nu}}} \,. \tag{5.120}$$

Table 5.61 summarizes the calculation of the 90% confidence level upper limit for each of the two analyses. The result from 1989 data has already been published [37], and is a factor of 55 improvement over the previous published result using the same π^+ kinematic region [34].

Table 5.61: Calculation of $K^+ \to \pi^+\nu\overline{\nu}$ branching ratio 90% confidence level upper limit for 1989 and 1991 data, based on equation 5.120. Refer to the text for a description of the items in the table.

Item	**1989**	**1991**
n_0	0	4
σ_s	0.1	0.1
N'	2.33	8.16
f_s	0.630 ± 0.010	0.6422 ± 0.0085
N_{KT}	8.6648×10^{10}	14.3613×10^{10}
$A_{\pi\nu\overline{\nu}}$	$(2.57 \pm 0.20) \times 10^{-3}$	$(1.77 \pm 0.11) \times 10^{-3}$
B($K^+ \to \pi^+\nu\overline{\nu}$) upper limit	1.7×10^{-8}	5.0×10^{-8}

5.5.2 Scalar and tensor interactions

Table 5.62 gives the 90% confidence level upper limits from 1989 and 1991 data calculated using the acceptance given in table 5.58. The 1989 results represent an improvement of a factor of approximately 50 over the previous published results [34].

Table 5.62: Branching ratio upper limit (90% C.L.) for $K^+ \to \pi^+\nu\overline{\nu}$ via scalar and tensor interactions.

Interaction	**Year**	
	1989	**1991**
Scalar	2.2×10^{-8}	6.8×10^{-8}
Tensor	1.4×10^{-8}	4.2×10^{-8}

5.5.3 $K^+ \to \pi^+ X^0$

Figure 5.87 shows the 90% C.L. upper limit on the branching ratio for $K^+ \to \pi^+ X^0$, as a function of M_{X^0}. Also shown is the previous published result covering the same region of M_{X^0}. This limit assumes that X_0 is a stable weakly interacting massive particle, or system of particles.

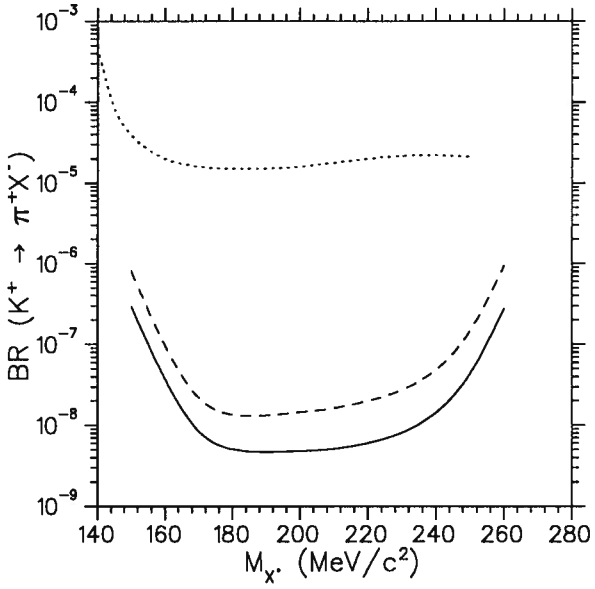

Figure 5.87: Branching ratio upper limit (90% C.L.) for $K^+ \to \pi^+ X^0$ as a function of M_{X^0}, the mass of the recoiling system. The full and dashed curves are from 1989 and 1991 data respectively. The dotted curve shows the previous published limit covering this range of M_{X^0} [38].

Chapter 6

Discussion

The single event sensitivity to $K^+ \to \pi^+\nu\overline{\nu}$ of the 1989 analysis was 7.3×10^{-9} and no events were observed, whereas for the 1991 analysis the sensitivity was 6.2×10^{-9} with 4 events observed. There is an obvious mismatch between the results. The first thing to understand is the origin of the events observed in 1991 data. This leads to a re-examination of the background estimates, and to further studies of the data. Furthermore, the analysis method used for the two data samples has to be compared in assessing the consistency between the results.

6.1 Origin of the observed 1991 events

The events remaining after all cuts were applied to the 1991 data sample are certainly not from Standard Model $K^+ \to \pi^+\nu\overline{\nu}$ decay, considering the expected range for the branching ratio based on current information about V_{td} (see figure 1.8). An analysis of 1989–1991 data in the kinematic region above the $K_{\pi 2}$ peak set a 90% C.L. upper limit of 3.7×10^{-9} for the branching ratio for $K^+ \to \pi^+\nu\overline{\nu}$ [30], lending further credence to the theoretical estimate. One possibility is that the observed events are from a non-Standard Model source. As was discussed in section 1.2.10, some theories predict an enhancement in $K^+ \to \pi^+$ *nothing* for the kinematic region below the $K_{\pi 2}$ peak, but there are no firm predictions. This is not reason enough to eliminate the possibility that new physics is responsible for the observed events. However, the potentially large systematic uncertainties in the background estimates do not allow us to support or rule out the new physics hypothesis.

If the remaining events are background, we have to identify the sources (or source) responsible and why the *a priori* studies underestimated the contribution. Muon and beam pion background are the least likely candidates. The studies for these background sources made use of real data and no large correlation between cuts was observed. Background sources that were estimated using Monte Carlo techniques are always suspect, considering that subtle effects not simulated can become significant at the 10^{-8} level. For K_{e4} , the kinematic distribution of the π^+ for the simulated events satisfying all cuts, shown in figure 4.76, is significantly different from the one for the final events from real data (figure 5.84). The K_{e4} background events are located in the lowest part of the $K^+ \to \pi^+\nu\bar{\nu}$ kinematic search region, contrary to the final events observed. Hence, it is unlikely that the K_{e4} background contribution was underestimated.

As stated in the description of the background studies, K^+ charge exchange simulation is inherently poor due to the lack of detailed knowledge of the processes involved. This is particularly true of charge exchange followed by hyperon production. However, the signature of these background processes is fairly clear; it should be possible to enhance those characteristics at some level in real data and identify events of this type. All such attempts failed, indicating that the estimates cannot be grossly underestimated, and perhaps were rather overestimated.

The validity of the background estimate for radiative $K_{\pi 2}$ decays hinges on the difference between the distribution of photons from π^0 decays for $K_{\pi 2\gamma}$ compared to $K_{\pi 2}$ and on the detection of the extra photon. In section 4.2.2, it was shown that the energy and direction distribution of photons from π^0 decays in $K_{\pi 2\gamma}$ is very similar to the one from $K_{\pi 2}$ decays before the application of any photon veto cuts. It is conceivable that subtle differences in the distributions not visible at that level become significant once photon veto cuts are applied. This may in turn affect the distribution of the radiated photons, resulting in a rejection lower than calculated. However, this effect would have to be some two orders of magnitude to push the estimate of 0.024 ± 0.004 events up to a number of events comparable to the total observed after all cuts; this is not very likely.

This leaves $K_{\pi 2}$ background as the most probable background origin for the observed events.

In the following sections the estimates given in section 4.2.1 are re-examined and further investigations are described.

6.2 $K_{\pi 2}$ background

The 1991 $K_{\pi 2}$ background estimate that was considered most trustworthy was from the so-called Method 2, even though it suffered from low statistics. The method relied on the hypothesis that the $K_{\pi 2}$ background is dominated by events in which the π^+ undergoes a nuclear interaction in the target. There is no doubt that such events do occur. However, if a significant portion of this type of background cannot be detected by either the TGFIT or VTX_PCA cuts, the estimate is not valid. Figure 6.88 shows the 90% C.L. upper limit on the number of background events as a function of the rejection of TGFIT, calculated according to equation 5.94. The rejection of TGFIT was estimated to be 2.02 ± 0.18 using a sample of events failing the VTX_PCA cut. Looking at table 5.36, we see that the rejection of TGFIT for the final data sample was 1.50 ± 0.20, lower than estimated. This would place the upper limit for the number of background events at 2.6 events, which still does not explain the four observed events. The rejection is of course a function of the sample used to measure it. For example, if TGFIT is applied as the very last cut for $\pi\nu\overline{\nu}$ events in the $K^+ \to \pi^+\nu\overline{\nu}$ signal region, it rejects no events at all. This indicates some level of correlation between TGFIT and the other cuts applied at Pass3 and Pass4, and makes the estimate even more uncertain. Because TGFIT and VTX_PCA were both inverted to select data samples used in this background estimate, their combined effect should encompass most of the $K_{\pi 2}$ background for the estimate to be reliable. In the end, it appears that these cuts did not have sufficient rejection to provide this.

The estimate from Method 1 was not trusted because of the large correlation observed between photon veto cuts and cuts designed to reject π^+ tracks with nuclear interactions in the target. Because the number of events predicted by that estimate is reasonably close to the observed number, it is tempting to consider it as correct after all. The value of the $K_{\pi 2}$ peak/tail ratio (η) was determined using a sample of events failing the full photon veto cuts (after Pass1). Measuring η with a sample of events with no photon veto cuts other than the online cuts gave

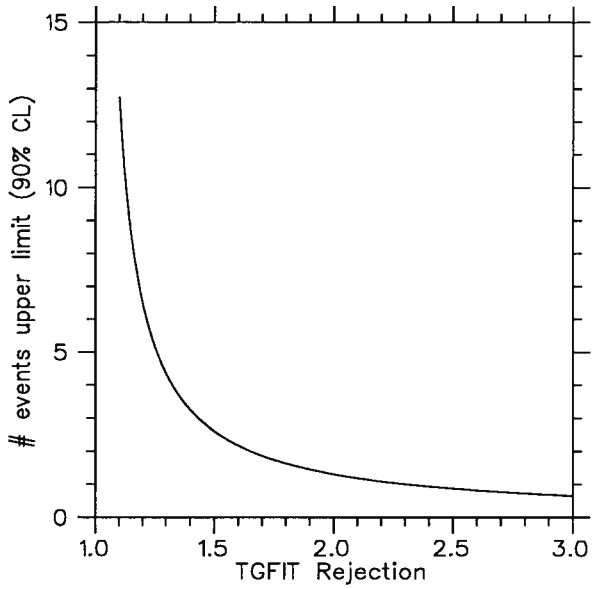

Figure 6.88: Upper limit on the number of 1991 $K_{\pi 2}$ background events as a function of the TGFIT cut rejection. The upper limit is calculated according to equation 5.94.

a similar value. It was unclear whether or not η would remain the same after all photon veto cuts were applied. Based on the numbers in section 5.1.2.3, the value of η after all cuts is $\eta = 30 \pm 15$, which has a large statistical error but is nonetheless consistent with 30.8 ± 3.5, the value used to estimate the expected background.

As a test of this estimation method, 1989 data was re-analyzed to select events which fail the photon veto cuts. All cuts were applied except the photon veto cuts beyond Pass1. Note that the photon veto cuts applied at Pass1 in the 1989 data analysis were considerably tighter than for the 1991 data Pass1. For 1989 data, cuts were applied with an energy threshold of 1.0 MeV in the RS, BV, EC, IC and VC, while for 1991 the energy threshold was 2.0 MeV for the RS and BV and 5.0 MeV for the EC; no photon veto cuts were applied on the IC and VC. The number of 1989 data events failing the photon veto cuts beyond Pass1 in the peak and tail were 85 and 17 respectively, for a ratio $\eta = 5.0 \pm 1.3$. There were 49 events left in the $K_{\pi 2}$ peak after all cuts. If we use these numbers, the prediction for the number of background events in the 1989 analysis is

$$N_{\rm bgd} = \frac{49 \pm 7}{5.0 \pm 1.3} = 9.8 \pm 2.9 \, . \tag{6.121}$$

No events were observed in the 1989 analysis after all cuts, about an order of magnitude less than this prediction, which is obviously wrong. This simply shows that the strong correlation between photon veto cuts and the number of events in the $K_{\pi 2}$ peak and tail regions makes this method unreliable. This casts serious doubt on the validity of the 1991 prediction, even though it is close to the final number. The agreement may just have been fortuitous.

The value of η measured for 1989 data is significantly worse than all numbers measured for 1991 data. One difference noted above is the level of photon veto. To attempt a more accurate comparison, the 1991 data sample failing the full photon veto cuts was re-analyzed to bring it to a level similar to 1989. Photon veto cuts were applied at an energy threshold of 1.0 MeV on the RS, BV, EC, IC and VC using the final coincidence time windows. For the RS and BV, the late edge of these windows is significantly later than the windows used for 1989 Pass1; the windows are comparable for the EC, IC and VC. With these additional constraints, there were 267 events in the $K_{\pi 2}$ peak and 7 in the tail, compared to 2191 and 71 previously (see table 4.19). To compare to the 1989 sample, these numbers have to be corrected for the fact that in 1989 π^+ tracks ending in range stack layer 12 were not accepted. The 1991 numbers for the sum of range stack layers B, C and 11 were 177 and 7 in the $K_{\pi 2}$ peak and tail region respectively, for a ratio $\eta = 26.3 \pm 9.7$. This is still significantly better than the value measured for 1989 data. One very likely reason for this difference is the addition of the lead-glass degrader and the use of TD cuts in the target; these two cuts clearly reject more events in the tail region than in the peak, thereby improving the ratio. The more troubling part is that even though a gain was made in background rejection by using these cuts, the level of background appears to be higher in 1991 than it was in 1989. Some other effect (or effects) must be responsible for the increased background level.

6.3 $K_{\pi 2}$ peak kinematics

It was observed in the search for $K^+ \to \pi^+ \nu\overline{\nu}$ in the kinematic region above the $K_{\pi 2}$ peak [30] that the position and width of the $K_{\pi 2}$ peak in total range, energy and momentum was different after all cuts than what could be expected based on the background samples. Such an effect

was looked for in this analysis. Table 6.63 gives the mean and sigma of Gaussian fits of the π^+ range, energy and momentum distributions for various data samples. There is no significant difference between them, implying that the events observed in the $K^+ \to \pi^+\nu\overline{\nu}$ search region after application of all cuts are are not the result of a systematic shift or broadening of the $K_{\pi 2}$ peak. This result might have been expected by simply looking at the kinematic distribution of the remaining events, and noticing that they are well within the search region. Some physical process must be responsible for their presence in the $K^+ \to \pi^+\nu\overline{\nu}$ search region, rather than an instrumental systematic effect.

Table 6.63: $K_{\pi 2}$ peak position and width for various data samples. The mean and sigma are from Gaussian fits with a flat background component.

Sample	Quantity	Range (cm)	Energy (MeV)	Momentum (MeV/c)
No $\overline{\gamma}$	Mean	29.78 ± 0.05	106.00 ± 0.16	204.36 ± 0.18
(553 events)	Sigma	1.06 ± 0.04	4.06 ± 0.15	3.92 ± 0.16
Fail Pass3 $\overline{\gamma}$	Mean	29.50 ± 0.04	105.47 ± 0.12	203.90 ± 0.13
(2191 events)	Sigma	1.27 ± 0.04	4.20 ± 0.10	4.07 ± 0.11
Pass3	Mean	29.56 ± 0.07	105.87 ± 0.25	203.78 ± 0.34
(159 events)	Sigma	1.09 ± 0.06	4.29 ± 0.23	4.25 ± 0.31

6.4 Photon Veto

One possibility for the increased level of background in 1991 data compared to 1989 is that the photon veto system did not perform as well. A good indicator of the photon veto performance is the number of events remaining after all cuts in the $K_{\pi 2}$ peak kinematic region. No particular effort is made in the preparation of the analysis cuts to reject the events in that region, since it is known that they will be rejected by the final kinematic cut. They are therefore an unbiased indicator of the photon rejection. It is important to note however that these events do not give an absolute measurement of the photon rejection for $K_{\pi 2}$ background events for which the π^+ is in the $K^+ \to \pi^+\nu\overline{\nu}$ kinematic search region. The distribution of photon direction and energy for the latter could be significantly different than for events in the $K_{\pi 2}$ peak region, affecting the photon veto performance. This study is a simple way of diagnosing a possible degradation

of the performance of the photon veto system.

For 1989 data, there were 49 events remaining in the $K_{\pi 2}$ peak after all cuts. To compare to this, the number of events observed in 1991 had to be corrected for the fact that range stack layer 12 stops were accepted by the $\pi\nu\overline{\nu}$ trigger; only the events in range stack layers B, C and 11 should be counted for comparison. Table 6.64 shows the number of events observed in the $K_{\pi 2}$ peak region for 1991 data for several different conditions. Also given for each case is the number of peak events in the 1989 analysis corrected for the differences in acceptance and integrated kaon flux, and the ratio of the numbers for 1991 and 1989 analysis.

In table 6.64, the "*" indicates that the TGFIT and PB-GLASS cuts were not used; these cuts were not available for use in 1989. The final row in the table refers to the analysis of $\pi\nu\overline{\nu}$ data without the use of online or offline photon veto cuts. These numbers provide the reference to which other numbers are compared. For 1989 data, use was made of a special data set taken with a modified $\pi\nu\overline{\nu}$ trigger in which the online photon veto cuts had been removed. After full analysis, a total of 2437 events were observed in the $K_{\pi 2}$ peak region, with a KT sum of 1.106×10^7. For 1991, the $K\pi 2(1)$ monitor data sample was used; the $\pi\nu\overline{\nu}$ trigger requirements were applied offline based on the recorded trigger information, except for the photon veto cuts. All offline analysis cuts were applied except direct photon veto cuts (INTIME, INTSE and PB-GLASS). A total of 553 events remained in the $K_{\pi 2}$ peak region, of which 292 stopped in range stack layers B, C and 11. The KT sum, corrected for the online pre-scale, was 1.104×10^6.

The only entry in table 6.64 not consistent within one standard deviation with the case where no photon veto was applied (last row) is the case where the PB-GLASS and TGFIT cuts were removed from the Pass3 analysis (first row). It should also be noted that the result without any photon veto shows an excess of events in 1991, about 25% more. Some of this discrepancy may due to the fact that in 1991, cuts were not applied on the energy deposition pattern of the π^+ in the range stack. Such cuts would reject events in which a low energy photon converted on top of the π^+ track. However, examination of the kinematic spectrum of the 553 events remaining after the analysis performed without direct photon veto cuts shows

that this effect is likely to be small. The effect is only enhanced after photon veto cuts are applied. As can be seen in figure 5.84, about 10% of the 1991 events remaining in the $K_{\pi 2}$ peak after Pass4 fall into that category.

It is difficult to attribute the excess of $K_{\pi 2}$ peak events in the 1991 analysis without direct photon veto cuts to one cut or group of cuts in particular. This effect may be partly responsible for the larger background level in 1991. However, the study described in this section shows that the 1991 Pass4 set of cuts provides as much photon rejection for $K_{\pi 2}$ peak events as the 1989 analysis.

Table 6.64: Number of events in $K_{\pi 2}$ peak region for 1991 data for various conditions. The number only includes stops in range stack layers B, C and 11. The "89 equivalent" number comes from the number of events observed in 1989 corrected for differences with the 1991 analysis in acceptance and integrated kaon flux.

Conditions	**Peak events**	**89 equivalent**	**91/89 ratio**
Pass3*	155	87 ± 0.15	1.79 ± 0.33
Pass3	101	70 ± 12	1.44 ± 0.28
Pass4*	109	72 ± 12	1.51 ± 0.29
Pass4	72	58.3 ± 9.9	1.23 ± 0.25
No $\overline{\gamma}$	292	237 ± 22	1.23 ± 0.13

6.5 Other cuts

Because the likelihood was low that muons and beam pion backgrounds were responsible for the observed events in 1991, only photon veto and target vertex cuts offered potential for increased background rejection. These cuts were therefore examined with more scrutiny. For photon veto cuts, tighter versions of INTIME and INTSE were described in section 5.1.2.3. The PB-GLASS and B4TD cuts could not be tightened further. For target vertex cuts, one of the parameters of TGTRACK was tightened, as described in section 5.1.2.3. The rejection of the TGFIT cut could not be improved beyond simple acceptance loss. Based on the available background samples, tightening VTX_PCA did not improve the rejection by the nominal factor of two above

acceptance loss.

One important point that was made in the section on background studies is that the background samples used in designing the cuts must be representative of the background studied for those cuts to be effective. For VTX_PCA, the background sample used to set the cut position was a sample of events failing the photon veto cuts beyond Pass1 and with range, energy and momentum in the $K^+ \to \pi^+\nu\bar{\nu}$ signal region. Figure 6.89 shows scatterplots of the two normalized components of the VTX_PCA principal component analysis for the events satisfying the cut. Remember that events for which the measured "kaon" energy in the target is in excess of what was expected based on the range of the K^+ in the target or the energy deposited by the K^+ in the B4 counter tend to have negative values for component 2.

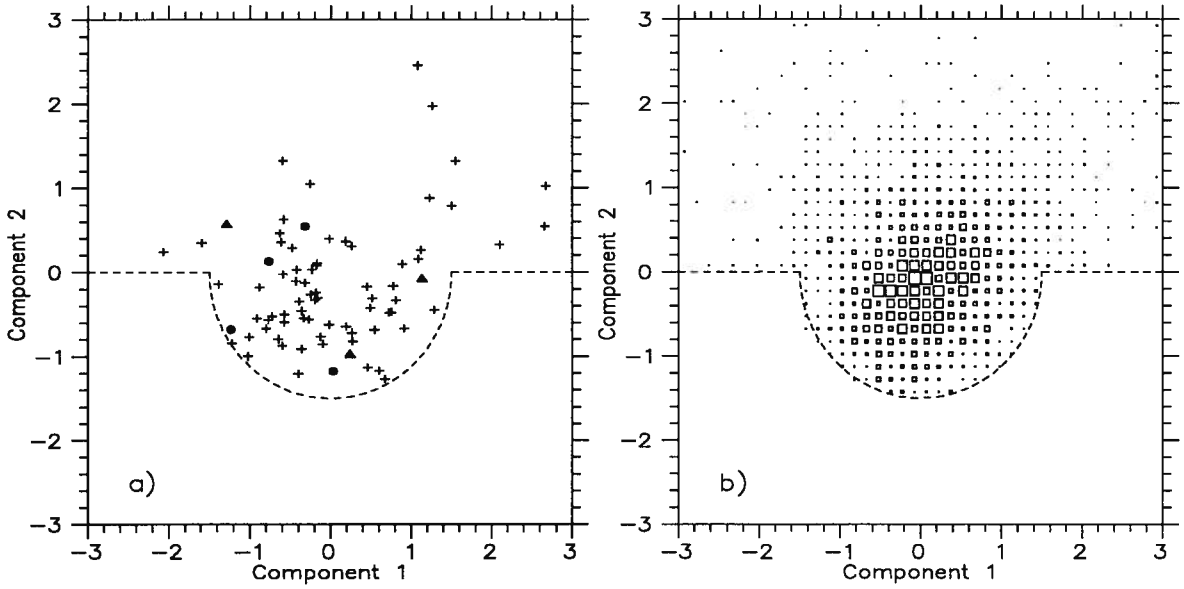

Figure 6.89: VTX_PCA components for events passing the cut for a) background sample (crosses), events satisfying only Pass3 requirements (triangles) and events satisfying all Pass4 requirements (circles) and b) $K_{\mu 2}$ events (density distribution). The dashed lines indicate the cut position.

Figure 6.89 a) shows the distribution for the background sample (crosses) and the seven events remaining after Pass3; the four events passing all Pass4 cuts are shown as circles while events rejected by Pass4 are shown as triangles. Figure 6.89 b) shows the density distribution for $K_{\mu 2}$ events. $\pi\nu\bar{\nu}$ events satisfying the Pass3 requirements tend to be towards the edge of

the accepted region, whereas it is clear that the background sample has a distribution similar to $K_{\mu 2}$ events. None of the seven Pass3 events appear near the center of the distribution, the region most densely populated by $K_{\mu 2}$ events. It is therefore quite possible that this cut was not optimized to obtain the best possible background rejection because the background sample used was not adequate.

A review of all available variables for the seven events remaining after Pass3 showed that the cut parameters of all cuts other than photon veto and target vertex cuts were properly set. A pile-up of events near the edge of a cut position would have been a clear signature for a particular background; no such effect was observed.

6.6 Analysis method

The observation that the background sample used to set the cut position for VTX_PCA may not have been the ideal sample to work with brings up the more general question of the effectiveness of the analysis method used for 1991 data. The entire approach was based on the realization that the standard analysis method, used for 1989 data, had problems. Designing cuts by examining distributions of various quantities extracted from the residual events at each step could lead to a biased result, particularly if the data sample used was small. This was not the ideal way to search for a small potential signal. The approach used for 1991 data removes concern about bias. It works well as long as the background data samples used allow the cuts to be set at or near their optimum effectiveness.

If the background level to contend with is relatively high, small fluctuations in the cuts may have significant effects on the final result. Of the 4 events remaining in the $K^+ \to \pi^+ \nu\overline{\nu}$ search region after 1991 Pass4, it is quite likely that a few and perhaps even all of them would have been rejected if the cuts had been set using data samples which included the candidate events, as demonstrated in the previous section. The standard analysis method allows for a better adjustment of the cuts to the real background than the new method, unless the background level is intrinsically low and small variations in the cuts are not important. For the search for $K^+ \to \pi^+ \nu\overline{\nu}$ below the $K_{\pi 2}$ peak, this is not the case; the detector was pushed to its limit in

terms of background rejection.

This is not an indictment of the philosophy of the analysis method used for 1991 data. It was extremely important to develop the techniques necessary for such an analysis and uncover its weak points to make further improvements. Two main weaknesses were identified :

1. If the intrinsic level of background is high, the choice of background samples representative of the true background is crucial in order to set the cuts appropriately

2. Systematic uncertainties in the background studies must be kept as small as possible in order to identify an unexpected signal. The corollary to this is that the correlation between cuts used to study background processes must be kept to a minimum.

6.7 Consistency between 1989 and 1991 results

There are two extreme scenarios explaining the mismatch between the results from the two data samples :

1. The 1989 result is entirely correct and the events observed in 1991 are from background sources. The background rejection in 1991 was poorer either because of a degradation of the performance of the detector or because the analysis method did not allow the cuts to be optimized.

2. The 1991 result is correct, and analysis bias is responsible for the elimination of all the expected events in 1989.

The true explanation is likely to be a combination of the above two cases. It is certainly possible that one or two events should have been observed after analysis of the 1989 data, either because of analysis bias or statistical fluctuation. The dominant $K_{\pi 2}$ background was estimated using a combination of real data analysis and Monte Carlo simulation to be at the level of one event or less, but as was the case in 1991 the systematic uncertainty was not known.

As discussed in the previous section, the method used in 1991 to prepare the offline analysis cuts was likely responsible for the presence of a few events. Therefore, considering the low statistics involved and the unknown and potentially large systematic uncertainties, the two results are not obviously inconsistent with each other.

Chapter 7

Conclusion

The result from the analysis of the 1991 $\pi\nu\overline{\nu}$ data set is most certainly disappointing, because no clear explanation for the observation has been found. Based on the result obtained with 1989 data, a significant gain in sensitivity was expected with 1991 data because of the larger number of kaons observed and the addition of the lead-glass degrader and the inner wire chamber. The IWC was to provide a modest improvement in tracking resolution, mostly for the z-axis component, so its impact was not expected to be very large; it performed as expected. The lead-glass detector was introduced to primarily reject photons from the component of $K_{\pi 2}$ background that was thought to be dominant. Its performance degraded significantly during the course of the 1991 data run because of radiation damage. In addition, light emitted by incoming kaons hindered the detector's ability to identify low energy electro-magnetic showers. Despite these problems, photons were clearly detected and as expected the rejection of events in the low energy $K_{\pi 2}$ tail was larger than for events in the $K_{\pi 2}$ peak region. However, the overall rejection obtained with the lead-glass detector was not as high as was initially expected.

The analysis technique used in 1991 likely reduced bias in the final result but may have had the unfortunate side effect of not providing a set of cuts pushing the rejection capability of the detector to its maximum. In some sense this method worked very well : a small number of events which were not examined at any point beforehand remained after all cuts were applied. The events satisfied all requirements for what would be expected of a signal. However, the large uncertainty in the background estimates does not allow us to differentiate signal and background. Further studies of the final results offer some indication, albeit flimsy, that the

remaining events are background, most likely from $K_{\pi 2}$ decays, with a chance of kaon charge exchange possibly followed by hyperon production and decay contributing as well.

The correct upper limit for $K^+ \to \pi^+ \nu\overline{\nu}$ in the kinematic region below the $K_{\pi 2}$ peak set by this experiment is likely somewhere between the values obtained in 1989 and 1991. The 1991 background rejection was not optimized because of the analysis techniques used while the 1989 result was probably at or beyond the best that could be achieved, depending on the level of bias in the analysis. It would not be strictly correct however to add the sensitivity of the two results for a combined upper limit. Even though the two data sets were collected using the same detector, there were differences not only in the sub-detectors themselves, but also in their performance and calibration, which might influence the results. The difference in kaon beam intensity may also have had an effect on the outcome, and certainly affected the detector performance.

The work presented here showed that the BNL E787 detector did not have sufficient sensitivity for the search for $K^+ \to \pi^+ \nu\overline{\nu}$ in the kinematic region below the $K_{\pi 2}$ peak. It leaves open the question of the origin of the events observed in the 1991 data set. More data collected in 1994 with a significantly upgraded detector may shed some light on this question. The upgrades and possible further improvements are discussed in the next and final section.

7.1 Possible improvements

The most important improvement necessary is to obtain more accurate background estimates, particularly for $K_{\pi 2}$ and charge exchange. For $K_{\pi 2}$, the correlation between π^+ nuclear interactions and photon veto must be reduced substantially. The simplest improvement is to enhance the photon veto capability of the detector and make it more uniform over the entire solid angle. In addition to reducing the correlation this would also improve the $K_{\pi 2}$ background rejection. Some steps have already been taken in that direction. The endcap lead–scintillator sandwich detectors have been replaced by fully active arrays of pure cesium iodide crystals. The geometric coverage of the new endcaps, both at the inner and outer radius, is greater than the old ones. Small lead–scintillator detectors were installed on the magnet iron behind the new

endcaps as close as possible to the beam axis, and another group of lead–scintillator detectors fills the gap between the V-counters and the magnet iron. The lead-glass cylinder was replaced by a more radiation resistant type of lead-glass, and the light collection efficiency was improved.

These changes should significantly enhance the photon rejection in the beam axis direction, where the most improvement was needed. The other crucial region is between the outer radius of the endcaps and the barrel veto near the ends of the detector. This would be improved by adding photon detectors between the range stack and the barrel veto. Several options are presently considered, but actual improvements will not be installed before 1996.

The other way to reduce correlations is to improve the π^+ nuclear interaction detection in the target. A new target with less non-active materials and using scintillating fibres with better light output performance has been installed. The output of each target channel will be individually recorded with 500 MHz gallium arsenide CCD transient digitizers [86], substantially improving the detection capability for large energy depositions overlapping with the energy from the stopping K^+ in the target. In the future, it might be possible to operate the digitizers at a frequency of 1 GHz; this would further improve the double pulse resolution.

For K^+ charge exchange, the main uncertainty in the background prediction is the rate at which this process occurs. It should be possible to select data samples, possibly using a special trigger, which would allow the study of this process in detail. The present estimation using the best available information for the Monte Carlo simulation is uncertain and at an uncomfortably high level. This background source cannot be ignored in future searches, and efforts should be made to understand it better. The improvements made to the target and its electronics will directly benefit any such study. Also beneficial will be the new central drift chamber, which will provide a factor of two improvement in momentum resolution, but most importantly will improve the z-axis position resolution by a factor of 2 to 3. This will result in much better resolution for the K^+ decay vertex position in the target.

All 21 layers of the range stack are now fully instrumented. This does not have much impact on the study of backgrounds, but will allow an improved TD and kinematic cuts acceptance, as well as better muon background rejection. The first data with the upgraded detector were

collected in 1994 and are still being analyzed. More will be collected in 1995. It is hoped that analysis of these data will explain the origin of the events observed in this work.

Bibliography

[1] F. Halzen and A.D. Martin, *Quarks and Leptons : An Introductory Course in Modern Particle Physics*, Wiley & Sons, 1984.

[2] G. Arnison *et al.* (UA1 Collaboration), Physics Letters **122B**, 103 (1983).

[3] T.D. Lee and C.N. Yang, Physical Review **104**, 254 (1956).

[4] R.P. Feynman and M. Gell-Mann, Physical Review **109**, 193 (1958).

[5] S. Weinberg, Physical Review Letters **19**, 1264 (1967).

[6] N. Cabibbo, Physical Review Letters **10**, 531 (1963).

[7] S.L. Glashow, J. Iliopoulos and L. Maiani, Physical Review **D2**, 1285 (1970).

[8] F.J. Hasert *et al.*, Physics Letters **46B**, 138 (1973).

[9] J.J. Aubert *et al.*, Physical Review Letters **33**, 1404 (1974).

[10] J.-E. Augustin *et al.*, Physical Review Letters **33**, 1406 (1974).

[11] G. Arnison *et al.* (UA1 Collaboration), Physics Letters **126B**, 398 (1983).

[12] M. Kobayashi and T. Maskawa, Progress of Theoretical Physics, **49**, 652 (1973).

[13] J.H. Christenson, J.W. Cronin, V.L. Fitch and R. Turlay, Physical Review Letters **13**, 138 (1964).

[14] L. Wolfenstein, Physical Review Letters **51**, 1945 (1983).

[15] T. Inami and C.S. Lim, Progress of Theoretical Physics **65**, 297 (1980).

[16] M.K. Gaillard and B.W. Lee, Physical Review **D10**, 897 (1974).

[17] Particle Data Group, L. Montanet *et al.*, Physical Review D **50**, 1173 (1994).

[18] C.O. Dib, I. Dunietz and F.J. Gilman, Modern Physics Letters **A6**, 3573 (1991).

[19] G. Buchalla and A.J. Buras, Nuclear Physics **B412**, 106 (1994).

[20] F. Abe *et al.* (CDF Collaboration), Physical Review Letters **73**, 225 (1994).

[21] J. Ellis, G.L. Fogli and E. Lisi, Physics Letters **B333**, 118 (1994).

[22] J.S. Hagelin and L.S. Littenberg, Progress in Particle and Nuclear Physics **23**, 1 (1989).

[23] D. Rein and L.M. Sehgal, Physical Review **D39**, 3325 (1989).

[24] M. Lu and M.B. Wise, Physics Letters **B337**, 133 (1994).

[25] A. Ali and D. London, *An Update of the CKM matrix*, CERN-TH.7408/94, 1994.

[26] J. Haggerty, BNL Experiment 787 Technical Note #196.

[27] A.J. Buras, M.E. Lautenbacher and G. Ostermaier, Physical Review **D50**, 3433 (1994).

[28] G. Buchalla and A.J. Buras, Physics Letters **B333**, 221 (1994).

[29] A.J. Buras and M.K. Harlander, *A Top Quark Story: Quark Mixing, CP Violation and Rare Decays in the Standard Model*, MPI-PAE/PTh 1/92, 1992.

[30] A.S. Turcot, *The Search for the Decay* $K^+ \to \pi^+ \nu\overline{\nu}$, Ph.D. Thesis, Department of Physics and Astronomy, University of Victoria, 1994.

[31] M.S. Atiya *et al.*, Physical Review Letters **65**, 1188 (1990).

[32] U. Camerini, D. Ljung, M. Sheaff and D. Cline, Physical Review Letters **23**, 326 (1969).

[33] J.H. Klems, R.H. Hildebrand and R. Stiening, Physical Review **D4**, 66 (1971).

[34] G.D. Cable, R.H. Hildebrand, C.Y. Pang and R. Stiening, Physical Review **D8**, 3807 (1973).

[35] Y. Asano *et al.*, Physics Letters **107B**, 159 (1981).

[36] M.S. Atiya *et al.*, Physical Review Letters **64**, 21 (1990).

[37] M.S. Atiya *et al.*, Physical Review **D48**, R1 (1993).

[38] T. Yamazaki *et al.*, Physical Review Letters **52**, 1089 (1984).

[39] I.I. Bigi and F. Gabbiani, Nuclear Physics **B367**, 3 (1991).

[40] L.-M. Chounet, J.-M. Gaillard and M.K. Gaillard, Physics Reports **4C**, 199 (1972).

[41] G.B. Gelmini and M. Roncadelli, Physics Letters **99B**, 411 (1981).

[42] T.M. Aliev, M.I. Dobroliubov and A.Yu. Ignatiev, Nuclear Physics **B335**, 311 (1990).

[43] S. Bertolini and S. Santamaria, Nuclear Physics **B315**, 558 (1989).

[44] The scale drawing of the magnets in this figure was provided by G.S. Clark, TRIUMF, and was based on information provided by J. Doornbos, TRIUMF.

[45] Figure provided by K. Li, Brookhaven National Laboratory.

[46] M.S. Atiya *et al.*, Nuclear Instruments and Methods in Physics Research **A321**, 129 (1992).

[47] *IEEE Standard FASTBUS Modular High-Speed Data Acquisition and Control System*, IEEE, New York, 1985.

[48] V. Fitch and R. Motley, Physical Review **101**, 496 (1956).

[49] D.A. Hutcheon, A. Konaka, Y. Kuno, J.A. Macdonald and Y. Yoshimura, BNL Experiment 787 Technical Note #223.

[50] V.A. Kujala, *An Inner Wire Chamber for the E787 Detector*, M.Sc. Thesis, Department of Physics and Astronomy, University of Victoria, 1991.

[51] M. Atiya, M. Ito, J. Haggerty, C. Ng and F.W. Sippach, Nuclear Instruments and Methods **A279**, 180 (1989).

[52] G. Keil, Nuclear Instruments and Methods **87**, 111 (1970).

[53] J. Roy, *Studies of a Lead-Scintillator Calorimeter With Fast Response*, M.Sc. Thesis, Department of Physics, University of British Columbia, 1988.

[54] *CAMAC : A Modular Instrumentation System for Data Handling – Revised Description and Specification*, AEC reference report TID-25875, 1972.

[55] D. Quarrie, *YBOS Programmers Reference Manual*, Version 3.3, CDF Note # 156, October 1985.

[56] R. Poutissou, B. Scheumann and M. Burke, KOFIA : Kaon Offline Interactive Analysis Program.

[57] J.B. Birks, *The Theory and Practice of Scintillation Counting*, Pergamon Press (1964).

[58] R.A. Johnson and D.W. Wichern, *Applied Multivariate Statistical Analysis*, Prentice Hall (1982).

[59] F. James and M. Roos, CERN Program Library entry D506.

[60] P. Meyers, BNL Experiment 787 Technical Note #165.

[61] W.B. Cottingame *et al.*, Physical Review C **36**, 230 (1987).

[62] D. Ashery *et al.*, Physical Review C **23**, 2173 (1981).

[63] F. Ajzenberg-Selove, Nuclear Physics **A506**, 1 (1990).

[64] J.D. Good, Physical Review **113**, 352 (1959)

[65] K.M. Smith *et al.*, Nuclear Physics B **109**, 173 (1976).

[66] T. Nakano and Y. Kuno, BNL Experiment 787 Technical Note #256.

[67] A. Pais and B. Treiman, Physical Review **168**, 1858 (1968).

[68] L. Rosselet *et al.*, Physical Review D **15**, 574 (1977).

[69] G. Mechtersheimer *et al.*, Physics Letters **73B**, 115 (1978).

[70] R. Madey *et al.*, Physical Review C **25**, 3050 (1982).

[71] M. Sevior, private communication.

[72] Ya.A. Berdnikov, S.N. Polishchuk, and S.G. Smith, Soviet Journal of Nuclear Physics **55**, 1470 (1992).

[73] W. Slater *et al.*, Physical Review Letters **7**, 378 (1961)

[74] R.G. Glasser *et al.*, Physical Review D **15**, 1200 (1977).

[75] D. Wright and D. Marlow, BNL Experiment 787 Technical Note #269.

[76] D.H. Perkins, Introduction to High Energy Physics, Third Edition, Addison-Wesley ed., 1987, pp. 243-246.

[77] G.A. Sayer *et al.*, Physical Review **169**, 1045 (1968).

[78] A.D. Martin, Low and Intermediate Energy Kaon-Nucleon Physics, E. Ferrari and G. Violini eds., 97-114 (1981).

[79] H. Davis *et al.*, Nuovo Cimento **53A**, 313 (1968).

[80] D. Akerib, D. Marlow and P. Meyers, BNL Experiment 787 Technical Note #168.

[81] R.D. Cousins and V.L. Highland, Nuclear Instruments and Methods in Physics Research **A320**, 331 (1992).

[82] D.R. Marlow, P.D. Meyers, W.C. Louis, L.S. Littenberg, G. Azuelos and A. Stevens, *UMC Monte Carlo Programme, Version 1.0.*

[83] W.R. Nelson, H. Hirayama and D.W.O. Rogers, *The EGS4 Code System*, SLAC-265 UC-32, 1985.

[84] T. Gabriel and R. Alsmiller, Physical Review **182**, 1035 (1969).

[85] R. McPherson, L. Felawka, J. Roy, D.S. Akerib, M.A. Selen and P.D. Meyers, *UMC Monte Carlo Programme, Version 4.0.*

[86] D. Bryman, J.V. Cresswell, M. LeNoble and R. Poutissou, IEEE Transactions in Nuclear Science **38**, 295 (1991).

[87] M.S. Atiya *et al.*, Physical Review Letters **66**, 2189 (1991).

Appendix A

BNL E787 Collaboration

Listed below are the names of the physicists who were members of the BNL E787 collaboration at the time the experiment reported in this thesis was performed.

S. Adler, M.S. Atiya, I-H. Chiang, J.S. Frank,
J.S. Haggerty, T.F. Kycia, K.K. Li, L.S. Littenberg,
A. Sambamurti, A. Stevens, R.C. Strand and C. Witczig
Brookhaven National Laboratory

W. C. Louis
Los Alamos National Laboratory

D.S. Akerib, M. Ardebili, M. Convery, M.M. Ito,
D.R. Marlow, R. McPherson, P.D. Meyers, M.A. Selen,
F.C. Shoemaker, and A.J.S. Smith
Princeton University

E.W. Blackmore, D.A. Bryman, L. Felawka, P. Kitching,
A. Konaka, Y. Kuno, J.A. Macdonald, T. Nakano,
T. Numao, P. Padley, J.-M. Poutissou, R. Poutissou,
J. Roy, R.A. Soluk, and A.S. Turcot
TRIUMF

Appendix B

Analysis details

This appendix contains full analysis results used in background studies and acceptance calculations.

B.1 Background studies

Table B.65: Beam pion background analysis for 1989 data. The data sample used was selected out of the Pass1 data.

Cut	# events	Rejection
Fail CERENKOV	3005	
BM_HOLE	2853	1.0533 ± 0.0044
B4TD	2413	1.1823 ± 0.0094
NK	2296	1.0510 ± 0.0048
PROMPT	129	17.8 ± 1.5
DISENPI	127	1.016 ± 0.011
DISENK	117	1.085 ± 0.028
INT_EB	76	1.54 ± 0.10
DC-CHI2	61	1.245 ± 0.071
NDC	55	1.109 ± 0.047
ICOUNTER	26	2.12 ± 0.30
RSPC	25	1.040 ± 0.041
INT_RIV	17	1.47 ± 0.20
FITPI	9	1.89 ± 0.43
ELECTRON	6	1.50 ± 0.35
TGTRACK	3	2.00 ± 0.82
FIDUCIAL	2	1.50 ± 0.61
ZDCTZ	1	2.0 ± 1.4
RGEMOM	0	—

Table B.66: 1991 $K_{\pi 2}$ background sample for estimation method 1.

Cut	# events	Rejection
Pass1	399958	
PROMPT	348794	1.1467 ± 0.0007
DC-SETUP	260033	1.341 ± 0.001
RS-TRACK	239065	1.0877 ± 0.0006
ICOUNTER	165311	1.446 ± 0.002
TRKTIM	100535	1.644 ± 0.003
FITPI	82235	1.222 ± 0.002
TD_MDA	76194	1.079 ± 0.001
TDFOOL	68605	1.111 ± 0.001
ELVETO	60919	1.126 ± 0.002
ELECTRON	49398	1.233 ± 0.002
FIDUCIAL	41513	1.190 ± 0.002
KINSCORE	37999	1.092 ± 0.002
BM_HOLE	37153	1.0228 ± 0.0008
B4_CNTR	36186	1.0267 ± 0.0009
CERENKOV	30283	1.195 ± 0.003
BWPC	28522	1.062 ± 0.002
Fail γ-veto	27512	1.037 ± 0.001

Table B.67: Analysis results for application of all cuts on 1991 events in the $K_{\pi 2}$ peak region.

Cut	# events	Rejection
Pass1	399958	
PROMPT	348794	1.1467 ± 0.0007
DC-SETUP	260033	1.341 ± 0.001
RS-TRACK	239065	1.0877 ± 0.0006
ICOUNTER	165311	1.446 ± 0.002
TRKTIM	100535	1.644 ± 0.003
INTIME	18952	5.30 ± 0.03
INTSE	14677	1.291 ± 0.005
FITPI	10255	1.431 ± 0.008
TD_MDA	9366	1.095 ± 0.003
TDFOOL	7113	1.317 ± 0.008
ELVETO	5219	1.363 ± 0.010
ELECTRON	3991	1.308 ± 0.010
FIDUCIAL	3199	1.248 ± 0.010
KINSCORE	2813	1.137 ± 0.007
BM_HOLE	2700	1.042 ± 0.004
B4_CNTR	2544	1.061 ± 0.005
CERENKOV	1604	1.586 ± 0.024
BWPC	1464	1.096 ± 0.008
Fail KINCUT	1202	
TGTRACK	279	4.3 ± 0.2
TGFIT	254	1.10 ± 0.02
VTX_PCA	231	1.10 ± 0.02
PB-GLASS	165	1.40 ± 0.06
B4TD	159	1.04 ± 0.02

Table B.68: 1991 Muon sample selection from $\pi\nu\overline{\nu}$ lev0 monitor data. The "Trigger" cut refers to the application of the $\overline{(13_{CT} + ... + 18_{CT})}$ and $\overline{(19 + 20 + 21)}$ Level 0 requirements, based on the trigger information recorded with the data.

Cut	# events	Rejection
$\pi\nu\overline{\nu}$ lev0	112702	
Trigger	5116	22.0 ± 0.3
TARGET	4997	1.024 ± 0.002
PROMPT	3746	1.33 ± 0.01
DC-SETUP	1840	2.04 ± 0.03
RS-TRACK	1608	1.14 ± 0.01
TRKTIM	1271	1.26 ± 0.02
KINCUT	219	5.8 ± 0.4

Table B.69: 1991 Muon sample selection from Kπ2(1) monitor data.

Cut	# events	Rejection
Kπ2(1)	166726	
Trigger	41981	3.97 ± 0.02
TARGET	40866	1.0273 ± 0.0008
PROMPT	22118	1.848 ± 0.008
DC-SETUP	14689	1.506 ± 0.007
RS-TRACK	13914	1.056 ± 0.002
ICOUNTER	12325	1.129 ± 0.003
TRKTIM	11521	1.070 ± 0.002
FIDUCIAL	10518	1.095 ± 0.003
KINCUT	1000	10.5 ± 0.3
TGTRACK	440	2.27 ± 0.08

Table B.70: Beam pion background event selection from 1991 $\pi\nu\overline{\nu}$ Pass1 data. All cuts are as described in section 3.3.

Cut	# events	Rejection
Pass1	399958	
DC-SETUP	301922	1.325 ± 0.001
RS-TRACK	301922	1.0829 ± 0.0006
INTIME	53609	5.20 ± 0.02
INTSE	43836	1.223 ± 0.002
FASFITPI	43723	1.0026 ± 0.0002
FITPI	33810	1.293 ± 0.003
TD_MDA	31107	1.087 ± 0.002
TDFOOL	25633	1.214 ± 0.003
ELVETO	21209	1.208 ± 0.003
ELECTRON	16849	1.259 ± 0.004
KINSCORE	12818	1.314 ± 0.006

Table B.71: K_{e4} background simulation and analysis. The RS-TRACK cut included a requirement that the true π^+ stopping counter be identical to the one found by the range stack tracking algorithm.

Cut	# events	Rejection
	1.0×10^7	
Pass kinematic constraints	725059	13.792 ± 0.016
Level 0 trigger simulation	102472	7.076 ± 0.020
Level 1 trigger simulation	92411	1.1089 ± 0.0011
	92411	
TARGET	90695	1.01892 ± 0.00046
PROMPT	70940	1.2785 ± 0.0022
DC-SETUP	58749	1.2075 ± 0.0021
RS-TRACK	49308	1.1915 ± 0.0022
ICOUNTER	45959	1.0729 ± 0.0013
TRKTIM	45550	1.00898 ± 0.00044
INTIME	4101	11.11 ± 0.16
π^+ decay at rest	4066	1.0086 ± 0.0015
FIDUCIAL	3764	1.0802 ± 0.0048
TGTRACK	19	198 ± 45
KINCUT	19	1.00 ± 0.00

Table B.72: Kaon charge exchange background simulation and analysis for $K_L^0 \to \pi^+\mu^-\overline{\nu}_\mu$ decay. Offline analysis cuts are the same as in table B.71.

Cut	**# events**	**Rejection**
	2.0×10^6	
Satisfy KT requirement	1993776	1.00312 ± 0.00004
Level 0 trigger simulation	382364	5.2143 ± 0.0076
Level 1 trigger simulation	271658	1.4075 ± 0.0014
	271658	
TARGET	233747	1.16219 ± 0.00090
DC-SETUP	105250	2.2208 ± 0.0051
RS-TRACK	81100	1.2978 ± 0.0022
ICOUNTER	74574	1.0875 ± 0.0011
TRKTIM	64688	1.1528 ± 0.0016
INTIME	31561	2.0496 ± 0.0082
π^+ decay at rest	30595	1.0316 ± 0.0010
FIDUCIAL	24280	1.2601 ± 0.0037
TGTRACK	901	26.95 ± 0.88
PROMPT	47	19.2 ± 2.7
KINCUT	37	1.270 ± 0.096
Sum of weights	4.96×10^{-3}	

Table B.73: Kaon charge exchange background simulation and analysis for $K_L^0 \to \pi^+ e^- \overline{\nu}_e$ decay, to be compared with table B.72.

Cut	# events	Rejection
	6.0×10^5	
Satisfy KT requirement	598053	1.00326 ± 0.00007
Level 0 trigger simulation	33654	17.771 ± 0.094
Level 1 trigger simulation	22042	1.5268 ± 0.0060
	22042	
TARGET	19249	1.1451 ± 0.0029
DC-SETUP	10263	1.876 ± 0.013
RS-TRACK	7093	1.4469 ± 0.0095
ICOUNTER	6485	1.0938 ± 0.0040
TRKTIM	5673	1.1431 ± 0.0054
INTIME	513	11.06 ± 0.46
π^+ decay at rest	497	1.0322 ± 0.0082
FIDUCIAL	381	1.304 ± 0.032
TGTRACK	14	27.2 ± 7.1
KINCUT	6	2.33 ± 0.72
Sum of weights	1.04×10^{-4}	

Table B.74: Σ^+ production background simulation and analysis.

Cut	# events	Rejection
	200000	
Satisfy KT requirement	193105	1.03570 ± 0.00044
Level 0 trigger simulation	47137	4.097 ± 0.016
Level 1 trigger simulation	40218	1.1720 ± 0.0022
	40218	
TARGET	35851	1.1218 ± 0.0020
DC-SETUP	34712	1.03281 ± 0.00099
RS-TRACK	28687	1.2100 ± 0.0030
ICOUNTER	27711	1.0352 ± 0.0011
TRKTIM	23523	1.1780 ± 0.0030
INTIME	13871	1.6958 ± 0.0092
π^+ decay at rest	13611	1.0191 ± 0.0012
FIDUCIAL	11284	1.2062 ± 0.0047
TGTRACK	1322	8.54 ± 0.22
PROMPT	101	13.1 ± 1.2
KINCUT	81	1.247 ± 0.062
Sum of weights	3.15×10^{-3}	

B.2 Acceptance

Table B.75: $K^+ \to \pi^+\nu\bar{\nu}$ simulation and analysis (1991 data). The OFF and ON columns refer to events simulated without and with π^+ decay and nuclear interactions turned on, respectively.

Cut	OFF	ON
Events generated	50000	50000
KT (stopped kaon)	47556	47501
$T \cdot A$	19434	19407
B_{CT}	16049	13485
Del. coinc.	15972	13152
$\overline{(13_{CT} + ... + 18_{CT})}$	11012	10028
$\overline{(19 + 20 + 21)}$	11012	9935
$\overline{(BV + ECM + ECP)}$	11012	9917
Hextant cut	11012	9906
	11012	9906
TARGET	10952	9858
DC-SETUP	10674	9442
RS-TRACK	9914	7693
ICOUNTER	9751	7571
TRKTIM	9321	7155
INTIME	9264	6893
π^+ decay at rest	9264	6729
FIDUCIAL	8587	6251
KINSCORE	8365	5742
TGTRACK	7507	4984
KINCUT	3906	2792

B.3 Integrated kaon flux

Table B.76: Analysis of 1989 $K\mu 2(1)$ data (real and Monte Carlo) for the f_s correction factor.

Cut	Data	MC
	45698	17476
Online del. coinc.	32221	—
CERENKOV	30558	—
TARGET	29925	17393
PROMPT	23503	—
DC-SETUP	16543	17105
ICOUNTER	16308	16892
RS-TRACK	16120	16880
FIDUCIAL	15068	15808
ZDCTG	14878	15556
$R_{\rm tot}$	13801	15107

Table B.77: Analysis of 1991 $K\mu 2(1)$ data (real and Monte Carlo) for the f_s correction factor.

Cut	Data	MC
	73766	10941
Online del. coinc.	49198	—
TARGET	48561	10839
PROMPT	41016	—
DC-SETUP	35144	10683
RS-TRACK	33545	10670
ICOUNTER	31910	10376
TRKTIM	30553	9691
FIDUCIAL	28988	9294
CERENKOV	28246	—
$R_{\rm tot}$,$P_{\rm tot}$	27531	9118

Note for tables B.78 and B.79.

The acceptance factors for Monte Carlo data were simply calculated from the numbers in tables B.76 and B.77, since the sample is pure $K_{\mu 2}$. For the real data, the acceptance

factors were taken from section 5.2.1; however, the acceptance of 1991 cuts other than the online and offline delayed coincidence was measured by re-analyzing the data sample without the PROMPT cut. This is because events with no target element struck by the charged track are rejected by both the PROMPT and TRKTIM cuts, and this acceptance loss is not counted in the acceptance for the PROMPT cut given in section 5.2.1. The acceptance factors obtained by analyzing the 1991 data without the PROMPT cut were consistent with the ones obtained in tables 5.42 and 5.43, except for TRKTIM and CERENKOV. The reason for the latter being different was that the other beam and target cuts were not applied in this case; there is some overlap in the rejection of accidental beam particles for the various cuts.

Table B.78: Acceptance factors for 1989 $K_{\mu 2}$ acceptance correction. The ZDCTG cut used here only included a cut on $Z_{\rm DC}$.

Factor	**Data**	**MC**
$A_{\rm L0Delc}$	0.8300 ± 0.0054	—
A_{TG}	0.97658 ± 0.00096	0.99525 ± 0.00052
$A_{\rm Delc}$	0.8527 ± 0.0065	—
A_{DC}	0.7086 ± 0.0029	0.98344 ± 0.00097
A_{IC}	0.9836 ± 0.0030	0.98755 ± 0.00085
A_{RS}	0.99562 ± 0.00075	0.99929 ± 0.00020
A_{FID}	0.9558 ± 0.0059	0.9365 ± 0.0019
A_{ZDC}	0.98739 ± 0.00091	0.9841 ± 0.0010
A_{C_π}	0.97338 ± 0.00091	—
Total correction	0.4962 ± 0.0058	

Table B.79: Acceptance factors for 1991 $K_{\mu 2}$ acceptance correction.

Factor	**Data**	**MC**
A_{L0Delc}	0.8131 ± 0.0035	—
A_{TG}	0.98705 ± 0.00051	0.99068 ± 0.00092
A_{Delc}	0.9333 ± 0.0025	—
A_{DC}	0.8519 ± 0.0016	0.9856 ± 0.0011
A_{RS}	0.99531 ± 0.00034	0.99878 ± 0.00034
A_{IC}	0.9418 ± 0.0012	0.9724 ± 0.0016
A_{TRK}	0.8824 ± 0.0017	0.9340 ± 0.0024
A_{FID}	0.9491 ± 0.0012	0.9590 ± 0.0020
A_{C_π}	0.97338 ± 0.00091	—
Total correction	0.5740 ± 0.0042	

B.4 $K_{\pi 2}$ branching ratio measurement

Table B.80: Analysis of $K\pi 2(1)$ monitor data and Monte Carlo simulated data for the 1989 $K_{\pi 2}$ branching ratio measurement.

Cut	**# events**	
	Data	**MC**
	41817	5295
Online del. coinc.	24701	—
CERENKOV	23315	—
π^+ decay at rest	—	4439
TARGET	22698	4387
PROMPT	18147	—
DC-SETUP	12167	4029
ICOUNTER	11825	3912
RS-TRACK	11490	3853
FASFITPI	4059	—
FITPI	2519	—
ELECTRON	2138	—
ELVETO	2127	—
Stop. counter match	—	3352
FIDUCIAL, ZDCTG	1916	2919
$25.5 < R_{\rm tot} < 35.0$	1748	2567

Table B.81: Analysis of $K\pi 2(1)$ monitor data and Monte Carlo simulated data for the 1991 $K_{\pi 2}$ branching ratio measurement.

Cut	**# events**	
	Data	**MC**
	166726	10496
TARGET	163048	10348
PROMPT	97428	—
DC-SETUP	71922	9023
RS-TRACK	29804	5502
ICOUNTER	26778	5375
TRKTIM	25232	5196
FASFITPI	19684	—
FITPI	10095	—
ELVETO	9638	—
ELECTRON	8058	—
π^+ decay at rest	—	4944
FIDUCIAL	7503	4555
CERENKOV	7297	—
$26.0 < R_{\rm tot} < 34.0$	6830	4099

Appendix C

Monte Carlo Simulation

A computer program, written specifically for the BNL E787 experiment, was used for all Monte Carlo simulations. Several members of the E787 collaboration contributed to the first version of the program [82]. It defined a detector geometry as close as possible to the actual detector. The propagation of photons and electrons through the various materials was handled by subroutines from the EGS4 Monte Carlo program, a well known and extensively used simulation code [83]. For heavy charged particles ($M \gg m_e$) the energy deposition was determined by adding the energy losses due to collisions with atomic electrons in the medium (ionization or excitation). Each particle was propagated through the detector in small steps; the number of collisions in each step was determined by dividing the total average energy deposited along the step, obtained using the Bethe-Bloch formula [17], by the minimum energy a particle loses in a collision. All unstable particles were allowed to decay to appropriate final states. For kaons, specific decay modes could be selected.

Subroutines were available to treat nuclear interactions of positively charged pions and kaons in plastic scintillator. Total and differential cross-sections for the various processes were taken from the available literature. Also, the program included a package of subroutines named PICA [84], for the treatment of photo-nuclear interactions.

The flow of the program was handled by several user supplied subroutines, giving access to the output variables generated by the code at every step. In this way, a significant amount of computer time could be saved by generating only interesting events. The version of the Monte Carlo program used in this thesis included a simulation of the Level 0 and Level 1 trigger, and

the ability to record the response of the sub-detectors for each event in YBOS format [85]. The recorded events could then be analyzed with the same program (KOFIA) that was used to analyze real data.

In typical simulations, a K^+ was initially started at the front face of the target. The position and momentum of the K^+ were chosen such that the distribution of stopping coordinates for a large number of K^+ matched the distribution observed in real data. The K^+ was then allowed to decay, and all particles in the final state were propagated in the detector. Once the particle propagation was complete, the energy deposited in each part of the detector as a function of time was examined to simulate the operation of the trigger. If the event satisfied the trigger requirements, it was recorded for further analysis. In addition to the information simulating the real detector response, the full information about the propagation of each particle was recorded with the event.

Some aspects of the detector response were not simulated, notably the segmentation of the B4 hodoscope and the lead-glass detector. These sub-detectors had a small effect on the simulations. Also not simulated was the response of the transient digitizers. To simulate their effect in selecting π^+ decays, the π^+ stopping in the range stack were required to stop in scintillator and to decay at rest. In addition, the stopping range stack counter determined by the range stack tracking algorithm had to be the same as the true stopping counter.

Appendix D

Contribution to BNL E787

Modern particle physics experiments are often performed by medium to large groups of physicists, with significant support from engineering and technical staff. It is sometimes difficult to assess an individual's contribution to the experiment. Therefore, at the request of my Ph.D. committee, this appendix describes my specific contributions to the BNL E787 collaboration (see appendix A).

I was first involved as a Masters degree student (1986–1988), when I contributed to the design, construction, installation and calibration of the endcap calorimeters. This work was reported in a thesis [53]. From October 1988, I contributed as a Ph.D. student. I was on site at BNL for the entire data collection periods in 1989, 1990 and 1991. Data for this thesis were collected in 1989 and 1991. While at BNL I was specifically responsible for the maintenance and calibration of the endcap calorimeters and the determination of the transfer function of logarithmic amplifiers installed on some range stack channels. My tasks also included overall maintenance of the detector and its electronics as well as data taking shifts. In addition, I developed software to be used on-line in the ACP system for the analysis of monitor events used in calibration, for the reduction of the transient digitizer information and for the determination of the TD fiducial time.

For off-line software used by the whole collaboration, I contributed improvements to the TD data analysis and prepared low level analysis and calibration software for the inner wire chamber installed in 1991. For 1989 data, I was a member of the three-person team in charge of the initial sorting of events according to trigger types. The 1989 data analysis for the search

for $K^+ \to \pi^+\nu\overline{\nu}$ below the $K_{\pi 2}$ peak reported in this thesis was done in collaboration with Akira Konaka. Both of us developed the high level software necessary for this analysis, more specifically for refined π^+ tracking in the target, I-counters and range stack, and for the search for photon hits with incomplete time and energy information in the range stack and barrel veto. I actively participated in the preparation of the publication reporting this analysis [37] and was responsible for communications with the editors of the journal. I was also a member of an E787 internal review committee for the publication describing a search for the decay $\pi^0 \to \nu\overline{\nu}$ [87].

For the 1990 and 1991 data I was in charge of the preparation of off-line software used for the combined first analysis pass of all events, including triggers other than $\pi\nu\overline{\nu}$. This meant the integration into a single program of software developed by other members of the collaboration for specific physics analyses. For 1991 $\pi\nu\overline{\nu}$ data, I performed all the analysis and background studies reported in this thesis, and developed the techniques necessary to attempt an unbiased analysis. Improvements to the analysis software were built on the experience acquired with the 1989 analysis. More specifically, the refined π^+ tracking in the target and the photon veto cuts were improved, multi-variate analysis techniques were introduced for TD, kinematic and vertex cuts, and software was developed to perform pulse fits on the target TD information.